Advances in the Synthesis, Ligand Exchange, and Electron Transfer Dynamics of Small Gold Nanoparticles

Joseph Frederick Parker

A dissertation submitted to the faculty of the University of North Carolina at Chapel Hill in partial fulfillment of the requirements for the degree of Doctor of Philosophy in the Department of Chemistry (Analytical Chemistry).

Chapel Hill
2010

Approved by:

Advisor: Royce W. Murray

Reader: R. Mark Wightman

Reader: James Jorgenson

Reader: Joseph Templeton

Reader: Wei You

ABSTRACT

Advances in the Synthesis, Ligand Exchange, and Electron Transfer Dynamics of Small Gold Nanoparticles

(Under the Direction of Dr. Royce W. Murray)

Chapter One is a general introduction into small gold nanoparticles, specifically $Au_{25}(SR)_{18}$. It highlights the achievements made by this and other research groups in the areas of synthesis, structure determination, mass spectrometry, electrochemical and optical properties, and bimetallic nanoparticles.

Chapter Two is a detailed description of the synthesis of $Au_{25}(SR)_{18}$. It includes a historical account of the synthesis, along with an updated synthesis which increases the yield and purity and reduces cost, waste, and reaction work-up time. Specific reaction modifications are explained, and the results are discussed with regards to the mechanism of $Au_{25}(SR)_{18}$ formation.

Chapter Three describes the characterization of electron self-exchange dynamics of the nanoparticle couple $Au_{25}(S(CH_2)_2Ph)_{18}^{1-/0}$ using ^1H NMR line-broadening analysis. The changes in peak broadening at varied nanoparticle concentration and at varied temperatures allows for the calculation of self-exchange rate constants, activation energy barriers, and estimates of the outer-sphere and inner-sphere reorganization energies. The magnitudes of these values implicate structural differences between the two oxidation states.

Chapter Four investigates the effects of strongly electron-withdrawing ligands on the redox properties of $Au_{25}(SR)_{18}$. The effect of each incoming ligand on the formal potentials was

assessed using NMR and voltammetry. Density functional theory (DFT) was used to study the effects on the electronic structure induced by exchanging electron-withdrawing ligands. The calculations show how electronegative functional groups change the polarization of the nanoparticle and the charge distribution among the ligands, the semirings, and the Au_{13} core.

Chapter Five studies the electronic communication among the ligands on $Au_{25}(SR)_{18}$ nanoparticles. Ferrocene-labeled ligands were electronically coupled to the nanoparticle core and the formal potential was assessed both in the presence and absence of electron-withdrawing ligands. The results show that there exists an electronic interaction among the ligands, yet only observable when there is a large amount of extremely electron-withdrawing ligands present. The magnitude of this effect was interpreted in relation to simple-molecule analogs and DFT calculations.

Chapter Six is a survey of important ligand exchange reactions over the last five years. It details how the resulting mixed-monolayers contributed in obtaining crucial information on molecular formula, oxidation state, kinetics, electron transfer dynamics, and more.

To my Mother who taught me the only human limitations are those we put on ourselves.

And to my Father who taught me the most basic, yet wise, arithmetic:

"In five years, you will be five years older."

ACKNOWLEDGEMENTS

Writing each chapter in this dissertation would have been impossible without the contributions from my co-workers and collaborators. The list of people who deserve acknowledgements is too lengthy to include in this space, so specific remarks will be made at the end of each chapter. However, I want to specifically recognize those who played vital roles in motivating and challenging me to pursue a doctorate in chemistry. I have been extremely fortunate with the caliber of teachers, instructors, and professors who guided me through all levels of education. Shane Kuykendall of Fayette County High School, in his challenging and professional demeanor, helped me realize that this was the career path that I would undoubtedly follow. Dr. Lawrence Bottomley at the Georgia Institute of Technology introduced me to the laboratory as an undergraduate and taught me the importance of chemical research.

Dr. Royce Murray, whose wisdom, guidance, and patience can not be understated. His ability to motivate and instill confidence in his students is absolutely unrivaled. Working in his laboratory over the last five years has been a true honor.

Finally, I would like to recognize my greatest collaborator, Christine Hebling.

She inspires me every day to be a better scientist and a better person.

TABLE OF CONTENTS

Page

LIST OF TABLES

Table

LIST OF FIGURES

Figure

LIST OF ABBREVIATIONS AND SYMBOLS

a	bond length
Å	angstroms
Abs	absorbance
Ag	silver
AgCl	silver chloride
AgQRE	silve quasi reference electrode
Ar	argon
Au	gold
AuNP	gold nanoparticle
But_4N^+	*tetra*-n-butylammonium
c	concentration
CCD	charge-coupled device
Ce	cerium
CD_2Cl_2	deuterated dichloromethane
CH_3OH	methanol
CID	collision induced dissociation
cm	centimeter
COSY	correlation spectroscopy
CV	cyclic voltammetry
Da	Daltons
DCTB	*trans*-2-[3-(4-*tert*-butylphenyl)-2-methyl-2-propenylidene]malononitrile

DFT	Density Functional Theory
DPV	differential pulse voltammetry
$\delta\nu$	change in the frequency
e	electron charge
ε_o	permittivity of free space
ε_{op}	optical dielectric constant
ε_s	static dielectric constant
E_A	activation energy
Eqn	equation
ESI-MS	Electrospray Ionization mass spectrometry
Et_4N^+	*tetra*-n-ethylammonium
FAB	fast atom bombardment
Fc	ferrocene
f_{ox}	fraction in the oxidized form
f_{red}	fraction in the reduced form
FRET	fluorescence resonance energy transfer
FTICR	fourier-transorm ion cyclotron resonance
fwhm	full width at half-maximum
ΔG^o	standard free energy change
ΔG_{is}^*	inner-sphere activation energy
ΔG_{os}^*	outer-sphere activation energy
h	hour
HOMO	highest occupied molecular orbital

HREELS	High Resolution Electron Energy Loss Spectroscopy
Hz	Hertz
k	self-exchange rate constant
k_{obs}	pseudo-first order rate constant
K	degrees Kelvin
KCl	potassium chloride
$K_{DISPROPORT}$	Equilibrium Constant of Disproportionation
kJ	kilojoules
λ	reorganization energy
L	angular momentum
LDI	laser desorption ionization
LDOS	local density of electronic states
LUMO	lowest unoccupied molecular orbital
M	molar, metal
MALDI	matrix assisted laser desorption ionization
mg	milligram
min	minute
mm	millimeter
MPC	Monolayer Protected Cluster
MS	mass spectrometry
mV	millivolt
N_A	Avogadro's Number
$NaBH_4$	sodium borohydride

NIR	near infrared
nm	nanometer
NMR	Nuclear Magnetic Resonance
NP	nanoparticle
^{o}C	degrees Celsius
Oct_4N^+	tetraoctylammonium
PAGE	poly acrylamide gel electrophoresis
Pd	palladium
PL	photoluminescence
ppm	parts per million
psec	picoseconds
Pt	platinum
QQQ	triple quadripole
r	Sulfur
SAM	Self-assembled monolayer
SC2Ph	phenylethanethiolate
sec	second
SG	glutathione
-S-PEG	methoxy penta(ethylene glycol) thiolate
-SPhX	*para*-substituted thiophenolate
SR	thiolate
T	temperature
THF	tetrahydrofuran

T_n	NMR relaxation times (n = 1, 2)
TOF	time-of-flight
µL	microliter
UV-vis	ultraviolet-visible
W	peak-width
wb	widebore
x	number of bonds

Chapter 1

The Story of a Monodisperse Gold Nanoparticle: $Au_{25}L_{18}^-$

1.1 Introduction

The strong organothiolate-gold bond has spawned three major research arenas, starting with self-assembled monolayers (SAMs) on planar Au surfaces, which have been objects of numerous surface chemistry investigations. Two more recent fields involve Au nanoparticles, one being the thiolation of large citrate-protected Au colloids with ensuing biomedically-oriented studies,[1] and the other being very small (dia.<3 nm) thiolated Au NP prepared in the early work of Brust, *et al*.[2] and Whetten, *et al*.[3] This laboratory's interest in small Au nanoparticles[4] was captured by recognizing the need to better chemically define these materials and by ensuing results on size-dependent electrochemical properties and the alteration and functionalization of their ligand shells. The metal-to-molecule transition was being encountered in these thiolated Au NPs.[5] An accompanying range of research spread into other properties—photoluminescence,[6] clusters of nanoparticles,[7] biological,[8] and catalytic.[9]

The $Au_{25}L_{18}$ NP emerged as an interesting target: obvious molecule-like properties, synthetic accessibility, and isolation with good monodispersity. Its small size was appealing for theoretical investigations, which have played important roles.

Analytical advances helped to settle its identity; it was initially mis-labelled as $Au_{28}(SG)_{16}$ (SG=glutathione),[10,11] and as $Au_{38}(SCH_2CH_2Ph)_{24}$.[12] Tsukuda, *et al.*,[13] analyzed a series of electrophoretically fractionated NPs by electrospray ionization mass spectrometry (ESI-MS) and re-labeled the glutathione-protected NP as $Au_{25}(SG)_{18}$. In the intervening periods, several works had been published mis-labeling the NPs as Au_{38} and Au_{28}.

Tracy, *et al.*[14,15] established by high resolution ESI-MS that the Au_{38} NP was an anionic species: $Au_{25}(SCH_2CH_2Ph)_{18}^-$. This was accented by a structure determination[16] of the salt, $[Oct_4N^+][Au_{25}(SCH_2CH_2Ph)_{18}^-]$, that serendipitously coincided with a concurring DFT prediction.[17] This breakthrough revealed a protecting ligand shell (Figure 1.1) very different from the thiolate "head-down" ligand bonding inferred by analogy with SAMs on planar Au(111) surfaces. The NP core is a (slightly) distorted Au_{13} centered icosahedron surrounded by six $Au_2(SR)_3$ semirings, giving three kinds of Au sites (center, icosahedral surface, and semiring) and two thiolate environments. A subsequent crystal structure[18] of the oxidized form ($Au_{25}(SCH_2CH_2Ph)_{18}^0$) revealed a structural difference between the protecting semirings in the oxidized neutral and native anionic form.

Somewhat earlier, Kornberg *et al.*[19] reported the structure of a Au_{102}(SPh-*p*-$CO_2H)_{44}$ NP capped by shorter -SR-Au-SR- semirings ("staples"), supporting earlier work by the Häkkinen group[20] proposing that semiring protecting structures could be involved in the thiolate chemistry of Au NPs. Au NP research thus arrived at an interesting confluence of experiment and theory, a striking feature of which is the semiring protecting ligand layer seen in Figure 1.1.

Figure 1.1. (left) X-ray crystal structure of $[Oct_4N^+][Au_{25}(SCH_2CH_2Ph)_{18}^-]$.[16] The icosahedral Au_{13} core is surrounded by six $Au_2(SR)_3$ semirings, which are slightly puckered in the reduced nanoparticle as shown for the semiring with more pronounced yellow and pink colors. (right) The icosahedral Au_{13} core (minus the center Au) is slightly distorted; the blue Au-Au bonds lying directly below the center of each semiring are on average 0.12 Å shorter than the yellow Au-Au bonds (average 2.96 Å). Overall Au-Au average 2.93 Å. Au_{13} core diameter 9.8 Å; overall nanoparticle diameter 23.9 Å. From Ref. 16.

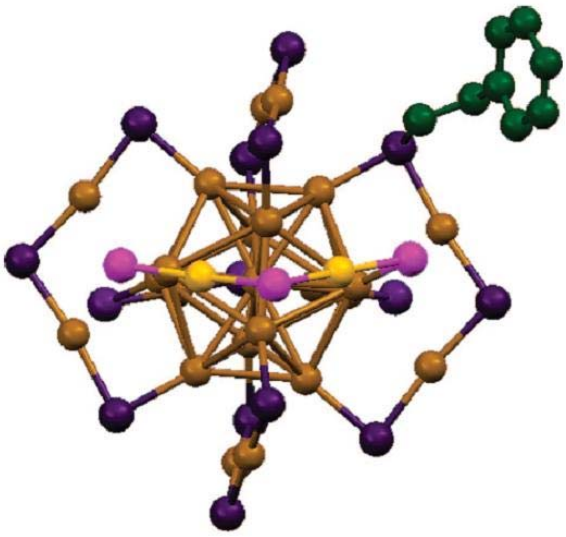

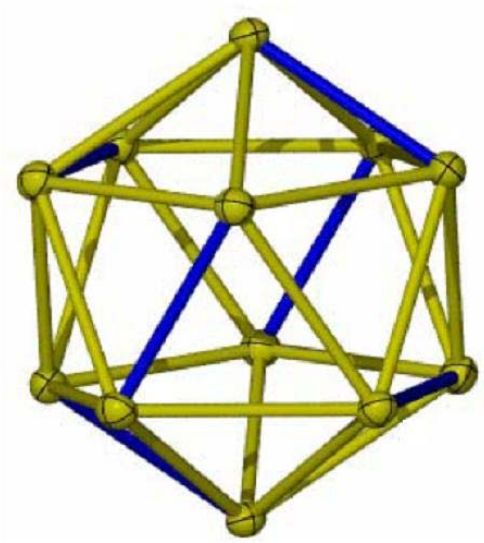

Other interesting aspects of $Au_{25}L_{18}$ are found in its voltammetry, optical spectra and photoluminescence, electron transfer chemistry, and mass spectrometry. This *Account* will expand on these and other observations.

1.2 Synthesis

Early syntheses of water-soluble glutathione-protected NPs by the Whetten[10] and Tsukuda[11,13] groups involved adding excess aqueous sodium borohydride to a cooled (0^oC) methanolic mixture of $HAuCl_4$ and glutathione. The methanol-washed, polydisperse brown-black precipitate was size-fractionated by polyacrylamide gel electrophoresis. This procedure, while pivotal in early investigations, was burdened by low yields, product polydispersity, and lengthy fractionation.

Our initial synthesis[12] of the organic-soluble $Au_{25}(SCH_2CH_2Ph)_{18}$ nanoparticle used a modified version of the "Brust reaction";[2] $AuCl_4^-$ is phase-transferred from water to toluene, reacted with $HSCH_2CH_2Ph$, and then reduced by adding aqueous $NaBH_4$. The $[Oct_4N^+][Au_{25}(SCH_2CH_2Ph)_{18}^-]$ nanoparticle product is fortuitously extractable by acetonitrile, as confirmed by (initially[12]) UV-Vis and ^1H NMR, and (later[14]) mass spectrometry, yielding ~15%.

Further procedural improvements[21,22] have increased the yield of the $–SCH_2CH_2Ph$ protected NP. Wu, *et al.*[21] enhanced the yield to *ca.* 40% by tuning the temperature and duration of different steps, hypothesizing that reduced temperature and prolonged slow stirring increases the Au(I):SR aggregates leading to Au_{25} clusters. In our own hands, this procedure produces partially oxidized NPs (Au_{25}^0), so we modified[23]

it to avoid this effect. It is now possible to produce substantial quantities (>500 mg/preparation) of pure Au_{25}^- NP with $–SCH_2CH_2PH$ or various other thiolate ligands.

The ligation of $Au_{25}L_{18}^-$ can be altered, partially[24] or completely,[25] by ligand exchanges, which have been valuable tools in exploring NP properties.[5] Characterized as associative reactions,[26] they are first-order in NP and incoming thiol. It is evident from Figure 1.1 that exchange of ligands on the semirings must involve breaking multiple Au-SR bonds, but the details of this reaction remain unclear.

1.3 Crystal Structure

A seminal step in understanding small Au was the report[19] of the "staple" coordination geometry of the thiolate ligands on the NP $Au_{102}(SPh\text{-}p\text{-}CO_2H)_{44}$. Shortly later, the structures[16,18] were also solved for the two redox states of Au_{25} (-1 and 0). While earlier predictions[27,28] regarding the Au_{25} structure were not supported experimentally, DFT calculations published concurrently[17] with the Au_{25}^- crystal result correctly represented the main structural details, including the semirings (Figure 1.1). Nuances of these crystal structures led to theoretical predictions on the structure of other sized nanoparticles, including $Au_{38}(SR)_{24}$.[29,30]

The $[Oct_4N^+][Au_{25}(SCH_2CH_2Ph)_{18}^-]$ crystal has a triclinic space group P1 and unit cell with Z=1, three different Au sites (centered, Au_{13} surface, semiring), and six semirings. The thiolate sulfur has two different environments, and the nearly linear -S-Au-S- coordination geometries is reminiscent of Au(I) chemistry. Au-Au distances within the Au_{13} core are typical for Au-Au atom bonding.[16] Both the icosahedron and the semirings are slightly distorted; core Au-Au bonds lying below the semiring centers

(Figure 1.1, right) are slightly shorter than the others. In the semirings, the terminal Au_{CORE}-S bonds are slightly longer (2.38 Å) than the others (2.32 Å), and the semirings are slightly puckered. These observations suggest an intimate structural relationship between the ligands and the core. DFT calculations assessing the high Au_{25} stability[17] concluded that the HOMO level is 3-fold degenerate and mainly P-character while the LUMO level is 2-fold degenerate with mainly D-symmetry. The energy gap is predicted as 1.2 eV, which is close to the reported 1.3 eV.[31] The Au_{13} core contains 14 valence electrons, the electronic density of states reveals a shell closing at 8 electrons, so the semirings localize one Au(6s) electron each via the formation of strongly polar covalent bonds. As a "monolayer protected cluster,"[5] the bidentate entity $Au_2(SR)_3$ constitutes the protecting ligand.

The crystal structure of the oxidized NP, $Au_{25}(SCH_2CH_2Ph)_{18}^0$ reported by Zhu *et al.*,[18] differs from that in Figure 1.1 in (at least) one major respect; the semirings are flattened. The structural difference between the two redox states implies that the electron transfer energy barrier includes an inner sphere reorganizational component, which was apparent in earlier reports.[32-34]

1.4 Mass Spectrometry

Many ionization modes have been applied in NP MS analysis, including Cf plasma desorption ionization,[35] laser desorption ionization (LDI),[10,22,36] and ESI.[11,13,37] ESI-MS is an attractive, low-fragmentation mode, and was employed in the correct compositional assignment of $Au_{25}L_{18}$ by Negishi, *et al.*,[13] using electrophoretically-separated water-soluble NPs with glutathione ligands. Implementing higher resolution

positive-mode ESI-MS, Tracy *et al.*[14] used methoxy penta(ethylene glycol) thiolate ligands (-S-$(C_2H_4O)_5CH_3$, –S-PEG) in the $Au_{25}L_{18}^-$ ligand shell to coordinate with alkali metal ions, producing 3+ and 4+ NP charge states (Figure 1.2a). The envelopes of these states contain peaks spaced by 130 Da (the mass difference between –S-PEG and –SCH_2CH_2Ph) that represent different numbers of exchange-incorporated –S-PEG ligands at the time of sampling. The 3+ ion spectra (Figure 1.2b) using Na^+ and Cs^+ salts are accurately reconciled by assuming –S-PEG coordination of four Na^+ or Cs^+, which concurrently reveals the nanoparticle as reduced and present as the $[Oct_4N^+][Au_{25}(SCH_2CH_2Ph)_{18}^-]$ salt. The ESI-MS analysis was expanded[15a] to other ligands (See Appendix Figures A1.1, A1.2), revealing a rich chemistry of ligand dissociation, fragmentation, and adduct formation. These results coincide with and sharpen the isolation and "magic stability" characterization of the $Au_{25}L_{18}$ NP by Tsukuda, *et al.*[38] Lessons learned in the ESI-MS analysis of Au_{25} have been important in extending exact ESI-MS analysis to higher mass NPs like $Au_{144/146}$.[15b]

Matrix assisted laser desorption ionization (MALDI-MS) and LDI[10,22,36,37] used in NP investigations typically yield extensive core and ligand fragmentation, complicating formula assignments. A change from typical proton-transfer matrices to one reputedly favoring electron-transfer and use of threshold laser fluences produced[39] unfragmented $Au_{25}(SCH_2CH_2Ph)_{18}$ spectra (Figure A1.3). A favored loss of a stable fragment Au_4L_4 forecasts an eventual better understanding of NP fragmentation chemistry.

The MALDI study,[39] and another (Figure A1.4) using fast atom bombardment (FAB) ionization,[40] stimulated a more explicit examination[41] by collision induced dissociation (CID MS/MS) of –S-PEG exchanged Au_{25} NP ions generated in ESI-MS. In

Figure 1.2. (a) Full ESI scan of $Au_{25}L_{18}$ with additional NaOAc. (b) Set of 3+ peaks acquired by adding NaOAc (black) and CsOAc (red) to the NPs before spraying. Insets show greater detail in selected regions. (c) High-resolution analysis of prominent 3+ ions acquired in the NaOAc experiments compared with simulations (black). From Ref. 14.

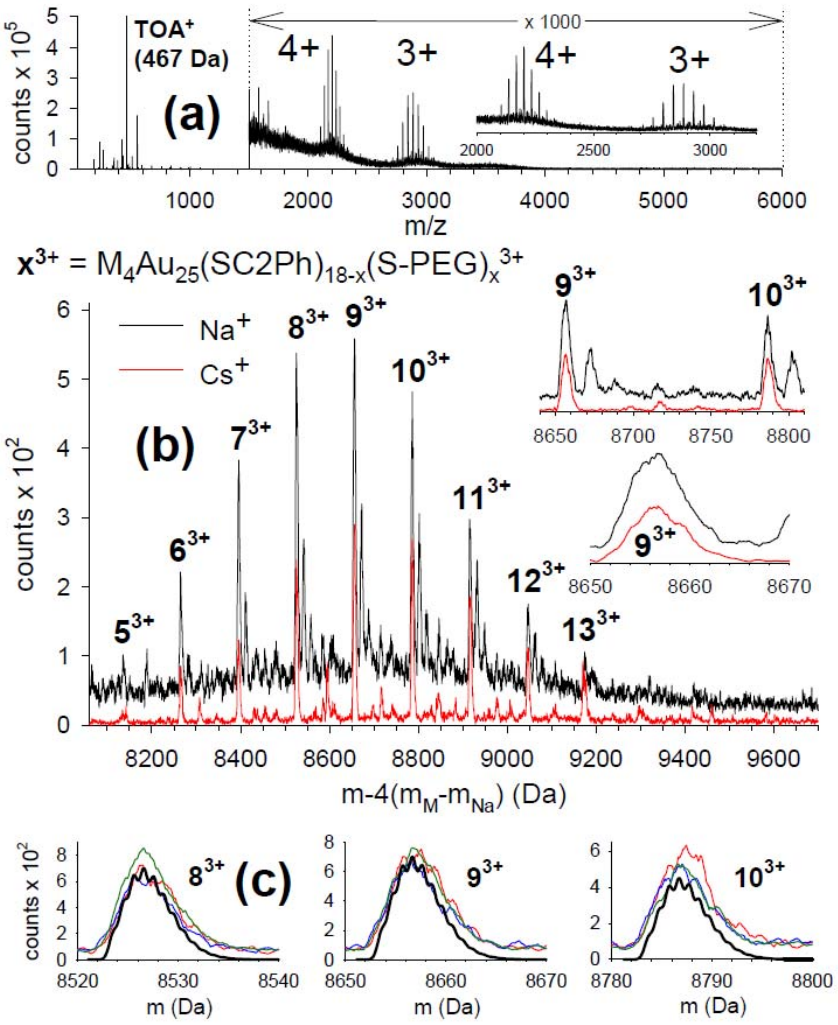
TOA+
(467 Da)
(a)
4+
3+
x 1000
counts x 10^5
m/z
x^3+ = M4Au25(SC2Ph)18-x(S-PEG)x^3+
Na+
Cs+
(b)
5^3+
6^3+
7^3+
8^3+
9^3+
10^3+
11^3+
12^3+
13^3+
counts x 10^2
m-4(mM-mNa) (Da)
(c)
8^3+
9^3+
10^3+
m (Da)

this ion trap-based experiment, selected precursor ions collide with Ar gas and the resulting fragments are mass analyzed (Figure A1.5). The detected low mass fragments include not only the loss of an entire semiring fragment Au_2SR_3, but also loss of the $Au_4(SR)_4$ moiety, which requires a rearrangement process involving more than one semiring. Under non-CID conditions, ESI-TOF-MS and ESI-FTICR-MS spectra (Figure A1.6) display the same small fragments at isotopic resolution. The CID results demonstrate that the small fragments are a consequence of the ESI process as opposed to contaminants in the NP samples. Some high mass fragments in the CID could be understood (such as $Au_{24}L_{16}$, indicating a AuL_2 loss, Figure A1.7), while other non-obvious high mass fragments shows that $Au_{25}L_{18}$ NP fragmentation chemistry is apparently multi-step and includes rearrangements.

The envelopes of 3+ and 4+ peaks (Figure 1.2a) have further interest because the distribution of peaks is related to whether ligand exchanges occur randomly and independently (of one another) over the 18 –SR binding sites on $Au_{25}L_{18}$. This was explored[42] using MALDI on NPs synthesized with different mole ratios of hexanethiol and phenylethanethiol (Figure 1.3). In each mixed-ligand nanoparticle, the relative numbers of hexanethiolate and phenylethanethiolate ligands follow the expected binominal distribution (as in Figure 1.2). The overall process, however, does favor a greater *average* incorporation of the phenylethanethiolate ligand as is clear from the central average of the peak distribution for the 50:50 starting ligand ratio.

Mixed ligand distributions can also be observed[42] as they develop during a ligand exchange reaction (like Figure 1.2). Statistically analyzing the profile of ligand exchange incorporation of –SC6 ligands onto $Au_{25}(SCH_2CH_2Ph)_{18}$ produces the binomial

Figure 1.3. Monolayer ligand distribution of the mixed Brust reaction product $Au_{25}(SCH_2CH_2Ph)_{18-x}(SC6)_x$ as observed by MALDI-MS spectrum using different starting ligand ratios 25:75, 50:50, and 75:25. From Ref. 42.

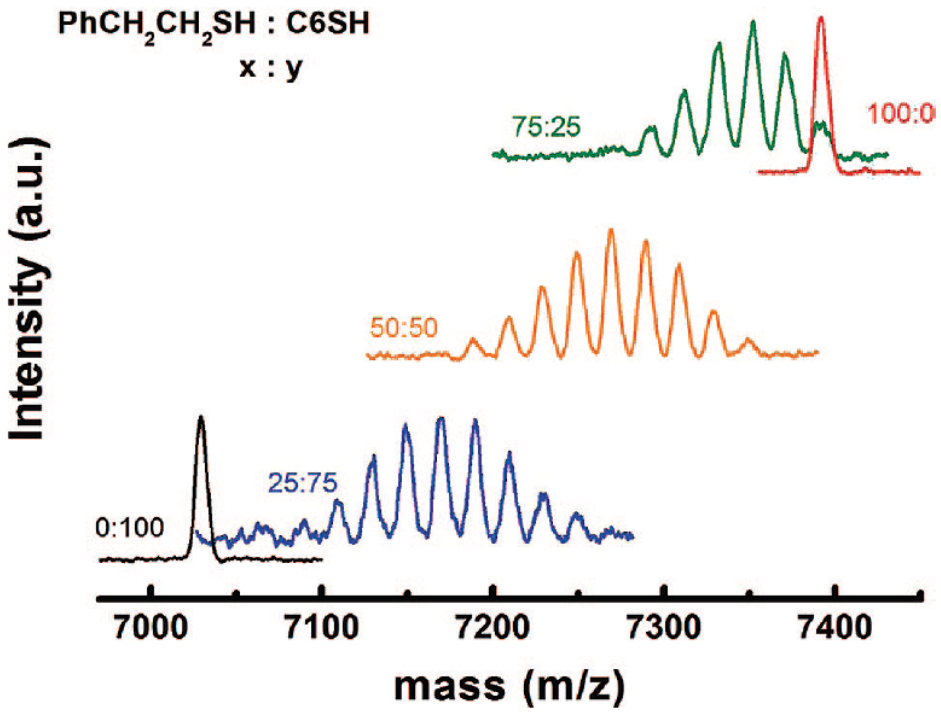
PhCH2CH2SH : C6SH
x : y
Intensity (a.u.)
75:25
100:0
50:50
25:75
0:100
7000
7100
7200
7300
7400
mass (m/z)

distribution expected for the 18 ligand sites having identical and independent reactivities. However, distributions from exchange of –SPh ligands were narrower than expected. It would appear that such ligand exchange data could be valuable in assessing intra-nanoparticle ligand interactions,[42] such as those invoked in phase segregated ligand shells.[43]

ESI-MS data were also useful for studying M_{25} bimetal nanoparticles synthesized[44] using a mixture of Au and Pd salts with the $HSCH_2CH_2Ph$ thiol and an isolation procedure targeting small NP products. Exchanges to introduce –S-PEG ligands and positive mode ESI-MS spectra (Figure A1.8) revealed that the product was a mixture of $Au_{25}(SCH_2CH_2Ph)_{18}$ and $Au_{24}Pd(SCH_2CH_2Ph)_{18}$. Larger numbers of introduced Pd sites were not observed. Substitution of Pd for Au in $Au_{25}(SR)_{18}$ is evidently not favorable. That introduction[44] of a single Pd atom substantially alters the distinctive $Au_{25}L_{18}$ optical and electrochemical signatures was supported by a DFT study,[45] concluding that the optical properties and energy gap differ according to the location of the Pd site (center, core surface, semiring), and that inclusion of additional Pd sites could lead to more readily oxidizable and less stable materials. DFT efforts[46,47] have also considered the possibilities of a wider range of (singly) incorporated elements, and it seems possible that the properties of $Au_{25-x}M_xL_{18}$ nanoparticles could be "tuned" in this way.

1.5 Voltammetry and Electron Transfer Properties

The voltammetry of small Au nanoparticles can be very informative about their electronic properties. Nanoparticles of "Au_{144}" and "Au_{225}" composition show quantized

double layer charging where the voltage spacing between neighboring voltammetric features is more or less uniform and dominated by capacitive properties. Smaller nanoparticles show an extra voltage spacing (the electrochemical energy gap) between the first oxidation and first reduction steps that reflects the emergence of a HOMO-LUMO energy gap.[48] The gap between the formal potentials of the $Au_{25}L_{18}^{0/1-}$ and $Au_{25}L_{18}^{1-/2-}$ couples (in CH_2Cl_2/electrolyte) is[31] 1.62 V (Figure 1.4). Estimating charging energy from the spacing between the $Au_{25}L_{18}^{0/1-}$ and $Au_{25}L_{18}^{1+/0}$ waves (0.29 V) gives a gap energy in agreement with the optically observed HOMO-LUMO gap energy of 1.33 eV.

The formal potential of the $Au_{25}L_{18}^{0/1-}$ couple (HOMO electronic level) is sensitive to the thiolate ligand employed. Replacing[25] the original $-SCH_2CH_2Ph$ ligands with thiophenolate ligands (–SPh-*p*-X, where X=NO_2, Br, H, CH_3, and OCH_3) shifts the formal potential positively as "X" becomes more electron-withdrawing—without change in the HOMO-LUMO gap energy. The ligand exchange kinetics follow an analogous order,[26] with $-NO_2$ being the fastest. It has been further found—experimentally and with DFT calculations[24]—that the $Au_{25}L_{18}^{0/1-}$ formal potential changes *linearly* with the number of exchanged ligands: 42 mV/ligand for exchange by $-SPhNO_2$ and 60 mV/ligand for (theoretical) exchange by $-SCH_2Cl$. Importantly, the DFT analysis shows that the ligand-induced transfer of charge occurs solely within the semiring structure (Figure 1.1), and not within the Au_{13} core.

Considerable information is also now available regarding the dynamics of electron transfers in the $Au_{25}(SCH_2CH_2Ph)_{18}^{0/1-}$ redox couple. The electron-hopping conductivities (which reflect electron self-exchange rates) of mixed valent films[33] of

Figure 1.4. (top) Differential pulse voltammogram (DPV) at 0.02 V/s, and (bottom) cyclic voltammogram (0.1 V/s) of $Au_{25}(SCH_2CH_2Ph)_{18}$ in 0.1 M Bu_4NPF_6 in degassed CH_2Cl_2 at 0.4 mm diameter Pt working, Ag quasi-reference (AgQRE), and Pt-wire counter electrodes. Both voltammograms were obtained at -70^{o}C. (Arrow indicates solution rest potentials.) From Ref. 31.

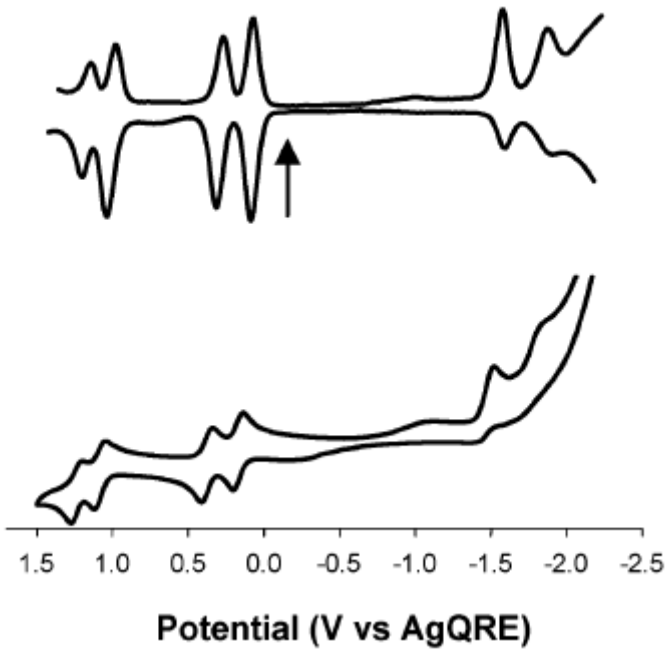
1.5
1.0
0.5
0.0
-0.5
-1.0
-1.5
-2.0
-2.5
Potential (V vs AgQRE)

$Au_{25}^{0/1-}$ and $Au_{144}^{1+/0}$ are remarkably different, the former being >10^3 slower. The activation barrier energies also differ sharply by 3-fold. Estimates[33] of the outer-sphere (Marcus) reorganizational energies for these two nanoparticle couples are both close to the experimental $Au_{144}^{1+/0}$ nanoparticle result, suggesting that the slow $Au_{25}^{0/1-}$ electron transfers reflect an "inner sphere" reorganizational energy barrier[49] component, i.e., changes in nuclear coordinates accompany electron transfer. Values of heterogeneous electron transfer rate constants and activation barrier energies in solution voltammetry reported by Antontello, *et al.*[24] supported that suggestion.

In a ^{1}H NMR investigation[32] of the $Au_{25}(SCH_2CH_2Ph)_{18}^{0/1-}$ electron transfer couple, and following the structural elucidation[16] of the reduced form, $Au_{25}(SCH_2CH_2Ph)_{18}^{1-}$, the chemical shift of the α-methylene proton resonances in solutions of solely the oxidized form was found to lie about 2 ppm downfield from that of the reduced form. The large chemical shift change is recognized as a consequence of an unpaired electron spin in the $Au_{25}(SCH_2CH_2Ph)_{18}^{0}$ nanoparticle, and indeed its electron spin resonance spectrum has since been reported.[50] Mixtures of $Au_{25}(SCH_2CH_2Ph)_{18}^{1-}$ and $Au_{25}(SCH_2CH_2Ph)_{18}^{0}$, show averaged chemical shifts[32] as expected for electron exchanges between the two states (Figure 1.5) and display an enhanced linewidth broadening which reflects a classical NMR two-state exchange process. Its analysis and temperature dependence produced[32] a room temperature electron self-exchange rate constant $k_{EX} = 3\times10^7$ $M^{-1}s^{-1}$ and a large activation energy (25 kJ/mol) that is consistent with the earlier results.[33,34] The suggestion[33] of a structural change accompanying electron transfer was confirmed by Raman spectroscopy; the Au-S stretches (now recognized as radial breathing modes[51]) of the ligand shell differ by 24 cm^{-1} between the

Figure 1.5. ^{1}H Nuclear magnetic resonance spectra of reduced $[Au_{25}(SCH_2CH_2)_{18}]^{1-}$, oxidized $[Au_{25}(SCH_2CH_2)_{18}]^{0}$, and mixtures of the two forms, presented as fraction of oxidized (*fox*) material present. The inset shows the linearity of chemical shift with *fox*, consistent with a fast exchange mechanism. The mixtures exhibit peak widths greater than those of the two pure forms. The fwhm is dependent on the total concentration of nanoparticle in solution and the relative fraction of each form. From Ref. 32.

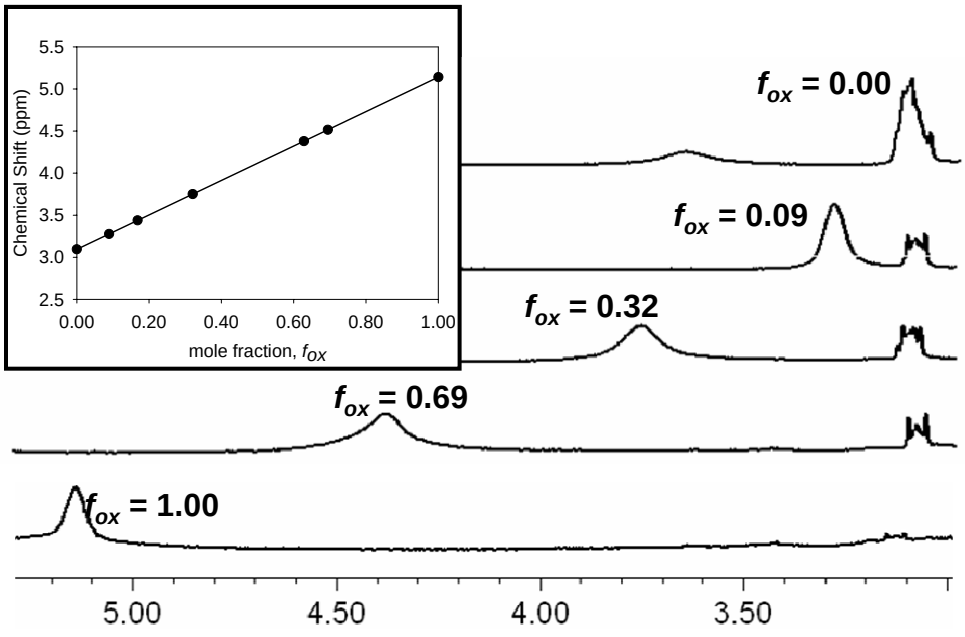
Chemical Shift (ppm)
5.5
5.0
4.5
4.0
3.5
3.0
2.5
0.00
0.20
0.40
0.60
0.80
1.00
mole fraction, f_{ox}
f_{ox} = 0.00
f_{ox} = 0.09
f_{ox} = 0.32
f_{ox} = 0.69
f_{ox} = 1.00
5.00
4.50
4.00
3.50

two states. The further piece of the electron transfer dynamics puzzle was added by solution[18] of the oxidized form's crystal structure, which showed that the "puckered" semirings of the reduced form become flattened upon oxidation. An alternate, theoretical view[51] suggests that the ring puckering may originate from interactions with the Oct_4N^+ counterion. The structural change indicated by the Raman result may possibly therefore be a different, more complex structural alteration.

The preceding analysis of structural aspects of the $Au_{25}(SCH_2CH_2Ph)_{18}^{0/1-}$ electron transfer couple dynamics, to which a variety of different experiments contributed, is the first nanoparticle analogy to the classical "inner sphere reorganization" in slowed electron transfers of the $Fe(H_2O)_6^{3+/2+}$ couple where the Fe-O bond length contracts in the oxidized form.[49]

1.6 Optical Spectroscopy

Au_{25} nanoparticles exhibit interesting optical absorbance and fluorescence characteristics. The optical dependence[31] on oxidation state of $Au_{25}(SCH_2CH_2Ph)_{18}$ is illustrated in Figure A1.9. The broad feature around 1.8 eV for the reduced state is two overlapped peaks (1.84 eV (675 nm) and 1.61 eV (770 nm)), the latter of which is extinguished upon oxidation and reflects a HOMO electron. The absorbance edge from these spectra, 1.33 eV, matches the electrochemical observations and is close to the 1.24 eV calculated[17] value. Calculations on these low energy optical transitions[17,52,53] have been consistent with the idea[54] of "superatomic orbitals" of the NP core.

Au_{25} nanoparticles exhibit near-IR photoluminescence, weakly[31] with–SCH_2CH_2Ph ligands but more intensely with electron-withdrawing ones.[6,55] The PL is attributed to

surface states since its energy is essentially invariant with the size of the nanoparticle.[56] The later discovery[16] of the semiring ligand architecture invites attention to it as the probable electronic locus of these emissions.

Attention is also turning to transient optical spectroscopy to map the dynamics of electronic relaxations. Upon excitation at 530 nm on fast timescales, pump-probe experiments show very fast (< 0.2 psec) relaxation of the core excitation with internal conversion to ligand shell states which relax on a slower, 1.2 psec timescale. The NIR PL of Au_{25} NPs has been determined by transient absorption to occur with lifetimes of 3 psec[57] and 4-5 psec.[58] Goodson and co-workers observed[59] two-photon cross-sections for Au_{25} NPs and found them much larger than those of organic macromolecules and semiconductor nanocrystals. Two photon absorptions can have a number of useful nonlinear optical applications in biological imaging, optical power limiting, and nanolithography. Au_{25} has also been shown to be an effective material for fluorescence resonance energy transfer (FRET)[60] between the core and ligand shell, specifically in the case of $Au_{25}(SG)_{18}$ and dansyl chromophores bound to the core via glutathione linkers. Efficient FRET was observed from the dansyl donor to the Au_{25} core, as observed by the reduced lifetime of the excited state and reduced fluorescence of the dansyl chromophore ligand. Concurrently, the Au_{25} emission at 700 nm was enhanced, which is consistent with FRET observations.

1.6 Conclusions

We report on what has become perhaps the most understood Au nanoparticle and track it through its history of (incorrect/correct) identification, structure determination,

and analytical properties. As the details of Au_{25} continue to be fleshed out, we believe the results summarized in this *Account* will be useful for further analyses and applications.

1.7 Acknowledgements

This research was supported by the National Science Foundation and Office of Naval Research. I also thank Christina Fields-Zinna for her contribution and discussion on the mass spectrometry sections. I would like to thank the many researchers, past and present, who have contributed to the advancement of the materials mentioned in this Chapter.

1.7 References

(1) Rose, N. L.; Mirkin, C. A. Nanostructures and Biodiagnostics. *Chem. Rev.* **2005**, *105*, 1547-1562.

(2) Brust, M.; Walker, M.; Bethell, D.; Schiffrin, D. J.; Whyman, R. Synthesis of thiol-derivatised gold nanoparticles in a two-phase Liquid–Liquid system. *J. Chem. Soc., Chem. Commun.* **1994**, 801-802.

(3) Whetten, R. L.; Khoury, J. T.; Alvarez, M. M.; Murthy, S.; Vezmar, I.; Wang, Z. L.; Stephens, P. W.; Cleveland, C. L.; Luedtke, W. D.; Landman, U. Nanocrystal Gold Molecules. *Adv. Mater.* **1996**, *8*, 428-433.

(4) Terrill, R. H.; Postlethwaite, T. A.; Chen, C.-h.; Poon, C.-D.; Terzis, A.; Chen, A.; Hutchison, J. W.; Clark, M. R.; Wignall, G.; Londono, J. D.; Superfine, R.; Falvo, M.; Johnson, C. S.; Samulski, E. T.; Murray. R. W. Monolayers in Three Dimensions: NMR, SAXS, Thermal, and Electron Hopping Studies of Alkanethiol Stabilized Gold Clusters. *J. Am. Chem. Soc*. **1995**, *117*, 12537-12548.

(5) Templeton, A. C; Wuelfing, W. P.; Murray, R. W. Monolayer-Protected Cluster Molecules. *Accts. Chem. Res.* **2000**, *33*, 27-36.

(6) Wang, G.; Huang, T.; Murray, R. W.; Menard, L.; Nuzzo, R. G. Near-IR Luminescence of Monolayer-Protected Metal Clusters. *J. Am. Chem. Soc.* **2005**, *127*, 812-813.

(7) McConnell, W. P.; Novak, J. P.; Brousseau, L. C., III; Fuierer, R. R.; Tenent, R. C.; Feldheim, D. L. Electronic and Optical Properties of Chemically Modified Metal Nanoparticles and Molecularly Bridged Nanoparticle Arrays. *J. Phys. Chem. B* **2000**, *104*, 8925-8930.

(8) Andres, R. P.; Bein, T.; Dorogi, M.; Feng, S.; Henderson, J. I.; Kubiak, C. P.; Mahoney, W.; Osifchin, R. G.; Reifenberger, R. "Coulomb Staircase" at Room Temperature in a Self-Assembled Molecular Nanostructure. *Science* **1996**, *272*, 1323-1325.

(9) Pasquato, L.; Pengo, P.; Scrimin, P. Functional gold nanoparticles for recognition and catalysis. *J. Mat. Chem.* **2004**, *14*, 3481-3487.

(10) Schaaf, T. D.; Knight, G.; Shafigullin, M. N.; Borkman, R. F.; Whetten, R. L. Isolation and Selected Properties of a 10.4 kDa Gold:Glutathione Cluster Compound. *J. Phys. Chem. B* **1998**, *102*, 10643-10646.

(11) Negishi, Y.; Takasugi, Y.; Sato, S.; Yao, H.; Kimura, K.; Tsukuda, T. Magic-Numbered Au_n Clusters Protected by Glutathione Monolayers (n=18, 21, 25, 28,

32, 39): Isolation and Spectroscopic Characterization. *J. Am. Chem. Soc.* **2004**, *126*, 6518-6519.

(12) Donkers, R. L.; Lee, D.; Murray, R. W. Synthesis and Isolation of the Molecule-like Cluster $Au_{38}(SCH_2CH_2Ph)_{24}$. *Langmuir* **2004**, *20*, 1945-1952.

(13) Negishi, Y.; Nobusada, K.; Tsukuda, T. Glutathione-Protected Gold Clusters Revisited: Bridging the Gap between Gold(I)−Thiolate Complexes and Thiolate-Protected Gold Nanocrystals. *J. Am. Chem. Soc.* **2005**, *127*, 5261-5270.

(14) Tracy, J. B.; Kalyuzhny, G.; Crowe, M. C.; Balasubramanian, R.; Choi, J.-P.; Murray, R. W. Poly(ethylene glycol) Ligands for High-Resolution Nanoparticle Mass Spectrometry. *J. Am. Chem. Soc.* **2007**, *129*, 6706-6707.

(15) a) Tracy, J. B.; Crowe, M. C.; Parker, J. F.; Hampe, O.; Fields-Zinna, C. A.; Dass, A.; Murray, R. W. Electrospray Ionization Mass Spectrometry of Uniform and Mixed Monolayer Nanoparticles: $Au_{25}[S(CH_2)_2Ph]_{18}$ and $Au_{25}[S(CH_2)_2Ph]_{18-x}(SR)_x$. *J. Am. Chem. Soc.* **2007**, *129*, 16209-16215. b) Fields-Zinna, C. A.; Sardar, R.; Beasley, C. A.; Murray, R. W. Electrospray Ionization Mass Spectrometry of Intrinsically Cationized Nanoparticles, $[Au_{144/146}(SC_{11}H_{22}N(CH_2CH_3)_3^+)_x(S(CH_2)_5CH_3)_y]^{x+}$. *J. Am. Chem. Soc*. **2009**, *131*, 13844-13851.

(16) Heaven, M. W.; Dass, A.; White, P. S.; Holt, K. M.; Murray, R. W. Crystal Structure of the Gold Nanoparticle $[N(C_8H_{17})_4][Au_{25}(SCH_2CH_2Ph)_{18}]$. *J. Am. Chem. Soc.* **2008**, *130*, 3754-3755.

(17) Akola, J.; Walter, M.; Whetten, R. L.; Häkkinen, H.; Grönbeck, H. On the Structure of Thiolate-Protected Au_{25}. *J. Am. Chem. Soc.* **2008**, *130*, 3756-3757.

(18) Zhu, M.; Eckenhoff, W. T.; Pintauer, T.; Jin, R. Conversion of Anionic $[Au_{25}(SCH_2CH_2Ph)_{18}]^-$ Cluster to Charge Neutral Cluster via Air Oxidation. *J. Phys. Chem. C* **2008**, *112*, 14221-14224.

(19) Jadzinsky, P. D.; Calero, G.; Ackerson, C. J.; Bushnell, D. A.; Kornberg, R. D. Structure of a Thiol Monolayer-Protected Gold Nanoparticle at 1.1 Å Resolution. *Science* **2007**, *318*, 430-433.

(20) Häkkinen, H.; Walter, M.; Grönbeck, H. Divide and Protect: Capping Gold Nanoclusters with Molecular Gold−Thiolate Rings. *J. Phys. Chem. B* **2006**, *110*, 9927-9931.

(21) Wu, Z.; Suhan, J.; Jin R. One-pot synthesis of atomically monodisperse, thiol-functionalized Au_{25} nanoclusters. *J. Mater. Chem.* **2009**, *19*, 622-626.

(22) Price, R. C.; Whetten, R. L. All-Aromatic, Nanometer-Scale, Gold-Cluster Thiolate Complexes. *J. Am. Chem. Soc.* **2005**, *127*, 13750-13751.

(23) Parker, J. F.; Weaver, J. E. F.; McCallum, F.; Murray, R. W. **2010**, *Manuscript in Preparation*.

(24) Parker, J. F.; Kacprzak, K. A.; Lopez-Acevedo, O.; Hakkinen, H.; Murray, R. W. Experimental and Density Functional Theory Analysis of Serial Introductions of Electron-Withdrawing Ligands into the Ligand Shell of a Thiolate-Protected Au_{25} Nanoparticle. *J. Phys. Chem. C* **2010**, *114*, 8276-8281

(25) Guo, R.; Murray, R. W. Substituent Effects on Redox Potentials and Optical Gap Energies of Molecule-like $Au_{38}(SPhX)_{24}$ Nanoparticles. *J. Am. Chem. Soc.* **2005**, *127*, 12140-12143.

(26) Guo, R.; Song, Y.; Wang, G.; Murray, R. W. Does Core Size Matter in the Kinetics of Ligand Exchanges of Monolayer-Protected Au Clusters? *J. Am. Chem. Soc.* **2005**, *127*, 2752-2757.

(27) Iwasa, T.; Nobusada, K. Theoretical Investigation of Optimized Structures of Thiolated Gold Cluster $[Au_{25}(SCH_3)_{18}]^+$. *J. Phys. Chem. C* **2007**, *111*, 45-49.

(28) Iwasa, T.; Nobusada, K. Gold-thiolate core-in-cage cluster $Au_{25}(SCH_3)_{18}$ shows localized spins in charged states. *Chem. Phys. Lett.* **2007**, *441*, 268-272.

(29) Jiang, D.; Tiago, M. L.; Luo, W.; Dai, S. The "Staple" Motif: A Key to Stability of Thiolate-Protected Gold Nanoclusters. *J. Am. Chem. Soc.* **2008**, *130*, 2777-2779.

(30) Jiang, D.; Luo, W.; Tiago, M. L.; Dai, S. In Search of a Structural Model for a Thiolate-protected Au_{38} Cluster. *J. Chem. Phys. C* **2008**, *112*, 13905-13910.

(31) Lee, D.; Donkers, R. L.; Wang, G.; Harper, A. S.; Murray, R. W. Electrochemistry and Optical Absorbance and Luminescence of Molecule-like Au_{38} Nanoparticles. *J. Am. Chem. Soc.* **2004**, *126*, 6193-6199.

(32) Parker, J. F.; Choi, J-P.; Wang, W.; Murray, R. W. Electron Self-exchange Dynamics of the Nanoparticle Couple $[Au_{25}(SC_2Ph)_{18}]^{0/1-}$ By Nuclear Magnetic Resonance Line-Broadening. *J. Phys. Chem. C* **2008**, *112*, 13976-13981.

(33) Choi, J-P.; Murray, R. W. Electron Self-Exchange between $Au_{140}^{+/0}$ Nanoparticles Is Faster Than That between $Au_{38}^{+/0}$ in Solid-State, Mixed-Valent Films. *J. Am. Chem. Soc.* **2006**, *128*, 10496-10502.

(34) Antonello, S.; Holm, A. H.; Instuli, E.; Maran, F. Molecular Electron-Transfer Properties of Au_{38} Clusters. *J. Am. Chem. Soc.* **2007**, *129*, 9836-9837.

(35) Fackler, J. P.; McNeal, C. J.; Winpenny, R. E. P.; Pignolet, L. H. Californium-252 Plasma Desorption Mass Spectrometry as a Tool for Studying Very Large Clusters; Evidence for Vertex-Sharing Icosahedra as Components of $Au_{67}(PPh_3)_{14}Cl_8$. *J. Am. Chem. Soc.* **1989**, *111*, 6434-6435.

(36) Schaaff, T. G.; Shafigullin, M. N.; Khoury, J. T.; Vezmar, I.; Whetten, R. L. Properties of a Ubiquitous 29 kDa Au:SR Cluster Compound. *J. Phys. Chem. B* **2001**, *105*, 8785-8796.

(37) a) Negishi, Y.; Takasugi, Y.; Sato, S.; Yao, H.; Kimura, K.; Tsukuda, T. Kinetic Stabilization of Growing Gold Clusters by Passivation with Thiolates. *J. Phys. Chem. B* **2006**, *110*, 12218-12221. b) Shichibu, Y.; Negishi, Y.; Tsukuda, T.; Teranishi, T. Large-Scale Synthesis of Thiolated Au_{25} Clusters via Ligand Exchange Reactions of Phosphine-Stabilized Au11 Clusters. *J. Am. Chem. Soc.* **2005**, *127*, 13464-13465.

(38) Negishi, Y.; Chaki, N. K.; Shichibu, Y.; Whetten, R. L.; Tsukuda, T. Origin of Magic Stability of Thiolated Gold Clusters: A Case Study on $Au_{25}(SC_6H_{13})_{18}$. *J. Am. Chem. Soc.* **2007**, *129*, 11322-11323.

(39) Dass, A.; Stevenson, A.; Dubay, G. R.; Tracy, J. B.; Murray, R. W. Nanoparticle MALDI-TOF Mass Spectrometry without Fragmentation: $Au_{25}(SCH_2CH_2Ph)_{18}$ and Mixed Monolayer $Au_{25}(SCH_2CH_2Ph)_{18-x}(L)_x$. *J. Am. Chem. Soc.* **2008**, *130*, 5940-5946.

(40) Dass, A.; Dubay, G. R.; Fields-Zinna, C. A.; Murray, R. W. FAB Mass Spectrometry of $Au_{25}(SR)_{18}$ Nanoparticles. *Anal. Chem.* **2008**, *80*, 6845-6849.

(41) Fields-Zinna, C. A.; Sampson, J. S.; Crowe, M. C.; Tracy, J. B.; Parker, J. F.; deNey, A. M.; Muddiman, D. C.; Murray, R. W. Tandem Mass Spectrometry of Thiolate-Protected Au Nanoparticles $Na_xAu_{25}(SC_2H_4Ph)_{18-y}(S(C_2H_4O)_5CH_3)_y$. *J. Am. Chem. Soc.* **2009**, *131*, 13844-13851.

(42) Dass, A.; Holt, K.; Parker, J. F.; Feldberg, S. W.; Murray, R. W. Mass Spectrometrically Detected Statistical Aspects of Ligand Populations in Mixed Monolayer $Au_{25}L_{18}$ Nanoparticles. *J. Phys. Chem. C* **2008**, *112*, 20276-20283.

(43) Jackson, A. M.; Hu, Y.; Silva, P. J.; Stellacci, F. From Homoligand- to Mixed-Ligand- Monolayer-Protected Metal Nanoparticles: A Scanning Tunneling Microscopy Investigation. *J. Am. Chem. Soc.* **2006**, *128*, 11135-11149.

(44) Fields-Zinna, C. A.; Crowe, M. C.; Dass, A.; Weaver, J. E. F.; Murray, R. W. Mass Spectrometry of Small Bimetal Monolayer-Protected Clusters. *Langmuir* **2009**, *25*, 7704-7710.

(45) Kacprzak, K. A.; Lehtovaara, L.; Akola, J.; Lopez-Acevedo, O.; Häkkinen, H. A Density Functional Investigation of Thiolate-Protected Bimetal $PdAu_{24}(SR)_{18}^{z}$ Clusters: Doping the Superatom Complex. *Phys. Chem. Chem. Phys.* **2009**, *33*, 7123-7129.

(46) Jiang, D.; Da, S. From Superatomic $Au_{25}(SR)_{18}^{-}$ to Superatomic $M@Au_{24}(SR)_{18}^{q}$ Core−Shell Clusters. *Inorg. Chem.* **2009**, *48*, 2720-2722.

(47) Walter, M.; Moseler, M. Ligand-Protected Gold Alloy Clusters: Doping the Superatom. *J. Phys. Chem. C.* **2009**, *113*, 15834-15837.

(48) Murray, R. W. Nanoelectrochemistry: Metal Nanoparticles, Nanoelectrodes, and Nanopores. *Chem. Rev.* **2008**, *108*, 2688-2720.

(49) Zhang, D.; Liu, C. Reorganization criteria and their effects on inner-sphere barriers for transition metal redox pairs $M(H_2O)_6^{2+/3+}$(M=V, Cr, Mn, Fe and Co). *New J. Chem.* **2002**, *26*, 361-366.

(50) Zhu, M.; Aikens, C. M.; Hendrich, M. P.; Gupta, R.; Qian, H.; Schatz, G. C.; Jin, R. Reversible Switching of Magnetism in Thiolate-Protected Au25 Superatoms. *J. Am. Chem. Soc.* **2009**, *131*, 2490-2492.

(51) Akola, J.; Kacprzak, K. A.; Lopez-Acevedo, O.; Walter, M.; Grönbeck, H.; Häkkinen, H. Thiolate-Protected Au_{25} Superatoms: Dimers and Crystals. *J. Phys. Chem.* **2010**, *Articles ASAP*.

(52) Zhu, M.; Aikens, C. M.; Hollander, F. J.; Schatz, G. C.; Jin, R. Correlating the Crystal Structure of A Thiol-Protected Au25 Cluster and Optical Properties. *J. Am. Chem. Soc.* **2008**, *130*, 5883-5885.

(53) Aikens, C.M. Origin of Discrete Optical Absorption Spectra of $M_{25}(SH)_{18}^{-}$ Nanoparticles (M=Au, Ag). *J. Phys. Chem. C* **2008**, *112*, 19797-19800.

(54) Walter, M.; Akola, J.; Lopez-Acevedo, O.; Jadzinsky, P.D.; Calero, G.; Ackerson, C.J.; Whetten, R.L.; Grönbeck, H.; Häkkinen, H. A unified view of ligand-protected gold clusters as superatom complexes. *Proc. Natl. Acad. Sci.* **2008**, *105*, 9157-9162.

(55) Wang, G.; Guo, R.; Kalyuzhny, G.; Choi, J-P.; Murray, R. W. NIR Luminescence Intensities Increase Linearly with Proportion of Polar Thiolate Ligands in Protecting Monolayers of Au_{38} and Au_{140} Quantum Dots. *J. Phys. Chem. B* **2006**, *110*, 20282-20289.

(56) Wang, G.; Huang, T.; Murray, R. W.; Menard, L.; Nuzzo, R. G. Near-IR Luminescence of Monolayer-Protected Metal Clusters. *J. Am. Chem. Soc.* **2005**, *127*, 812-813.

(57) Varnavski, O.; Ramakrishna, G.; Kim, J.; Lee, D.; Goodson, T. Critical Size for the Observation of Quantum Confinement in Optically Excited Gold Clusters. *J. Am. Chem. Soc.* **2010**, *132*, 16-17.

(58) Miller, S. A.; Womick, J. M.; Parker, J. F.; Murray, R. W.; Moran, A. M. Femtosecond Relaxation Dynamics of $Au_{25}L_{18}^-$ Monolayer-Protected Cluster. *J. Phys. Chem. C* **2009**, *113*, 9440-9444.

(59) Ramakrishna, G.; Varnavski, O.; Kim, J.; Lee, D; Goodson, T. Quantum-Sized Gold Clusters as Efficient Two-Photon Absorbers. *J. Am. Chem. Soc.* **2008**, *130*, 5032-5033.

(60) Muhammed, M. A. H.; Shaw, A. K.; Pal, S. K.; Pradeep, T. Quantum Clusters of Gold Exhibiting FRET. *J. Phys. Chem. C* **2008**, *112*, 14324-14330.

Appendix 1

The Story of a Monodisperse Gold Nanoparticle: $Au_{25}L_{18}$

The materials in this Appendix are the supplementary data of the recently accepted paper to published in *Accounts of Chemical Research.*

Mass Spectrometry Conditions:

ESI-TOF-MS/ESI-QQQ-MS: 1 mg/mL Au_{25} in various solvent mixtures (100% methanol, 70:30 Methanol:Toluene, 70:30 Methanol:Dichloromethane) depending on functionalization/solubility of nanoparticle. When alkali metal salts are added to samples, the ratio is typically 75:1 salt:nanoparticle. Calibration can be done internally in the presence of alkali metal salts, or externally with cesium acetate. Samples were run on two instruments. One is a Bruker BioTOF II mass spectrometer (Billerica, MA) equipped with the Apollo electrospray ionization source, where samples are infused at a flow rate of 65 μL/h. The ion transfer time is set at 120-150 μs, with higher transfer times allowing for detection of higher m/z species. Typically, 50,000 scans are averaged in the data presented. The other instrument is Micromass Quattro II, a triple quad mass spectrometer with a nanoelectrospray ionization source. Instrumental parameters were set for optimal detection of the molecular ions with the capillary set at 1.33 V, cone at 25 V, and temperature at 100°C. For MS/MS experiments, collision voltages used were between 75-100 V.

ESI-FTICR: The second instrument was a Bruker APEX II Fourier transform ion cyclotron resonance (FT-ICR) mass spectrometer equipped with an electrospray ionization source (Analytica of Branford, Branford, CT). Negative-mode samples of $Au_{25}(SC2Ph)_{18}^-$ are dissolved in 3 mg/mL toluene, and methanol is added to a final concentration of 1 mg/mL. Typical infusion rates are 90 μL/h, and a desolvation capillary temperature is set at 80 °C. For calibration, an aqueous solution of CsI is analyzed under virtually identical conditions, producing $(CsI)_nI^-$ ($n < 30$) clusters.

MALDI-MS: MALDI-TOF mass spectrometry experiments were performed using an Applied Biosystems Voyager-DE Pro (reflectron mode) time-of-flight mass spectrometer equipped with a nitrogen laser (337 nm). The accelerating voltage was held at 25 kV, and the laser pulse intensity was optimized to reduce nanoparticle fragmentation. 10 mM DCTB matrix and nanoparticle solutions in CH_2Cl_2 were mixed at a matrix:analyte mole ratio 1000:1, with 1 to 2 μL of this solution applied to a gold sample plate and air drying.

Data Analysis: The raw data is smoothed using the Savitzky-Golay (17-point quadratic) method, and for high resolution assignments the publicly available software, Molecular Weight Calculator, was used to simulate mass spectra.

Figure A1.1: High-resolution mass spectra for the HS-PEG-biotin exchange product using 50 mmol NaOAc : 1 mmol $Au_{25}(SCH_2CH_2Ph)_{18-x}(S\text{-}PEG\text{-}biotin)_x$ in 25% toluene / 75% CH_3OH. The core charge is given in parentheses. Thick lines are simulations. From Ref. 15a.

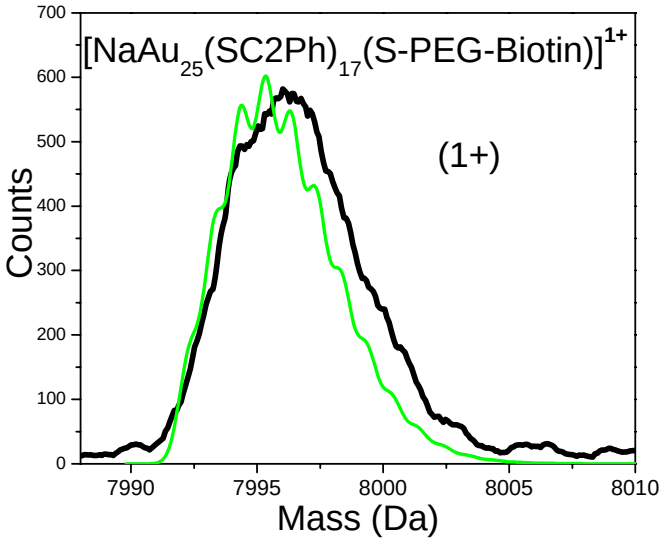
[NaAu25(SC2Ph)17(S-PEG-Biotin)]1+
(1+)
Counts
Mass (Da)
0
100
200
300
400
500
600
700
7990
7995
8000
8005
8010

Figure A1.2: Mass spectra for the HSPhCOOH exchange product, acquired in 100% CH_3OH. The data for the 2- ions are scaled by 4×. Left column: sets of peaks for (b) $Au_{25}(SCH_2CH_2Ph)_{18-x}(SPhCOO)_xH_{x-n}(Oct_4N)_2^{z-}$, and (d) $Au_{24}(SCH_2CH_2Ph)_{16-x}(SPhCOO)_xH_{x-n}^{z-}$. Right column: high-resolution comparison between data (thin lines) and simulations (thick lines) shows an excellent match for (c) $Au_{25}(SCH_2CH_2Ph)_4(SPhCOO)_{14}H_{10}(Oct_4N)_2^{3-}$ and (e) $Au_{24}(SCH_2CH_2Ph)_4(SPhCOO)_{12}H_9^{3-}$. From Ref. 15a.

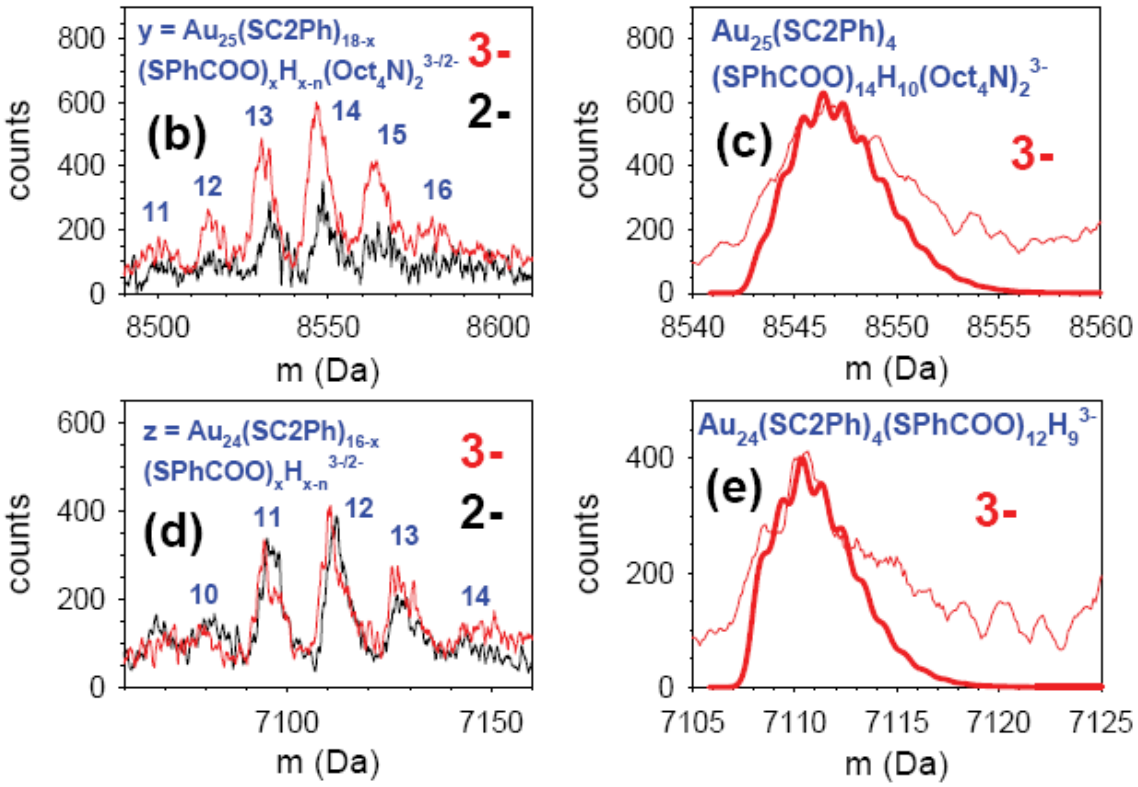
y = Au25(SC2Ph)18-x
(SPhCOO)xHx-n(Oct4N)2 3-/2-
3-
2-
(b)
11
12
13
14
15
16
counts
m (Da)
Au25(SC2Ph)4
(SPhCOO)14H10(Oct4N)2 3-
(c)
3-
z = Au24(SC2Ph)16-x
(SPhCOO)xHx-n 3-/2-
(d)
10
11
12
13
14
Au24(SC2Ph)4(SPhCOO)12H9 3-
(e)

Figure A1.3: MALDI-TOF-MS spectra (Applied Biosystems Voyager-DE Pro) of $Au_{25}(SCH_2CH_2Ph)_{18}$ in DCTB matrix with varying laser intensity delineating the molecular ions from fragment ions in positive and negative linear mode. Some spectra here are clipped at the top. From Ref. 39.

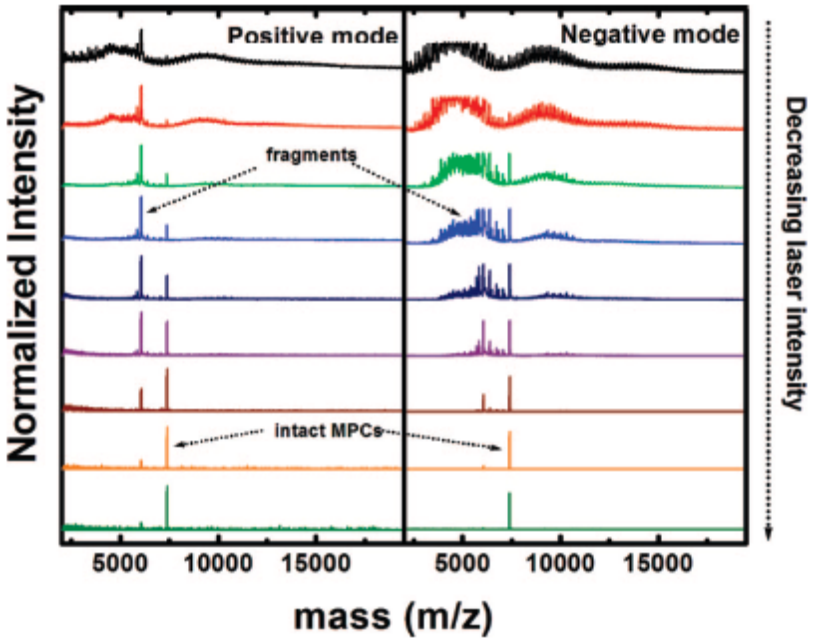
Positive mode
Negative mode
fragments
intact MPCs
Normalized Intensity
Decreasing laser intensity
5000
10000
15000
5000
10000
15000
mass (m/z)

Figure A1.4: Positive FAB-MS spectrum of $Au_{25}(SCH_2CH_2Ph)_{18}$ with 3-nitrobenzyl alcohol matrix in the intermediate mass range 3691-5350 m/z. The set of related peaks that differ by 32 Da (mass of sulfur atom) is denoted by the same color. Adjacent sets of peaks that differ by one Au atom are alternatively color-coded solid green and orange to differentiate. From Ref. 40.

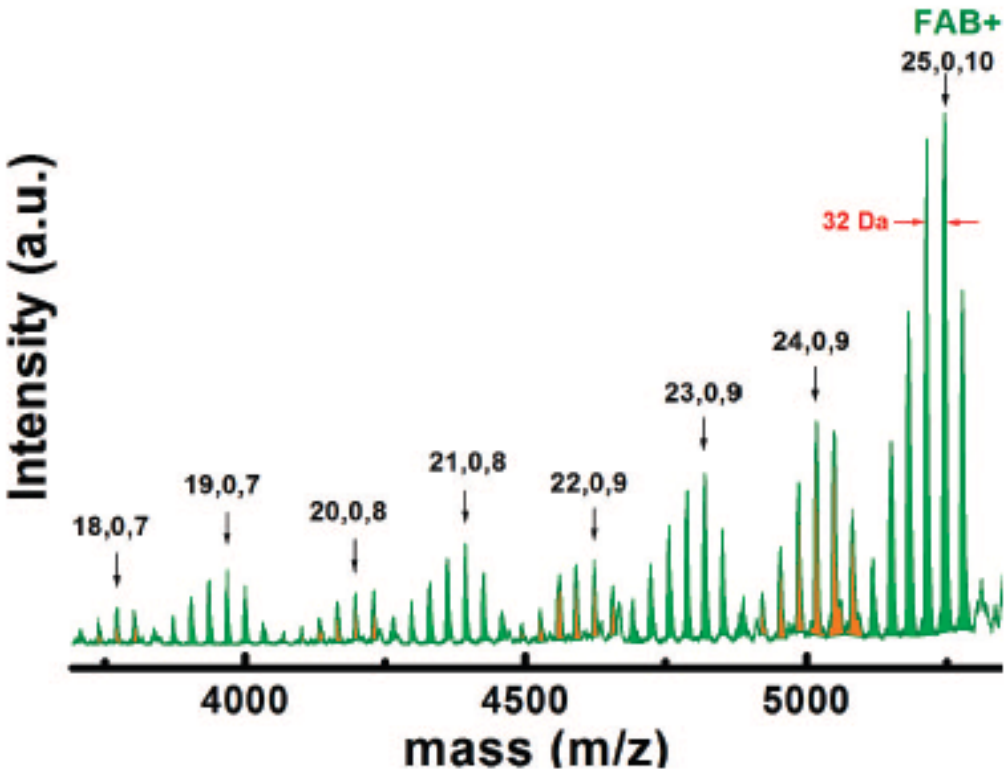
FAB+
25,0,10
32 Da
24,0,9
23,0,9
21,0,8
22,0,9
19,0,7
20,0,8
18,0,7
Intensity (a.u.)
4000
4500
5000
mass (m/z)

Figure A1.5. ESI-QQQ-MS/MS spectrum of PEGylated Au_{25} (in methanol with excess NaOAc) after fragmentation under CID conditions. The CID spectrum shows low m/z fragment ions produced from $[Na_4Au_{25}(SCH_2CH_2Ph)_8(SPEG)_{10}]^{3+}$ (m/z = 2929). Brackets and arrows indicate Au_NL_M species, where L is a distribution of ligands (SCH_2CH_2Ph and SPEG) in which SPEG is more prominent. The AuL_2 and Au_4L_4 species have the highest intensity peaks. From Ref. 41.

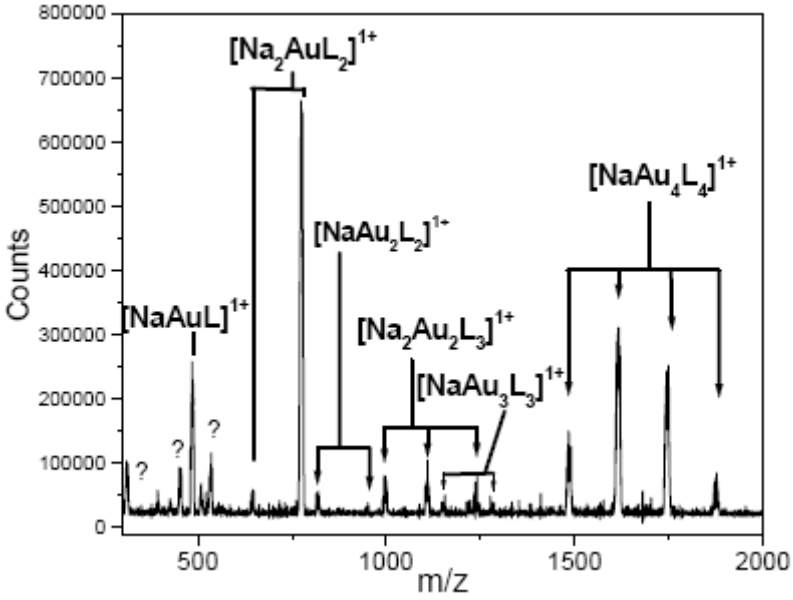
800000
700000
600000
500000
400000
300000
200000
100000
0
Counts
500
1000
1500
2000
m/z
[Na2AuL2]1+
[NaAu4L4]1+
[NaAu2L2]1+
[NaAuL]1+
[Na2Au2L3]1+
[NaAu3L3]1+
?
?
?

Figure A1.6. ESI-FTICR spectrum of $NaAu_4L_4$ fragments from the PEGylated $Au_{25}L_{18}$ sample in methanol, acquired without CID conditions. Experimental data is shown in solid black line, simulation curve by a dotted red line. This isotopic resolution under non-CID conditions confirms assignments from lower resolution ESI-QQQ-MS/MS experiment, as well as revealing that $Au_{25}L_{18}$ fragments during ESI spraying process. From Ref. 41.

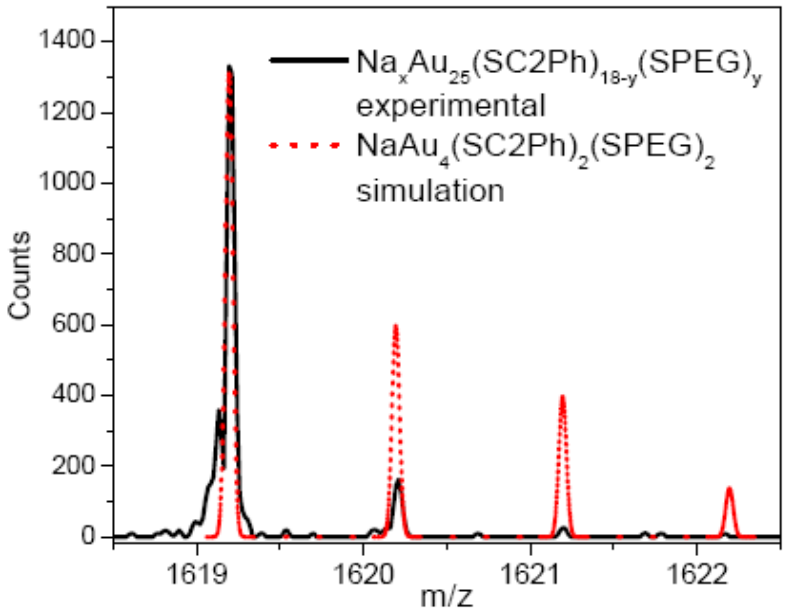
1400
1200
1000
800
600
400
200
0
Counts
1619
1620
1621
1622
m/z
Na$_x$Au$_{25}$(SC2Ph)$_{18-y}$(SPEG)$_y$
experimental
NaAu$_4$(SC2Ph)$_2$(SPEG)$_2$
simulation

Figure A1.7. ESI-QQQ-MS/MS of high m/z region fragment ions produced from selected precursor $[Na_5Au_{25}(SC2Ph)_7(SPEG)_{11}]^{4+}$ (m/z = 2235). The mass of these species is obtained by simply multiplying the value of their charge state by the x-axis. Samples are dissolved in methanol with NaOAc. Presence of peaks at higher m/z values than molecular ion confirms multiple charging. From Ref. 41.

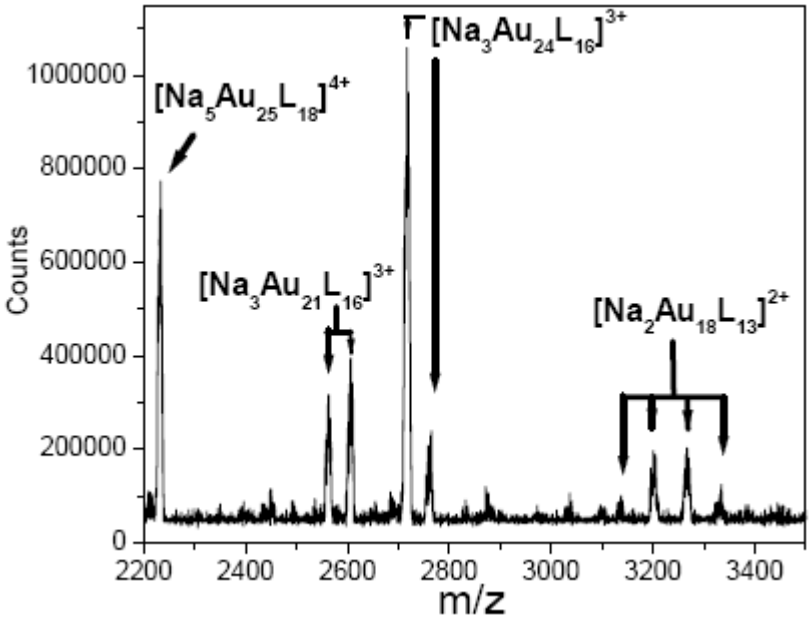
[Na3Au24L16]3+
[Na5Au25L18]4+
[Na3Au21L16]3+
[Na2Au18L13]2+
Counts
m/z
0
200000
400000
600000
800000
1000000
2200
2400
2600
2800
3000
3200
3400

Figure A1.8. ESI mass spectrum of the $AuNP^{3+}$ charge state of the PEGylated and extensively purified sample prepared using a 1:0.9 Au:Pd mole ratio. The sample was electrosprayed as a solution of 30% CH_2Cl_2 and 70% CH_3OH and 75:1 NaOAc:MPC. Assignments reveal similar species to the 9:1 Au:Pd mole ratio sample, though there is now a higher relative intensity of the $Au_{24}PdL_{18}$ bimetal species. Asterisks indicate species of oxidized $Au_{25}L_{18}$ with fewer Na atoms coordinated to the PEG chain. From Ref. 44.

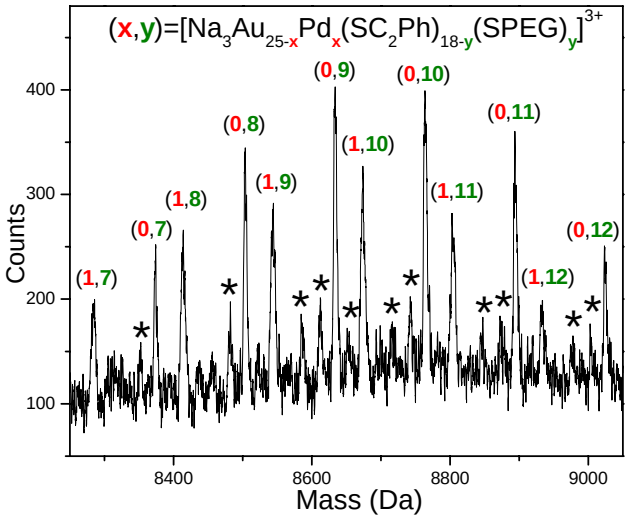
(x,y)=[Na3Au25-xPdx(SC2Ph)18-y(SPEG)y]3+
(0,9)
(0,10)
(0,11)
(0,8)
(1,10)
(1,9)
(1,11)
(1,8)
(0,7)
(0,12)
(1,7)
(1,12)
Counts
400
300
200
100
8400
8600
8800
9000
Mass (Da)

Figure A1.9. UV-vis spectra (25 °C) of (a) $Au_{25}(SCH_2CH_2Ph)_{18}^{1-}$ (black line), (b)$Au_{25}(SCH_2CH_2Ph)_{18}^{0}$ (red line), and (c) $Au_{25}(SCH_2CH_2Ph)_{18}^{1+}$ (green line) in CH_2Cl_2. The three spectra are of the same solution; the 0 and 1- charge states were generated by electrolysis in a spectroelectrochemical cell. From Ref. 31.

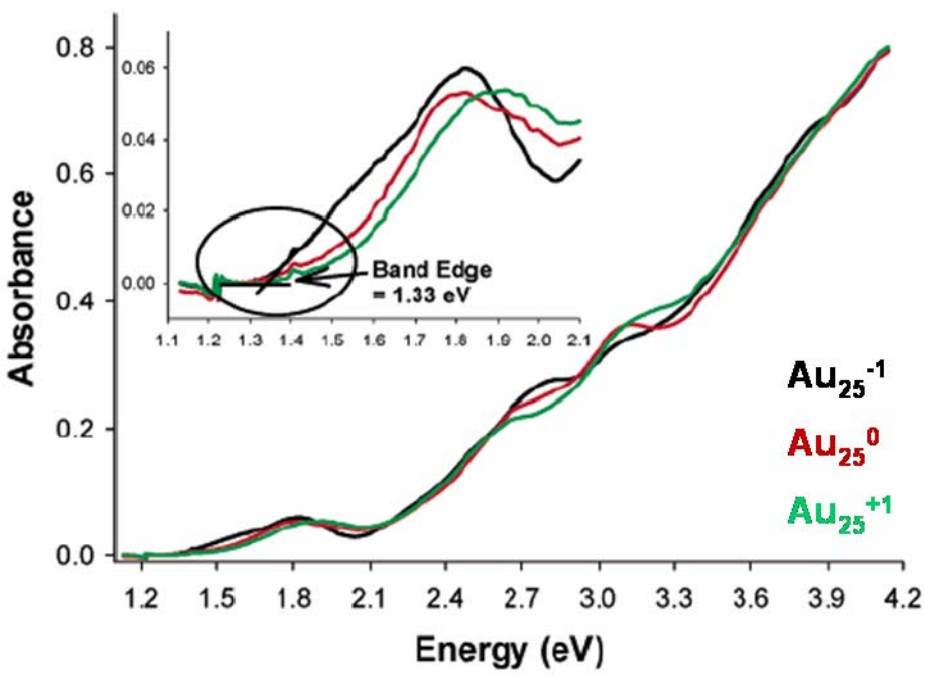
Absorbance
Energy (eV)
Band Edge
= 1.33 eV
Au25-1
Au250
Au25+1

REMAINING LIST OF Au_{25} FOCUSED REFERENCES:

(A1) Choi, J-P.; Fields-Zinna, C. A.; Stiles, R. L.; Balasubramanian, R.; Douglas, A. D.; Crowe, M. C.; Murray, Royce W. Reactivity of $[Au_{25}(SCH_2CH_2Ph)_{18}]^{1-}$ Nanoparticles with Metal Ions. *J. Phys. Chem. C*, **2010**, *Articles ASAP*.

(A2) Zhu, Y.; Qian, H.; Drake, B. A.; Jin, R. Atomically Precise $Au_{25}(SR)_{18}$ Nanoparticles as Catalysts for the Selective Hydrogenation of α,β-Unsaturated Ketones and Aldehydes. *Angew. Chem. Int. Ed.* **2010**, *49*, 1295-1298

(A3) Retnakumari, A.; Setua, S.; Menon, D.; Ravindran, P.; Muhammed, H.; Pradeep, T.; Nair, S.; Koyakutty, M. Molecular-receptor-specific, non-toxic, near-infrared-emitting Au cluster-protein nanoconjugates for targeted cancer imaging. *Nanotechnology* **2010**, *21*, 055103/1-055103/12.

(A4) Sanchez-Castillo, A.; Noguez, C.; Garzon, I. L. On the Origin of the Optical Activity Displayed by Chiral-Ligand-Protected Metallic Nanoclusters. *J. Am. Chem. Soc.* **2010**, *132*, 1504-1505.

(A5) Liu, Y.; Tsunoyama, H.; Akita, T.; Tsukuda, T. Efficient and selective epoxidation of styrene with TBHP catalyzed by Au_{25} clusters on hydroxyapatite. *Chem. Commun.* **2010**, *46*, 550-552.

(A6) Simms, G. A.; Padmos, J. D.; Zhang, P. Structural and electronic properties of protein/thiolate-protected gold nanocluster with "staple" motif: A XAS, L-DOS, and XPS study. *J. Chem. Phys.* **2009**, *131*, 214703/1-214703/9.

(A7) Ramasamy, P.; Guha, S.; Shibu, E. S.; Sreeprasad, T. S.; Bag, S.; Banerjee, A.; Pradeep, T. Size tuning of Au nanoparticles formed by electron beam irradiation of Au_{25} quantum clusters anchored within and outside of dipeptide nanotubes. *J. Mater. Chem.* **2009**, *19*, 8456-8462.

(A8) Muhammed, M. A. H.; Verma, P. K.; Pal, S. K.; Kumar, R. C. A.; Paul, S.; Omkumar, R. V.; Pradeep, T. Bright, NIR-Emitting Au_{23} from Au_{25}: Characterization and Applications Including Biolabeling. *Chemistry-A European Journal* **2009**, *15*, 10110-10120.

(A9) Jiang, D-e.; Whetten, R. L. Magnetic doping of a thiolated-gold superatom: First-principles density functional theory calculations. *Phys. Rev. B: Condensed Matter and Materials Physics* **2009**, *80*, 115402/1-115402/5.

(A10) Qian, H.; Zhu, M.; Lanni, E.; Zhu, Y.; Bier, M. E.; Jin, R. Conversion of polydisperse Au nanoparticles into monodisperse Au25 nanorods and nanospheres. *J. Phys. Chem. C* **2009**, *113*, 17599-17603.

(A11) Aikens, C. M. Effects of Core Distances, Solvent, Ligand, and Level of Theory on the TDDFT Optical Absorption Spectrum of the Thiolate-Protected Au25 Nanoparticle. *J. Phys. Chem. A* **2009**, *113*, 10811-10817.

(A12) Si, S.; Gautier, C.; Boudon, J.; Taras, R.; Gladiali, S.; Burgi, T. Ligand Exchange on Au25 Cluster with Chiral Thiols. *J. Phys. Chem. C* **2009**, *113*, 12966-12969.

(A13) Jiang, D-e; Whetten, R. L.; Luo, W.; Dai, S. The Smallest Thiolated Gold Superatom Complexes. *J. Phys. Chem. C* **2009**, *113*, 17291-17295.

(A14) Wu, Z.; Jin, R. Stability of the Two Au-S Binding Modes in $Au_{25}(SG)_{18}$ Nanoclusters Probed by NMR and Optical Spectroscopy. *ACS Nano* **2009**, *3*, 2036-2042.

(A15) Garcia-Raya, D.; Madueno, R.; Blazquez, M.; Pineda, T. Electrochemistry of Molecule-like Au25 Nanoclusters Protected by Hexanethiolate. *J. Phys. Chem. C* **2009**, *113*, 8756-8761.

(A16) Shichibu, Y.; Negishi, Y.; Tsukuda, T.; Teranishi, T. Large-Scale Synthesis of Thiolated Au25 Clusters via Ligand Exchange Reactions of Phosphine-Stabilized Au11 Clusters. *J. Am. Chem. Soc*. **2005**, *127*, 13464-13465.

(A17) Choi, J-P; Coble, M. M.; Branham, M. R.; DeSimone, J. M.; Murray, R. W. Dynamics of CO_2-Plasticized Electron Transport in Au Nanoparticle Films: Opposing Effects of Tunneling Distance and Local Site Mobility. *J. Phys. Chem. C* **2007**, *111*, 3778-3785.

(A18) Wang, W.; Murray, R. W. Electrochemistry and Contact Angles of an Ionic Liquid Sessile Droplet on Films of Monolayer-Protected Au Nanoparticles. *Anal. Chem.* **2007**, *79*, 1213-1220.

(A19) Holm, A. H.; Ceccato, M.; Donkers, R. L.; Fabris, L.; Pace, G.; Maran, F. Effect of Peptide Ligand Dipole Moments on the Redox Potentials of Au_{38} and Au_{140} Nanoparticles. *Langmuir* **2006**, *22*, 10584-10589.

(A20) Wang, W.; Lee, D.; Murray, R. W. Electron Transport Dynamics in a Room-Temperature Au Nanoparticle Molten Salt. *J. Phys. Chem. B* **2006**, *110*, 10258-10265.

(A21) Batista, R. J. C.; Mazzoni, M. S. C.; Garzon, I. L.; Beltran, M. R.; Chacham, H, Electron States in a Lattice of Au Nanoparticles: The Role of Strain and Functionalization. *Phys. Rev. Lett*. **2006**, *96*, 116802/1-116802/4.

(A22) Kim, J.; Lee, D. Electron Hopping Dynamics in Au_{38} Nanoparticle Langmuir Monolayers at the Air/Water Interface. *J. Am. Chem. Soc.* **2006**, *128*, 4518-4519.

(A23) Wang, W.; Murray, R. W. Reaction of Triphenylphosphine with Phenylethanethiolate-Protected Au38 Nanoparticles. *Langmuir* **2005**, *21*, 7015-7022.

(A24) Song, Y.; Harper, A. S.; Murray, R. W. Ligand Heterogeneity on Monolayer-Protected Gold Clusters. *Langmuir* **2005**, *21*, 5492-5500.

(A25) Georganopoulou, D. G.; Mirkin, M. V.; Murray, R. W. SECM Measurement of the Fast Electron Transfer Dynamics between Au_{38}^{1+} Nanoparticles and Aqueous Redox Species at a Liquid/Liquid Interface. *Nano Lett.* **2004**, *4*, 1763-1767.

(A26) Song, Y.; Heien, M. L. A. V.; Jimenez, V.; Wightman, R. M.; Murray, R. W. Voltammetric Detection of Metal Nanoparticles Separated by Liquid Chromatography *Anal. Chem.* **2004**, *76*, 4911-4919.

(A27) Jimenez, V. L.; Georganopoulou, D. G.; White, R. J.; Harper, A. S.; Mills, A. J.; Lee, D.; Murray, R. W. Hexanethiolate Monolayer Protected 38 Gold Atom Cluster. *Langmuir* **2004**, *20*, 6864-6870.

(A28) Lee, D.; Donkers, R. L.; DeSimone, J. M.; Murray, R. W. Voltammetry and Electron-Transfer Dynamics in a Molecular Melt of a 1.2 nm Metal Quantum Dot. *J. Am. Chem. Soc.* **2003**, *125*, 1182-1183.

(A29) Garzon, I. L.; Reyes-Nava, J. A.; Rodriguez-Hernandez, J. I.; Sigal, I.; Beltran, M. R.; Michaelian, K. Chirality in bare and passivated gold nanoclusters. *Phys. Rev, B: Condensed Matter and Materials Physics* **2002**, *66*, 073403/1-073403/4.

(A30) Wilson, N. T.; Johnston, R. L. Passivated clusters: a theoretical investigation of the effect of surface ligation on cluster geometry. *Phys. Chem. Chem. Phys.* **2002**, *4*, 4168-4171.

Chapter 2

On the Synthesis of Monodisperse $[Oct_4N^+][Au_{25}(SR)_{18}^-]$ Nanoparticles, with Some Mechanistic Observations

2.1 Introduction

Small thiolated gold nanoparticles have experienced substantial research attention over the last decade, especially those with core diameters less than 2 nm that lie in the metal-to-molecule transition range and consequently exhibit size-dependent properties.[1-5] Of the identified small gold nanoparticles, $Au_{25}(SR)_{18}$ has become perhaps the most heavily studied;[6] it is an attractive research target being amenable to theory and having a crystallographically known structure.[7-8] This nanoparticle (NP) shows emerging application in nanocluster catalysis,[9] and can be synthesized in respectable yield with exceptional monodispersity. It was first synthesized in appreciable yields in 1998 by Whetten and co-workers[10] using glutathione (HSG) as the protecting or passivating ligand. Since that initial report, a number of research groups[6,11-15] have contributed to an understanding of the structure and properties of this Au NP and to ways to improve its synthetic yield and purity.

The nanoparticle referred to here as $Au_{25}(SR)_{18}$ experienced several mis-labelings—illustrating needs for improving analytical tools to determine chemical formulæ of nanoparticles—before mass spectrometric developments[13,16,17] correctly

assessed its formula and (native) -1 charge. The synthesis by Whetten, *et al.*[10] involved reducing a mixture of $HAuCl_4$ and HSG in methanol/water with rapid addition of aqueous sodium borohydride, fractionating the polydisperse nanoparticle product with gel electrophoresis. Tsukuda, *et al.*[12,13] later examined the products of this synthesis and separated a number of small thiolated Au nanoparticles by poly-acrylamide gel electrophoresis (PAGE), characterizing them with ESI-MS. This led to the first correct formulaic assignment of $Au_{25}(SG)_{18}$.[13] Separately, Donkers, *et al*.[11] synthesized and isolated with good monodispersity a nanoparticle that was initially mis-labeled as Au_{38}, but later correctly identified as $Au_{25}(S(CH_2)_2Ph)_{18}^-$. The two-phase synthesis used[11] was a modification of the Brust method,[18] wherein isolation from the polydisperse product mixture involved an extraction of the sought NP into acetonitrile as a rather pure, reduced form $Au_{25}(S(CH_2)_2)_{18}^-$ (albeit with mediocre yield).

There have been many subsequent efforts to enhance the yield of $Au_{25}(SR)_{18}$ and to study aspects of the "bottom-up" mechanism of its formation. Wu, *et al.*,[14] introduced a single-phase tetrahydrofuran (THF) procedure that produced monodisperse $Au_{25}(SR)_{18}$ where SR was variable, including phenylethanethiol and glutathione, reporting that control of stirring rates and temperature caused a controlled evolution of nanoparticle formation eventually arriving at monodisperse $Au_{25}(SR)_{18}$. Dharmaratne, *et al.*[15a] expanded on this procedure, conducting it successfully at room temperature without strictures of precise stirring conditions. We noticed that these important synthetic developments did not include adding $Oct_4N^+Br^-$ (the phase transfer reagent employed in the two-phase Brust method,[18]) and reasoned that the absence of associations with this cation might be adverse to formation of the anionic form (reduced, native, occupied

HOMO levels) of the nanoparticle; UV-Vis spectra of the single phase synthetic products[14] suggested an oxidized form. Mass spectrometry,[16,17] NMR,[19] and x-ray crystallographic[7,8] results show that the NP native charge state is -1; a single crystal structure determination was of the salt $[Oct_4N^+][Au_{25}(S(CH_2)_2Ph)_{18}^-]$. We here confirm by experiment and UV-Vis spectra that NP product from the previous procedures[14,15a] is oxidized, e.g., in the neutral, Au_{25}^0 state. Our spectral recognition was aided by previous experiments[20] in which the reduced form was extracted into acetonitrile and the oxidized form subsequently produced by chemical oxidation, and by our use of electrolytic oxidation state control in an NMR electron exchange study.[19]

This report improves the high yield synthesis of highly pure, fully reduced $Au_{25}(SR)_{18}^-$ nanoparticle, by the addition of the surfactant salt $Oct_4N^+Br^-$ to the single phase synthesis. The procedure described is successful with several, but not all, thiolate ligands. In the course of exploring nuances of this synthetic development, we gained insight into some important factors influencing the bottom-up nanoparticle synthesis and pathways to its production from larger, initially produced Au NPs.

2.2 Experimental Section

2.2.1 Chemicals. Phenylethanethiol (Aldrich, 98%), benzylmercaptan (Fluka, 99%), hexanethiol (Aldrich, 95%), dodecanethiol (Aldrich, 98%), 2-methyl-1-propanethiol (Aldrich, 92%), 4-bromothiophenol (Aldrich, 95%), 4-*tert*-butylthiophenol (Aldrich, 97%), 4-methoxythiophenol (Acros, 98%), benzenethiol (Aldrich, 99%), *tetra-n*-octylammonium bromide ($Oct_4N^+Br^-$, Aldrich, 98%), sodium borohydride (Aldrich, 99%), tetrahydrofuran (Fisher, 99.9%), toluene (Fisher, 99.9%), methanol (Fisher,

99.9%), dichloromethane (Fisher, 99.9%), *tetra*-*n*-ethylammonium bromide (Et_4NBr, Aldrich, 99%), and *tetra*-*n*-butylammonium perchlorate (Bu_4NClO_4, Aldrich, 99%) were all used as received. $HAuCl_4 \cdot 3H_2O$ was prepared as previously described.[21]

2.2.2 Synthesis of $[Oct_4N^+][Au_{25}(S(CH_2)_2Ph)_{18}^-]$. $HAuCl_4 \cdot 3H_2O$ (2.00 g, 5.08 mmol) and *tetra*-*n*-octylammonium bromide ($Oct_4N^+Br^-$, 3.12 g, 5.70 mmol) were co-dissolved in tetrahydrofuran (THF, 140 mL) and stirred for 15 minutes. Phenylethanethiol (3.60 mL, 26.8 mmol) was added at room temperature and stirred for at least 12 hours until the solution was completely colorless. Meanwhile, sodium borohydride ($NaBH_4$, 1.93 g, 51.2 mmol) was dissolved in 48 mL Nanopure water and stirred at 0°C for 1 hour prior to rapid addition to the THF solution. The reaction mixture was allowed to quietly stir for ≥ 48 hours. Over the course of the reaction, the solution color slowly evolves from blackish to a murky brown color which we have learned to be indicative of a high proportion of $Au_{25}(S(CH_2)_2Ph)_{18}^-$.

The product solution was then gravity filtered to remove any insoluble materials and the filtered solution rotovapped to remove the tetrahydrofuran solvent. Toluene (100 mL) was added, dissolving the product, and the solution transferred to a separatory funnel and extracted four times using 200 mL Nanopure water. The toluene layer was subsequently rotovapped to dryness and the resulting product filtered and washed thoroughly with methanol to remove any traces of excess thiol and $Oct_4N^+Br^-$, leaving pure $[Oct_4N^+][Au_{25}(S(CH_2)_2Ph)_{18}^-]$ (780 mg, 49% yield by Au) which was collected by dissolving in dichloromethane. MALDI-TOF mass spectrometry of this product was performed using an Applied Biosystems Voyager DE Pro instrument and the matrix *trans*-2-[3-(4-*tert*-butylphenyl)-2-methyl-2-propenylidene]malononitrile (DCTB) as

previously described.[22] Solid yellow-brown byproducts remaining on the frit were insoluble in most solvents. Electrospray-ionization mass spectrometry was performed on the byproducts of the reaction, using Micromass Quattro II, a triple quad mass spectrometer with a nanoelectrospray ionization source. The yellow-brown byproducts of the reaction were washed thoroughly with methanol to eliminate any excess thiol or Oct_4N^+. They were re-suspended in 70:30 methanol:acetone and sonicated for a period to induce dissolution, for ESI mass spectral analysis.

Several variations of the above synthesis were implemented in order to explore the generality of the procedure as well as to study various aspects of the mechanism. Other *tetra-n*-alkylammonium salts were substituted for $Oct_4N^+Br^-$, including tetra-ethylammonium bromide ($Et_4N^+Br^-$) and tetra-butylammonium perchlorate ($Bu_4N^+ClO_4^-$). The synthesis was also performed using different thiols, including hexanethiol, dodecanethiol, 2-methyl-1-propanethiol, benzylmercaptan, and a series of *para*-substituted thiophenols. Each thiol was used in the same mole ratio and the products worked up exactly as described above.

Following the evolution of $Au_{25}(SR)_{18}$ from initially produced larger nanoparticles as reported by Dharmaratne, *et al*.,[15a] described as an "aging" process, we sought to delineate parameters that influence it. In part, this involved inspecting how our procedure differs from the traditional two-phase Brust method.[18] The latter involves phase-transfer of $HAuCl_4 \cdot 3H_2O$ from water into toluene using $Oct_4N^+Br^-$ and then removing the water phase prior to $NaBH_4$ addition. The present and earlier[14,15a] procedures, being single-phase, do not involve a phase transfer step. The present procedure nonetheless includes the $Oct_4N^+Br^-$ reagent, so that both excess acid and

bromide—as well as Oct_4N^+ –from $HAuCl_4$ and $Oct_4N^+Br^-$are present throughout the course of the reaction. To examine the effect of acidity in the "aging" process, we co-dissolved $HAuCl_4 \cdot 3H_2O$ in water and $Oct_4N^+Br^-$ in toluene and then thoroughly dried the toluene layer and re-dissolved the $[Oct_4N][AuCl_4]$ salt into THF. Using the $[Oct_4N][AuCl_4]$ salt allowed examination whether an absence of acidity in the reaction solution altered the product formation. To inspect the effect of bromide, Bu_4NClO_4 was utilized instead of $Oct_4N^+Br^-$.

In order to study the role of oxygen in the reaction, the entire synthetic procedure was performed under an inert (Ar) atmosphere. For this experiment, $HAuCl_4 \cdot 3H_2O$ was dissolved in THF followed by the addition of phenylethanethiol and constant stirring overnight at room temperature. Meanwhile, sodium borohydride was dissolved in Nanopure water and stirred at 0^oC for 1 hour. Both of these solutions were purged with Ar for 15 minutes prior to adding the $NaBH_4$ solution to the THF solution. The reaction mixture was stirred for 5 days under a continuous Ar atmosphere.

2.3 Results and Discussion

2.3.1 Synthesis of $Au_{25}(SR)_{18}^-$ Nanoparticles. This study describes a facile, ligand-versatile synthesis of the nanoparticle $[Oct_4N^+][Au_{25}(SR)_{18}^-]$ in a pure and fully reduced form. Synthetic control of oxidation state, and knowing how to recognize the state of oxidation, is an important distinction since investigations[19,23,24] of nanoparticle properties show differences according to NP oxidation state. For the earlier used[20] phenylethanethiolate ($-S(CH_2)_2Ph$) ligand, we now attain a yield of *ca*. 50%, by mass of Au. In early, two-phase Brust syntheses, the phase transfer agent $Oct_4N^+Br^-$ was used to

solubilize the gold complex precursor in toluene solvent. As noted above, the recent single-phase syntheses[14,15a] successfully produce $Au_{25}(SR)_{18}$ nanoparticles (in procedures omitting the $Oct_4N^+Br^-$ agent), but in our own experiments the single phase procedure produces nanoparticles recognizable as oxidized. This is most clearly judged by examination of the details of UV-Visible spectra (Figure 2.1).

Figure 2.1B compares UV-Vis spectra of $Au_{25}(S(CH_2)_2Ph)_{18}$ NPs produced in the single-phase synthesis with and without inclusion of the $Oct_4N^+Br^-$ reagent. The spectra obviously differ in the fine structure in the 390 to 450 nm range. The spectra of oxidized and reduced NP (Figure 2.1A) were obtained by extracting the reduced form into acetonitrile (in which the oxidized form is insoluble[19]) and by chemical oxidation with Ce^{IV}.[23] The key distinction lies in the relative absorbance of the 399 and 446 nm peaks; the former becomes more pronounced upon oxidation and the latter is prominent when the nanoparticle is in the reduced state. Specifically, after normalizing absorbances of the two solutions at 300 nm to 1.00 as is done in Figure 2.1A, the absorbance ratio of A_{399}/A_{446} is 1.2 for the fully reduced NP ($Au_{25}(SR)_{18}^{1-}$) and 1.4 when the NP is in the oxidized state ($Au_{25}(SR)_{18}^{0}$). In Figure 2.1B, A_{399}/A_{446} ratios seen with and without $Oct_4N^+Br^-$ equal 1.2 and 1.4, respectively, showing that NP synthesis in the absence of Oct_4N^+ results in oxidized product. As a secondary indicator, the absorbance at 680 nm shifts to slightly higher energy and the broad 800 nm band (which represents the HOMO occupancy[20,25]) is eliminated by oxidation.

Figure 2.2 shows the MALDI (matrix assisted laser desorption ionization) mass spectrum of the $Au_{25}(S(CH_2)_2Ph)_{18}$ nanoparticle, and clearly indicates the monodispersity of this product, which required no further fractionation.

Figure 2.1. (A) UV-Visible Spectra in CH_2Cl_2 of $Au_{25}(S(CH_2)_2Ph)_{18}$ in the reduced (black) form, isolated by extraction into acetonitrile (in which the oxidized form is insoluble) and of the oxidized (red) form prepared by chemical oxidation using Ce^{IV} (spectrum from Ref. 23). (B) Synthetic NP products obtained in single phase THF synthesis in the presence (black) and absence (red) of $Oct_4N^+Br^-$. The relative sizes of the peaks at 399 and 440 nm provide an indication of oxidation state. Specifically, the peak at 440 nm is more pronounced when the NP is in a reduced state, and that at 399 nm grows when the NP becomes oxidized.

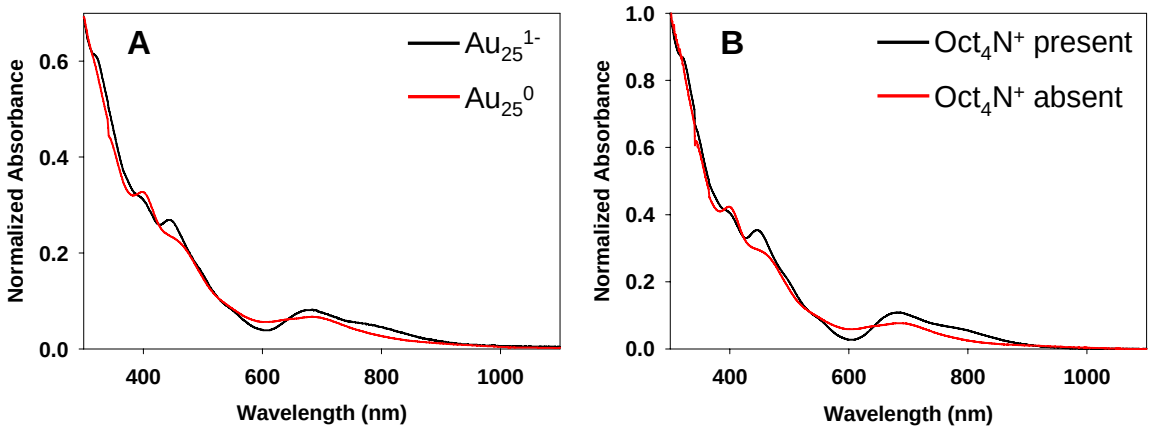
A
Au_{25}^{1-}
Au_{25}^{0}
Normalized Absorbance
0.0
0.2
0.4
0.6
400
600
800
1000
Wavelength (nm)
B
Oct_4N^+ present
Oct_4N^+ absent
Normalized Absorbance
0.0
0.2
0.4
0.6
0.8
1.0
400
600
800
1000
Wavelength (nm)

Figure 2.2. Matrix assisted laser desorption ionization (MALDI) MS of $[Oct_4N^+][Au_{25}(S(CH_2)_2Ph)_{18}^-]$ as synthesized in THF by the present procedure. The matrix used is *trans*-2-[3-(4-tert-butylphenyl)-2-methyl-2-propenylidene]malonotrile (DCTB). The spectrum shows a non-fragmented, monodisperse product.

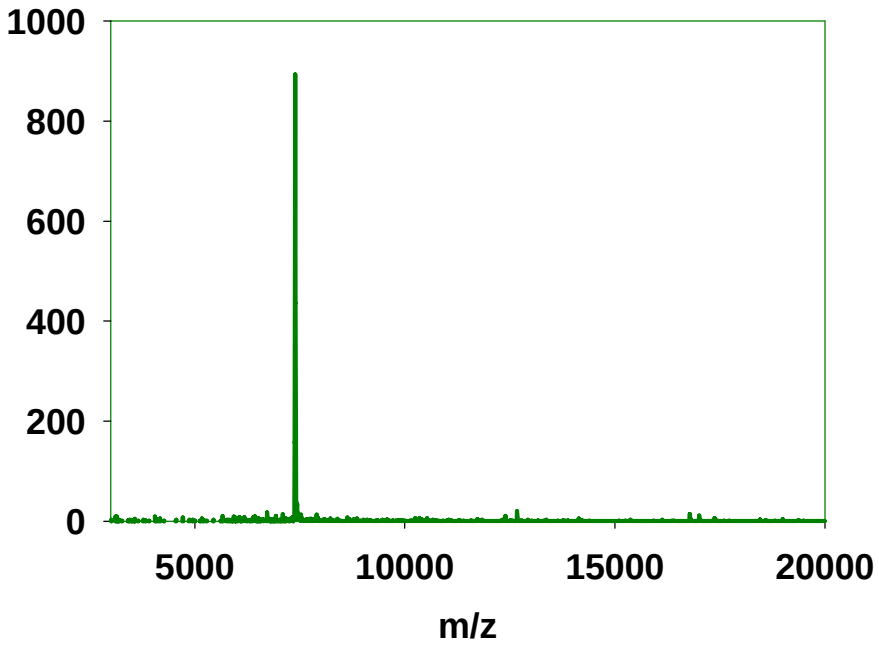
1000
800
600
400
200
0
5000
10000
15000
20000
m/z

Other thiols tested in the presence of $Oct_4N^+Br^-$ included hexanethiol ($HS(CH_2)_5CH_3$), dodecanethiol ($HS(CH_2)_{11}CH_3$), 2-methyl-1-propanethiol ($HSCH_2CH(CH_3)_2$), benzylmercaptan ($HSCH_2Ph$), and a series of *para*-substituted thiophenols (HSPh-X, X = Br, H, tert-butyl, OCH_3). The *p*-substituted thiophenols failed to make $Au_{25}(SR)_{18}$ nanoparticles in any form, with or without the presence of $Oct_4N^+Br^-$. The others followed the same reaction behavior as the $HS(CH_2)_2Ph$ thiol, the reaction mixture eventually producing the murky brown solution indicative of monodisperse $Au_{25}(SR)_{18}$. Figure 2.3 shows the UV-Visible spectra of Au_{25} prepared with $–S(CH_2)_2Ph$, $–S(CH_2)_5CH_3$, $–S(CH_2)_{11}CH_3$, and $–SCH_2CH(CH_3)_2$ ligands (all prepared as described in Experimental). All displayed the broad 680 nm peak and 800 nm shoulder indicative of reduced Au_{25} and the spectra for all nearly overlap.

Synthesis with the $–SCH_2Ph$ ligand was also attempted, but the NP product spectrum exhibits higher absorbances below 600 nm and less well-defined voltammetry than its $–S(CH_2)_2Ph$ analog. Its spectrum does contain the 680 nm peak and 800 nm shoulder indicative of reduced NP. The impurities may arise from residual gold-thiolate polymer; these NP products had not been subjected to any further cleanup procedures (See Figures A2.2 and A2.3 in Appendix 2).

The *para*-substituted thiophenols (HSPh-X) did not yield stable nanoparticles in this synthesis, with or without $Oct_4N^+Br^-$. X was H, *tert*-butyl, Br, and OCH_3, running the gamut of substituent size and electron-withdrawing and donating character. In all cases, nanoparticles were formed upon rapid addition of sodium borohydride (dark solution), but within minutes the solution cleared, indicating a prompt degradation. This behavior has been noticed previously[26] in thiolated Pd nanoparticle syntheses, and is not

Figure 2.3. UV-Vis spectra of $[Oct_4N^+][Au_{25}(SR)_{18}^-]$ where SR = $S(CH_2)_2Ph$ (black), $S(CH_2)_5CH_3$ (blue), $SCH_2CH(CH_3)_2$ (red) and $S(CH_2)_{11}CH_3$ (dark yellow). All display the broad peak at 680 nm and the 800 nm shoulder indicative of reduced Au_{25}. The spectra nearly coincide at all wavelengths.

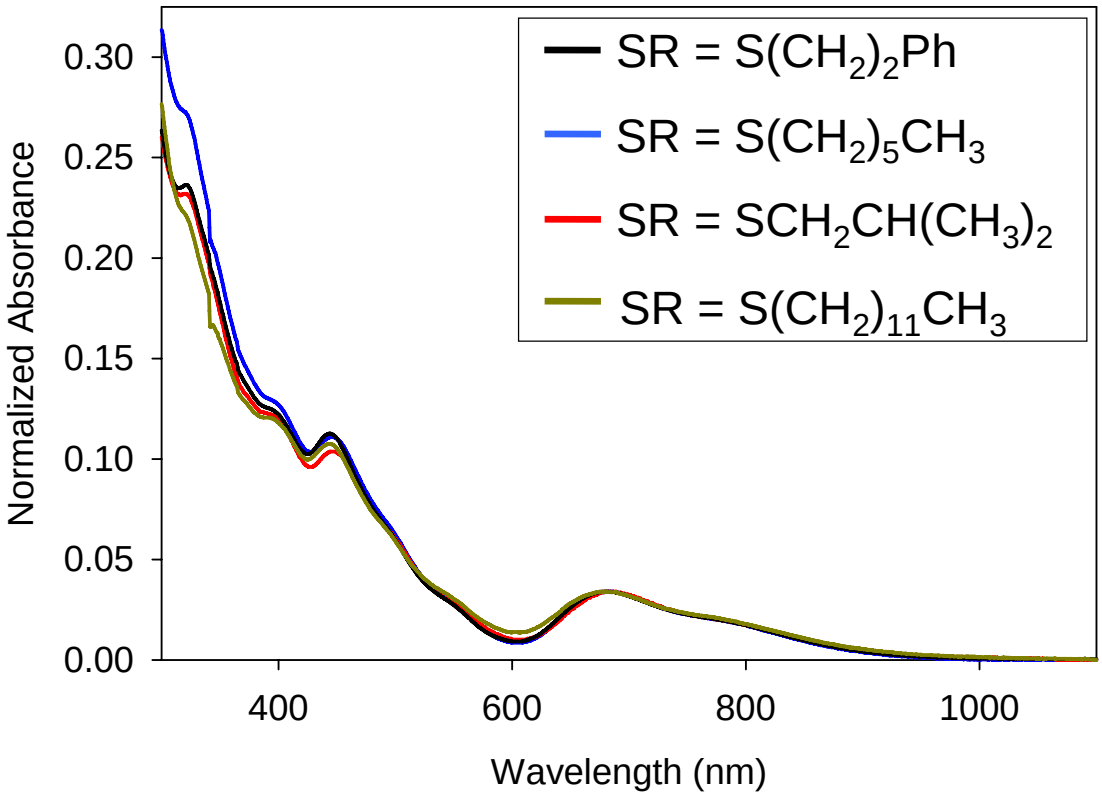
SR = S(CH2)2Ph
SR = S(CH2)5CH3
SR = SCH2CH(CH3)2
SR = S(CH2)11CH3
Normalized Absorbance
0.30
0.25
0.20
0.15
0.10
0.05
0.00
400
600
800
1000
Wavelength (nm)

understood. It is especially curious since Au_{25} nanoparticles with –SPhX ligands can be made by ligand exchange from the $Au_{25}(S(CH_2)_2Ph)_{18}^-$ nanoparticle.[28]

2.3.2 Influences of H^+, Br^-, and O_2 in the Synthesis. The Brust reaction[18] involves the phase transfer of $AuCl_4^-$ into toluene using Oct_4N^+, followed by a water wash to remove excess H^+ and Br^-. In the current synthesis, both $HAuCl_4$ and $Oct_4N^+Br^-$ are present in the THF solvent, so excess acid and Br^- remains in the solution throughout the reaction course. To inquire whether acidity or Br^- impact the nanoparticle synthesis, we eliminated them by using a $[Oct_4N][AuCl_4]$ salt (prepared as described in Experimental) and added the reducing agent to its solution in THF, carrying the reaction procedure forward as above. The reaction does produce nanoparticles, but larger ones; no $Au_{25}(S(CH_2)_2Ph)_{18}$ could be isolated. The specific importance of Br^- in the synthesis was inspected by repeating the synthesis as described in Experimental but using $Bu_4N^+ClO_4^-$ instead of $Oct_4N^+Br^-$. The reaction appeared to proceed just as with $Oct_4N^+Br^-$, but the $Au_{25}(SR)_{18}$ nanoparticles obtained were partially oxidized. These observations clearly indicate that acidity is somehow involved in the formation of $Au_{25}(SR)_{18}$, while Br^- aids in avoiding NP oxidation it does not participate in steering the reaction towards the desired small nanoparticle, as in Ref. 14.

The synthesis of $Au_{25}(S(CH_2)_2Ph)_{18}$ was also attempted in the absence of dioxygen by purging the gold-thiolate polymer and sodium borohydride solutions with Ar before combining them, and then maintaining the reaction mixture under an Ar atmosphere for five days. $Au_{25}(SR)_{18}$ was not observed in the product mixture, nor were soluble larger nanoparticles (Figure 2.4). The product is an insoluble mixture of white and grey materials. Clearly, dioxygen plays a crucial role in nanoparticle synthesis in

Figure 2.4: Successful synthesis of $Au_{25}(SR)_{18}$ in the presence of dioxygen (A) and the failed synthesis in the presence of argon (B). The reaction under Ar did not produce the usual, organic-soluble nanoparticles, of any size; rather, the product was a mixture of white and gray materials with no appreciable solubility in common organic solvents.

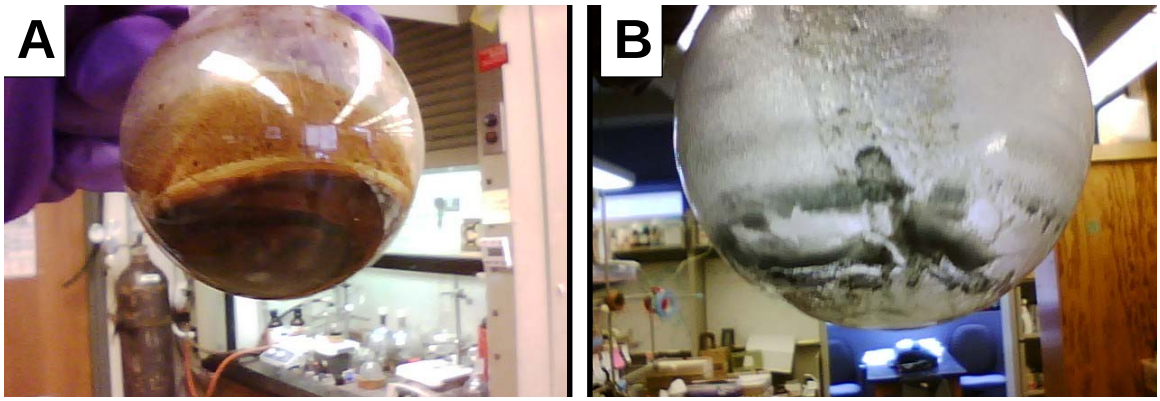
A
B

THF. Dioxygen has nearly equal solubility in toluene and THF (Bunsen solubility coefficients = 0.22 and 0.24, respectively[28,29]), so the effect is not one of O_2 concentration, but of its absence. We next speculate on the role of O_2 in the reaction and the THF solvent.

Dioxygen has been previously shown to influence nanoparticle reactions, in particular in ligand exchange reactions between nanoparticles in two phases.[30] That report involved contacting toluene solutions of hexanethiolate-protected Au NPs with aqueous solutions of Au NPs coated by tiopronin thiolate ligands. In air, metal and ligand exchange reactions were observed between the two phases, but in an inert atmosphere, no exchange took place. Exchanges *did* occur under N_2 in the presence of added gold thiolates (Au(I)-SR). These observations suggested that Au(I)-SR aided transfers between the two phases, and that its presence was promoted by the presence of dioxygen, or by formation of peroxides in solution.

It is instructive to take note of the role of O_2 in peroxide formation in THF; this solvent readily forms peroxides, notably tetrahydrofuran hydroperoxides, which are both reactive and unstable. In the presence of atmospheric oxygen, a pseudo-equilibrium is reached for the formation and decomposition of these hydroperoxides when they attain a concentration of about 2%.[31] In the NP syntheses, the tendency of THF to constantly regenerate hydroperoxides in the presence of oxygen might explain the relative ease of reforming larger-sized Au nanoparticles to smaller $Au_{25}(SR)_{18}$ nanoparticles during synthesis in this solvent. Dharmaratne and co-workers[15a] showed that the reaction in THF involves formation of a polydisperse mixture of nanoparticles, followed by an "aging" process leading to monodisperse $Au_{25}(SR)_{18}$ as the final nanoparticle product.

Figure 2.5: Positive mode electrospray-ionization mass spectrometry (ESI-MS) of the solution byproducts of a reaction synthesizing $Au_{25}(S(CH_2)_2Ph)_{18}$. The byproduct solution had been dried, washed copiously with methanol to remove any excess free thiol, and sonicated in 70:30 methanol:acetone to induce re-dissolution. The peaks at 139 m/z and 197 m/z are thought to originate from fragmentation of Au(I)-thiolates that are produced in the degradation reaction that reforms large nanoparticles to Au_{25}.

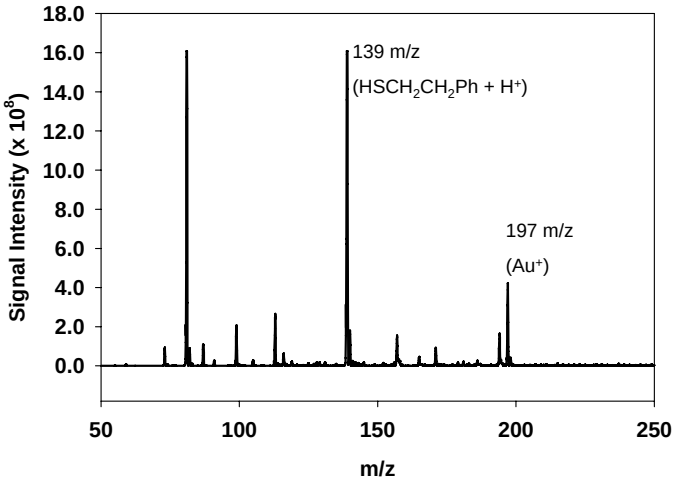
18.0
16.0
14.0
12.0
10.0
8.0
6.0
4.0
2.0
0.0
Signal Intensity (x 10^8)
139 m/z
(HSCH2CH2Ph + H+)
197 m/z
(Au+)
50
100
150
200
250
m/z

In the present procedure, all of the nanoparticle product after the 48 hours of reaction is $Au_{25}(SR)_{18}^-$ and the remainder of the original gold feed reactant is a solution by-product. We speculate that the missing gold remains as gold-thiolate polymer, Au(I)-SR, and/or as Au(I)Br formed by reaction with hydroperoxides. Au(I) thiolates tend, once dried thoroughly, to resist redissolution, as does the dried solution by-product. The dried by-product was washed copiously with methanol to remove any free thiol. Figure 2.5 shows a electrospray-ionization mass spectra of the byproduct material from a reaction synthesizing $Au_{25}(S(CH_2)_2Ph)_{18}$. The intense peak at 139 m/z is indicative of $HS(CH_2)_2Ph$ (+ H^+) and that peak at 197 m/z is Au(I). This spectrum provides evidence that Au(I)-thiolates remain at the end of the reaction; we speculate that these are byproducts of the aging process.

That Au(I)-thiolates result from excess thiol-based etching reactions of large nanoparticles has indeed been shown previously,[32] in experiments in which Au NPs protected $-S(CH_2)_5CH_3$ ligands were heated in neat dodecanethiol. The reaction products were monitored over the course of 40 hours using laser desorption-ionization mass spectra. As the etching reaction progressed, smaller nanoparticles were formed, and the intensity of Au(I)-thiolate peaks in the mass spectra increased. Dass, *et al*,[15b] described a synthesis of small gold nanoparticles in ethanol/dichloromethane, and found a mixture of NPs in the range of Au_{16}-Au_{31}, with Au(I)-thiolate byproducts. Additionally, Tsukuda, *et al*,[33] reported on the unusually high resistivity to core etching of small glutathione-capped nanoparticles, specifically $Au_{25}(SG)_{18}$. This led to a description of a reaction of triphenylphosphine-stabilized Au_{11} clusters with excess glutathione, leading solely to $Au_{25}(SG)_{18}$ clusters in respectable yield.[34]

These observations lend support to our hypothesis that the aging process most likely involves the degradation of larger nanoparticles into $Au_{25}(SR)_{18}$ through the formation of Au(I)-thiolates. Using THF as a solvent increases the rate of this process, possibly through reactions with hydroperoxides formed from the reaction with THF and O_2.

2.4 Conclusions

We present a detailed description of the synthesis of reduced, monodisperse $[Oct_4N^+][Au_{25}(SR)_{18}^-]$. The choice to include Oct_4N^+ is to ensure the nanoparticle is both reduced and in the same form that has been heavily studied in recent years, including the detailed crystal structure.[7] The synthesis described in this report enhances the NP yield to *ca.* 50% by Au atom, and leaves only one nanoparticle product: $Au_{25}(SR)_{18}^-$. Furthermore, it can be tuned to include a variety of different types of ligands, provided they have at least one methylene spacer between the Au-S and the ligand's R-group. Performing the reaction in the absence of H^+ and oxygen provides some insight into the mechanism of the reaction in THF, i.e., the so-called "aging process" is proposed to be a degradative NP reaction with hydroperoxides formed from THF and oxygen.

2.5 Acknowledgements

This research was supported by the National Science Foundation and Office of Naval Research. I would like to acknowledge the contributions of Joshua Weaver and Finlay McCallum, as well as George Dubay at the Duke University mass spectrometry facility.

2.6 References:

(1) Wang, G.; Huang, T.; Murray, R. W.; Menard, L.; Nuzzo, R. G. *J. Am. Chem. Soc.* **2005**, *127*, 812-813.

(2) Jimenez, V. L.; Georganopoulou, D. G.; White, R. J.; Harper, A. S.; Mills, A. J.; Lee, D.; Murray, R. W. *Langmuir* **2004**, *20*, 6864-6870.

(3) Sardar, R.; Funston, A. M.; Mulvaney, P.; Murray, R. W. *Langmuir* **2009**, *25*, 13840-13851.

(4) Hicks, J. F.; Miles, D. T.; Murray, R. W. *J. Am. Chem. Soc.* **2002**, *124*, 13322-13328.

(5) Murray, R. W. *Chem. Rev*. **2008**, *108*, 2688-2720.

(6) Parker, J. F.; Fields-Zinna, C. A.; Murray, R. W., *Accts. Chem. Res.* **2010** *Articles ASAP*.

(7) Heaven, M. W.; Dass, A.; White, P. S.; Holt, K. M.; Murray, R. W. *J. Am. Chem. Soc.* **2008**, *130*, 3754-3755.

(8) Akola, J.; Walter, M.; Whetten, R. L.; Häkkinen, H.; Grönbeck, H. *J. Am. Chem. Soc.* **2008**, *130*, 3756-3757.

(9) Zhu, Y.; Qian, H.; Drake, B. A.; Jin, R. *Angew. Chem. Int. Ed.* **2010**, *49*, 1295-1298.

(10) Schaaff, T. D.; Knight, G.; Shafigullin, M. N.; Borkman, R. F.; Whetten, R. L. *J. Phys. Chem. B* **1998**, *102*, 10643-10646.

(11) Donkers, R. L.; Lee, D.; Murray, R. W. *Langmuir* **2004**, *20*, 1945-1952.

(12) Negishi, Y.; Takasugi, Y.; Sato, S.; Yao, H.; Kimura, K.; Tsukuda, T. *J. Am. Chem. Soc.* **2004**, *126*, 6518-6519.

(13) Negishi, Y.; Nobusada, K.; Tsukuda, T. *J. Am. Chem. Soc.* **2005**, *127*, 5261-5270.

(14) Wu, Z.; Suhan, J.; Jin, R. *J. Mater. Chem.* **2009**, *19*, 622-626.

(15) a) Dharmaratne, A. C.; Krick, T.; Dass, A. *J. Am. Chem. Soc.* **2009**, *131*, 13604-13605. b) Reilly, S. M.; Krick, T.; Dass, A. *J. Phys. Chem. C.* **2010**, *114*, 741-745.

(16) Tracy, J. B.; Kalyuzhny, G.; Crowe, M. C.; Balasubramanian, R.; Choi, J.-P.; Murray, R. W. *J. Am. Chem. Soc.* **2007**, *129*, 6706-6707.

(17) Tracy, J. B.; Crowe, M. C.; Parker, J. F.; Hampe, O.; Fields-Zinna, C. A.; Dass, A.; Murray, R. W. *J. Am. Chem. Soc.* **2007**, *129*, 16209-16215.

(18) Brust, M.; Walker, M.; Bethell, D.; Schiffrin, D. J.; Whyman, R. *J. Chem. Soc. Chem. Commun.* **1994**, 801-802.

(19) Parker, J. F.; Choi, J-P.; Wang, W.; Murray, R. W. *J. Phys. Chem. C* **2008**, *112*, 13976-13981.

(20) Lee, D.; Donkers, R. L.; Wang, G.; Harper, A. S.; Murray, R. W. *J. Am. Chem. Soc.* **2004**, *126*, 6193-6199.

(21) In *Handbook of Preparative Inorganic Chemistry*; Brauer, G., Ed.; Academic Press: New York, 1965; p 1054.

(22) Dass, A.; Stevenson, A.; Dubay, G. R.; Tracy, J. B.; Murray, R. W. *J. Am. Chem. Soc.* **2008**, *130*, 5940-5946.

(23) Choi, J-P.; Murray, R. W. *J. Am. Chem. Soc*. **2006**, *128*, 10496-10502.

(24) Choi, J-P.; Fields-Zinna, C. A.; Stiles, R. L.; Balasubramanian, R.; Douglas, A. D.; Crowe, M. C.; Murray, R. W. *J. Phys. Chem. C*, **2010**, *Articles ASAP*.

(25) Zhu, M. Z.; Eckenhoff, W. T.; Pintauer, T.; Jin, R. *J. Phys. Chem. C* **2008**, *112*, 14221–14224.

(26) Zamborini, F. P.; Gross, S. M.; Murray, R. W. *Langmuir* **2001**, *17*, 481-488.

(27) Guo, R.; Murray, R. W. *J. Am. Chem. Soc.* **2005**, *127*, 12140-12143.

(28) Inamo, M.; Hoshino, M. *Photochem. Photobiol.* **1999**, *70*, 596-601.

(29) Miyashita, Y.; Niizuma, S.; Kokubun, H.; Koizumi, M. *Bull. Chem. Soc. Japan* **1970**, *43*, 3435-3443.

(30) Song, Y.; Huang, T.; Murray, R. W. *J. Am. Chem. Soc.*, **2003**, *125*, 11694–11701.

(31) In *Tetrahydrofuran (THF) Storage and Handling*; BASF Corporation: Mount Olive, NJ, 1998; p 3.

(32) Schaaff, T. G.; Whetten, R. L. *J. Phys. Chem. B.* **1999**, *103*, 9394-9396.

(33) Shichibu, Y.; Negishi, Y.; Tsunoyama, H.; Kanehara, M.; Teranishi, T.; Tsukuda, T. *Small* **2007**, *3*, 835-839.

(34) Shichibu, Y.; Negishi, Y.; Tsukuda, T.; Teranishi, T. *J. Am. Chem. Soc.* **2005**, *127*, 12464-13465.

Appendix 2

On the Synthesis of Monodisperse $[Oct_4N^+][Au_{25}(SR)_{18}^-]$ Nanoparticles, with Some Mechanistic Observations

Table A2.1. Comparison of Absorbance values in the reduced and oxidized states, for SR = -S(CH_2)$_2$Ph, as prepared by extraction into acetonitrile and chemical oxidation respectively, as well as the result of the syntheses with Oct_4N^+ present or absent. The relative size of the peaks at 399 and 446 nm are indicators of oxidation state and vary from 1.2 (reduced) to 1.4 (oxidized).

	Extracted into MeCN Au_{25}^{-1}	**Chemically Oxidized Au_{25}^{0}**
Abs_{399} (nm)	0.452	0.472
Abs_{446} (nm)	0.388	0.340
$\frac{Abs_{399}}{Abs_{446}}$	1.2	1.4
Synthetic product		
	Au_{25} (Oct_4N^+ present)	**Au_{25} (Oct_4N^+ absent)**
Abs_{399} (nm)	0.408	0.423
Abs_{446} (nm)	0.354	0.297
$\frac{Abs_{399}}{Abs_{446}}$	1.2	1.4

Figure A2.1. (A) Cyclic Voltammetry and (B) Differential Pulse Voltammetry results for $Au_{25}(S(CH_3)_5CH_3)_{18}$. Both experiments utilized a 2 mm Pt-disk working, Pt-coil counter, and Ag quasi reference electrode (AgQRE). The nanoparticle concentration was about 1.0 μM in 0.1 M CH_2Cl_2/But_4NClO_4. The electrochemical bandgap is 1.68 V, the $\Delta E^{o'}$ between $Au_{25}^{1-/0}$ and $Au_{25}^{0/1+}$ is 0.28 V, and that between $Au_{25}^{0/1+}$ and $Au_{25}^{1+/2+}$ is 0.78 V.

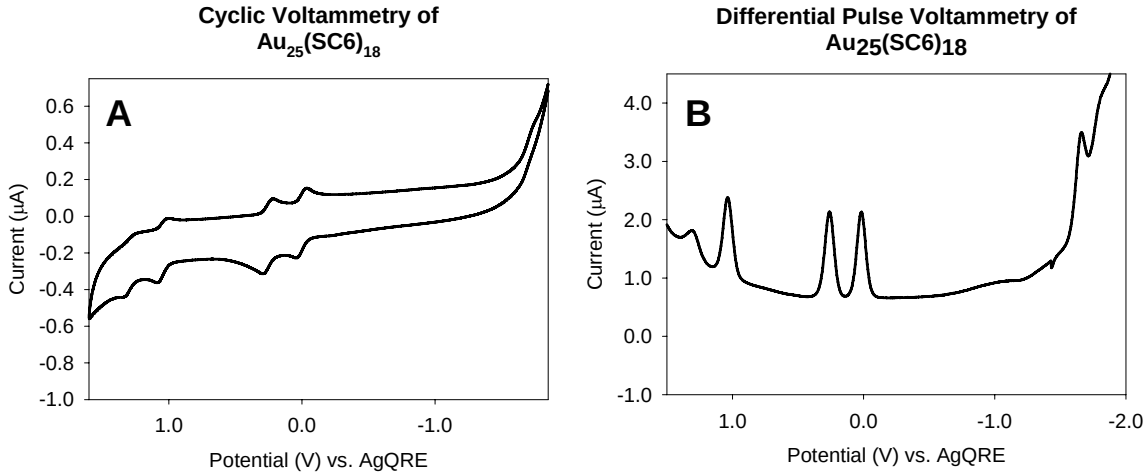
Cyclic Voltammetry of
Au25(SC6)18
A
Current (μA)
0.6
0.4
0.2
0.0
-0.2
-0.4
-0.6
-0.8
-1.0
1.0
0.0
-1.0
Potential (V) vs. AgQRE
Differential Pulse Voltammetry of
Au25(SC6)18
B
Current (μA)
4.0
3.0
2.0
1.0
0.0
-1.0
1.0
0.0
-1.0
-2.0
Potential (V) vs. AgQRE

Figure A2.2. UV-Vis spectra of $[Oct_4N^+][Au_{25}(S(CH_2)_2Ph)_{18}^-]$ (black) and the product of the synthesis using benzylmercaptan ($HSCH_2Ph$) (red). The peak 680 nm and the shoulder at 800 nm suggested successful production of reduced Au_{25} in both cases, but the increased absorbance below 600 nm suggested an impure material, possibly due to changes in solubility associated with this ligand that leads to insufficient clean-up of remaining gold-thiolates. The solution color and voltammetry (Figure A2.3) suggest that Au_{25} is the main product. No further purification was attempted.

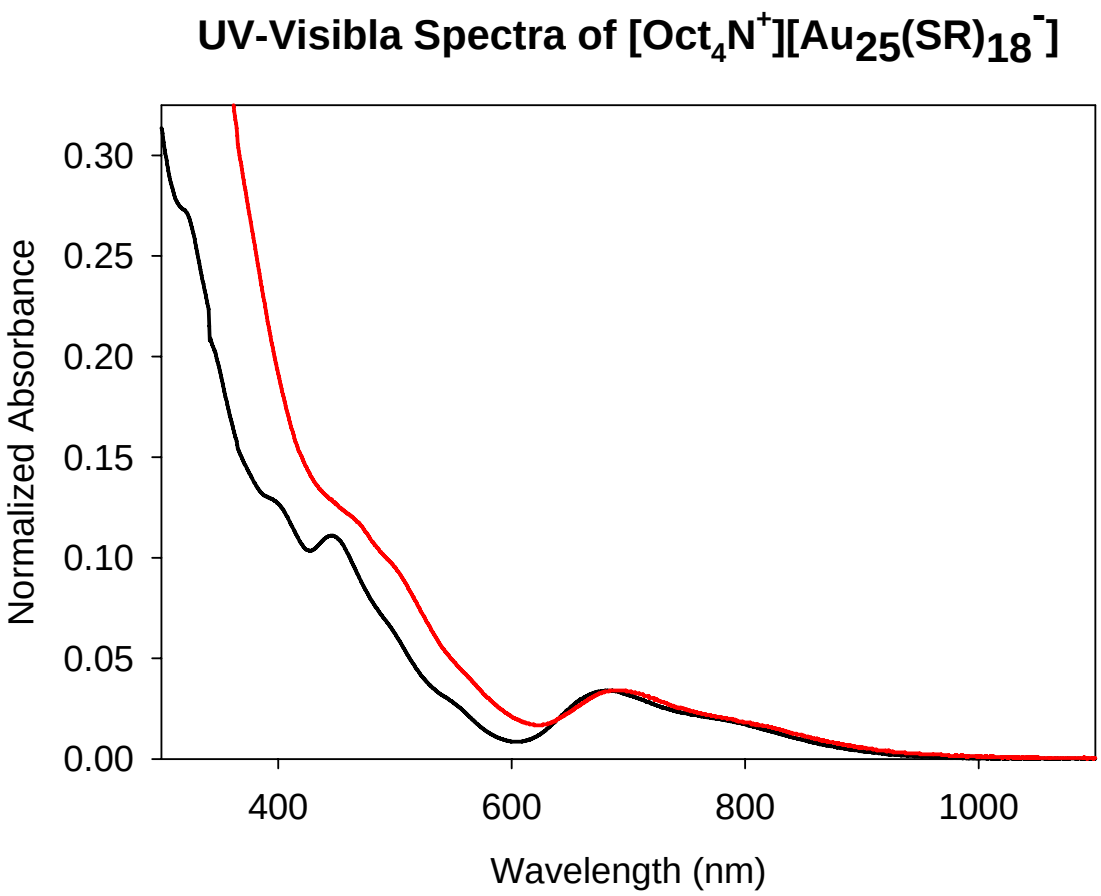
UV-Visibla Spectra of [Oct4N+][Au25(SR)18-]
Normalized Absorbance
0.30
0.25
0.20
0.15
0.10
0.05
0.00
400
600
800
1000
Wavelength (nm)

Figure A2.3. (A) Cyclic Voltammetry and (B) Differential Pulse Voltammetry results for $Au_{25}(SCH_2Ph)_{18}$. Both experiments utilized a 2 mm Pt-disk working, Pt-coil counter, and Ag quasi reference electrode (AgQRE). The nanoparticle concentration was about 1.0 μM in 0.1 M CH_2Cl_2/But_4NClO_4. The electrochemical bandgap is 1.61 V, the $\Delta E^{o'}$ between $Au_{25}^{1-/0}$ and $Au_{25}^{0/1+}$ is 0.21 V, and that between $Au_{25}^{0/1+}$ and $Au_{25}^{1+/2+}$ is 0.68 V. The broad peak at -1.0 V is due to oxygen impurity, while other minor peaks are unknown but could arise from contaminants of the gold-thiolate polymer.

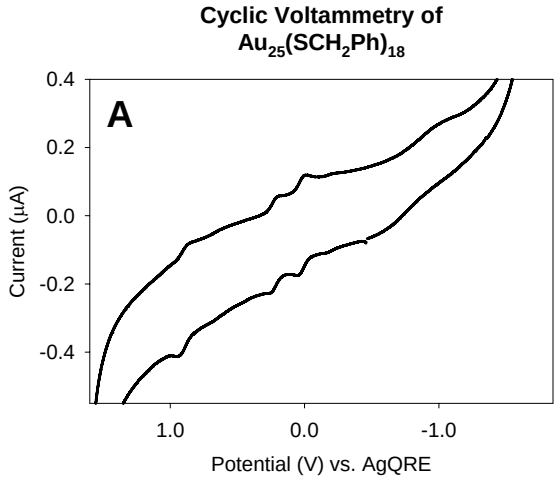
Cyclic Voltammetry of
Au25(SCH2Ph)18
A
0.4
0.2
0.0
-0.2
-0.4
Current (μA)
1.0
0.0
-1.0
Potential (V) vs. AgQRE

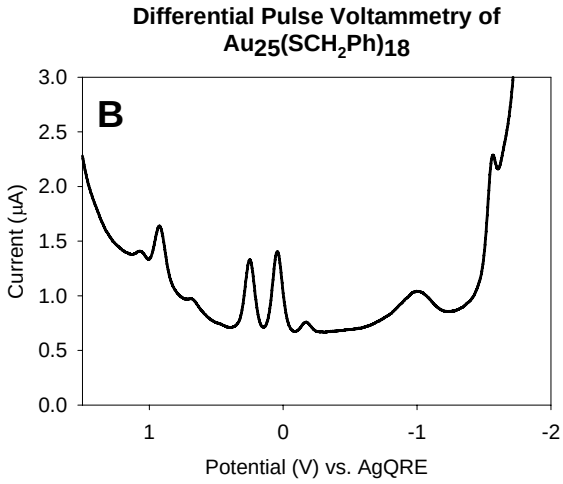
Differential Pulse Voltammetry of
Au25(SCH2Ph)18
B
3.0
2.5
2.0
1.5
1.0
0.5
0.0
Current (μA)
1
0
-1
-2
Potential (V) vs. AgQRE

Chapter 3

Electron Self-Exchange Dynamics of the Nanoparticle Couple $[Au_{25}(S(CH_2)_2Ph)_{18}]^{0/1-}$ By Nuclear Magnetic Resonance Line-Broadening

3.1 Introduction

Gold monolayer protected clusters (MPCs) are a class of novel materials consisting of a core of gold atoms surrounded and stabilized by a shell of organic ligands, typically thiolates. Au nanoparticles with core diameters < 3 nm lie in the metal-to-molecule transition range and display interesting, size-dependent properties. These are, for example, readily seen in the size dependence of the voltammetry of very small MPCs,[1-5] and in research on electronic,[6,7] biological,[8,9] and catalytic[10,11] properties. Larger dimensioned nanoparticles display properties associated with a continuum of electronic states, but at smaller MPC core diameters the electronic energies condense into discrete levels, and molecule-like one-electron redox processes emerge. $[Au_{25}(S(CH_2)_2Ph)_{18}]$ is of the latter nanoparticle family, having according to its recently reported crystal structure[12] an overall diameter of about 2.4 nm (including ligands) and a core diameter of ~1.3 nm (including outermost Au sites of its $Au_2(SR)_3$ semi-rings). The native (reduced) nanoparticle $[Au_{25}(S(CH_2)_2Ph)_{18}]$ is a 1- anion and the crystal

structure—an abbreviated representation of which is shown in Figure 3.1—was of the salt $[Oct_4N][Au_{25}(S(CH_2)_2Ph)_{18}]$. The nanoparticle salt is soluble and stable in organic solvents and has experienced photoluminescence,[13] mass spectral,[14-16] and electron transfer chemistry[17,18] studies. (The mass spectral observations[14,15] corrected earlier mis-assignment as a Au_{38} nanoparticle.) The $[Au_{25}(S(CH_2)_2Ph)_{18}]$ nanoparticle exhibits electrochemically stable charge states of -1, 0, and +1.[15,17,19]

This report describes measurement of the electron self-exchange dynamics of the $[Au_{25}(S(CH_2)_2Ph)_{18}]^{0/1-}$ couple (abbrev. Au_{25}^{0} and Au_{25}^{1-}) using the classical line-broadening analysis of ^1H nuclear magnetic resonance (NMR) first introduced by McConnell.[20] Since one-electron transfer couples generally have one member with an odd electron count, that member's magnetism typically causes the resonances of the reduced and oxidized components of the couple to lie at well-separated chemical shifts. Assuming fast-exchange kinetics, and that the electron transfer rate exceeds the Larmor periods of the components,[21] transfer of magnetization from one to the other can be measured using NMR. The component with the odd electron count shortens the T_1 and T_2 relaxation times of nearby proton sites, causing line-broadening and increase in the full width at half-maximum (fwhm) of their peaks by the relationship $W = (\pi T_2)^{-1}$.

As examples of previous measurements, Yang, *et al.*[22] measured the electron exchange rate between ferrocene and (paramagnetic) ferrocenium by observing the peak broadening and varying chemical shifts of the cyclopentadiene resonances when a small amount of ferrocenium was present. Coddington, *et al.*[23] reported a similar study on electron exchange kinetics of rhenium complexes. Detailed reviews of electron and other chemical exchanges in NMR and of the effects of paramagnetism are available.[24,25] The

Figure 3.1. Simplified X-ray crystal structure of $[Oct_4N^+][Au_{25}(S(CH_2)_2Ph)_{18}^{1-}]$. The icosahedral, Au_{13}, core is surrounded by 6 –S-Au-S-Au-S- semi-rings. Two sulfur environments are present in the nanoparticle: twelve sulfur atoms are connected to the Au_{13} core and the semi-rings while six sulfur atoms are found only on the vertices of the semi-rings. The bond angles for the two environments are 86.7 ± 0.8º and 101.2 ± 0.6º respectively. The semi-rings in the reduced MPC do not align along the plane, exhibiting a puckering of the S-Au-S bond as shown in the black rectangle. (Legend: Gold = yellow, Sulfur = violet, Carbon = green, hydrogens not shown).

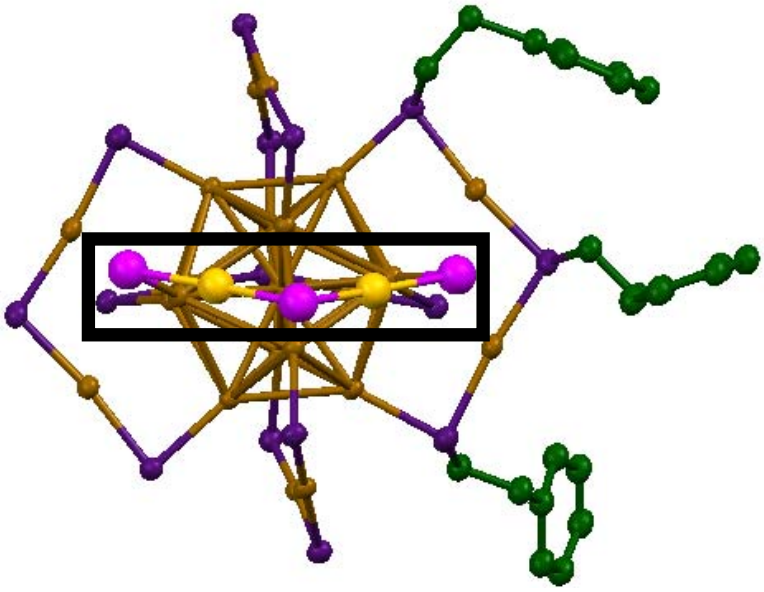

present report, however, is the first use of NMR to investigate electron exchange kinetics of metal nanoparticles, in this case specifically of the $[Au_{25}(S(CH_2)_2Ph)_{18}]^{0/1-}$ couple.

Proton NMR spectra of the $[Au_{25}(S(CH_2)_2Ph)_{18}]$ nanoparticle, discussed previously,[26,27] exhibit peaks for the phenyl protons and the methylene protons α and β to the sulfur. The slightly broadened and split α-CH_2 proton resonance for the completely reduced Au_{25}^{1-} state, in CD_2Cl_2 solutions, is centered at 3.17 ppm. The broadening presumably reflects variation of chemical shifts with binding site and other environmental effects over the nanoparticle's 18 ligands. That NMR chemical shifts of thiolate ligands can vary with their binding site on the nanoparticle surface is known.[28-30] Multiple chemical shifts are clearly evident in ^{13}C NMR by doublets of each phenyl ring carbon peak, an observation consistent with ligand exchange kinetic[26,31] and crystallographic[12] data (Figure 3.1) that show two distinct types of ligand binding. The α-CH_2 chemical shift was seen at 3.17 ppm, however, only for *carefully reduced* nanoparticles, otherwise the α-CH_2 peak chemical shift and fwhm seemed variable from day-to-day. This confusing behavior was clarified when it was realized that the adventitious presence of small amounts of oxidized MPCs (i.e., Au_{25}^{0}) in the nanoparticle samples might evoke these effects through an electron self-exchange process, namely

$$Au_{25}(SC2Ph)_{18}^{1-} + Au_{25}(SC2Ph)_{18}^{0} \rightleftharpoons Au_{25}(SC2Ph)_{18}^{0} + Au_{25}(SC2Ph)_{18}^{1-} \quad (1)$$

NMR analysis of electron transfers by line-broadening, assuming that the rate is in the fast-exchange region and exceeds the isotropic shift (*kc >> 2π(δν)*),[32] relies on the relation

$$W_{MIX} = f_{ox}W_{ox} + f_{red}W_{red} + \frac{4\pi f_{ox}f_{red}(\delta\nu)^2}{kc} \quad (2)$$

where the *W* terms are the full-width-half-maxima of resonance peaks for solutions of fully oxidized, fully reduced, and mixtures of the two states, *c* is the total concentration (oxidized plus reduced), and *k* is the second order self-exchange rate constant. In the present case, the isotropic shift ($\delta\nu$, Hz) is the peak separation between the α-CH_2 protons of the fully oxidized and fully reduced (Au_{25}^0 and Au_{25}^{1-}) nanoparticles. Equation (2) predicts that at a fixed mole fraction of oxidized MPC (f_{ox}), W_{MIX} of the α-CH_2 proton peak should vary inversely with reciprocal overall concentration (*c*). The slope of such a plot yields the rate constant *k*.

^{1}H NMR rate constant determinations were carried out at four temperatures in order to estimate the exchange reaction's activation energy E_A and pre-exponential factor. We observe a large reorganization barrier energy (25.0 kJ/mol), which in comparison to outer sphere energy barrier (as in Marcus[33,34] electron transfer theory) estimates is calculated to be 69% inner-sphere. This result agrees with earlier results[10,35] that suggested the presence of a substantial inner sphere reorganizational energy barrier term for reaction (1). Antonello *et al.*[10] reported a large inner-sphere term for this nanoparticle based on the temperature dependence of a heterogeneous electron transfer rate constant determined using cyclic voltammetry. The ΔG_{is}^* was estimated to be in the range of 72-83% of the total reorganization energy. The implication of such a large inner-sphere term suggests a rearrangement of the bond lengths and/or bond angles between the two charge states of Au_{25}. This implication is consistent with Raman spectroscopy evidence, presented here, that the Au-S bond stretch energies differ for the Au_{25}^0 *vs*. Au_{25}^{1-} nanoparticles. Given the structure in Figure 3.1, containing six slightly puckered Au_2S_3 semi-rings arranged around a Au_{13} icosahedral core, the changes are almost certain to

involve more than just Au-S bond length changes. The semi-rings may flatten or become more puckered, for example, altering all Au-S bond lengths and angles. Since the crystal structure of the neutral Au_{25}^0 nanoparticle has yet to be determined, such structural change(s) are a matter of conjecture.

3.2 Experimental

$[Au_{25}(S(CH_2)_2Ph)_{18}]$ was synthesized using a modified version of the Brust synthesis.[36-38] Hydrogen tetrachloroaurate (3.1 g, 11.1 mol) was dissolved in toluene using the phase-transfer reagent tetraoctylammonium bromide ($Oct_4N^+Br^-$). A 3.2 molar excess of phenylethanethiol was added to the solution at room temperature, forming the intermediate colorless gold-thiolate polymer, followed by immediate reduction by ice-cold sodium borohydride in excess, stirring for 20 hours. The black product solution contains a mixture of MPC core sizes and oxidation states; the reduced (which we also call the native form) $[Oct_4N^+][Au_{25}(S(CH_2)_2Ph)_{18}^{1-}]$ is fortuitously the only species with appreciable solubility in acetonitrile and thus was extracted from the dried reaction mixture and copiously washed with methanol to remove excess free thiol and Oct_4N^+ salts. Some Oct_4N^+, now understood[12,16] to be its charge-balancing counterion, persistently remains (by ^1H NMR) in a 1:1 mole ratio to the MPC.

All ^1H NMR measurements were made using a Bruker AC500 spectrometer and in CD_2Cl_2 solutions, with a D1 of 1.00 sec. Spectra were obtained for purified $[Oct_4N^+][Au_{25}(S(CH_2)_2Ph)_{18}^{1-}]$ and for the oxidized form $[Au_{25}(S(CH_2)_2Ph)_{18}]^0$ at 300, 295, 290, and 285 K, shimming and re-tuning at each temperature. Electrochemical experiments were performed in 100 mM Bu_4NClO_4 / CH_2Cl_2 using a Model 100B

Bioanalytical Systems analyzer. The working electrode was a 2 mm diameter Pt disk for voltammetry and a Pt mesh for bulk electrolysis; counter and reference electrodes were a Pt coil and Ag/AgCl/1.0 M KCl, respectively. Bulk electrolysis was performed to obtain the oxidized MPC, $[Au_{25}(S(CH_2)_2Ph)_{18}]^0$, by charging the solution until it exhibits a final potential of +110 mV *vs*. Ag/AgCl. The oxidized, neutral $[Au_{25}(S(CH_2)_2Ph)_{18}]^0$ is insoluble in acetonitrile, so residual reduced nanoparticle was readily removed by acetonitrile washing. Further, after electrolysis to the one-electron oxidized state, Au_{25}^0, the Oct_4N^+ cation NMR peaks nearly vanish.

For kinetic measurements, a mixture of oxidized and reduced (i.e., Au_{25}^- and Au_{25}^0) nanoparticles having a combined mass of 14.6 mg was dissolved in 800 μL CD_2Cl_2 and proton NMR spectra measured at 300, 295, 290, and 285 K. The total nanoparticle concentration was subsequently lowered by serially adding seven 100 μL increments of pure CD_2Cl_2, observing the peak widths at the various temperatures for each total concentration. The actual fraction of oxidized MPC present, estimated when mixing the two forms, was confirmed by observing the chemical shift, ν_{mix}, compared to the overall isotropic shift, $\delta\nu$, using the relationship $f_{ox} = (\nu_{mix} - \nu_{red})/\delta\nu$. Invoking Equation (2), the observed fwhm, W_{MIX} , of the α-CH_2 proton peak was plotted *vs*. $1/c$ to produce a second-order self-exchange rate constant for each temperature. The only contribution to the ionic strength of these solutions was the presence of the Oct_4N^+ counterion of the reduced Au_{25}^{1-} nanoparticles; the resulting small variation in ionic strength at various f_{red} is assumed to not be significant.

For Raman studies, $[Au_{25}(S(CH_2)_2Ph)_{18}]^{1-}$ nanoparticles were chemically oxidized by contact of CH_2Cl_2 solutions with aqueous Ce(IV) as previously reported for this and

Au_{140} MPCs.[35,39] Raman spectra of MPC films drop-cast on glass slides were taken with a LabRAM ARAMIS Raman spectrometer (HORIBA Jobin Yvon, Inc., Edison, NJ) equipped with a microscope and 785 nm diode laser source, using a 10% transmission D1 filter, 25 μm slit-width, CCD camera cooled to −70°C, 100x microscope objective, 20 sec. of exposure, and 30 spectral accumulation scans. The spectrometer was calibrated using scattering bands of silicon (520 cm^{-1}) and Teflon (1300 cm^{-1}). Further aspects of these Raman experiments will be reported elsewhere.[40]

3.3 Results and Discussion

3.3.1 The $[Au_{25}(S(CH_2)_2Ph)_{18}]$ ^{1}H NMR Spectrum.

NMR analysis of the electron exchange kinetics of the Au_{25} MPC required improving the current[26,27,31,38] understanding of its proton NMR spectra. The ligand has three sets of protons. The phenyl proton peaks (7.00 to 7.25 ppm) seem to be only slightly affected by the MPC oxidation state. In the free thiol, the α-CH_2 (-S-***CH_2***-CH_2-Ph) group appears as a quartet at 2.83 ppm, in CD_2Cl_2, whereas in the reduced Au_{25}^{1-} MPC state, the α-CH_2 is a broad peak with indistinct fine structure, shifted slightly downfield to ~3.17 ppm[27] (Figure 3.2). The β-CH_2 protons appear as two distinct resonances—a triplet at 2.99 ppm and a very broad resonance at ~3.8 ppm. The latter is seen only in the pure Au_{25}^{1-} state, becoming broadened to apparent oblivion when a small percentage of the MPC is oxidized. These assignments are based on two-dimensional Correlation Spectroscopy (COSY) measurements (see Appendix II). The integrals of the α-CH_2 and (summed) β-CH_2 peaks are equal as expected, and each is 2/5 of the phenyl resonances.

Figure 3.2. ^{1}H NMR spectrum of pure, reduced state $[Au_{25}(S(CH_2)_2Ph)_{18}]^{1-}$ at 300 K in CD_2Cl_2. Peaks at 7.00 – 7.25 ppm are attributed to the phenyl groups, containing rich splitting features similar to the free thiol. The broadened multiplet at 3.17 ppm from the α-CH_2 of the 18 thiolate ligands is not simply a triplet presumably owing to differences between the two kinds of thiolate ligand sites.[12] The β-CH_2 peaks at 2.99 and 3.79 ppm are similarly different due to different ligand sites and configurations, but a full interpretation is not yet attained. The peak at 3.08 ppm reflects –C**H$_2$**N of the $(Oct)_4N^+$ counterion.

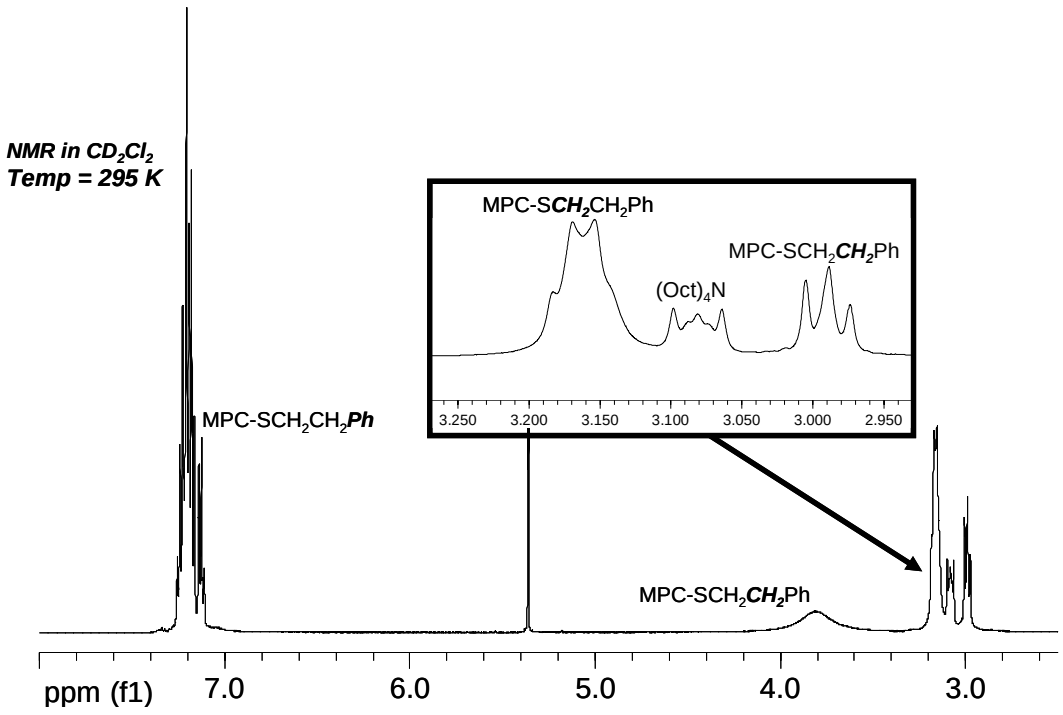
NMR in CD2Cl2
Temp = 295 K
MPC-SCH2CH2Ph
MPC-SCH2CH2Ph
MPC-SCH2CH2Ph
(Oct)4N
MPC-SCH2CH2Ph
3.250
3.200
3.150
3.100
3.050
3.000
2.950
ppm (f1)
7.0
6.0
5.0
4.0
3.0

Our understanding of the splitting and broadening of the β-CH_2 resonances is incomplete. The current structural information[12] (Figure 3.1) makes clear that there are two different types of thiolate ligand binding sites (in the solid state Au_{25}^{1-} salt) and encourages a proposal that the splitting reflects somehow the different chemical shifts of those sites. That there are two different ligand populations and corresponding ^{13}C chemical shifts was already signaled[26,38] by splitting of the ^{13}C phenyl resonances.

It became understood in the current study that the broadening of the α-CH_2 peak is enhanced when the Au_{25}^{1-} MPC solution contains even a small portion of the oxidized form Au_{25}^{0}. This observation and the ensuing downfield shift of the α-CH_2 protons as larger fractions of the oxidized Au_{25}^{0} form are present (Figure 3.3), indicated the presence of a two-state exchange mechanism and led to the present evaluation of electron self-exchange kinetics.

^1H NMR spectra of solutions of reduced Au_{25} nanoparticles have persistently shown the presence of the Oct_4N^+ cation, regardless of the extent of washing with methanol. We now understand from mass spectrometry[14-16] and ensuing crystallographic[12] results that the acetonitrile-soluble nanoparticle is in fact an anion, Au_{25}^{1-}, and thus necessarily has a counterion. The Oct_4N^+ species in samples of reduced Au_{25}^{1-} can be exchanged with other cations, such as But_4N^+ and Et_4N^+ (See Appendix II); there is no special structural interaction with the Oct_4N^+ counterion. In each case, the cationic counterion appears in a 1:1 mole ratio (by peak integration) in the NMR spectrum of carefully purified, fully reduced Au_{25}^{1-} MPC. These results are fully consistent with the crystallographic and mass spectrometric evidence,[12,14-16] that the

Figure 3.3: ^{1}H Nuclear magnetic resonance spectra of reduced $[Au_{25}(S(CH_2)_2Ph)_{18}]^{1-}$, oxidized $[Au_{25}(S(CH_2)_2Ph)_{18}]^{0}$, and mixtures of the two forms, presented as fraction of oxidized (f_{ox}) material present. Inset shows the linearity of chemical shift with f_{ox}, consistent with a fast exchange mechanism. The mixtures exhibit peak widths greater than those of the two pure forms (see Table 3.1). The full-width at half-maximum is dependent on the total concentration of MPC in solution and the relative fraction of each form, consistent with an electron self-exchange process.

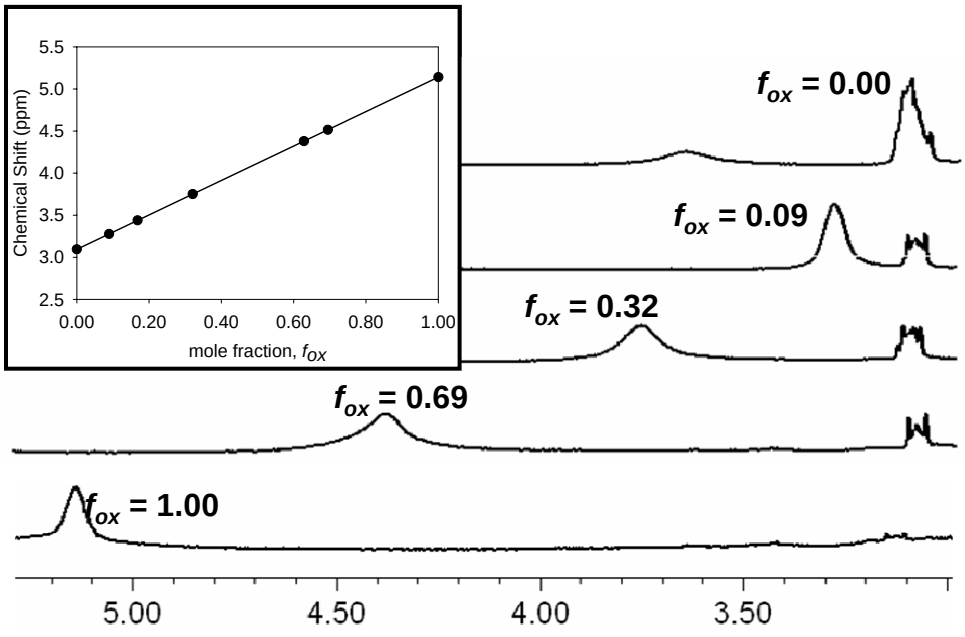
Chemical Shift (ppm)
5.5
5.0
4.5
4.0
3.5
3.0
2.5
0.00
0.20
0.40
0.60
0.80
1.00
mole fraction, f_{ox}
f_{ox} = 0.00
f_{ox} = 0.09
f_{ox} = 0.32
f_{ox} = 0.69
f_{ox} = 1.00
5.00
4.50
4.00
3.50

oxidized nanoparticle is $[Au_{25}(S(CH_2)_2Ph)_{18}]^0$ and the reduced material $[Au_{25}(S(CH_2)_2Ph)_{18}]^{1-}$.

3.3.2 Electron Self-Exchange Kinetics of the $[Au_{25}(S(CH_2)_2Ph)_{18}]^{0/1-}$ Couple.

As noted above, the presence of oxidized Au_{25}^0 MPC causes a downfield shift of the α-CH_2 resonance and an increase in its peak width. Figure 3.3, inset shows that in mixtures of oxidized and reduced Au_{25} nanoparticles, the α-CH_2 chemical shift changes linearly with the mole fraction of oxidized nanoparticle. This shows unequivocally that the chemical shift is an average of that of the oxidized and reduced forms and that the electron exchange reaction is in the "fast limit". Importantly, the averaging is not at the fastest exchange limit, since the fwhm of peaks in the mixture solutions (W_{MIX}) are larger than those of the fully oxidized and reduced nanoparticles (Figure 3.3). Additionally, W_{MIX} increases as the total nanoparticle concentration decreases (Table 3.1) since the exchange rate in a bimolecular process (Eqn. 1) is slowed by dilution.

In further analysis of the exchange process, the difference in chemical shifts of the pure oxidized and reduced species—the isotropic shift $\delta\nu$, was determined at four different temperatures (Table 3.1). The oxidized state, Au_{25}^0, was obtained by exhaustive oxidative electrolysis. The temperature range used was constrained to 285-300 K due to excessive peak broadening (and ensuing uncertainty in peak fwhm) at lower temperatures and at higher temperatures by CD_2Cl_2 volatility. A fixed fraction of oxidized MPC, f_{ox} = 0.25, was chosen for kinetic experiments in which the α-CH_2 peak width was measured at seven concentrations, at each temperature (Figure 3.4 and Table 3.1). f_{ox} is not significantly changed by disproportionation of Au_{25}^0 (into Au_{25}^+ and Au_{25}^{1-}); the

Figure 3.4. ^{1}H NMR peak width of α-CH_2 protons in MPC reduced/oxidized mixtures (25% oxidized) *vs*. reciprocal MPC concentration, at 285-300 K, according to Equation (2). The slope of each line is $4\pi f_{ox} f_{red} (\delta\nu)^2/k$. The rate constants at each temperature are shown on the figure above each curve.

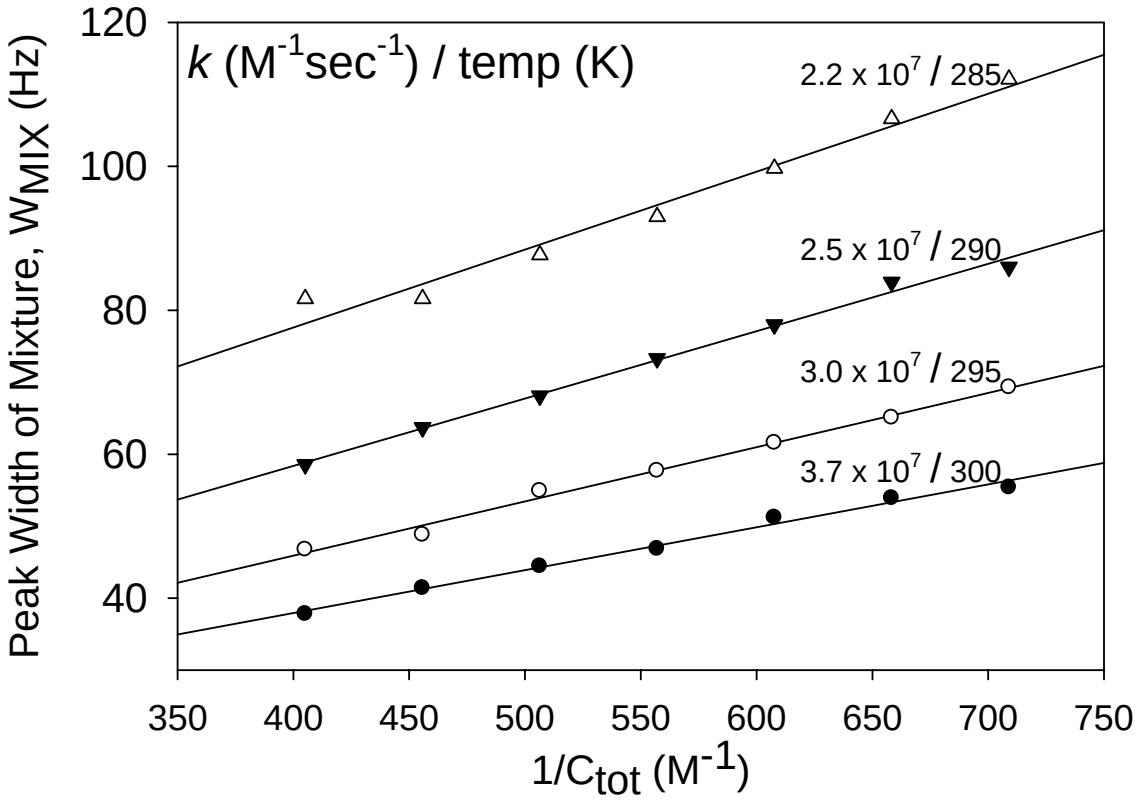
k (M-1sec-1) / temp (K)
2.2 x 10^7 / 285
2.5 x 10^7 / 290
3.0 x 10^7 / 295
3.7 x 10^7 / 300
Peak Width of Mixture, WMIX (Hz)
120
100
80
60
40
350
400
450
500
550
600
650
700
750
1/Ctot (M-1)

Table 3.1. Electron exchange rate constants and peak width fwhm data as a function of total MPC concentration and temperature. The fraction of oxidized MPC present is f_{ox} = 0.25.

Temp. (K)	Total Concentration $c \times 10^3$ [M]	W_{mix} (Hz)	k (M^{-1} s^{-1})
300 ($\delta\nu$ = 970.0 Hz)	2.47 2.19 1.97 1.80 1.65 1.52 1.41	37.8 41.4 44.5 46.9 51.2 53.9 55.4	$(3.7 \pm 0.2) \times 10^7$
295 ($\delta\nu$ = 982.6 Hz)	2.47 2.19 1.97 1.80 1.65 1.52 1.41	46.8 48.8 54.9 57.7 61.6 65.1 69.3	$(3.0 \pm 0.1) \times 10^7$
290 ($\delta\nu$ = 994.2 Hz)	2.47 2.19 1.97 1.80 1.65 1.52 1.41	58.6 63.7 68.1 73.3 78.0 83.9 86.0	$(2.5 \pm 0.1) \times 10^7$
285 ($\delta\nu$ = 1006.3 Hz)	2.47 2.19 1.97 1.80 1.65 1.52 1.41	81.6 81.6 87.7 93.0 99.7 106.6 112.1	$(2.2 \pm 0.2) \times 10^7$

voltammetric[19] peak separation $E^{'}_{1+/0}$ - $E'_{0/-1}$ = 300 mV so that $K_{DISPROPORT}$ is small, only ~8×10^{-6}. Figure 3.4 shows that W_{MIX} (of the α-CH_2 fwhm) increases linearly with the reciprocal of nanoparticle concentration (c) in a mixture of oxidized and reduced Au_{25} mixture (f_{ox} = 0.25). Equation (2) predicts that plots of W_{MIX} against reciprocal concentration ($1/c$) should be linear, with slopes containing the rate constant k. Figure 3.4 shows such plots at different temperatures. Table 3.1 gives the total Au_{25} concentration and NMR peak width data and resulting rate constants. The rate constant at 22ºC is $3.0(\pm 0.1)\times 10^7$ $M^{-1}s^{-1}$.

The rate constant of reaction (1) was also estimated by measuring W_{MIX} at varied f_{ox}, giving $3.5(\pm 0.3)\times 10^7$ $M^{-1}s^{-1}$ (Appendix II). This method requires the inclusion of the intercept terms and a varying concentration term as well, which introduce more sources of possible error into the rate constant calculation. It is preferable to measure the rate constant at a fixed fraction of oxidized and reduced forms as done in Figure 3.4.

The rate constants decrease with decreasing temperature and yield an Arrhenius activation plot (*ln k vs. 1/T,* Figure 3.5) with a slope corresponding to an activation energy barrier E_A = 25.0(±1.5) kJ/mol. This E_A result is similar to that of electron hopping[35] (~20 kJ/mol) in solid-state mixed valent films of this same nanoparticle, and to that determined by Antonello *et al.*[10] (5 kcal/mol, ~21 kJ/mol) using cyclic voltammetry. The intercept of the Figure 3.5 plot gives a pre-exponential factor $9(\pm 6)\times 10^{11}$ $M^{-1}s^{-1}$. The large uncertainty of the pre-exponential term is plausible given the narrow temperature range of the experiments, and its actual value is unremarkable.

Figure 3.5. Activation plot, whose linear regression slope gives E_A = 25.0±1.5 kJ/mol and intercept (pre-exponential factor A) = 9(±6)×10^{11} $M^{-1}s^{-1}$ based on the equation $k = A\ exp(-E_A/RT)$. Uncertainty of the slope reflects a least squares fit. The intercept uncertainty reflects multiplying the uncertainty of the slope by the square root of the sum of the squares of the 1/T values.[50]

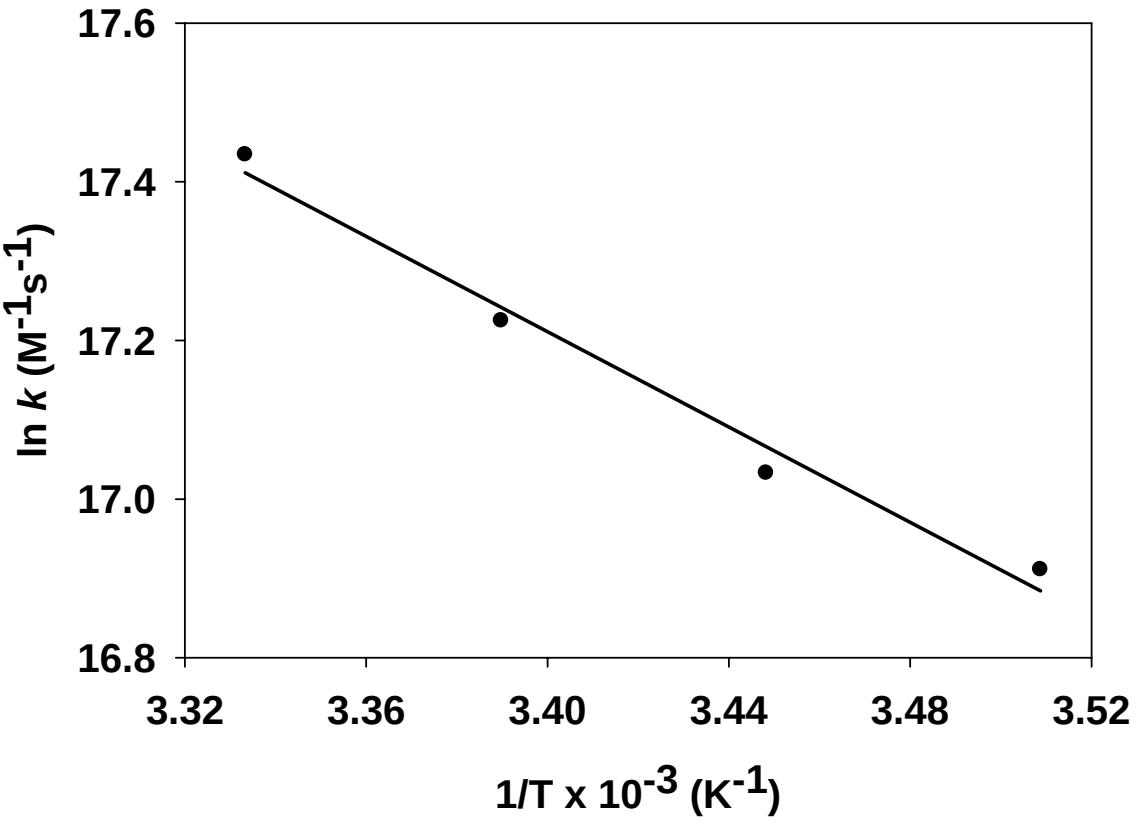
17.6
17.4
17.2
17.0
16.8
ln k (M-1s-1)
3.32
3.36
3.40
3.44
3.48
3.52
1/T x 10-3 (K-1)

The experimental activation barrier energy can be equated to the activation free energy since the reaction is a symmetrical self-exchange. Its large magnitude can be inspected using the Marcus descriptions of reorganization energy barrier factors,

$$\Delta G^{*} = \frac{\lambda}{4}\left(1+\frac{\Delta G^{o}}{\lambda}\right)^{2} \qquad (3)$$

where λ is the sum of the inner and outer-sphere contributions and ΔG^{o} is free energy change of the electron transfer reaction. ΔG^{o} is zero in the case of electron self-exchange. The outer-sphere contribution to the activation energy can be estimated by

$$\Delta G^{*}_{os} = \frac{\lambda_o}{4} = \frac{e^2 N_A}{16\pi\varepsilon_o}\left(\frac{1}{2r_1}+\frac{1}{2r_2}-\frac{1}{r_{12}}\right)\left(\frac{1}{\varepsilon_{op}}-\frac{1}{\varepsilon_s}\right) \qquad (4)$$

where e is the electron charge, ε_o the permittivity of free space (8.854×10^{-12} F/m), r the assumed reactant radii ($r_1 = r_2 = 0.55$ nm[35]), r_{12} the collision diameter ($r_{12} = 2.3$ nm[35,41]), ε_{op} the optical dielectric constant (2.4), and ε_s the static dielectric constant (3.9).[42] The optical dielectric constant is the square of the refractive index of free phenylethanethiol and the static dielectric constant was determined experimentally from analyzing the relationship between those of phenylethane ($\varepsilon_s = 2.3$) and its thiolate counterpart when attached to a gold self-assembled monolayer.[42-44] The calculated ΔG_{os}^{*} is 7.7 kJ/mol, significantly less than the experimental 25 kJ/mol E_A value determined from Figure 3.5. We assign the difference to an inner-sphere contribution, ΔG_{is}^{*}, which from $E_A - \Delta G_{os}$* is 17.3 kJ/mol (4.1 kcal/mol, 0.18 eV). This describes the electron transfer energy barrier as 69% inner-sphere in character. This result is very similar to the solid-state[35] mixed valent conductivity (62%) and solution voltammetry[10] (72 – 83%) results. The inner-sphere term may be slightly overestimated by omitting the static dielectric constant of the

solvent, dichloromethane, since it assumes that the primary contribution to the dielectric medium surrounding the gold core is the monolayer.[44]

The classical implication[45,46] of ΔG_{is}^{*} results like the above is that the atomic coordinates of the structural components (bond lengths and/or angles) of Au_{25}^{1-} and Au_{25}^{0} MPCs in solution differ in some manner(s). The structures are thermally activated for electron transfer by rearrangement of atomic coordinates so as to resemble one another at the cusp of the activation barrier. In electron exchanges between simple aromatic compounds, the typical inner-sphere contribution to the total reorganization energy is ~5%, unless large shape or configurational changes accompany electron transfer.[45] The 69% inner-sphere barrier component in this study indicates a significant change in nanoparticle bond lengths/angles, leading to a slower electron-exchange reaction. It is worth noting that any lowered electronic coupling between reacting nanoparticles occasioned by the surrounding ligand shell would slow the electron exchange by changes in the pre-exponential not in the energy barrier term. Also, the relationship between the locus of nanoparticle electroactivity and structure remains unknown and emphasized by the more complex "semi-ring protecting monolayer" shown in Figure 3.1.

3.3.3 Raman Au-S Stretch Spectra of Au_{25}^{1-} and Au_{25}^{0}.

The bond most likely to be affected by a change in nanoparticle charge state is the Au-S bond, so Raman spectra of solid state samples of oxidized and reduced nanoparticles were measured, with results as shown in Figure 3.6. Identifying the Au-S stretch vibrational energy region was guided by previous HREELS measurements.[47] The Raman bands are broad, and have some structure, but from the central maxima there is an

Figure 3.6. Solid state Raman spectra for $[Au_{25}(S(CH_2)_2Ph)_{18}]^0$ and $[Au_{25}(S(CH_2)_2Ph)_{18}]^{1-}$. The Raman bands are broad, and have some structure, but from the central maxima there is a ~24 cm^{-1} change in the Au-S bond stretch energy, with the oxidized form exhibiting a lower stretch energy.

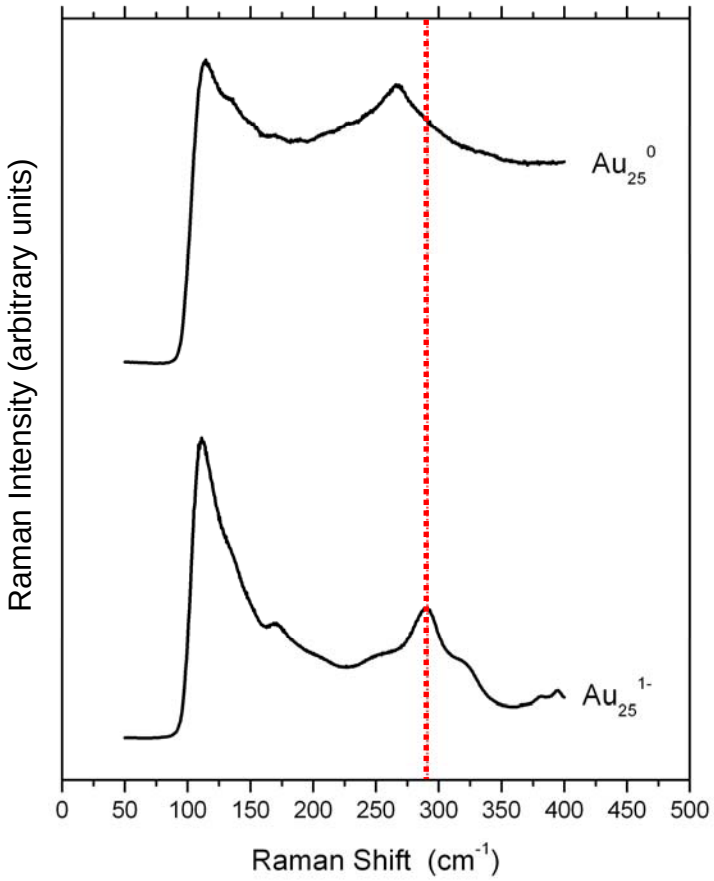
Raman Intensity (arbitrary units)
Au25 0
Au25 1-
0 50 100 150 200 250 300 350 400 450 500
Raman Shift (cm-1)

evident ~24 cm^{-1} change in the bond stretch energy, with the oxidized form exhibiting a lower stretch energy. Importantly, in samples of reduced and oxidized Au_{140} nanoparticles, which in solid state mixed-valent measurements display an activation energy close to outer sphere reorganizational energy barrier expectations, the Raman Au-S stretch energies do *not* perceptibly differ. Further details of these Raman comparisons will be published elsewhere.[40]

The Figure 3.1 structure contains 36 Au-S bonds (and associated bond angles of bridging Au-SR-Au segments), so translating the ~24 cm^{-1} Raman shift between Au-S stretch energies in Au_{25}^{1-} and Au_{25}^{0} faces substantial complexity. It may be nonetheless informative to ask, if the energy change were *only* in the Au-S bonds, and uniformly averaged over all of them, the approximate magnitude of the bond length change. This can be done using the classical expression:[48]

$$\lambda_{in} = 4(\Delta G^{*}_{in}) = \frac{1}{2}(f_i)(\Delta a)^2(2x)C \qquad (5)$$

where f_i is the reduced *average* force constant[42] (6.2×10^{-9} J/Å) of the Au-S bonds, and Δa is the average difference in bond lengths between the two oxidation states, averaged over (x) 36 Au-S bonds. This gives a bond length change of 0.07 Å which is a large value even when averaged over 36 Au-S bonds, making it likely that Au-S-Au bond angle changes occur in addition to average length changes, i.e., changes in the semi-ring puckering, formation of a structure less symmetrical than that in Figure 3.1, and/or even an induced distortion of the Au_{13} icosahedral core. The bond length change of 0.07 Å has to be taken as a highly simplified approximation, therefore. A full resolution of the nature of the inner-sphere reorganization for the Au_{25} MPC will await crystallographic

information for the Au_{25}^{0} nanoparticle, by analogy to classical studies of metal complexes.[49]

The present confirmation of an inner-sphere reorganization energy barrier that slows the rates of electron transfer in the $Au_{25}^{0/1-}$ redox couple—initially suggested by Choi *et al.*[35] and supported by Antonello *et al.*[10] provides a solid case for the first known example of a structural change affecting the electron transfer dynamics of a Au (or any other) nanoparticle. The Raman results in particular offer "smoking gun" evidence for a structural alteration accompanying the electron transfer reaction.

3.4 Conclusions

The NMR peak shapes associated with the ligands of small Au nanoparticles can have several sources, including a variation of chemical shift associated with ligand binding sites, with paramagnetism of the nanoparticle core, and as shown here, with exchange processes like electron transfer between different oxidation states. The line-broadening method of nuclear magnetic resonance is a durable tool in analysis of the latter effect, in describing the fast (although slowed!) electron exchange kinetics of the small monolayer protected cluster, $[Au_{25}(S(CH_2)_2Ph)_{18}]^{1-/0}$ (3.0×10^{7} $M^{-1}s^{-1}$ at 22 °C).

3.5 Acknowledgements

I would like to thank Jai-Pil Choi, Wei Wang, Prof. C. S. Johnson of UNC Chemistry, Stephen Feldberg and Marshall D. Newton of Brookhaven National Laboratory, and Marc ter Horst and David Harris of the UNC NMR facility for helpful discussions. This project was supported by the National Science Foundation and Office of Naval Research.

3.6 References

(1) Wang, G.; Huang, T.; Murray, R. W.; Menard, L.; Nuzzo, R. G. *J. Am. Chem. Soc.* **2005**, *127*, 812-813.

(2) Jimenez, V. L.; Georganopoulou, D. G.; White, R. J.; Harper, A. S.; Mills, A. J.; Lee, D.; Murray, R. W. *Langmuir* **2004**, *20*, 6864-6870.

(3) Balasubramanian, R.; Guo, R.; Mills, A. J.; Murray, R. W. *J. Am. Chem. Soc.* **2005**, *127*, 8126-8132.

(4) Hicks, J. F.; Miles, D. T.; Murray, R. W. *J. Am. Chem. Soc.* **2002**, *124*, 13322-13328.

(5) Wolfe, R. L.; Murray, R. W. *Anal. Chem.* **2006**, *78*, 1167-1173.

(6) McConnell, W. P.; Novak, J. P.; Brousseau, L. C., III; Fuierer, R. R.; Tenent, R. C.; Feldheim, D. L. *J. Phys. Chem. B* **2000**, *104*, 8925-8930.

(7) Andres, R. P.; Bein, T.; Dorogi, M.; Feng, S.; Henderson, J. I.; Kubiak, C. P.; Mahoney, W.; Osifchin, R. G.; Reifenberger, R. *Science* **1996**, *272*, 1323-1325.

(8) Han, G.; Martin, C. T.; Rotello, V. M. *Chem. Biol. Drug. Des.* **2006**, *67*, 78-82.

(9) Rothrock, A. R.; Donkers, R. L.; Schoenfisch, M. H. *J. Am. Chem. Soc.* **2005**, *127*, 9362-9363.

(10) Antonello, S.; Holm, A. H.; Instuli, E.; Maran, F. *J. Am. Chem. Soc.* **2007**, *129*, 9836-9837.

(11) Pasquato, L.; Pengo, P.; Scrimin, P. *J. Mat. Chem.* **2004**, *14*, 3481-3487.

(12) Heaven, M. W.; Dass, A.; White, P. S.; Holt, K. M.; Murray, R. W. *J. Am. Chem. Soc.* **2008**, *130*, 3754-3755

(13) Wang, G.; Guo, R.; Kalyuzhny, G.; Choi, J.-P.; Murray, R. W. *J. Phys. Chem. B* **2006**, *110*, 20282-20289.

(14) Tracy, J. B.; Crowe, M. C.; Parker, J. F.; Hampe, O.; Fields-Zinna, C. A.; Dass, A.; Murray, R. W. *J. Am. Chem. Soc.* **2007**, *129*, 16209-16215.

(15) Negishi, Y.; Chaki, N. K.; Shichibu, Y.; Whetten, R. L.; Tsukuda, T. *J. Am. Chem. Soc.* **2007**, *129*, 11322-11323.

(16) Tracy, J. B.; Kalyuzhny, G.; Crowe, M. C.; Balasubramanian, R.; Choi, J.-P.; Murray, R. W. *J. Am. Chem. Soc.* **2007**, *129*, 6706-6707.

(17) Chen, S.; Ingram, R. S.; Hostetler, M. J.; Pietron, J. J.; Murray, R. W.; Schaaff, T. G.; Khoury, J. T.; Alvarez, M. M.; Whetten, R. L. *Science* **1998**, *280*, 2098-2101.

(18) Guo, R.; Murray, R. W. *J. Am. Chem. Soc.* **2005**, *127*, 12140-12143.

(19) Lee, D.; Donkers, R. L.; Wang, G.; Harper, A. S.; Murray, R. W. *J. Am. Chem. Soc.* **2004**, *126*, 6193-6199.

(20) McConnell, H. M. *J. Chem. Phys.* **1958**, *28*, 430-431.

(21) McLachlan, C. *Introduction to Magnetic Resonance with Applications to Chemistry and Chemical Physics*; First ed.; Harper & Row: New York, 1967.

(22) Yang, E. S.; Chan, M.-S.; Wahl, A. C. *J. Phys. Chem.* **1975**, *79*, 2049-2052.

(23) Coddington, J.; Wherland, S. *Inorg. Chem.* **1997**, *36*, 6235-6237.

(24) Sharp, R. R. *Nuc. Magn. Res.* **1999**, *28*, 485-521.

(25) Bain, A. D. *Prog. Nuc. Magn. Res. Spec.* **2003**, *43*, 63-103.

(26) Song, Y.; Harper, A. S.; Murray, R. W. *Langmuir* **2005**, *21*, 5492-5500.

(27) Guo, R.; Song, Y.; Wang, G.; Murray, R. W. *J. Am. Chem. Soc.* **2005**, *127*, 2752-2757.

(28) Kohlmann, O.; Steinmetz, W. E.; Mao, X.-A.; Wuelfing, W. P.; Templeton, A. C.; Murray, R. W.; Johnson, C. S., Jr. *J. Phys. Chem. B* **2001**, *105*, 8801-8809.

(29) Schaaff, T. G.; Shafigullin, M. N.; Khoury, J. T.; Vezmar, I.; Whetten, R. L. *J. Phys. Chem. B* **2001**, *105*, 8785-8796.

(30) Badia, A.; Gao, W.; Singh, S.; Demers, L.; Cuccia, L.; Reven, L. *Langmuir* **1996**, *12*, 1262-1269.

(31) Donkers, R. L.; Song, Y.; Murray, R. W. *Langmuir* **2004**, *20*, 4703-4707.

(32) Yang, E. S.; Chan, M.-S.; Wahl, A. C. *J. Phys. Chem.* **1980**, *84*, 3094-3099.

(33) Marcus, R. A. *J. Chem. Phys.* **1965**, *43*, 1598-605.

(34) Marcus, R. A. *J. Chem. Phys.* **1965**, *43*, 679-701.

(35) Choi, J.-P.; Murray, R. W. *J. Am. Chem. Soc.* **2006**, *128*, 10496-10502.

(36) Brust, M.; Walker, M.; Bethell, D.; Schiffrin, D. J.; Whyman, R. *J. Chem. Soc., Chem. Commun.* **1994**, 801-802.

(37) Hostetler, M. J.; Wingate, J. E.; Zhong, C.-J.; Harris, J. E.; Vachet, R. W.; Clark, M. R.; Londono, J. D.; Green, S. J.; Stokes, J. J.; Wignall, G. D.; Glish, G. L.; Porter, M. D.; Evans, N. D.; Murray, R. W. *Langmuir* **1998**, *14*, 17-30.

(38) a) Donkers, R. L.; Lee, D.; Murray, R. W. *Langmuir* **2004**, *20*, 1945-1952. b) This paper mis-labeled the synthesized MPC as a Au_{38} nanoparticle; subsequent[16] mass spectrometry revealed that synthesis to produce a Au_{25} nanoparticle.

(39) Wuelfing, W. P.; Green, S. J.; Pietron, J. J.; Cliffel, D. E.; Murray, R. W. *J. Am. Chem. Soc.* **2000**, *122*, 11465-11472.

(40) Choi, J.-P.; Murray, R.W. unpublished results, UNC-CH, 2007.

(41) This collision diameter assumes no ligand interdigitation in the activated complex. Interdigitation would slightly elevate the estimated outer sphere reorganizational energy.

(42) Wuelfing, W. P.; Murray, R. W. *J. Phys. Chem. B* **2002**, *106*, 3139-3145.

(43) Porter, M. D.; Bright, T. B.; Allara, D. L.; Chidsey, C. E. D. *J. Am. Chem. Soc.* **1987,** *109*, 3559-3568.

(44) The chosen dielectric constants assume that the ε_{op} and ε_s environment of the MPC core is determined by the $-S(CH_2)_2Ph$ ligands, i.e., assume that effects of CH_2Cl_2 solvent intrusion are negligible. ε_{op} of the two phases differs little, but ε_s values differ more. Assuming an ε_s core environment of solely CH_2Cl_2 would increase ΔG_{os} (but still fall far short of the large observed E_A) and decrease the ΔG_{is} to around 30%,. The truth for Au_{25} is probably somewhere in between. That solvent intrusion into MPC monolayers on Au_{140} MPCs is not a dominant factor in electron transfer (outer sphere) dynamics was suggested by results[42] for Au_{140} MPCs where neglecting intrusion effects gave ΔG_{os} estimates most consistent with experimental results.

(45) Hale, J. M. *Reactions of Molecules at Electrodes, Chapter 4*; Wiley-Interscience: New York. NY, 1971.

(46) Kojima, H.; Bard, A. J. *J. Am. Chem. Soc.* **1975**, *97*, 6317-6324.

(47) Kato, H. S.; Noh, J.; Hara, M.; Kawai, M. *J. Phys. Chem. B* **2002**, *106*, 9655-9658.

(48) Brunschwig, B. S.; Creutz, C.; Macartney, D. H.; Sham, T. K.; Sutin, N. *Farad. Disc. Chem. Soc.* **1982**, 113-127.

(49) Zhang, D.; Liu, C. *New J. Chem.* **2002**, *26*, 361-366.

(50) Higbie, J. *Am. J. Phys.* **1991**, *59*, 184-185.

Appendix 3

Electron Self-Exchange Dynamics of the Nanoparticle Couple $[Au_{25}(S(CH_2)_2Ph)_{18}]^{0/1-}$ By Nuclear Magnetic Resonance Line-Broadening

The materials in this Appendix are the supplementary data published as Supporting Information in the Journal of Physical Chemistry C article which comprised Chapter 3.

Figure A3.1: Series of ^{1}H NMR spectra of $Au_{25}(S(CH_2)_2Ph)_{18}$ with increasing concentration of tetraoctylammonium bromide, ranging from 1 $(Oct)_4N^+$/MPC to 3 $(Oct)_4N^+$/MPC. The chemical shift of the protons closest to the nitrogen of $(Oct)_4N^+$ differs depending on the anion (Au_{25}^{1-} vs. Br^-). The addition of excess $(Oct)_4N^+Br^-$ is required to fully resolve the peaks to prepare them for the 2-Dimensional COSY experiment (Figure A3.2) and integration analysis (Figure A3.3).

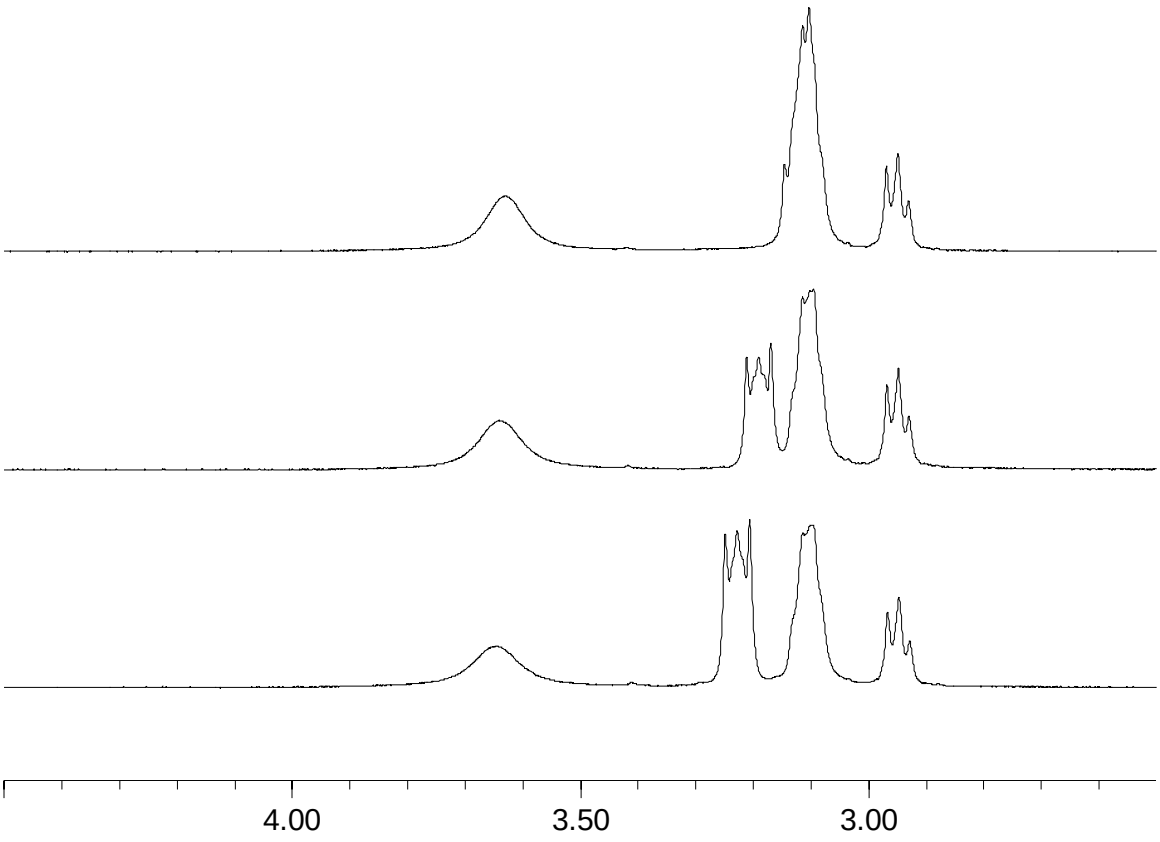
4.00
3.50
3.00

Figure A3.2: 2-Dimensional Correlation Spectroscopy (COSY) of $Au_{25}(S(CH_2)_2Ph)_{18}$ in dicholoromethane-d_2. Orange cross peaks represent the coupling of the methylene protons while the blue cross peaks represent the coupling of the tetraoctylammonium protons. Two sets of methylene protons are coupled to the α-CH_2 protons, indicating two types of β-CH_2 protons.

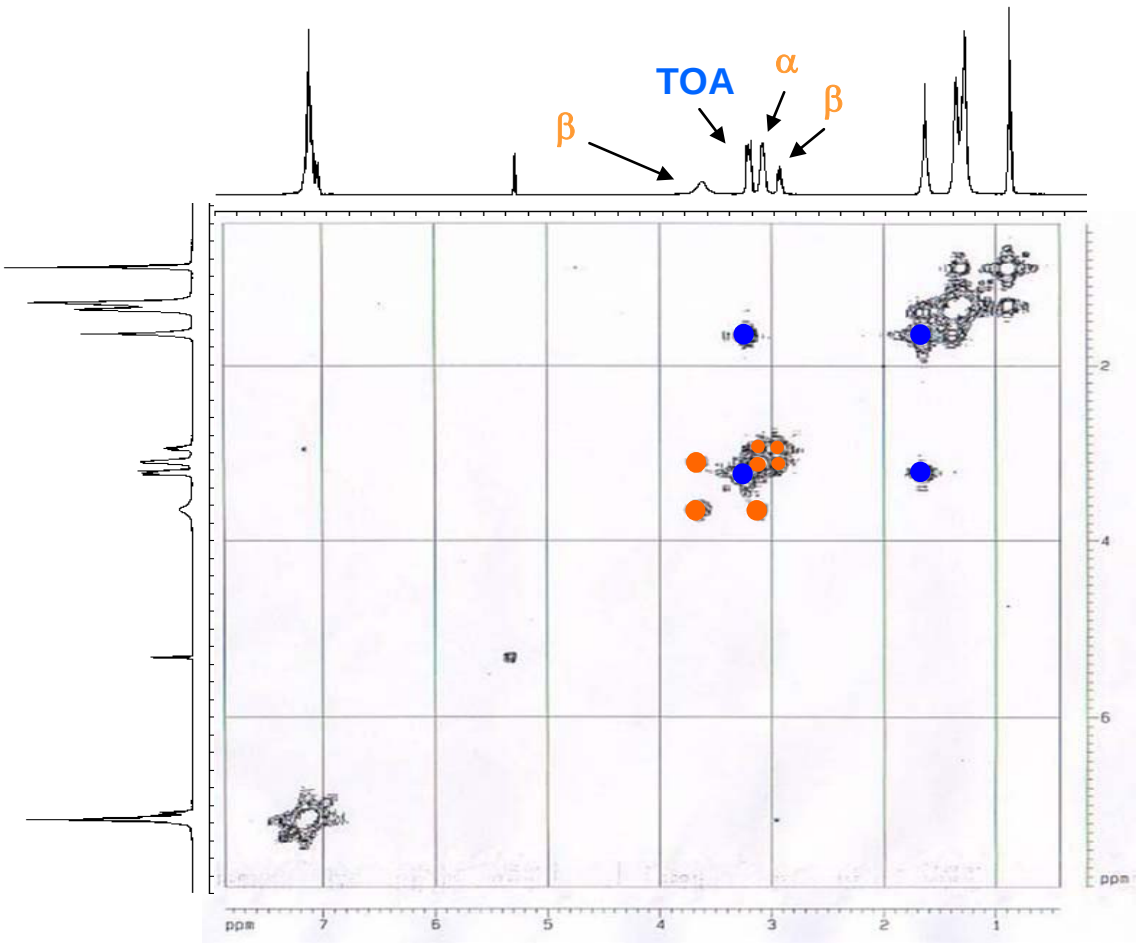
TOA
α
β
β
ppm
7
6
5
4
3
2
1
2
4
6
ppm

Figure A3.3: Integration analysis of $Au_{25}(S(CH_2)_2Ph)_{18}^{1-}$. Referencing the phenyl peaks as 5H: the α-CH_2 and the β-CH_2 peaks should integrate to 2H each. The α-CH_2 at 3.10 ppm gives the predicted 2H and the sum of the two β-CH_2 peaks at 2.95 and 3.65 ppm gives 2H.

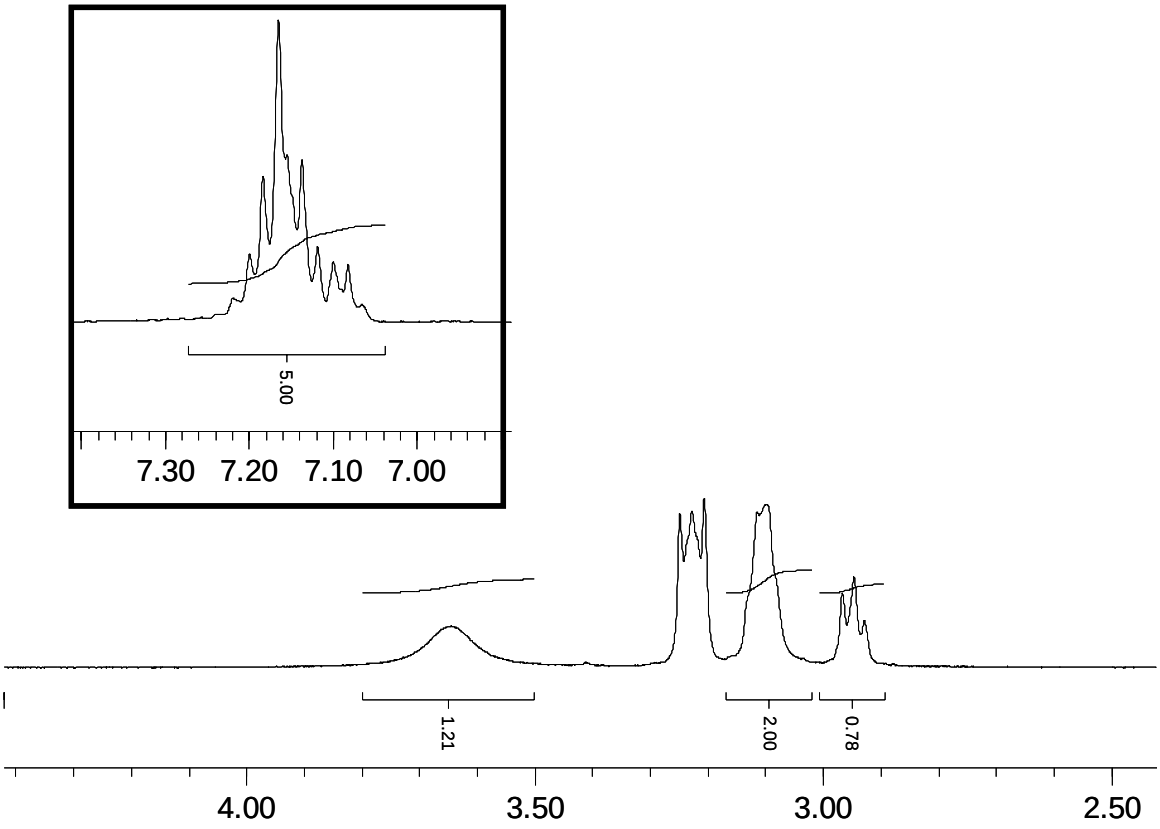
5.00
7.30
7.20
7.10
7.00
1.21
2.00
0.78
4.00
3.50
3.00
2.50

Figure A3.4: ^{1}H NMR of $Au_{25}(S(CH_2)_2Ph)_{18}^{1-}$ in the reduced, as prepared, state containing **A)** tetraoctylammonium and after ion metathesis with **B)** tetrabutylammonium and **C)** tetraethylammonium. The amount of alkylammonium cations per MPC is 1.1, 1.0, and 1.1 respectively even after very judicious purification, confirming the charge state of the as prepared MPC as 1-.

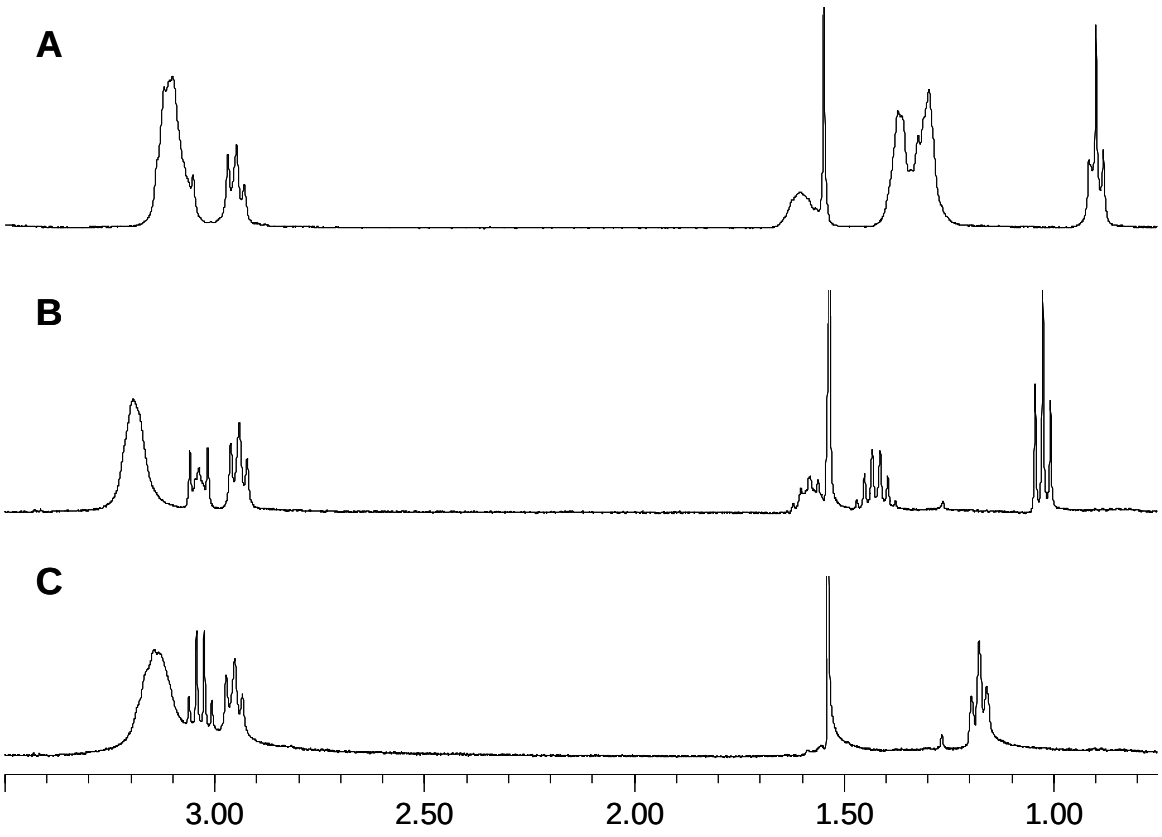
A
B
C
3.00
2.50
2.00
1.50
1.00

Figure A3.5: An alternative method for extrapolating the rate constant for self exchange: a plot of the peak width of the α-CH_2 resonances at various f_{ox} (Au_{25}^0) present. The linear fit follows Equation (2) and allows for the determination of the rate constant to be $3.5(\pm 0.3)\times 10^7$ $M^{-1}s^{-1}$ which is roughly in agreement with the values obtained in the Results. The presence of the intercept terms in Equation (2) introduce sources of error that can otherwise be eliminated when using the more preferable method from the text.

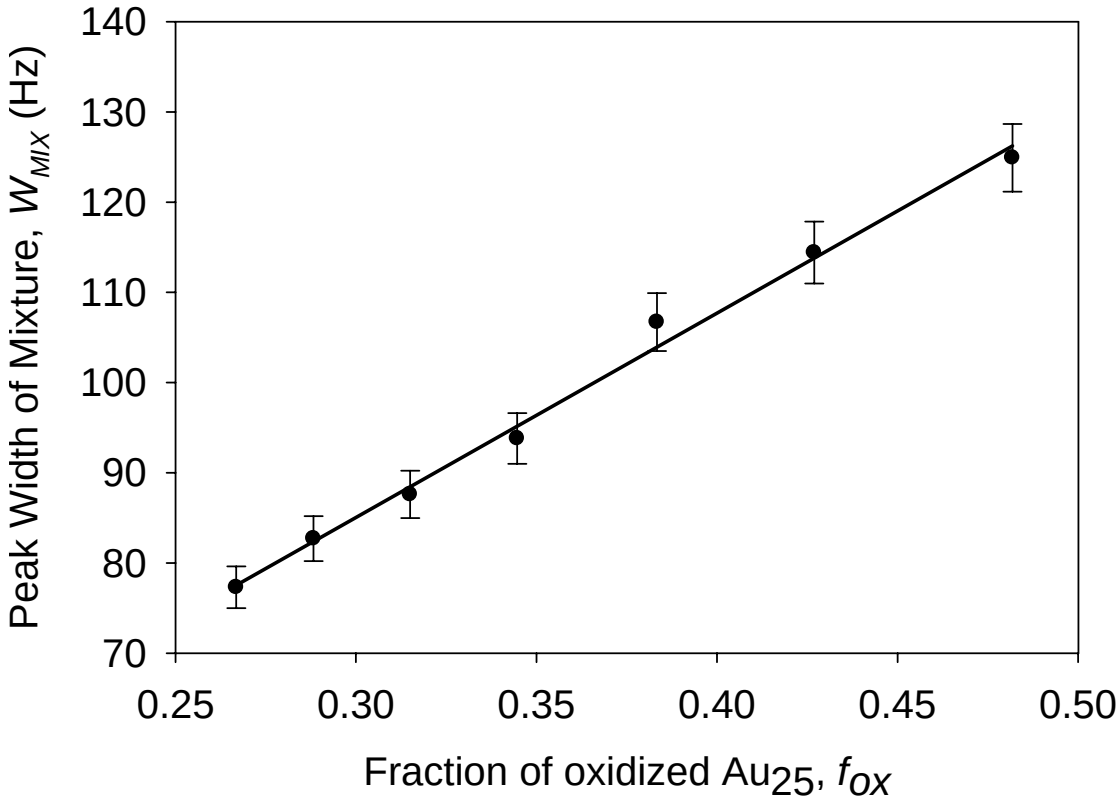
140
130
120
110
100
90
80
70
Peak Width of Mixture, W_{MIX} (Hz)
0.25
0.30
0.35
0.40
0.45
0.50
Fraction of oxidized Au_{25}, f_{ox}

Chapter 4

Experimental and Density Functional Theory Analysis of Serial Introductions of Electron-Withdrawing Ligands into the Ligand Shell of a Thiolate-Protected Au_{25} Nanoparticle

4.1 Introduction

Gold nanoparticles with thiolate protecting ligands have received considerable research attention over the last decade due to their interesting size-dependent properties. The electronic structure of very small gold nanoparticles (< 1.5 nm) reveals a transition from bulk metallic properties to molecule-like HOMO-LUMO energy gaps. The anion $Au_{25}(S(CH_2)_2Ph)_{18}^-$ is an example of a small nanoparticle with a distinct HOMO-LUMO energy gap (ca. 1.33 eV) as measured by voltammetry and spectral band edges.[1] The Au_{25} nanoparticle can be synthesized in respectable yield with high monodispersity,[2-4] is stable in air and at room temperature, and the ligands can be readily replaced by ligand exchange reactions.[3] A recent single crystal and theoretical analysis of the Au_{25} structure[5-7] has drawn attention to understanding properties of this nanoparticle that were observed prior to its detailed structural analysis. This paper examines how serial exchanges of the original $-S(CH_2)_2Ph$ ligands of $Au_{25}(SR)_{18}^-$ with the thiolates of more electron-withdrawing ligands ($-SPhNO_2$ and $-SPhBr$) changes the electrochemically-

measured HOMO energy levels of the nanoparticle. Density Functional Theory (DFT) is used to elucidate how the charge distribution in the nanoparticle changes over the course of the serial ligand exchanges.

We reported previously[8] that the ligand exchange reaction kinetics of the $Au_{25}(SR)_{18}^-$ nanoparticle follow an associative mechanism—first order in nanoparticle and in in-coming ligand—with rate constants dependent on the X substituent of incoming *p*-thiophenolates (–SPhX). In the completely exchanged nanoparticle ($Au_{25}(SPhX)_{18}$), the more electron-withdrawing substituents induced substantial changes of the HOMO and the LUMO energies, making the (HOMO) oxidation process more difficult. This was exhibited in the voltammetry of the $Au_{25}(SPhX)_{18}$ nanoparticles as a shift of the -1/0 and 0/+1 formal redox potentials to more positive values. The energy of the LUMO shifted to the same degree, resulting in no significant change in the electrochemical bandgap. The HOMO formal potential shifts correlated with linear free-energy Hammett σ constants.[8] The optical energy gap also remained unchanged, although modest changes in the step-like absorbance spectrum are seen.[8]

The previous[8] observations of HOMO formal potential shifts were for fully exchanged $Au_{25}(SPhX)_{18}$ nanoparticles. It is desirable to understand the evolution of the apparent energy level changes, and the bandgap, as a function of number of ligands exchanged. This was experimentally performed by observing cyclic voltammetric formal potentials and ^{1}H NMR resonances on a common timescale so as to correlate the average numbers of exchanged ligands with formal potential shifts, in real time, for incoming –SPhX thiolate ligands where X = Br and NO_2. Density Functional Theory (DFT) was used concordantly by our collaborators in Finland (Katarzyna A. Kacprzak, Olga Lopez-

Acevedo, and Hannu Häkkinen of the University of Jyväskylä) to model the course of an analogous reaction where the original ligand was $–SCH_3$ and the incoming thiolate was $–SCH_2Cl$, and to predict the disposition of the charge density among the gold core, the semirings, and the electron-withdrawing ligands.

4.2 Experimental

4.2.1 Chemicals. 4-Nitrothiophenol (Aldrich, 80%), 4-bromothiophenol (Aldrich, 95%), phenylethanethiol ($HS(CH_2)_2Ph$, Aldrich, 98%), *tetra-n*-octylammonium bromide ($Oct_4N^+Br^-$, Fluka, 98%), sodium borohydride (Aldrich, 99%), toluene (Fisher), methanol (Fisher), ethanol (Fisher), acetonitrile (Fisher), and d_2-methylene chloride (Cambridge Isotope Laboratories, 99.9%) were all used as received. Hydrogen tetrachloroaurate trihydrate was prepared as previously published[9] from 99.999% pure gold and stored at -20°C. Deionized water was obtained from a Millipore Nanopure water purification system.

4.2.2 Synthesis of $[Oct_4N^+][Au_{25}(S(CH_2)_2Ph)_{18}^-]$. This nanoparticle was synthesized using a modified version of the Brust synthesis.[2,3] Hydrogen tetrachloroaurate (3.1 g, 11.1 mol) was dissolved in toluene using the phase-transfer reagent *tetra-n*-octylammonium bromide ($Oct_4N^+Br^-$). A 3.2 molar excess of phenylethanethiol was added to the solution at room temperature, forming the intermediate colorless gold-thiolate polymer, followed by immediate reduction by ice-cold sodium borohydride in excess, stirring for 20 hours. The black product solution contains a mixture of nanoparticle core sizes and oxidation states. The cluster in the form $[Oct_4N^+][Au_{25}(S(CH_2)_2Ph)_{18}^-]$ is the only species with appreciable solubility in

acetonitrile and thus was extracted from the dried reaction mixture and copiously washed with methanol to remove excess free thiol and Oct_4N^+ salts to yield a mono-disperse nanoparticle.

4.2.3 Monitoring Ligand Exchange by ^{1}H NMR Spectroscopy. All ^{1}H NMR measurements were made using a Bruker 400wb spectrometer in CD_2Cl_2 solutions at room temperature with a D1 of 1.00 sec. ^{1}H NMR spectra were obtained for solution mixtures of $Au_{25}(S(CH_2)_2Ph)_{18}^-$ and HSPhX (X = NO_2 or Br). For the $–NO_2$ ligand, the mixture contained $Au_{25}(S(CH_2)_2Ph)_{18}^-$ at 2.4 mM and $HSPhNO_2$ at a 2× molar excess (relative to the Au_{25} ligands). For the –Br ligand, the mixture contained $Au_{25}(S(CH_2)_2Ph)_{18}^-$ at 1.3 mM and HSPhBr at a 2× molar excess. These concentrations are less than those which would aim at complete exchange.[8] The intrinsic constituent Oct_4N^+ is a constant concentration in each sample and was used as an internal standard for both experiments. For each ligand exchange reaction, the mixture was placed into the pre-shimmed spectrometer and programmed for automatic repetitive scans. The acquisition time equaled roughly 17 s, measuring in the range of 0-10 ppm. A reaction time was programmed in order to report spectra roughly once every minute. The quartet (HS-***CH$_2$***-CH_2Ph) that is liberated from the Au_{25} nanoparticle during ligand exchange is observed at ~2.8 ppm and is used to quantify the average extent of ligand exchange.

4.2.4 Monitoring Ligand Exchange by Cyclic Voltammetry. All electrochemical measurements were made on a Bioanalytical Systems, Inc. (BAS) analyzer using a Pt disk electrode and an electrolyte solution of 0.1 M Bu_4NClO_4/CH_2Cl_2. Each sweep cyclically scanned the potential range of -400 mV to +1200 mV at 100 mV/sec with a sampling interval of 1 mV. The concentrations of nanoparticle and

exchanging HSPhX were the same as in the NMR experimental section. After the reagents were mixed, voltammograms were obtained at various times throughout the exchange (See Figures A4.1 to A4.4). For the HSPhBr exchange, the formal potential ($E^{o'}$, average of E_{PEAK} of oxidation and reduction peaks) of the $Au_{25}^{0/1-}$ redox wave was monitored. For the $HSPhNO_2$ exchange, because of poor definition of the $Au_{25}^{0/1-}$ formal potential, the $Au_{25}^{1+/0}$ formal potential was monitored. The shifts of these formal potentials were combined with the (average) numbers of ligands exchanged as determined from the NMR results, at comparable reaction times.

4.2.5 Computational Methods. We employed Grid-based Projector-Augmented Wave (GPAW) code to perform DFT calculations.[10] All clusters were set into a box with dimensions of 22.3×23.8×24.5 $Å^3$, so there is up to 4 Å vacuum region around the cluster. Each of the clusters was optimized with no symmetry constraints until residual forces between atoms were smaller than 0.05 eV/Å. The Perdew-Burke-Ernzerhof (PBE) form of the generalized-gradient approximation (GGA) was chosen in order to evaluate the exchange-correlation interaction.[11] Au was treated in a scalar-relativistic level with $5d^{10}6s^1$ electrons in the valence. For charge analysis we used the Bader method.[12] We have applied this computational method successfully for several thiolate-protected Au clusters in the recent past.[6,13-15] Molecular graphics was visualized using the UCSF Chimera package.[16]

4.3 Results and Discussion

4.3.1 Monitoring Ligand Exchange by ^{1}H NMR. The experimental part of this investigation aims at correlating the electrochemical formal potentials of the

$Au_{25}(S(CH_2)_2Ph)_{18}^-$ nanoparticle, as its ligands are successively replaced by more electron-withdrawing –SPhBr or $–SPhNO_2$ ligands, with the average numbers of replaced ligands as measured using ^1H NMR. The cyclic voltammetric and NMR data sets were collected in separate experiments but at identical concentrations of nanoparticle and (excess) in-coming –SPhX ligand.

Figure 4.1 illustrates typical NMR spectra at increasing times during the course of the ligand exchange reaction, where –SPhBr is the in-coming ligand. Using the –Br exchange as an example, as the reaction proceeds, -SPhBr replaces $–S(CH_2)_2Ph$ on the core and the latter is liberated. The quartet ($HS\boldsymbol{CH_2}CH_2Ph$) at ~2.8 ppm is used to quantify the course of the reaction and to solve for the number of exchanged ligands. It is important to recognize that the NMR procedure provides the *average* number of ligands exchanged. In the exchange solution, owing to the statistical nature of the exchange process, there will be a binomial distribution of nanoparticles, some with more and others with fewer ligands, than the average number of exchanged ligands. The binomial distribution has been observed[17] by MALDI-MS, and the number of ligands at its center (its average) is very close to the average number of ligands exchanged as observed by ^1H NMR.

The kinetics of the exchanges can be followed by observing the extent of the ligands exchanged over time (Figure A4.5), or more specifically, by plotting the ln{average fraction of unexchanged $–S(CH_2)_2Ph$ ligands on the nanoparticles}, versus time (Figure A4.6). The slope of this plot gives pseudo-first order rate constants, k_{obs}, of 2.70×10^{-4} s^{-1} and 0.41×10^{-4} s^{-1} for the $–NO_2$ and –Br exchanges, respectively. It has been established that the exchange reaction is first order in both nanoparticle and in-coming

Figure 4.1. Proton NMR spectra of $Au_{25}(S(CH_2)_2Ph)_{18}^-$ as its ligands are serially replaced, by exchange reaction, with –SPhBr. As the exchange reaction proceeds, free phenylethanethiol is liberated from the gold nanoparticle as *p*-bromothiophenol is consumed. On the nanoparticle, the α-CH_2 resonance lies at ~3.1 ppm; once liberated as a free thiol it appears as a quartet at ~2.8 ppm. The integration of this peak is monitored over time and compared to the terminal methyl resonances of the $(Oct)_4N^+$ counterion (at lower chemical shift, not shown) as an internal standard.

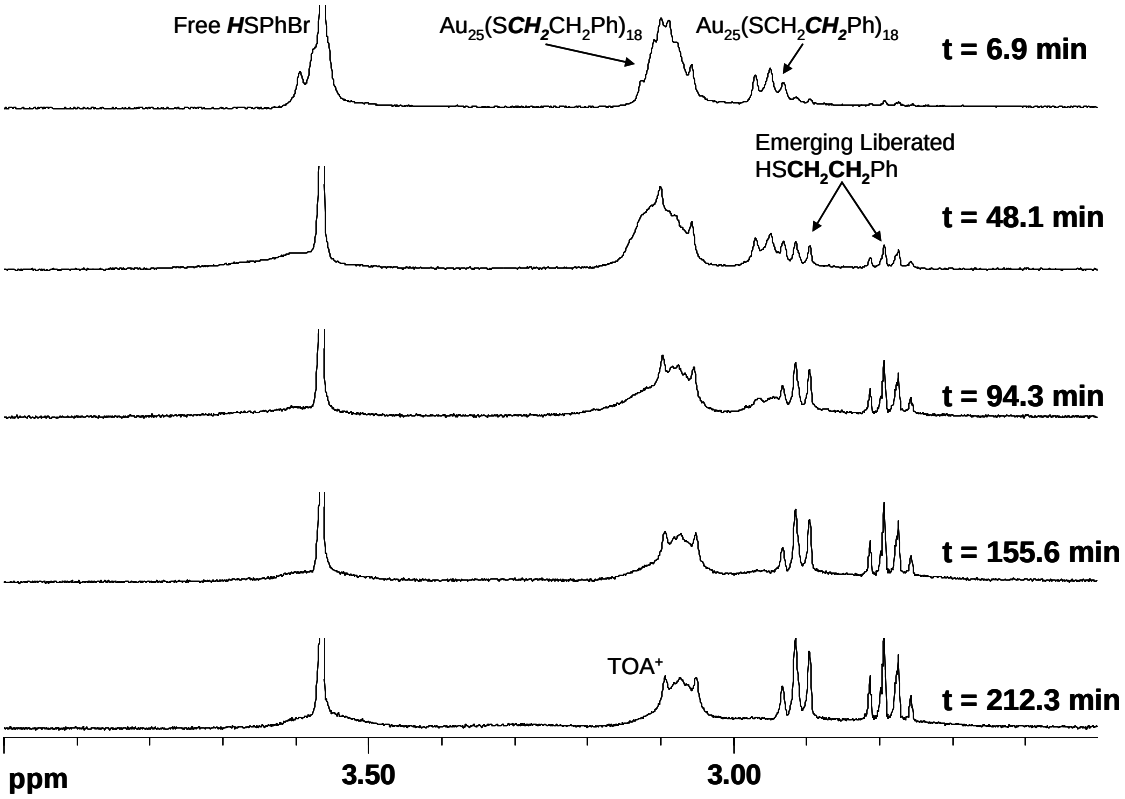
Free HSPhBr
Au25(SCH2CH2Ph)18
Au25(SCH2CH2Ph)18
t = 6.9 min
Emerging Liberated
HSCH2CH2Ph
t = 48.1 min
t = 94.3 min
t = 155.6 min
TOA+
t = 212.3 min
ppm
3.50
3.00

thiolate ligand, and it has been concluded that the exchange reaction is a second-order, associative reaction.[18] The pseudo-first order rate constants observed, expressed in terms of second order rate constants, are 3.1×10^{-3} and 0.89×10^{-3} $M^{-1}s^{-1}$ for the $-SPhNO_2$ and –SPhBr ligands, respectively, which is comparable (within a factor of three) to those previously published.[18]

4.3.2 Monitoring Ligand Exchange by Cyclic Voltammetry. The progress of the ligand exchange reactions was monitored *in situ* using cyclic voltammetry (in the raw reaction mixture containing in-coming and exited thiols as well as nanoparticles). As reported earlier,[8] replacement of the $-S(CH_2)_2Ph$ ligands with thiolate ligands capable of inductive electron-withdrawing effects, causes a shift of the nanoparticles' $Au_{25}^{0/1-}$ and $Au_{25}^{+1/0}$ redox potentials towards more positive values. This trend is consistent with classical descriptions[19] that electron-withdrawing ligands drive molecular formal redox potentials to values more favoring reduction and disfavoring oxidations.

The cyclic voltammograms and redox potentials observed during the two ligand exchange reaction are illustrated in Figures A4.1 to A4.3. For both HSPhBr and $HSPhNO_2$ reactions, in agreement with the previous study,[8] the redox potentials shift to more positive values over the course of the exchange reaction. In addition, in the $-SPhNO_2$ case, the difference in formal potentials ($\Delta E^{o'}$) of the 0/-1 and +1/0 peaks slowly decreases over time, presumably due to changes in charging energy. The decrease in peak separation made it difficult to track the 0/-1 peak over time, so the +1/0 formal potential was monitored instead.

Finally, the formal potential shift is greater for $-SPhNO_2$ ligands becoming incorporated into the nanoparticles' ligand shells than the –SPhBr ligands. It is apparent

that the formal potential of the HOMO in Au_{25} is shifted almost +300 mV in the case of –SPhBr exchange and +500 mV in the case of $–SPhNO_2$. A minor portion (ca. 16%) of the difference between the formal potential shifts in the $–SPhNO_2$ and –SPhBr exchanges can be attributed to measuring the +1/0 formal potential of the former and 0/1- formal potential of the latter.

4.3.3 Combining ^{1}H NMR and Electrochemistry Data. Figure 4.2 shows the result of combining the voltammetry and NMR data, to reveal the dependence of the $Au_{25}^{0/1-}$ formal potential E°' on the average number of –SPhBr ligands incorporated into the nanoparticle ligand shell. The exact data collection times in the NMR and voltammetry experiments do not match perfectly, so a best fit line through the ^{1}H NMR data (Figure A4.5) was used to select NMR data at times matching those of the voltammetry. Figure 4.2 shows that E°' changes nearly linearly with increasing number of ligands exchanged, after the first 1-2 ligands have been exchanged. Figure 4.3 shows the analogous data for the $–SPhNO_2$ ligands, using the $Au_{25}^{1+/0}$ formal potential (see captions of Figures A4.3 and A4.4). Again, linearity of E°' with ligands exchange is observed after the first *ca*. two ligands have been exchanged. Using regression lines of the linear segments of Figures 4.2 and 4.3 gives shifts of E°' of 25 mV/-SPhBr ligand and 42 mV/-$SPhNO_2$ ligand.

It is important to recognize that the formal potential and NMR data both represent an average of the nanoparticle ligand shell composition at any one time. The ligand exchange has a statistical aspect,[17] in that for example, when an average of one ligand has been exchanged, there will be a substantial population of nanoparticles with two and with none exchanged. The distribution will ultimately follow a binominal distribution. The

Figure 4.2. Combined ^{1}H NMR and cyclic voltammetric data sets, removing the time axis of the HSPhBr reaction. Fractional ligand exchanges are simply a consequence of the NMR data giving average numbers of ligands exchanged over the entire nanoparticle population. As seen, the formal potential E^{o}' of the 0/-1 wave forms a linear dependence on the average number of ligands exchanged, after an average of about two ligands become exchanged. The inset shows the initial (t = 0) cyclic voltammogram with the $Au_{25}^{0/1-}$ redox potential indicated in red. The regression line fitting the data after 2 ligands exchanged, gives a potential shift of 25 mV/ –SPhBr ligand.

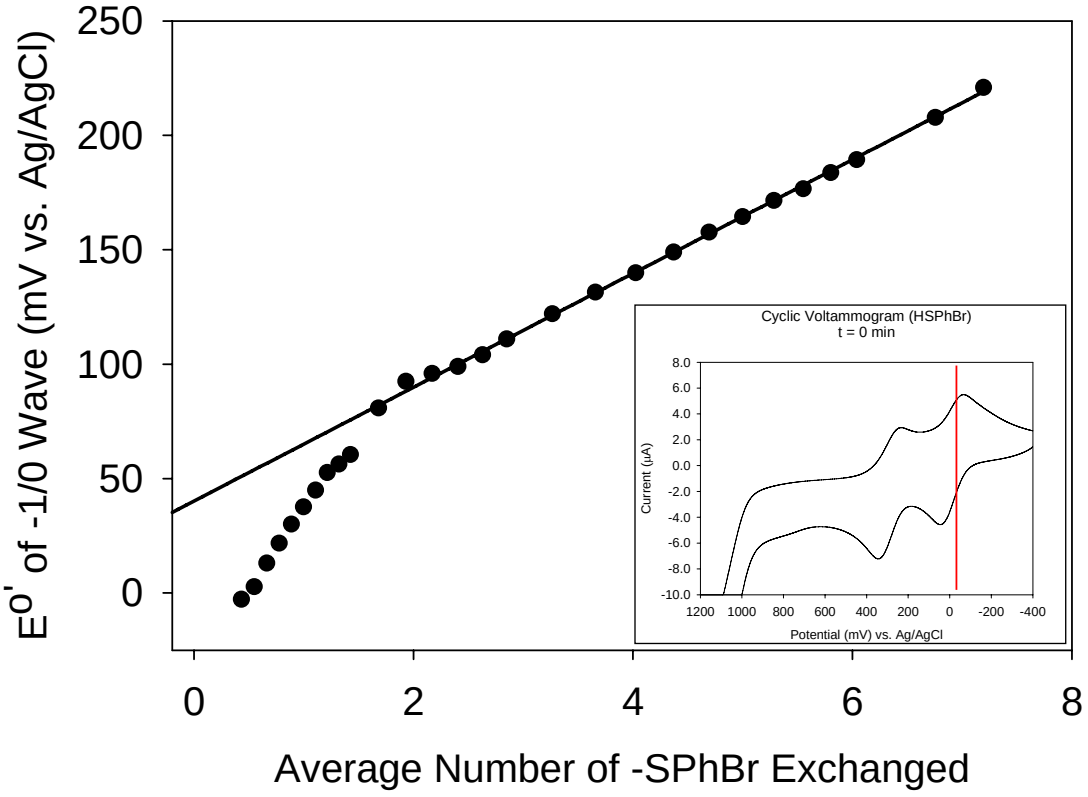
250
200
150
100
50
0
E°' of -1/0 Wave (mV vs. Ag/AgCl)
0
2
4
6
8
Average Number of -SPhBr Exchanged
Cyclic Voltammogram (HSPhBr)
t = 0 min
8.0
6.0
4.0
2.0
0.0
-2.0
-4.0
-6.0
-8.0
-10.0
Current (µA)
1200
1000
800
600
400
200
0
-200
-400
Potential (mV) vs. Ag/AgCl

Figure 4.3. Combined ^{1}H NMR and cyclic voltammetric data sets, removing the time axis of the $HSPhNO_2$ reaction. The $Au_{25}^{1+/0}$ redox potential (see red line) was monitored, being better defined at later reaction times than the $Au_{25}^{0/1-}$ potential. As in Figure 4.2, the redox potential shifts become nearly linear with ligands exchanged after an average of about two ligands are exchanged. The regression line through the linear segment gives an average potential shift of 42 mV/–$SPhNO_2$ ligand.

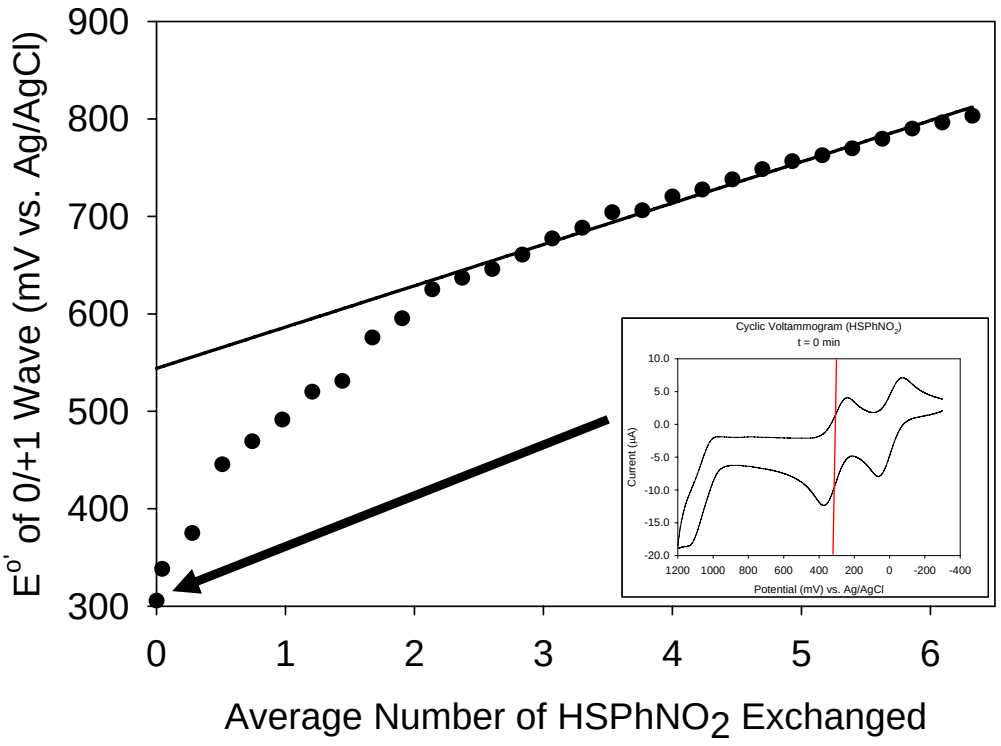
900
800
700
600
500
400
300
E°' of 0/+1 Wave (mV vs. Ag/AgCl)
0
1
2
3
4
5
6
Average Number of HSPhNO2 Exchanged
Cyclic Voltammogram (HSPhNO2)
t = 0 min
10.0
5.0
0.0
-5.0
-10.0
-15.0
-20.0
Current (µA)
1200
1000
800
600
400
200
0
-200
-400
Potential (mV) vs. Ag/AgCl

curvatures seen in Figures 4.2 and 4.3 at low numbers of ligand exchanged may possibly reflect averaging within an initially distorted binominal distribution.

Given the known structure of the nanoparticle, consisting of a Au_{13} core surrounded by six –SR-Au-SR-Au-SR– motifs ("semirings"), one can now study in detail what happens to the electronic structure of the nanoparticle with the presence of electron-withdrawing ligands, i.e., what parts of the nanoparticle are affected? To accomplish this, a ligand exchange of $–SCH_3$ with a simple electron-withdrawing ligand –S CH_2Cl was modeled using density functional theory. The results of the calculations shed light on how the electronegative –X group changes the polarization of the nanoparticle and how it affects the charge in the ligands, the semirings, and the Au_{13} core.

4.3.4 DFT Results and Discussion. To model the experiments, we considered the theoretical model of the methylthiolate-passivated Au_{25} cluster anion, which can be written[6] as $Au_{25}(SCH_3)_{18}^- = Au_{13}[Au_2(SCH_3)_3]_6^-$, and systematically replaced the methylthiolate ligands in the $Au_2(SCH_3)_3$ "semirings" with corresponding chlorinated ones, giving a composition $Au_{25}(SCH_3)_{18-x}(SCH_2Cl)_x^-$ with $0 \le x \le 18$. Several isomers of each cluster with a given x were checked, in order to find clusters with the lowest total energy. In some structural isomers, interaction between the chlorine in the chlorinated methylthiolate and hydrogen from the nearest-neighbor methylthiolate led to formation of hydrogen-bonded Cl···H, but in those cases the total energy of the cluster was not optimal. Additionally, we found that it is energetically optimal to exchange first the twelve $–SCH_3$ ligands that are closest to the Au_{13} core.

The character of the frontier orbitals remains similar for any x, i.e., the $Au_{25}(SCH_3)_{18-x}(SCH_2Cl)_x^-$ clusters are all so-called 8 electron "superatoms" where the

cluster valence configuration, derived from Au(6s) electrons, can be written as S^2P^6 with a three-fold degenerate HOMO of P-symmetry.[6] The five D-like empty orbitals are split in two groups by the ligand field, with two-fold LUMO and three-fold LUMO+1 (Figure 4.4). The HOMO-LUMO gap remains the same for all x, at 1.25 eV. Both HOMO and LUMO states are stabilized as a function of x in a rather linear fashion, the downshift of the orbital energy being about 0.06 eV per each added SCH_2Cl (Figure 4.5). We also checked the electron detachment energy of the chlorinated cluster anions in vacuum, and observed the same trend, i.e., a linear increase of the detachment energy as a function of the number of chlorinated ligands (Figure A4.7).

Charge analysis (Figure 4.6 and Table A4.1) suggests no significant changes in the Au_{13} core of any chlorinated cluster; rather, the charge is transferred inside the semirings of ligands, mostly from nearest-neighbor atoms. In the completely chlorinated cluster $Au_{25}(SCH_2Cl)_{18}^-$ the chlorine atoms attract a total negative charge of -4.42 |e| (-0.246 |e| per Cl), which originates from the 12 Au atoms in the semirings (total of +0.36 |e|), sulfurs (+0.94 |e|), and CH_2 moieties (+3.12 |e|). This strong charge-transfer inside the semirings induces a strong modification of the electric dipoles in the ligand shell (Figure A4.8) which are responsible for the stabilization of the metal electron states of the Au_{13} core. The net dipole vector originates from the Cl–C bonds and has the largest component in a radial direction Au(core center) → C (pointing towards the Au_{13} core). A single chlorinated semi-ring unit $Au_2(SCH_2Cl)_3$ has a net dipole change of 2.3 Debye in the vacuum compared to the non-chlorinated semi-ring (projected onto the S-Au-S-Au-S plane of the semi-ring). This result is in line with earlier estimates (1.2 Debye) of the net change of dipoles that result in the electrochemical stabilization of the metal states of this

Figure 4.4: The projected local density of electron states (Kohn-Sham orbitals) in the frontier orbital region for the all-methylthiolate-passivated Au_{25} (upper panel) and for the cluster where all ligands are chlorinated (bottom panel). The angular momentum character of the Kohn-Sham orbitals is analyzed by projection onto spherical harmonics, centered at the cluster center of mass, and with a radius that encompassed the Au_{13} core. The major components of the angular momentum (L) analysis are shown by the colored lines up to L=2 (D-symmetry). The grey line denotes all the higher components L>2. The metal-electron shell structure (8 electron closed-shell configuration) of the Au_{13} core is not disturbed by the chlorinated ligands.

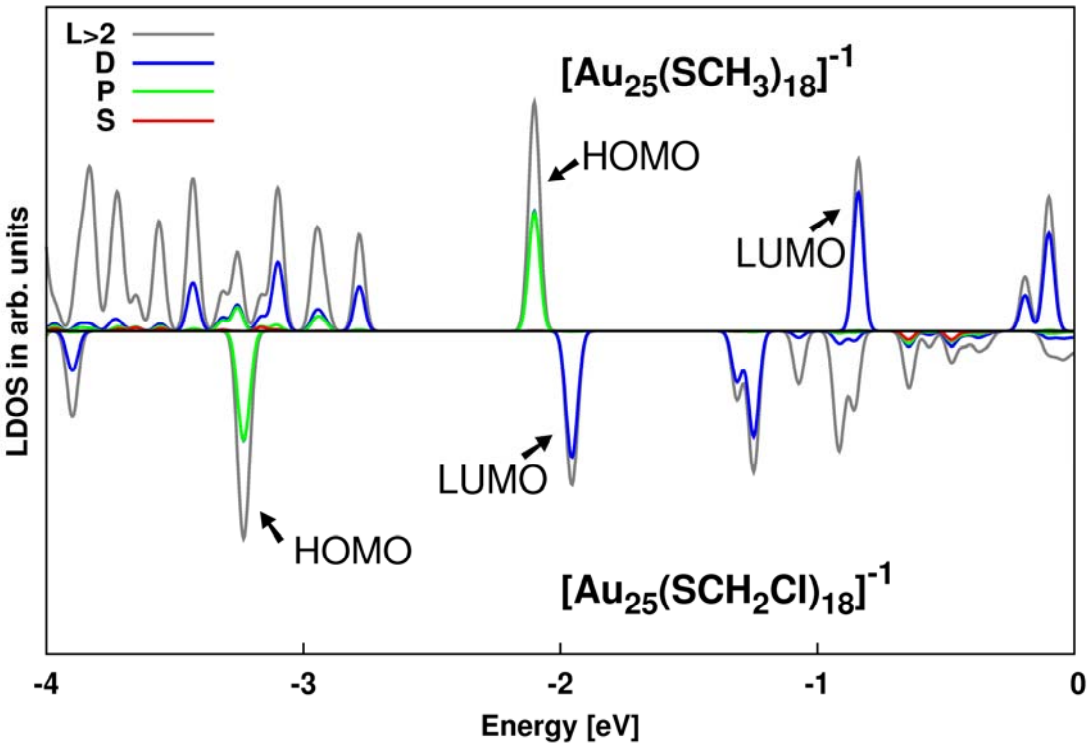
L>2
D
P
S
[Au25(SCH3)18]-1
HOMO
LUMO
LUMO
HOMO
[Au25(SCH2Cl)18]-1
LDOS in arb. units
-4
-3
-2
-1
0
Energy [eV]

Figure 4.5: Energies of the HOMO and LUMO states as a function of chlorinated ligands in the model cluster $Au_{25}[SCH_3]_{18-x}[SCH_2Cl]_x^-$. The solid symbols correspond to the HOMO and LUMO energies of the optimal-energy isomers at a given x and the open symbols are the HOMO and LUMO energy of higher energy isomers. The HOMO-LUMO gap remains constant, but both HOMO and LUMO energies shift downwards (are stabilized) with the increasing number of SCH_2Cl. Accordingly, the vertical detachment energy increases linearly by exactly the same quantity (Figure A4.7).

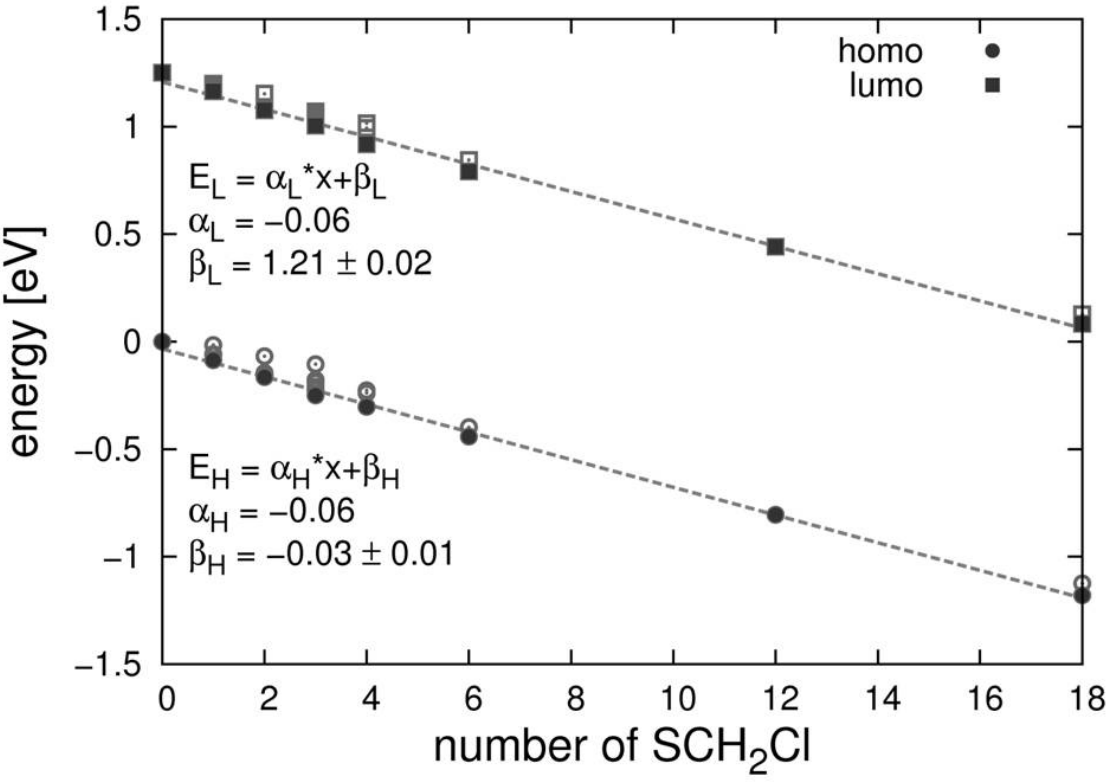
homo
lumo
$E_L = \alpha_L * x + \beta_L$
$\alpha_L = -0.06$
$\beta_L = 1.21 \pm 0.02$
$E_H = \alpha_H * x + \beta_H$
$\alpha_H = -0.06$
$\beta_H = -0.03 \pm 0.01$
energy [eV]
number of SCH_2Cl
1.5
1
0.5
0
−0.5
−1
−1.5
0
2
4
6
8
10
12
14
16
18

Figure 4.6: Bader charges (in |e|) versus number of exchanged ligands in the model cluster $Au_{25}[SCH_3]_{18-x}[SCH_2Cl]_x^-$. The Au_{13} core remains at the same weakly positively charge state as in the non-chlorinated cluster (with x = 0). The total Chlorine charge (negative) increases linearly with x. The charge is depleted from the Au and S atoms and the CH moieties in the gold-thiolate units ("semirings").

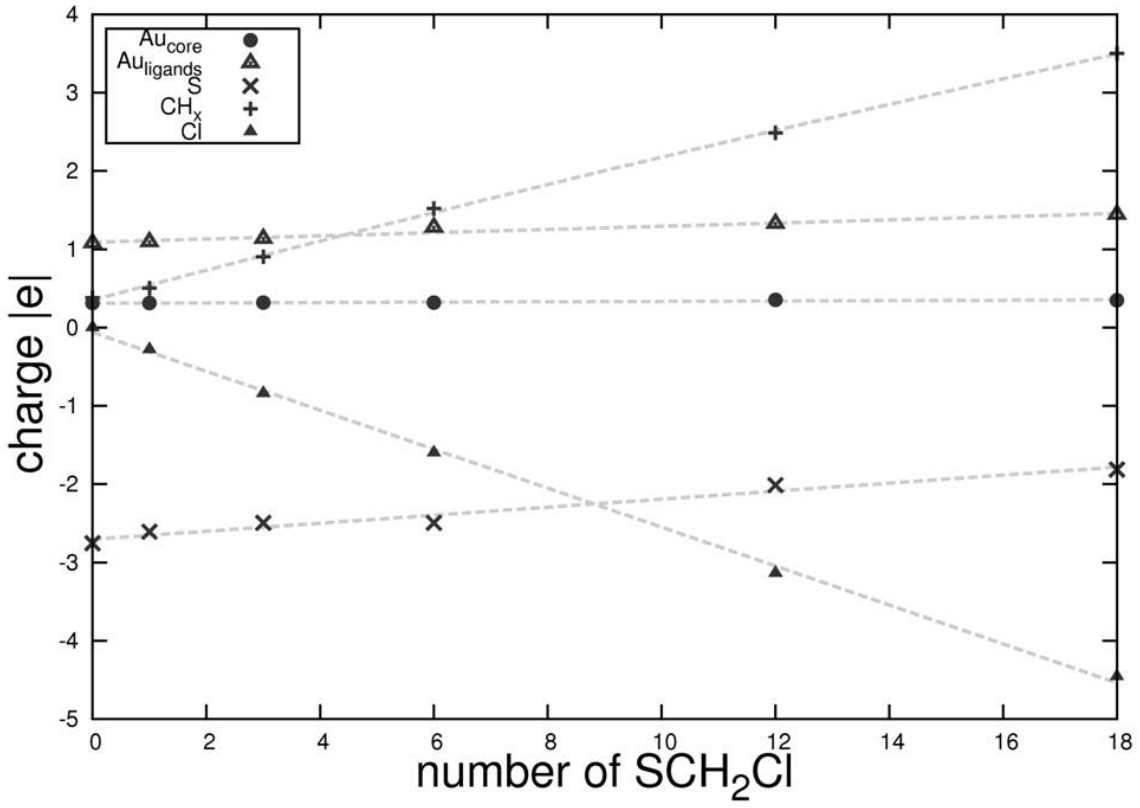
Au_core
Au_ligands
S
CH_x
Cl
charge |e|
number of SCH2Cl
4
3
2
1
0
-1
-2
-3
-4
-5
0
2
4
6
8
10
12
14
16
18

nanoparticle in solution by exchanging $–S(CH_2)_2Ph$ into $–SPhNO_2$.[8] The strong depletion of the charge from the CH_2 moieties is also reflected in the analysis of the local atomic orbitals in the carbon bound to Cl that shows comparable weights of the C(2s) and C(2p) with 50% each, signaling significant changes to the sp^3 hybridization (Figure A4.9).

4.4 Conclusions

The presence of strongly electron-withdrawing X groups on incoming –SPhX ligands prompts a shift to more positive potentials of the nanoparticle's redox waves in a nearly linear relationship. Experimental ligand exchanges with $–SPhNO_2$ and –SPhBr ligands, and the theoretical exchange with $–SCH_2Cl$ ligands, shift the redox waves by 42 mV, 25 mV, and 60 mV per ligand, respectively, compared to the original ligand shell. Density functional theory (DFT) was also used to elucidate the changes in electronic charge distribution of the nanoparticle during exchange. Confirming earlier reports, the HOMO-LUMO gap remains the same during the course of the reaction, with both states being stabilized by the presence of each incoming ligand. Charge analysis suggests no significant changes in the Au_{13} core, even after complete exchange. Rather, the charge is transferred inside the ligands, mostly from nearest-neighbor atoms.

Lastly, we call attention to earlier, as yet unexplained observations[20] of linear relationships between increases in near-infrared luminescence intensities of Au_{25} and of another nanoparticle during ligand exchanges that included use of the same HSPhBr and $HSPhNO_2$ thiols as employed in this paper. It is likely that further study will show an involvement of electronic polarization effects in the semirings that is related to those illustrated in the calculations presented in this paper.

4.5 Acknowledgements

This research was supported by the National Science Foundation, Office of Naval Research, and the Academy of Finland. Molecular graphics images were produced using the UCSF Chimera package from the Resource for Biocomputing, Visualization, and Informatics at the University of California, San Francisco (supported by NIH P41 RR-01081). I would also like to specifically thank Dr. Hannu Häkkinen and his research group for this collaborative effort.

4.6 References

(1) Lee, D.; Donkers, R. L.; Wang, G.; Harper, A. S.; Murray, R. W. *J. Am. Chem. Soc.* **2004**, *126*, 6193-6199.

(2) Brust, M.; Walker, M.; Bethell, D.; Schiffrin, D. J.; Whyman, R. *J. Chem. Soc., Chem. Commun.* **1994**, 801-802.

(3) Donkers, R. L.; Lee, D.; Murray, R. W. *Langmuir* **2004**, *20*, 1945-1952.

(4) Wu, Z.; Suhan, J.; Jin R. *J. Mater. Chem.* **2009**, *19*, 622-626.

(5) Heaven, M. W.; Dass, A.; White, P. S.; Holt, K. M.; Murray, R. W. *J. Am. Chem. Soc.* **2008**, *130*, 3754-3755.

(6) Akola, J.; Walter, M.; Whetten, R. L.; Häkkinen, H.; Grönbeck, H. *J. Am. Chem. Soc.* **2008**, *130*, 3756-3757.

(7) Zhu, M.; Aikens, C. M.; Hollander, F. J.; Schatz, G. C.; Jin, R. *J. Am. Chem. Soc.* **2008**, *130*, 5883-5885.

(8) Guo, R.; Murray, R. W. *J. Am. Chem. Soc.* **2005**, *127*, 12140-12143.

(9) In *Handbook of Preparative Inorganic Chemistry*; Brauer, G., Ed.; Academic Press: New York, 1965; p 1054.

(10) Mortensen, J. J.; Hansen, L. B.; Jacobsen, K. W. *Physical Review B* **2005,** *71,* 035109; https://wiki.fysik.dtu.dk/gpaw/.

(11) Perdew, J.P.; Burke, K.; Ernzerhof, M. *Phys. Rev. Lett.* **1996***, 77*, 3865.

(12) Henkelman, G.; Arnaldsson, A.; Jónsson, H. *Comput. Mater. Sci.* **2006**, *36,* 354-360.

(13) Walter, M.; Akola, J.; Lopez-Acevedo, O.; Jadzinsky, P.D.; Calero, G.; Ackerson, C.J.; Whetten, R.L.; Grönbeck, H.; Häkkinen, H. *Proc. Natl. Acad. Sci.* **2008**, *105*, 9157-9162.

(14) Kacprzak, K.; Lehtovaara, L.; Akola, J.; Lopez-Acevedo O.; Häkkinen, H. *Phys. Chem. Chem. Phys.* **2009**, *11*, 7123-7129.

(15) Lopez-Acevedo, O.; Akola, J.; Whetten, R.L.; Grönbeck, H.; Häkkinen, H. *J. Phys. Chem. C* **2009**, *113*, 5035-5038.

(16) Pettersen, E. F.; Goddard, T.D.; Huang, C.C.; Couch, G.S.; Greenblatt, D.M.; Meng, E.C.; Ferrin, T.E. *J. Comput Chem.* **2004**, *25*, 1605-12.

(17) Dass, A.; Holt, K.; Parker, J. F.; Feldberg, S. W.; Murray, R. W. *J. Phys. Chem. C.* **2008**, 112, 20276-20283.

(18) Guo, R.; Song, Y.; Wang, G.; Murray, R. W. *J. Am. Chem. Soc.* **2005**, *127*, 2752-2757.

(19) (a) Zuman, P. *Substituent Effects in Organic Polarography*; Plenum: New York, 1967; Chapter 1, Tables III-1,4. (b) Lin, C.; Fang, M.; Cheng, S. *J. Electroanal. Chem*. **2002**, *531*, 155-162. (c) Graff, J. N.; McElhaney, A. E.; Basu, P.; Gruhn, N. E.; Chang, C.; Enemark, *J. H. Inorg. Chem.* **2002**, *41*, 2642-2647. (d) Batterjee, S. M.; Marzouk, M. I.; Aazab, M. E.; EIhashash, M. A. *Appl. Organomet. Chem.* **2003**, *17*, 291-297. (e) Johnston, R. F.; Borjas, R. E.; Furilla, J. L. *Electrochim. Acta* **1995**, *40*, 473-477. (f) Hansch, C.; Leo, A.; Taft, R. W. *Chem. Rev.* **1991**, *91*, 165-195.

(20) Wang, G.; Guo, R.; Kalyuzhny, G.; Choi, J.P.; Murray, R. W. *J. Phys. Chem. B* **2006,** *110*, 20282-20289.

Appendix 4

Experimental and Density Functional Theory Analysis of Serial Introductions of Electron-Withdrawing Ligands into the Ligand Shell of a Thiolate-Protected Au_{25} Nanoparticle

The materials in this Appendix are the supplementary data published as Supporting Information in the Journal of Physical Chemistry C article which comprised Chapter 4.

Figure A4.1: Formal potential versus time curves for the ligand exchange of (A) HSPhBr and (B) $HSPhNO_2$. The HSPhBr exchange was monitored by the $E^{o'}$ of the 0/1- wave as described in Figure 4.2. For better resolution of the formal potential, the $HSPhNO_2$ exchange was monitored by the $E^{o'}$ of the 0/1+ wave.

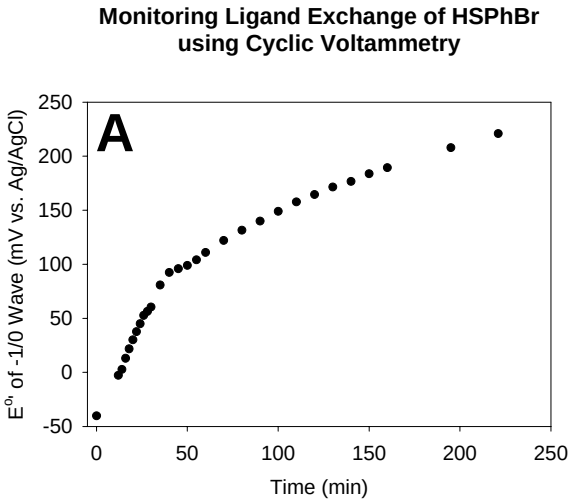
Monitoring Ligand Exchange of HSPhBr using Cyclic Voltammetry
A
E°' of -1/0 Wave (mV vs. Ag/AgCl)
Time (min)
250
200
150
100
50
0
-50
0
50
100
150
200
250

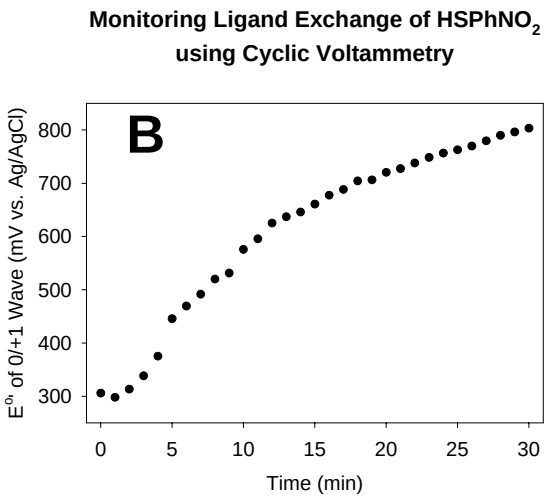
Monitoring Ligand Exchange of HSPhNO2 using Cyclic Voltammetry
B
E°' of 0/+1 Wave (mV vs. Ag/AgCl)
Time (min)
800
700
600
500
400
300
0
5
10
15
20
25
30

Figure A4.2: Cyclic voltammetry (0.1 V/s) of the Au_{25} nanoparticle at a Pt electrode in 0.1 M Bu_4NClO_4/CH_2Cl_2 during ligand exchange with HSPhBr, at t = 0, 30, 60, 100, 150, and 221 minutes after start of exchange. The dotted red lines on each voltammogram represent the measurements of $E^{o'}$ of the 0/-1 wave at those times.

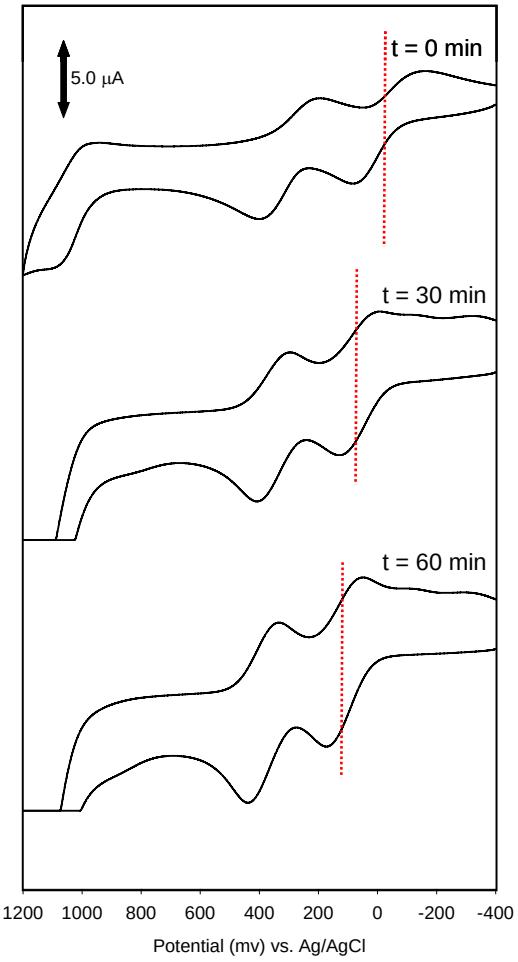
5.0 μA
t = 0 min
t = 30 min
t = 60 min
1200 1000 800 600 400 200 0 -200 -400
Potential (mv) vs. Ag/AgCl

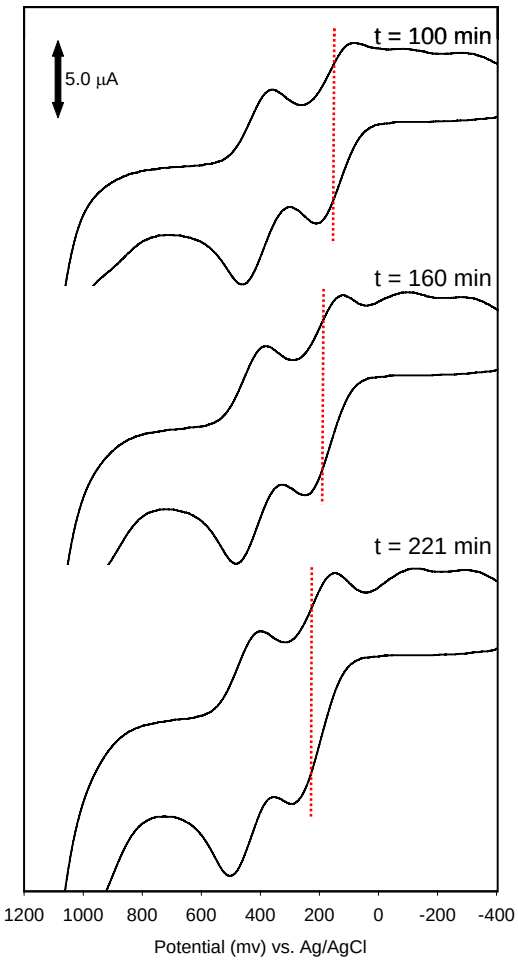
5.0 μA
t = 100 min
t = 160 min
t = 221 min
1200 1000 800 600 400 200 0 -200 -400
Potential (mv) vs. Ag/AgCl

Figure A4.3: Cyclic voltammetry (0.1 V/s) of the Au_{25} nanoparticle at a Pt electrode in 0.1M Bu_4NClO_4/CH_2Cl_2 during ligand exchange with $HSPhNO_2$ at t = 0, 4, 10, 15, 20, and 30 minutes. Dotted red line on each voltammogram estimates the measurements of $E^{o'}$ of the 1+/0 wave during the reaction. The 1+/0 wave, rather than the 0/1- wave, was used chosen because during the reaction, the two waves seem to converge somewhat, making peak definition more problematical in the latter phase of the reaction. To some extent this is attributed to the background of the thiol-containing reaction solution; when the product of the 30 minute reaction was worked up to isolate the nanoparticle, clearer voltammetry was seen for both waves, as shown in Figure A4.4.

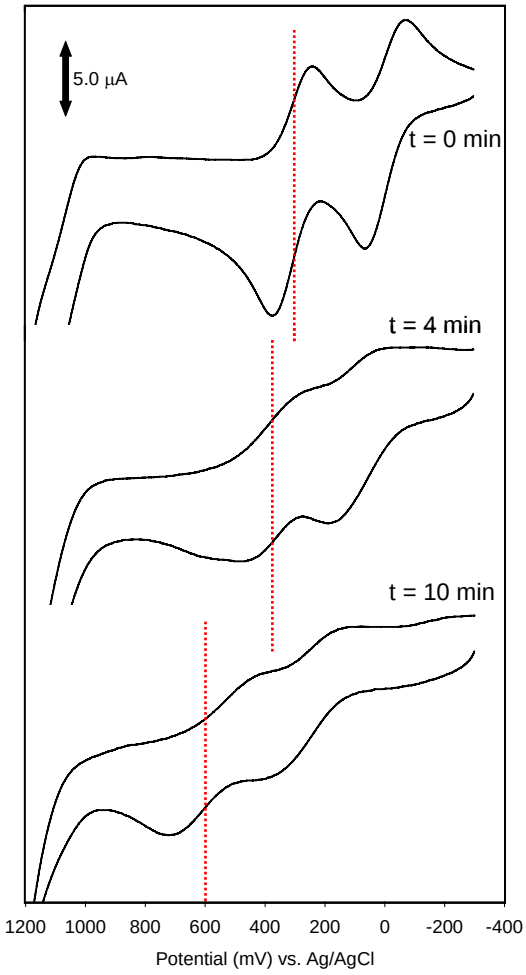
5.0 μA
t = 0 min
t = 4 min
t = 10 min
1200 1000 800 600 400 200 0 -200 -400
Potential (mV) vs. Ag/AgCl

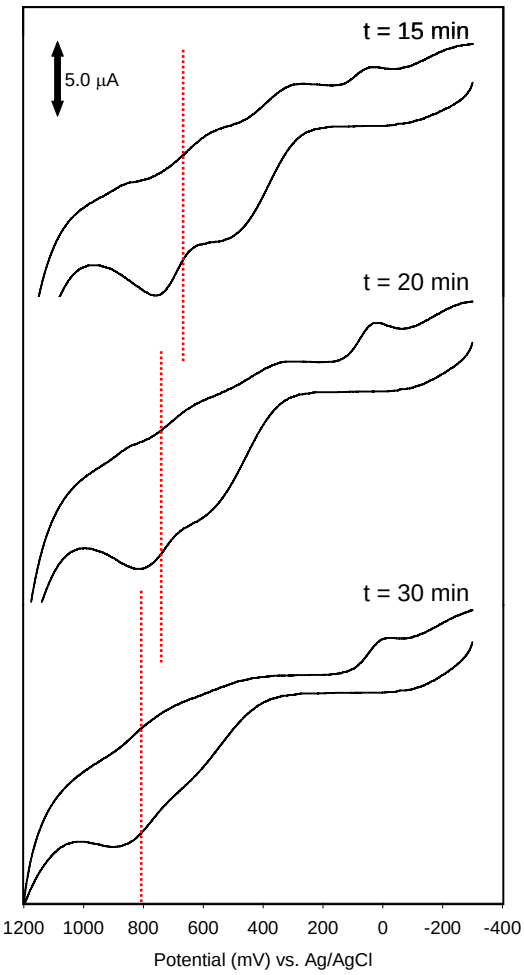
5.0 μA
t = 15 min
t = 20 min
t = 30 min
1200 1000 800 600 400 200 0 -200 -400
Potential (mV) vs. Ag/AgCl

Figure A4.4: Cyclic Voltammogram (A) and Differential Pulse Voltammogram (B) of $Au_{25}(S(CH_2)_2Ph)_{18-x}(SPhNO_2)_x$. Data was obtained after the ligand exchange reaction from Figure A4.3, washed with methanol to remove any free thiols, and polished the platinum electrode to remove an adsorbed material. Voltammetry confirms that the two waves remain stable and reversible, yet with waves with smaller potential differences compared to the unexchanged $Au_{25}(S(CH_2)_2Ph)_{18}$. Exchanged product as a ΔE_{peak} of 300 mV while the exchanged product has a ΔE_{peak} of 220 mV, making it more difficult to ascertain the $E^{o'}$ of the -1/0 wave.

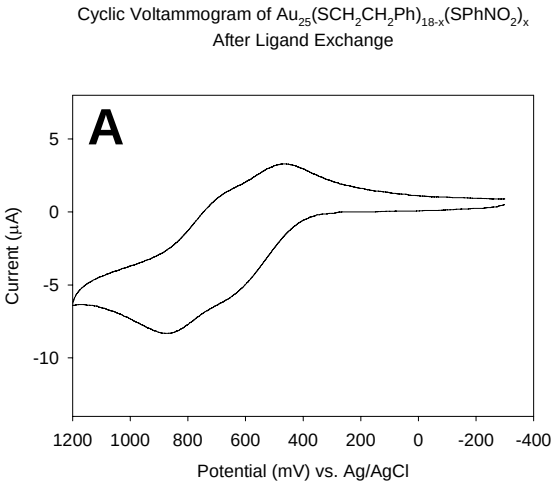
Cyclic Voltammogram of $Au_{25}(SCH_2CH_2Ph)_{18-x}(SPhNO_2)_x$
After Ligand Exchange
A
Current (μA)
5
0
-5
-10
1200 1000 800 600 400 200 0 -200 -400
Potential (mV) vs. Ag/AgCl

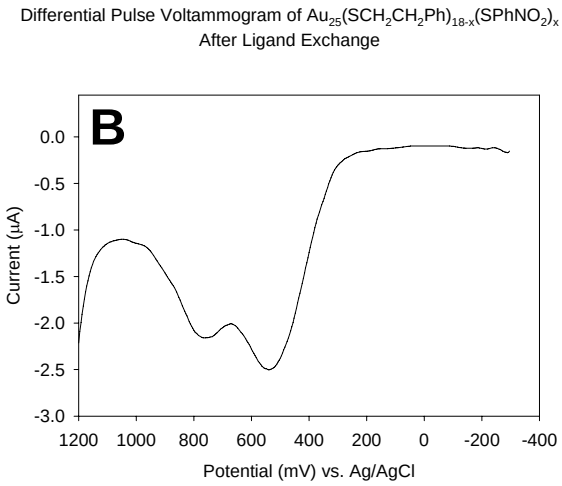
Differential Pulse Voltammogram of $Au_{25}(SCH_2CH_2Ph)_{18-x}(SPhNO_2)_x$
After Ligand Exchange
B
Current (μA)
0.0
-0.5
-1.0
-1.5
-2.0
-2.5
-3.0
1200 1000 800 600 400 200 0 -200 -400
Potential (mV) vs. Ag/AgCl

Figure A4.5: Average number of Au_{25} nanoparticles' original $-S(CH_2)_2Ph$ ligands exchanged for –SPhBr and $-SPhNO_2$ ligands versus time, as measured by ^1H NMR, as detailed in Figure 4.1. Spectra were acquired repeatedly over the time course of the reaction. The integration of the quartet from the liberated $HS(CH_2)_2Ph$ thiol was compared to the methyl protons of the Oct_4N^+ counterion, as an internal standard, to determine the number of ligands exchanged. The number of ligands exchanged appears to plateau around 10 for the –Br case and 7 for the –NO2 case. This is a consequence of the timescale of the reaction and the reactant concentration leading to an equilibrium number exchanged.

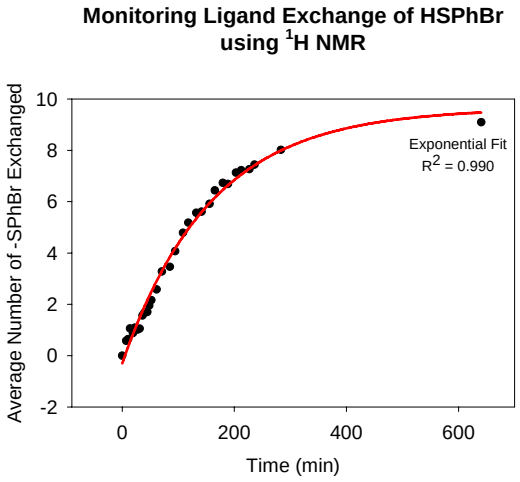
Monitoring Ligand Exchange of HSPhBr using 1H NMR
Average Number of -SPhBr Exchanged
Time (min)
Exponential Fit
R2 = 0.990
10
8
6
4
2
0
-2
0
200
400
600

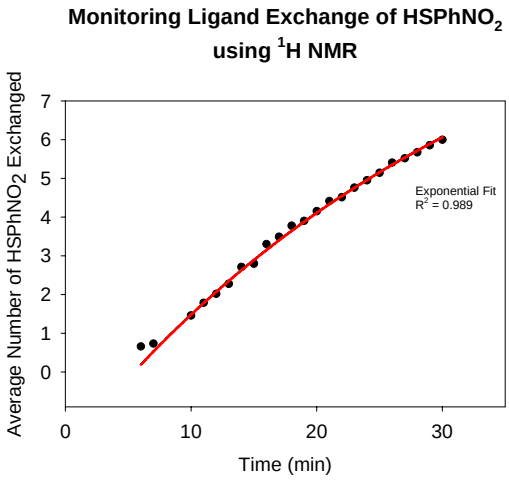
Monitoring Ligand Exchange of HSPhNO2 using 1H NMR
Average Number of HSPhNO2 Exchanged
Time (min)
Exponential Fit
R2 = 0.989
7
6
5
4
3
2
1
0
0
10
20
30

Figure A4.6: Pseudo first-order kinetic study of the ligand exchange with HSPhBr and $HSPhNO_2$ respectively as observed from ^1H NMR analysis. The "fraction unexchanged" refers to the fraction of original $–S(CH_2)_2Ph$ ligands not yet exchanged, as judged from the resonances for liberated $HS(CH_2)_2Ph$ thiols (Figure 4.1). The equations for the two cases are given in the insets with the slopes equal to the observed pseudo-first order rate constant (k_{obs}). The first order rate constants from plot slopes, for the HSPhBr and $HSPhNO_2$ exchanges, are 0.41×10^{-4} s^{-1} and 2.7×10^{-4} s^{-1} respectively.

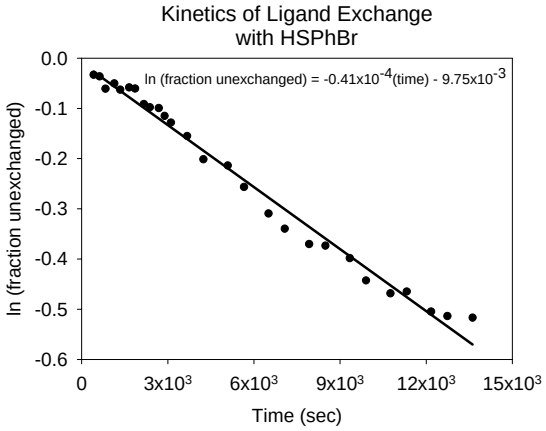
Kinetics of Ligand Exchange
with HSPhBr
ln (fraction unexchanged) = -0.41x10-4(time) - 9.75x10-3
ln (fraction unexchanged)
0.0
-0.1
-0.2
-0.3
-0.4
-0.5
-0.6
0
3x10³
6x10³
9x10³
12x10³
15x10³
Time (sec)

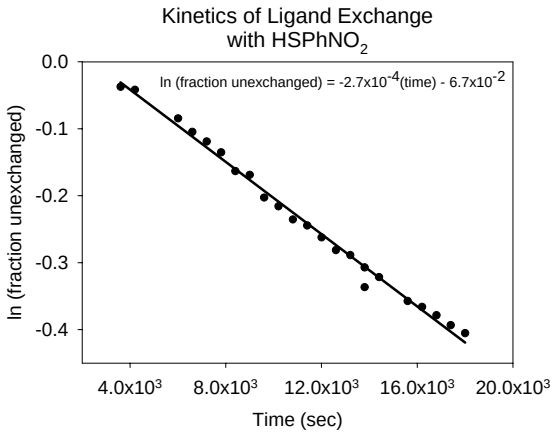
Kinetics of Ligand Exchange
with HSPhNO2
ln (fraction unexchanged) = -2.7x10-4(time) - 6.7x10-2
ln (fraction unexchanged)
0.0
-0.1
-0.2
-0.3
-0.4
4.0x10³
8.0x10³
12.0x10³
16.0x10³
20.0x10³
Time (sec)

Figure A4.7: The vertical detachment energy of $Au_{25}(SCH_2Cl)_x(SCH_3)_{18-x}$. Note that the linear correlation has the same slope (0.06 eV per added SCH_2Cl) as the shift of frontier orbital energies (Fig. 4.5 in the main text).

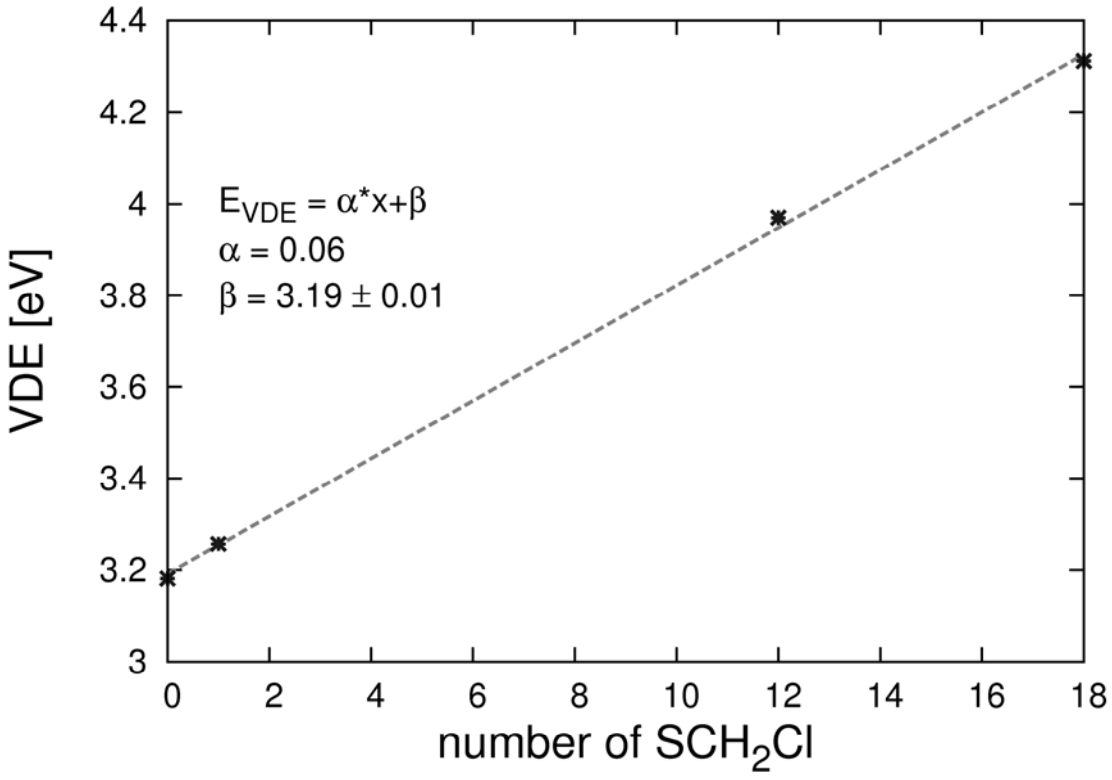
4.4
4.2
4
3.8
3.6
3.4
3.2
3
VDE [eV]
$E_{VDE} = \alpha^*x+\beta$
$\alpha = 0.06$
$\beta = 3.19 \pm 0.01$
0
2
4
6
8
10
12
14
16
18
number of SCH_2Cl

Figure A4.8: The induced differences in the electron density upon introducing 1 (left) or 18 (right) SCH_2Cl ligands in the cluster. Cl atom is green. The red and blue colors indicate accumulation and depletion of electron charge, respectively. The stong polarizing effect of the chlorine in the ligand shell is clearly seen. Note the absence of induced differences in the Au_{13} core.

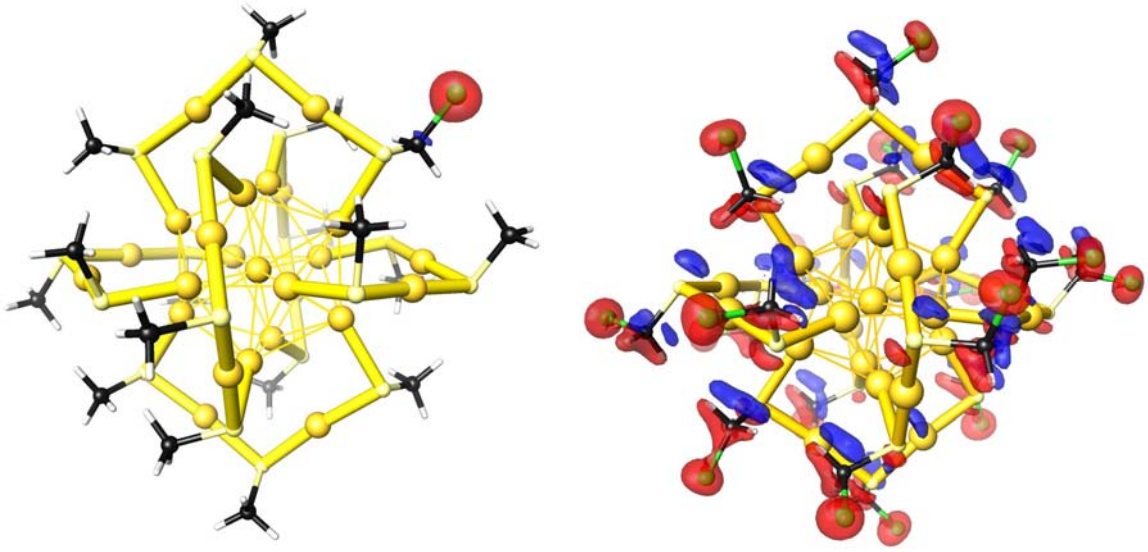

Figure A4.9: Local density of electron states (LDOS) around carbon atoms. The upper three images display LDOS around the three inequivalent carbon atoms C(1) to C(3) in a $Au_2SCH_2Cl(SCH_3)_2$ semi-ring, the lower three panels show the corresponding analysis for C(1) to C(3) in a $Au_2(SCH_3)_3$ semi-ring. HOMO is the highest occupied state of the cluster, LUMO is the lowest unoccupied state of the cluster; H is the highest occupied state of the $Au_{25}(SCH_3)_{18}^-$.

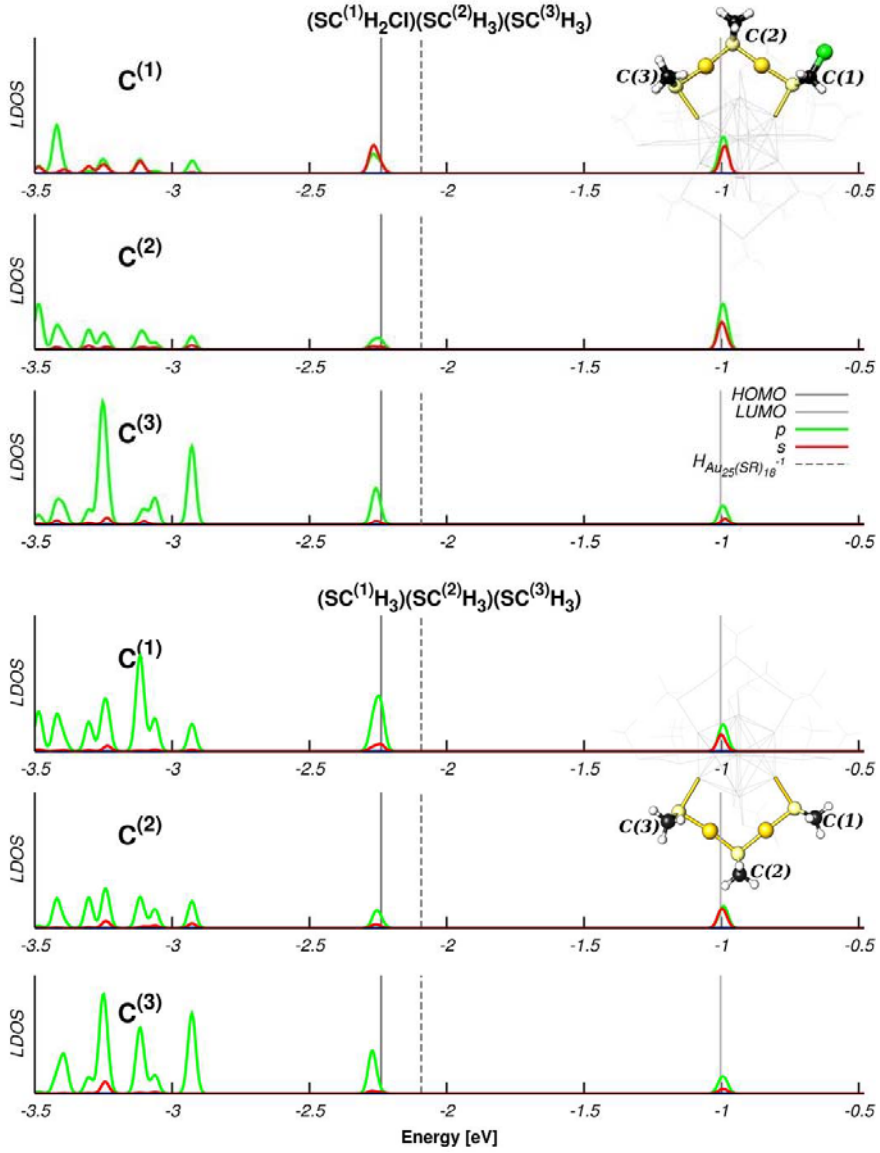
(SC(1)H2Cl)(SC(2)H3)(SC(3)H3)
C(1)
C(2)
C(3)
LDOS
C(1)
C(2)
C(3)
HOMO
LUMO
p
s
H_Au25(SR)18^-1
-3.5
-3
-2.5
-2
-1.5
-1
-0.5
(SC(1)H3)(SC(2)H3)(SC(3)H3)
Energy [eV]

Table A4.1: Bader analysis of averaged charge distribution (per atom type shown, in |e|) of the clusters $Au_{25}(SCH_3)_{18-X}(SCH_2Cl)_X^-$, for X=0 and 18.

X =	0	18
Au in the core	+0.02	+0.03
Au in the semi-ring	+0.09	+0.12
S	-0.15	-0.10
C	-0.17	-0.03
H	+0.06	+0.11
Cl	--	-0.25

Chapter 5

Electronic Communication Among *para*-substituted Thiophenolate Ligands on $Au_{25}(SR)_{18}$ Nanoparticles

5.1 Introduction

Small gold nanoparticles (AuNP, 1-2 nm) with thiolate protecting ligands have undergone intense and exhaustive scrutiny over the last several years. In the case of $Au_{25}(SR)_{18}$, an *Accounts of Chemical Research* was published describing the synthetic and analytical progress made over the last decade.[1] This nanoparticle is especially interesting because it can be synthesized with high yield with atomic monodispersity,[2-4] is stable in air and at various temperatures (up to 100°C), the ligands can be readily replaced by ligand exchange reactions,[5,6] and the crystal structure has been solved for the anionic form, giving rise to several insights into the unexpected geometry of the molecule.[7,8] Furthermore, what began as a study on fundamental size-dependent properties of nanomaterials, has begun to evolve into several important applications, especially in its remarkable activity for certain catalytic reactions.[9] For these reasons, it is especially desirable to further understand the electronics of this AuNP, both with regard to simple thiolate ligands such as $-S(CH_2)_2Ph$ and also with electron-withdrawing and electron-

donating ligands that are electronically coupled to the core. Further studies into these properties would give invaluable insight into present and future applications in electronic miniaturization and catalysis.

The electronic structure of very small gold nanoparticles (< 1.5 nm) reveals a transition from bulk metallic properties to discrete molecule-like energy gaps and single electron redox processes.[10] The anion $Au_{25}(SR)_{18}^-$ is a nanoparticle with an electrochemical bandgap of 1.6 V and a defined HOMO-LUMO gap (1.3 V) as measured by voltammetry and spectral band edges.[11] The first oxidation ($Au_{25}^{1-} \rightarrow Au_{25}^{0}$) is observed near 0 mV, and the second oxidation ($Au_{25}^{0} \rightarrow Au_{25}^{1+}$) at +300 mV vs. Ag/AgCl. We reported previously[5] that introduction of electron-withdrawing or electron-donating ligands into the ligand shell of $Au_{25}(SR)_{18}$ by ligand exchange results in the shifting of the redox wave to more positive potentials based on the electronic nature of the introduced ligands. Specifically, the X-groups on *para*-substituted thiophenols (X = NO_2, Br, Cl, H, OCH_3, etc.) shift the redox potentials to an extent that follows Hammett σ_p constants. Additionally, it was found that the incoming ligands shift the potentials nearly *linearly* with each added incoming ligand.[12] The changes in these potentials are often dramatic, e.g., in the case of $–SPhNO_2$ the $Au_{25}^{0/1+}$ wave can shift more than 500 mV. Surprisingly, however, the electrochemical bandgap remains the same, regardless of the ligand on $Au_{25}(SR)_{18}$ (where SR = $S(CH_2)_2Ph$, SPhBr, $SPhNO_2$, $S(CH_2)_5CH_3$, SCH_2Ph, and others). Analyzing a model ligand exchange reaction with Density Functional Theory (DFT) revealed concurring results, as well as detailing the accumulation of the charge on the electron-withdrawing functional groups by nearest

neighbor atoms on the –SR–Au–SR–Au–SR– semirings, with no effect on the Au_{13} core charge.[12]

This chapter examines not only the effect that electron-withdrawing ligands have on nanoparticle formal potentials, but it attempts to assess electronic communication among ligands by interactions through the Au_{13} core and/or through the –SR–Au–SR–Au–SR– "semirings." This will be accomplished by co-exchanging two incoming ligands: a strongly electron-withdrawing ligand (–SPhBr or $–SPhNO_2$) along with a redox labeled ligand (–SPhFc). Any substantial electronic coupling through the core or through the ligand's semirings should result in a difference in the –Fc redox formal potential ($E^{o'}$) in the absence (versus the presence) of the electron-withdrawing ligand.

5.2 Experimental

5.2.1 Chemicals. 4-Nitrothiophenol (Aldrich, 80%), 4-bromothiophenol (Aldrich, 95%), phenylethanethiol ($HS(CH_2)_2Ph$, Aldrich, 98%), *tetra*-*n*-octylammonium bromide ($Oct_4N^+Br^-$, Fluka, 98%), sodium borohydride (Aldrich, 99%), toluene (Fisher), methanol (Fisher), ethanol (Fisher), acetonitrile (Fisher), acetic acid (Fisher), sulfuric acid (Fisher), ferrocene (Aldrich), 4-aminophenyl disulfide (Aldrich, 98%), sodium nitrite (Aldrich, 99%), sodium bisulfate (Aldrich, 95%), sodium bicarbonate (Fisher, 99.9%), *trans*-2-[3-(4-*tert*-butylphenyl)-2-methyl-2-propenylidene]malononitrile (DCTB, Fluka, 99%), and d_2-methylene chloride (Cambridge Isotope Laboratories, 99.9%) were all used as received. Hydrogen tetrachloroaurate trihydrate was prepared as previously published[13] from 99.999% pure gold and stored at -20°C. Deionized water was obtained from a Millipore Nanopure water purification system.

5.2.2 Synthesis of 4-ferrocenethiophenol. Ferrocene (7.44 g, 40 mmol) was dissolved in 100 mL dichloromethane and 150 mL acetic acid in a 1 L round-bottom flask and cooled to 0°C in an ice bath. Meanwhile, 4-aminophenyl disulfide (4.97 g, 20 mmol) was dissolved in 30 mL concentrated sulfuric acid, also at 0°C. To this solution, sodium nitrite (2.90 g, 42 mmol) dissolved in 20 mL Nanopure water was added dropwise over 2 hrs, generating the diazonium salt of the 4-aminophenyl disulfide. This solution was added to the ferrocene solution and the reaction mixture was stirred under Ar for 24 hrs.

The reaction was quenched with excess sodium bisulfate, followed by extraction with excess dichloromethane to recover the product. The dichloromethane solution was neutralized by washing with a concentrated sodium bicarbonate solution until the pH reached 7.0, as judged by pH paper. The aqueous layer was discarded, and the dichloromethane layer dried over solid Na_2SO_4. The solvent was removed by rotary evaporation and the resulting orange solid collected as the disulfide [$(Fc\text{-}Ph\text{-}S)_2$] (11.7 g, 20 mmol).

A quantity of the disulfide intermediate $(FcPhS)_2$ (0.55 g, 0.94 mmol) was dissolved in 20 mL tetrahydrofuran (THF), and to this solution was added 0.9 mL of a 2.4 M solution of $LiAlH_4$ in THF (2.16 mmol). The reaction mixture was heated to 60°C for 15 minutes. The reaction was quenched with a few milliliters of Nanopure water, and the product was collected by extraction with dichloromethane. The putative orange solid product, HSPhFc (0.554 g), was collected and purified by column chromatography (silica column with hexanes and ethyl acetate).

5.2.3 Synthesis of $[Oct_4N^+][Au_{25}(S(CH_2)_2Ph)_{18}^-]$. This nanoparticle was synthesized using a modified version of the Brust synthesis.[2,3] Hydrogen tetrachloroaurate (3.1 g, 11.1 mmol) was dissolved in toluene using the phase-transfer reagent *tetra*-*n*-octylammonium bromide ($Oct_4N^+Br^-$). A 3.2 molar excess of phenylethanethiol ($HS(CH_2)_2Ph$) was added to the solution at room temperature, forming the intermediate colorless gold-thiolate polymer solution. After 12 hours, an ice-cold aqueous solution of sodium borohydride was added in excess to rapidly form the mixture of gold nanoparticles, followed by stirring for 20 hours. The black product solution contains a mixture of nanoparticle core sizes and oxidation states. The cluster in the form $[Oct_4N^+][Au_{25}(S(CH_2)_2Ph)_{18}^-]$ is the only species with appreciable solubility in acetonitrile and thus was extracted from the dried reaction mixture and copiously washed with methanol to remove excess free thiol and Oct_4N^+ salts to yield a monodisperse nanoparticle.

5.2.4 Ligand Exchange Reactions. All ligand exchange reactions were performed in dichloromethane. For the reaction with HSPhFc alone, $[Oct_4N^+][Au_{25}(SCH_2CH_2Ph)_{18}^-]$ (2.9 mg, 0.37 μmol) was dissolved in dichloromethane along with 4-ferrocenethiophenol (2.0 mg, 6.8 μmol) to give a final Au_{25} concentration of 0.25 mM with the incoming thiol in excess by 1× per bound $-S(CH_2)_2Ph$ (or 18× per nanoparticle). The reaction proceeded for 2.5 hours at room temperature. To clean up the reaction, the exchange product was precipitated with a large excess of methanol and centrifuged at 8000 rpm and the orange excess thiol solution discarded. The product was re-dissolved in a small amount of dichloromethane and the process repeated until the supernatant was clear of any evidence of free thiols.

For the reaction exchanging both HSPhFc and HSPhBr, $[Oct_4N^+][Au_{25}(S(CH_2)_2Ph)_{18}^-]$ (2.1 mg, 0.27 μmol) was dissolved in dichloromethane to give a total Au_{25} concentration of 0.25 mM. In this case, both incoming thiols were exchanged simultaneously. 4-ferrocenethiophenol (0.70 mg, 2.3 μmol) was added with an excess of 0.5× and 4-bromothiophenol (0.45 mg, 2.3 μmol) with 0.5×, both with respect to the nanoparticle's original ligands. The reaction was allowed to proceed for 2.5 hours and was cleaned up in the same way as described above.

For the reaction exchanging both HSPhFc and $HSPhNO_2$, $[Oct_4N^+][Au_{25}(S(CH_2)_2Ph)_{18}^-]$ (3.9 mg, 0.50 μmol) was dissolved in dichloromethane to give a total Au_{25} concentration of 0.25 mM along with 4-ferrocenethiophenol (1.3 mg, 4.5 μmol) and 4-nitrothiophenol (1.38 mg, 8.9 μmol) with excesses of 0.5× and 1.0× respectively. The reaction was allowed to proceed for 2.5 hours and cleaned up in the same way as the two syntheses above.

5.2.5 Nanoparticle Characterization. All electrochemical measurements were made on a Bioanalytical Systems, Inc. (BAS) analyzer using a Pt-disk working, Pt-wire counter, and Ag/AgCl reference electrodes with a supporting electrolyte solution of 0.1 M Bu_4NClO_4/CH_2Cl_2. Each potential sweep cyclically scanned the range of -500 mV to +1200 mV at 100 mV/sec with a sampling interval of 1 mV. ^1H NMR measurements were made using a Bruker 400wb spectrometer in CD_2Cl_2 solutions at room temperature with a D1 of 1.00 sec. MALDI-TOF mass spectrometry data were obtained using an Applied Biosystems Voyager DE Pro instrument and the matrix *trans*-2-[3-(4-*tert*-butylphenyl)-2-methyl-2-propenylidene]malononitrile (DCTB) as previously described.[14,15]

5.3 Results and Discussion

5.3.1 Ligand Exchange with 4-ferrocenethiophenol. It was reported previously[5] that electron-withdrawing groups bound to $Au_{25}(SR)_{18}$ nanoparticles induce a strong polarization effect that results in a shift to more positive potentials in the redox waves. This is explained from classical descriptions[16] that electron-withdrawing substituents that are conjugated to a redox center will make it harder to oxidize. Electron-donating groups have the opposite effect. Our collaborators modeled the effect of serial introductions of electron-withdrawing ligands using Density Functional Theory (DFT)[12] and showed that while there is a strong accumulation of negative charge onto the electronegative atom on the ligand, that charge is mainly due to polarization of nearest neighbor atoms and has only a small polarizing effect on the nanoparticle semirings and no observable effect on the Au_{13} core atoms. In this report, we aimed to further ascertain any potential electronic coupling and/or polarization interactions among ligands *through* the Au_{13} core or the semirings, that is, do the ligands which are electronically coupled to the core communicate with one another? To accomplish this, we exchanged 4-ferrocenethiophenol (HSPhFc), a redox-active and electronically-coupling ligand along with a strongly electron-withdrawing ligand (HSPhX, X = Br or NO_2). The ferrocene moiety on the thiolate bound to Au_{25} has a certain electrochemical formal potential ($E^{o'}$). If that formal potential changes in the presence of HSPhBr or $HSPhNO_2$, then there is indeed an interaction among the ligands that can be probed.

The MALDI-TOF mass spectrometry and cyclic voltammetry results of the ligand exchange reaction with HSPhFc alone are given in Figures 5.1 and 5.2. The envelope of peaks observed in Figure 5.1 shows the extent of ligand exchange. The separation in the

Figure 5.1. Matrix Assisted Laser Desorption Ionization Time-of-Flight (MALDI-TOF) mass spectrum of the ligand exchange product $Au_{25}(S(CH_2)_2Ph)_{18-x}(SPhFc)_x$. Distribution of products reveals intense peaks with a m/z separation of 156, indicating the difference in molecular mass between $–S(CH_2)_2Ph$ and –SPhFc. Ligand exchange conditions consisted of 0.25 mM $[Au_{25}]$ with a 1× excess of [HSPhFc] per bound ligand. The peaks labeled with (*) are unknown, and may result from fragmentation.

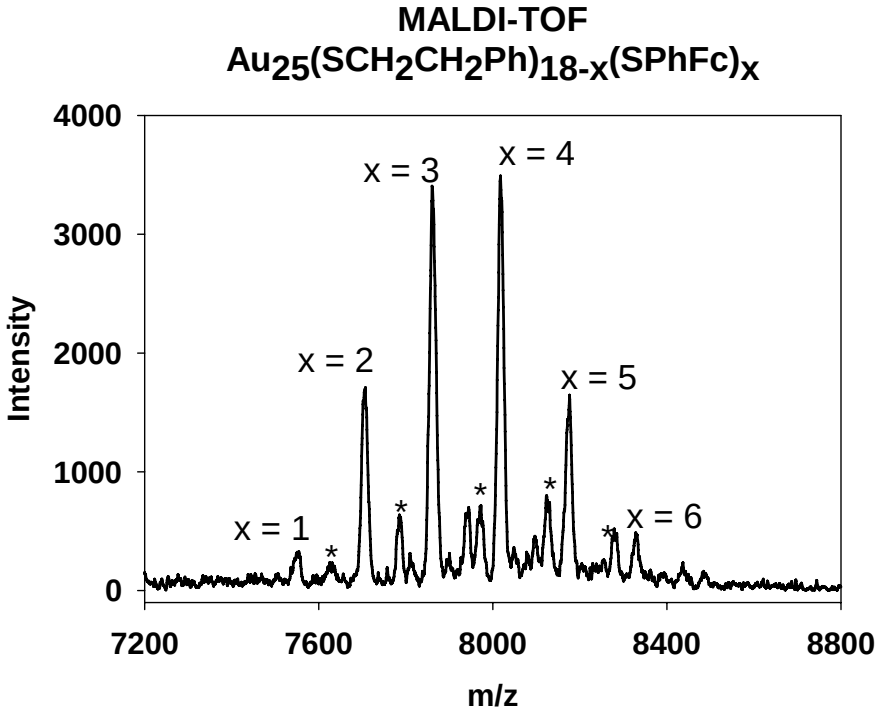
MALDI-TOF
Au25(SCH2CH2Ph)18-x(SPhFc)x
4000
3000
2000
1000
0
Intensity
x = 1
x = 2
x = 3
x = 4
x = 5
x = 6
*
7200
7600
8000
8400
8800
m/z

Figure 5.2. Cyclic voltammetry of the ligand exchange product with the average molecular formula $Au_{25}(S(CH_2)_2Ph)_{14}(SPhFc)_4$ in 0.1 M TBAP/CH_2Cl with a Pt disk working electrode, Pt wire counter electrode, and Ag/AgCl reference with a potential scan rate of 25 mV/sec. Waves labeled with (*) are the $Au_{25}^{0/-1}$ and $Au_{25}^{+/0}$ reduction peaks of Au_{25} and the peak at 0.57 V is the $-SPhFc^{0/+}$ wave.

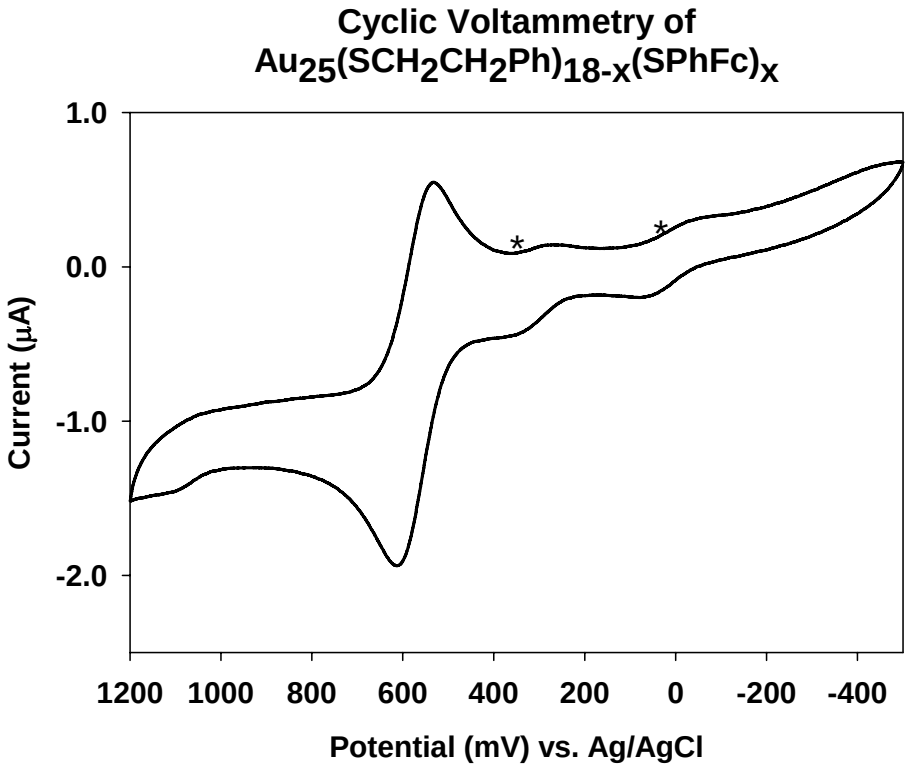
Cyclic Voltammetry of
Au25(SCH2CH2Ph)18-x(SPhFc)x
1.0
0.0
-1.0
-2.0
Current (μA)
1200
1000
800
600
400
200
0
-200
-400
Potential (mV) vs. Ag/AgCl
*
*

most abundant peaks average 156 m/z, which is the difference in molecular weight between phenylethanethiolate (137.23 m/z) and 4-ferrocenethiophenolate (293.18 m/z). It is clearly observed that the average number of –SPhFc ligands exchanged is around 4, with a maximum of 6. The minor peaks labeled with (*) in Figure 5.1 are most likely fragment ions, but have not been accounted for with certainty. There exists the potential for these ions to be the result of thiol byproducts in the synthesis of 4-ferrocenethiophenol, but no such byproducts are observed in the ^{1}H NMR (Figure A5.1).

The cyclic voltammogram of the exchange product with the average molecular formula of $Au_{25}(S(CH_2)_2Ph)_{14}(SPhFc)_4$ is given in Figure 5.2, and is used largely as a control to compare to future experiments. The waves at 0.02 V and 0.31 V are indicative of the redox processes of the Au_{25} nanoparticle while the wave at 0.57 V arises from the ferrocene group on the newly introduced ligand. (The free HSPhFc displays a ferrocene redox wave at 0.61 V vs. Ag/AgCl, a 40 mV shift relative to when –SPhFc is attached to the nanoparticle, See Figure A5.2).

5.3.2 Ligand Exchange with 4-ferrocenethiophenol and 4-bromothiophenol.

Our initial goal was a simple plan: exchange a moderately strong electron-withdrawing ligand (e.g. HSPhBr) to a small degree while *also* exchanging the redox labeled ligand, HSPhFc. After multiple ligand exchange experiments–some resulting in large amounts of ligands exchanged–the reaction was optimized to limit the number of each ligand attached to the nanoparticle. The excess incoming HSPhBr and HSPhFc ligands were optimized to 0.5× per ligand each (9× per Au_{25}), resulting in a small amount of both the bromo and ferrocene ligands exchanged onto the nanoparticle, as judged by the MALDI MS in Figure 5.3B and the cyclic voltammogram in Figure 5.4B. Analyzing the ligand

Figure 5.3. MALDI-TOF MS of (A) an example ligand exchange with –SPhBr alone. The binomial distribution centers around 14 exchanged, with a much narrower distribution than in (B): the simultaneous ligand exchanges of both –SPhBr and –SPhFc, where the wider distribution of products is a result of the many combinations of products present. The black curve in (B) is the experimental curve; the blue, red, and green are simulations of the distribution of products with 5 –SPhBr exchanged and 0, 1, and 2 –SPhFc present, respectively.

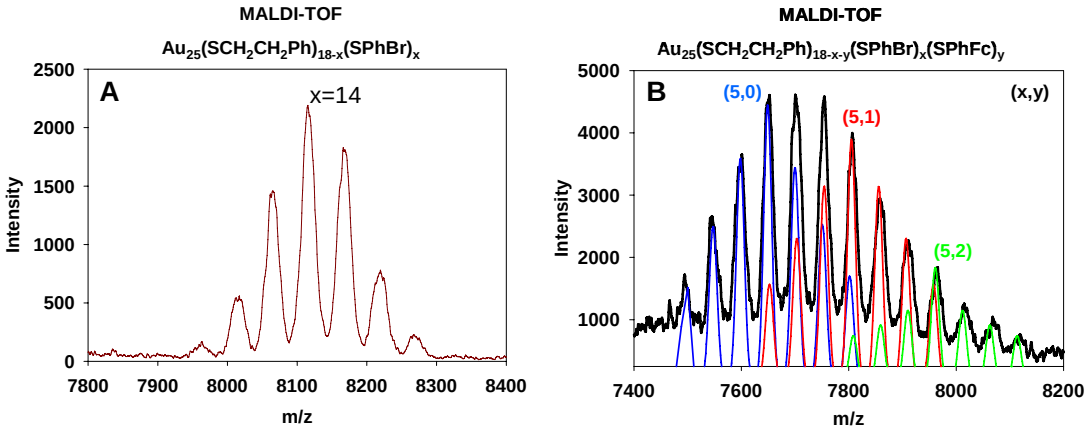
MALDI-TOF
Au25(SCH2CH2Ph)18-x(SPhBr)x
A
x=14
Intensity
m/z
MALDI-TOF
Au25(SCH2CH2Ph)18-x-y(SPhBr)x(SPhFc)y
B
(5,0)
(5,1)
(5,2)
(x,y)
Intensity
m/z

Figure 5.4. Comparison of (A) the ligand exchange product containing only –SPhFc and (B) the product that contains both –SPhFc and –SPhBr. The blue and red dotted drop-down lines highlight the shifting of the $Au_{25}^{-1/0}$ and $Au_{25}^{0/+1}$ waves to more positive potentials, expected by the presence of –SPhBr. The $E^{o'}$ of the Fc wave is 0.573 V in both cases, indicating no observable polarization by the ligands. Voltammetric conditions are identical to those described in Figure 5.2.

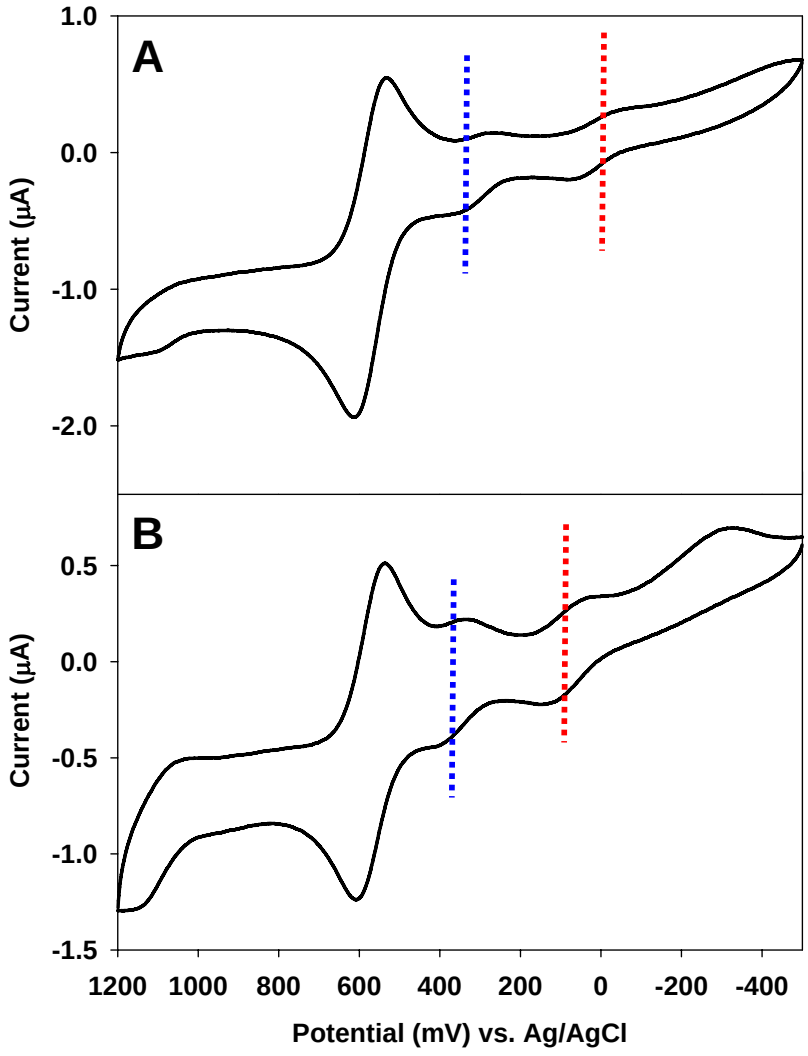
A
B
1.0
0.0
-1.0
-2.0
0.5
-0.5
-1.5
Current (μA)
1200
1000
800
600
400
200
0
-200
-400
Potential (mV) vs. Ag/AgCl

distribution with MALDI was not trivial for this product due to the overlapping of possibilities when attempting to assign the peaks with the formula $Au_{25}(S(CH_2)_2)_{18-x-y}(SPhBr)_x(SPhFc)_y$. When observing the differences, however, in the MALDI between $Au_{25}(S(CH_2)_2Ph)_{18-x}(SPhBr)_x$ (Figure 5.3A) and $Au_{25}(S(CH_2)_2Ph)_{18-x-y}(SPhBr)_x(SPhFc)_y$ (Figure 5.3B), it is apparent that the distribution has changed dramatically. The many peaks in the spectrum could be labeled with a number of different molecular formulæ, as seen in Table A5.1. A series of overlapping theoretical binomial distributions was plotted in Figure 5.4B, giving rise to the most likely exchange product containing an average of five –SPhBr ligands and from zero to two –SPhFc ligands. Given the voltammogram in Figure 5.3B, this assignment seems reasonable due to the relative peak currents of the ferrocene wave versus the Au_{25} waves as well as the magnitude of the positive shift of the Au_{25} waves due to the presence of –SPhBr.[12]

Comparing the voltammograms in Figure 5.4, both in the absence and presence of an electron-withdrawing ligand, the $E^{o'}$ of the ferrocene wave remains unaffected (0.573 V vs. Ag/AgCl in both cases). This observation makes it apparent that a small number of *these* electron-withdrawing ligands do not exert an observable electronic polarization effect on the redox labeled ferrocene ligand.

5.3.3 Ligand Exchange with 4-ferrocenethiophenol and 4-nitrothiophenol.

Given the results of the –SPhFc and –SPhBr experiment, it was now desirable to use an even *stronger* electron-withdrawing ligand, with an even higher number exchanged, while maintaining a low number of –SPhFc ligands as before. For these reasons, 4-nitrothiophenol ($HSPhNO_2$) was used in a ligand exchange at an increased excess concentration (1× per ligand) along with 4-ferrocenethiophenol (0.5× per ligand). The

resulting product of this ligand exchange reaction was characterized using MALDI MS. Figure 5.5A shows the resulting spectrum with m/z domain from 4000-9000 and clearly shows intense peaks at 7564 and 6219 m/z. These follow the same patterns as described previously[14] using MALDI, showing the typical fragmentation of $Au_{25}L_{18}$ to $Au_{21}L_{14}$ and successive losses of AuL in between. Figure 5.4B highlights the domain of this mass spectrum from 7000 to 8000 m/z. The broadness of the peak at 7564 m/z is a result of the closeness in molecular weights between $–S(CH_2)_2Ph$ and $–SPhNO_2$ (137.2 vs. 154.2 m/z respectively). In previous results,[14,15] the ligand exchange products observed in MALDI have been distinguishable based on their differences in molecular weight, giving rise to defined, evenly spaced peaks in a binomial distribution. The difference in these two ligands is only 17 m/z, which results in what appears to be a broad peak, yet the center of this broad peak is also the center of the binomial distribution of ligand exchange products. See Figure A5.3 for a detailed description of this issue. The peak at 7564 is labeled as $Au_{25}(S(CH_2)_2Ph)_8(SPhNO_2)_{10}$, that is, an average number of ten $–SPhNO_2$ and zero –SPhFc ligands have been exchanged.

The peak at 7720 m/z in Figure 5.5B is shifted to a larger m/z by about 156 (which is the difference in molecular weights between $–S(CH_2)_2Ph$ and –SPhFc). So the peak at 7720 m/z is labeled $Au_{25}(S(CH_2)_2Ph)_7(SPhNO_2)_{10}(SPhFc)_1$ and the small peak at 7876 m/z is labeled $Au_{25}(S(CH_2)_2Ph)_6(SPhNO_2)_{10}(SPhFc)_2$. These results strongly suggest that we successfully exchanged an average of ten $–SPhNO_2$ ligands and from zero to two –SPhFc ligands.

Figure 5.5. MALDI-TOF mass spectrum of the ligand exchange product $Au_{25}(S(CH_2)_2Ph)_{18-x-y}(SPhNO_2)_x(SPhFc)_y$ in the m/z window of (A) 4000-9000 and (B) 7000-8000 m/z. The broadness of the peak at 7564 m/z is a result of the closeness in molecular weights between $–S(CH_2)_2Ph$ and $–SPhNO_2$ (only 17 m/z). The center of this peak is expected to be the center of the binomial distribution of ligand exchange products. Simulated binomial distributions are available in Figure A5.3. The peak at 7564 is labeled $Au_{25}(S(CH_2)_2Ph)_8(SPhNO_2)_{10}$. The peak at 7720 m/z is shifted to a larger m/z by 156 (the difference in M.W. between $–S(CH_2)_2Ph$ and –SPhFc), therefore the peak at 7720 m/z is labeled $Au_{25}(S(CH_2)_2Ph)_7(SPhNO_2)_{10}(SPhFc)_1$ and the peak at 7876 m/z $Au_{25}(S(CH_2)_2Ph)_6(SPhNO_2)_{10}(SPhFc)_2$. The abundant fragment ion at 6219 m/z is the result of a loss of four Au atoms, three $–S(CH_2)_2Ph$ ligands, and one $–SPhNO_2$ ligand. The other fragments are combinations of losses of four ligands from this complicated ligand population.

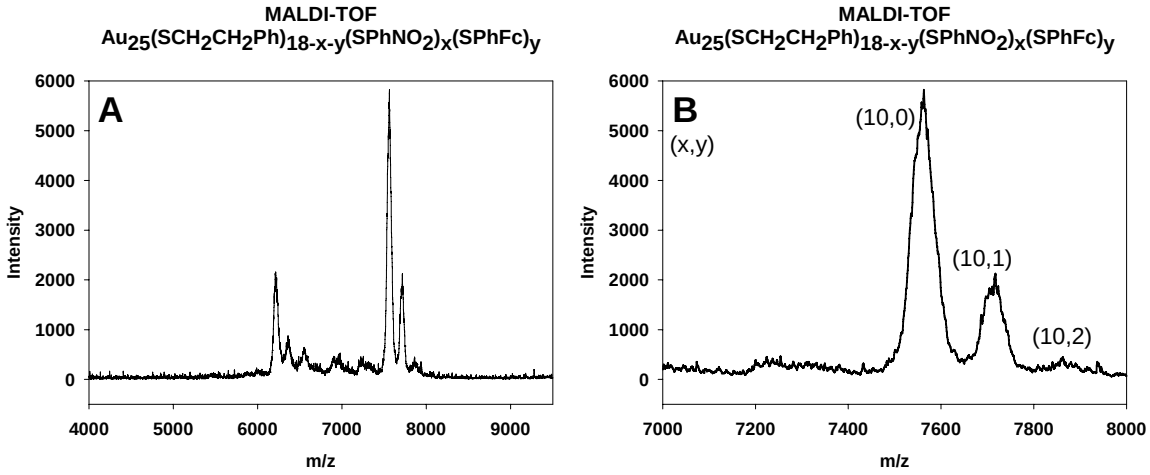
MALDI-TOF
$Au_{25}(SCH_2CH_2Ph)_{18-x-y}(SPhNO_2)_x(SPhFc)_y$
A
Intensity
m/z
6000
5000
4000
3000
2000
1000
0
4000
5000
6000
7000
8000
9000
MALDI-TOF
$Au_{25}(SCH_2CH_2Ph)_{18-x-y}(SPhNO_2)_x(SPhFc)_y$
B
(x,y)
(10,0)
(10,1)
(10,2)
Intensity
m/z
7000
7200
7400
7600
7800
8000

The most abundant fragment ion at 6219 m/z is the result of a loss of four Au atoms, three $-S(CH_2)_2Ph$ ligands, and one $-SPhNO_2$ ligand. The other fragments are other combinations of losses of four ligands from this complicated ligand population.

Figure 5.6 shows the comparison of the cyclic voltammograms of Au_{25} exchanged with –SPhFc in the absence (Figure 5.6A) or presence (Figure 5.6B) of an average of ten $-SPhNO_2$ ligands. In this case, the Au_{25} redox waves were not visible, most likely because the shifting of the peaks to more positive potentials forced the ferrocene wave to overlap the $Au_{25}^{-1/0}$ and $Au_{25}^{0/+1}$ waves. Furthermore, previous studies have shown,[5,12] that as the ligand exchange with $-SPhNO_2$ proceeds, the $Au_{25}^{-1/0}$ and $Au_{25}^{0/+1}$ waves become increasingly more difficult to ascertain. Nevertheless, the MALDI shows a clean spectrum indicating we can definitively assign the material an average molecular formula of $Au_{25}(S(CH_2)_2Ph)_7(SPhNO_2)_{10}(SPhFc)_1$ and comparisons can be made analyzing the $E^{o'}$ of the ferrocene wave. The $E^{o'}$ of the ferrocene in this example was 0.60 V vs. Ag/AgCl. This is a 30 mV shift from the previous experiments (0.57 V) as summarized in Table 5.1. This shifting shows that, indeed, the presence of a larger amount of extremely electron-withdrawing ligands coupled to Au_{25} does have an effect on the electrochemical potential of another ligand of the nanoparticle. (An even more electron-withdrawing ligand was attempted (HSPhCN) but resulted in an unstable nanoparticle with ambiguous voltammetric results).

The magnitude of this communication (0 mV in the case of five –SPhBr and 30 mV in the case of ten $-SPhNO_2$) can be compared to previous results where ferrocene derivatives were analyzed in the presence of electron-withdrawing substituents.[17-18] In an electrochemical study of simple arylferrocene derivatives (*p*-X-PhFc), it was found that

Figure 5.6. Cyclic voltammograms of Au_{25} exchanged with (A) just –SPhFc and (B) both –SPhFc and $–SPhNO_2$. In (B), the Au_{25} redox waves are not visible, most likely because the shifting of the peaks to more positive potentials resulted in the ferrocene wave overlapping the $Au_{25}^{-1/0}$ and $Au_{25}^{0/+1}$ waves. The E°' of the ferrocene in this example was 0.60 V vs. Ag/AgCl (a +30 mV shift from that in (A)). Voltammetric conditions are identical to those in Figure 5.2.

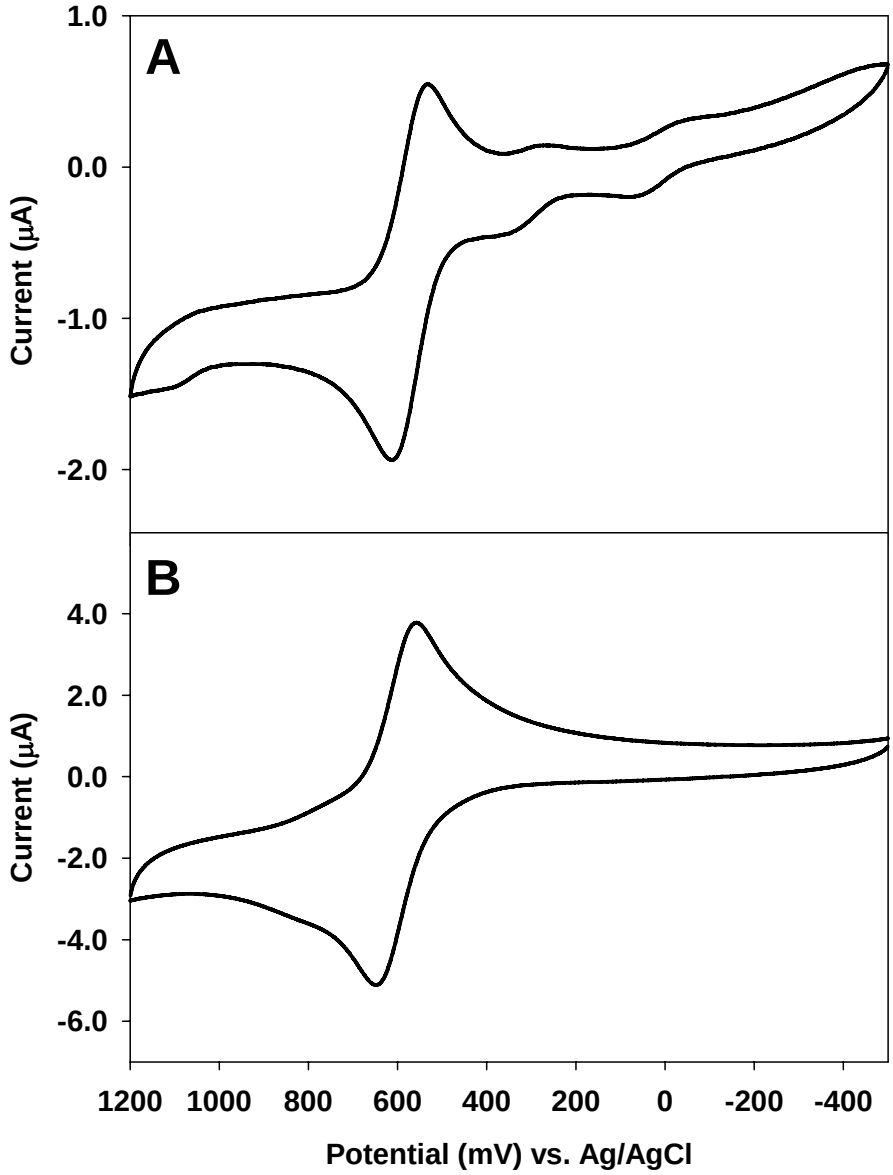
A
B
1.0
0.0
-1.0
-2.0
4.0
2.0
0.0
-2.0
-4.0
-6.0
Current (μA)
Current (μA)
1200
1000
800
600
400
200
0
-200
-400
Potential (mV) vs. Ag/AgCl

Table 5.1: Comparison of the E$^{o'}$ for the ferrocene redox waves with the presence of strongly electron-withdrawing groups. The molecular formulæ of the products from reaction 2 and 3 was ascertained by MALDI-TOF, showing a distribution of 0, 1, and 2 ligands exchanged in both cases.

Reaction	Average Molecular Formula	E$^{o'}$ of Ferrocene Redox Wave (V)
1	$Au_{25}(SCH_2CH_2Ph)_{14}(SPhFc)_4$	0.57
2	$Au_{25}(SCH_2CH_2Ph)_{12}(SPhBr)_5(SPhFc)_1$	0.57
3	$Au_{25}(SCH_2CH_2Ph)_7(SPhNO_2)_{10}(SPhFc)_1$	0.60

the oxidation potential depends on the X ligand, where when X = NO_2 the potential shifts 92 mV versus H-$PhFc^{0/+}$.[17] As the Fc gets further away from the location of the X group, as in chalcone derivatives (*p*-X-Ph-CH=CH-CO-Fc), the NO_2 affects the oxidation potential by a mere 12 mV versus X = H and only 3 mV in the case of X = Br. These results mirror our data, in that coupling is observed, but only when an average of ten –$SPhNO_2$ are present, and no coupling is observed in the case of five –SPhBr. Compared to the simple molecule results, the coupling with ten –$SPhNO_2$ is quite low (30 mV), especially given that ten –$SPhNO_2$ ligands have shown to shift the Au_{25} redox waves by amounts greater than 400 mV.[12]

The origin of the coupling can be further rationalized by looking at Density Functional Theory (DFT) calculations that we published earlier on the effect electron-withdrawing ligands has on neighboring atoms. Figure 5.7, used with permission from reference 12, attempted to model the disposition of charge density throughout a model ligand exchange reaction by replacing –SCH_3 with –SCH_2Cl on Au_{25}. The atoms on the ligands exhibit an accumulation or depletion of charge, depending on their relative distances from the electronegative substituent. For example the methylene unit closest to the Cl (CH_2,+) experiences the greatest depletion of negative charge, followed by the sulfur (×), then the Au on the semirings (▲) to a much lesser degree. The gold that makes up the Au_{13} core (●) does not experience any change, regardless of the extent of exchange. For this reason, we can speculate that any communication among ligands is the result of nearest-neighbor effects on the semirings ([XPhS-$Au]_n$-SPhFc, n = 1 or 2), not *through* the Au_{13} icosahedran core.

Figure 5.7: Bader charges (in |e|) versus number of exchanged ligands in the model cluster $Au_{25}(SCH_3)_{18-x}(SCH_2Cl)_x^-$. The Au_{13} core remains at the same weakly positively charge state as in the non-chlorinated cluster (with x = 0). The total Chlorine charge (negative) increases linearly with x. The charge is depleted from the Au and S atoms and the CH moieties in the gold-thiolate units ("semirings"), and the Au on the semirings to a lesser degree. Figure used with permission from Ref. 12.

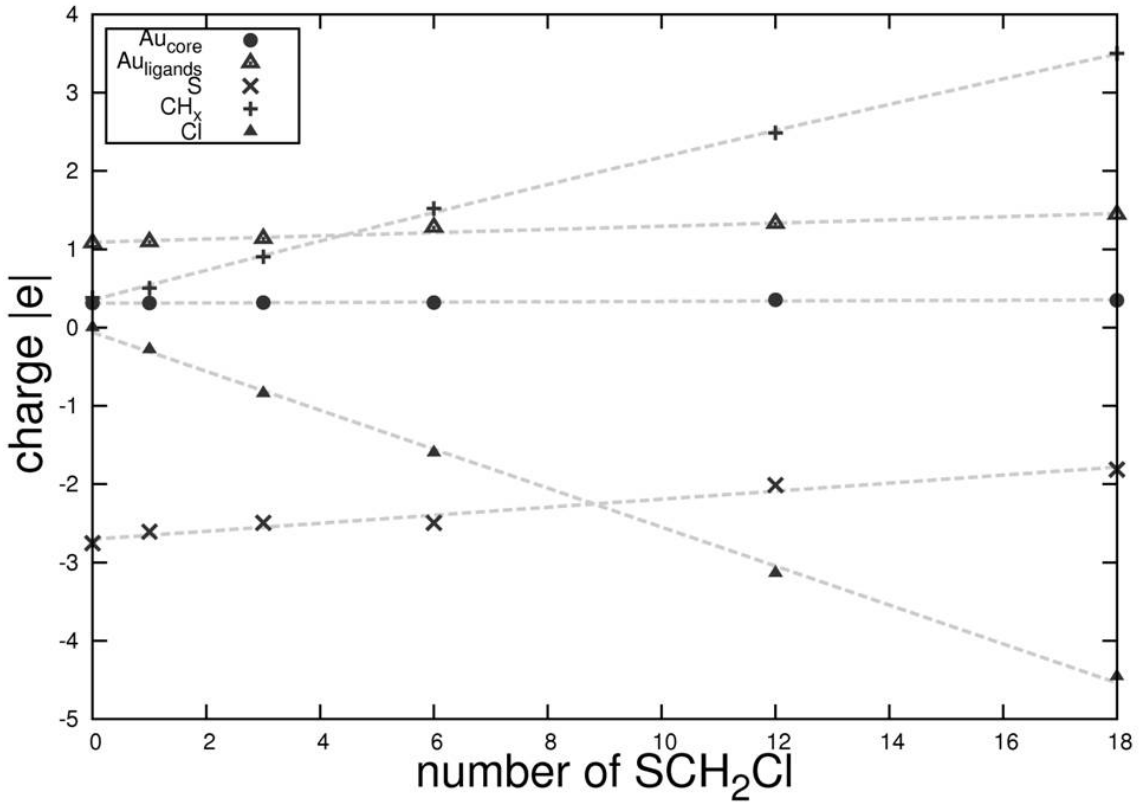
Au_core
Au_ligands
S
CH_x
Cl
charge |e|
number of SCH2Cl
4
3
2
1
0
-1
-2
-3
-4
-5
0
2
4
6
8
10
12
14
16
18

5.4 Conclusions

In this chapter, further details of the electronic properties of $Au_{25}(S(CH_2)_2Ph)_{18}$ are revealed. By exchanging two types of –SPhX ligands (X = ferrocene and NO_2, or ferrocene and Br), the extent of electronic communication among the ligands was observed by monitoring the redox potential of the ferrocene wave with and without the presence of strongly electron-withdrawing ligands. The formal potential of the ferrocene wave ($E^{o'}$) was effected by a very small degree (30 mV) and only in the case when the majority of the other ligands on Au_{25} was the extremely electron-withdrawing $–SPhNO_2$. This observation was analyzed with regard to previously published DFT calculations to speculate that any electronic communication was due to neighboring ligands on the semirings, not through the Au_{13} core.

5.5 Acknowledgements. I would like to acknowledge the doctoral thesis of Kara S. Weber and her adviser, Dr. Stephen Creager, at Clemson University for helpful discussion on our synthesis of 4-ferrocenethiophenol, as well as Joshua Weaver, Christina Fields-Zinna, Amala Dass, and Dr. George Dubay at the Duke Mass Spectrometry facility.

5.6 References

(1) Parker, J.F.; Fields-Zinna, C. A.; Murray, R. W. *Accts. Chem. Res.* **2010**, *Articles ASAP*

(2) Brust, M.; Walker, M.; Bethell, D.; Schiffrin, D. J.; Whyman, R. *J. Chem. Soc., Chem. Commun.* **1994**, 801-802.

(3) Donkers, R. L.; Lee, D.; Murray, R. W. *Langmuir* **2004**, *20*, 1945-1952.

(4) Wu, Z.; Suhan, J.; Jin R. *J. Mater. Chem.* **2009**, *19*, 622-626.

(5) Guo, R.; Murray, R. W. *J. Am. Chem. Soc.* **2005**, *127*, 12140-12143.

(6) Guo, R.; Song, Y.; Wang, G.; Murray, R. W. *J. Am. Chem. Soc.* **2005**, *127*, 2752-2757.

(7) Heaven, M. W.; Dass, A.; White, P. S.; Holt, K. M.; Murray, R. W. *J. Am. Chem. Soc.* **2008**, *130*, 3754-3755.

(8) Akola, J.; Walter, M.; Whetten, R. L.; Häkkinen, H.; Grönbeck, H. *J. Am. Chem. Soc.* **2008**, *130*, 3756-3757.

(9) Zhu, Y.; Qian, H.; Drake, B. A.; Jin, R. *Angew. Chem. Int. Ed.* **2010**, *49*, 1295-1298.

(10) Sardar, R.; Funston, A. M.; Mulvaney, P.; Murray, R. W. *Langmuir*. **2009**, *25*, 13840-13851.

(11) Lee, D.; Donkers, R. L.; Wang, G.; Harper, A. S.; Murray, R. W. *J. Am. Chem. Soc.* **2004**, *126*, 6193-6199.

(12) Parker, J. F.; Kacprzak, K. A.; Lopez-Acevedo, O.; Hakkinen, H.; Murray, R. W. *J. Phys. Chem. C* **2010**, *114*, 8276-8281

(13) In *Handbook of Preparative Inorganic Chemistry*; Brauer, G., Ed.; Academic Press: New York, 1965; p 1054.

(14) Dass, A.; Stevenson, A.; Dubay, G. R.; Tracy, J. B.; Murray, R. W. *J. Am. Chem. Soc.* **2008**, *130*, 5940-5946.

(15) Dass, A.; Holt, K.; Parker, J. F.; Feldberg, S. W.; Murray, R. W. *J. Phys. Chem. C* **2008**, *112*, 20276-20283.

(16) (a) Zuman, P. *Substituent Effects in Organic Polarography*; Plenum: New York, 1967; Chapter 1, Tables III-1,4. (b) Lin, C.; Fang, M.; Cheng, S. *J. Electroanal.*

Chem. **2002**, *531*, 155-162. (c) Graff, J. N.; McElhaney, A. E.; Basu, P.; Gruhn, N. E.; Chang, C.; Enemark, *J. H. Inorg. Chem.* **2002**, *41*, 2642-2647. (d) Batterjee, S. M.; Marzouk, M. I.; Aazab, M. E.; Elhashash, M. A. *Appl. Organomet. Chem.* **2003**, *17*, 291-297. (e) Johnston, R. F.; Borjas, R. E.; Furilla, J. L. *Electrochim. Acta* **1995**, *40*, 473-477. (f) Hansch, C.; Leo, A.; Taft, R. W. *Chem. Rev.* **1991**, *91*, 165-195.

(17) Nagy, A. G.; Toma, S. *J. Organomet. Chem.* **1984**, *266*, 257-268.

(18) Mason, J. G.; Rosenblum, M. *J. Am. Chem. Soc.* **1960**, *82*, 4206-4208.

Appendix 5

Electronic Communication Among *para*-substituted Thiophenolate Ligands on $Au_{25}(SR)_{18}$ Nanoparticles

Synthesis of 4-cyanothiophenol.

In a 125 mL flask, *p*-hydroxybenzonitrile (7.3 g, 61 mmol) and the catalyst 1,4-diazabicyclo[2.2.2]octane (DABCO, 17.2 g, 153 mmol) were dissolved in 70.5 mL dimethylformamide (DMF). While stirring, N,N-dimethylthiocarbamoyl chloride (9.33 g, 75 mmol) was added. The resulting mixture was heated (60-70ºC) and monitored for 1.5 hours. The mixture was poured into ice-cold water and acidified to pH 3 with 6.0 M hydrochloric acid, precipitating the crude intermediate species: O-4-cyanophenyl N,N-dimethylthiocarbamate, followed by recrystallization from ethanol to yield 6.85 g.

Next, solid O-4-cyanophenyl N,N-dimethylthiocarbamate (4.06 g) was added to a 100 mL flask attached to a reflux condenser connected to a mineral oil bubbler, while under an Ar atmosphere. The flask was immersed in a preheated oil bath maintained at 210 ºC, and the mixture was stirred well. The reaction was complete in 2 h, yielding a single, clean, rearranged product, S,4-cyanophenyl N,N-dimethylthiocarbamate. This second intermediate crystallized upon cooling in 100% yield.

S,4-cyanophenyl N,N-dimethylthiocarbamate (4.06 g) was dissolved in 25.4 mL THF. A second solution of KOH (0.286 g in 1.22 mL MeOH) was added to the THF solution. The mixture was stirred at room temperature for 3 hours to complete the hydrolysis. The mixture was poured into ice-cold nanopure water, acidified with 6.0 M hydrochloric acid to attain a final pH value of 2, as estimated by pH paper. The mixture was kept under rapid stirring until the product precipitated out of solution, followed by washing with ice-cold water and dried to yield 2.2 g (81%) of 4-cyanobenzenethiol as a cream-colored solid.

Figure A5.1. Sample ^{1}H NMR spectrum of the ligand exchange product $Au_{25}(S(CH_2)_2Ph)_{18-x}(SPhFc)_x$. The broad multiplet at 7.1 ppm is the combination of all the phenyl peaks on both ligands on the monolayer. (&) represents the cyclopentadiene on ferrocene furthest away from the core, while (#) is the cyclopentadiene closest to the phenyl rings. The α and β peaks are arise from the phenylethanethiolate ligand are very small in this example, indicating a very high extent of HSPhFc exchange. The other peaks arise from Oct_4N^+, the necessary cation for charge balance, CH_2Cl_2, and H_2O.

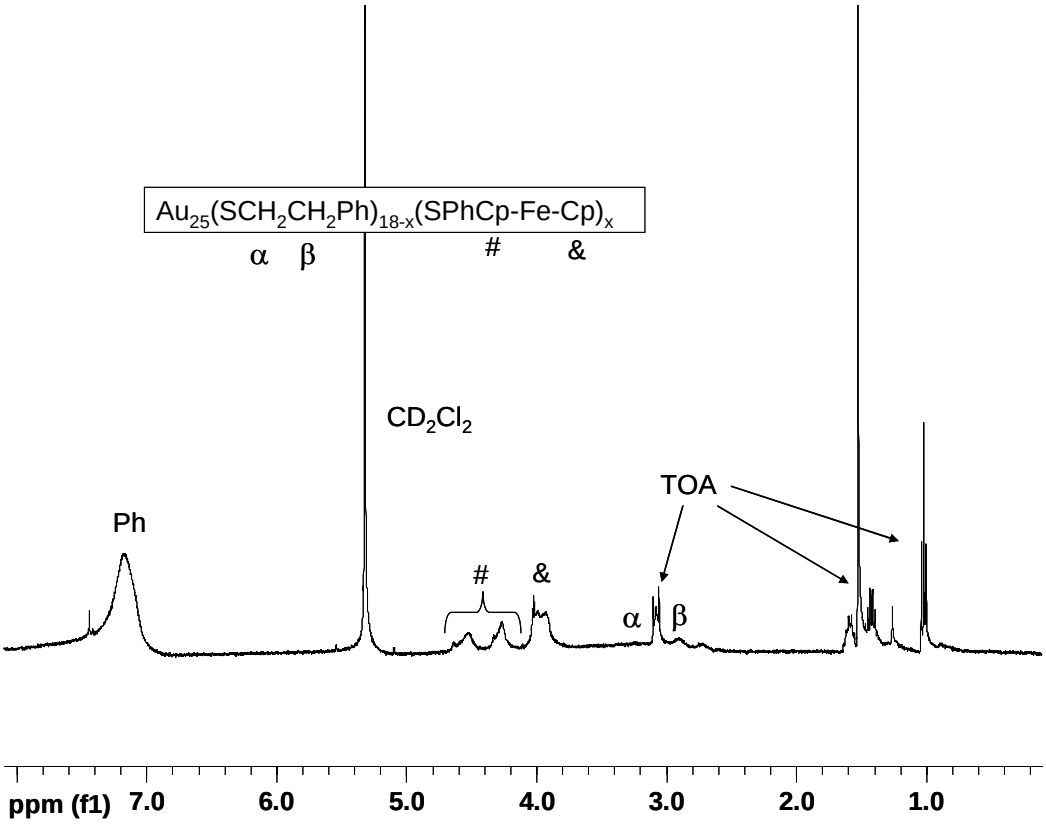
Au25(SCH2CH2Ph)18-x(SPhCp-Fe-Cp)x
α β
&
CD2Cl2
TOA
Ph
&
α β
ppm (f1) 7.0 6.0 5.0 4.0 3.0 2.0 1.0

Figure A5.2. Cyclic voltammogram of the free 4-ferrocenethiophenol (HSPhFc) in 0.1 M TBAP/CH_2Cl_2 using a 1.5 mm Pt-disk (working), Pt-wire (counter), and Ag/AgCl (reference) and a scan rate of 10 mV/sec. The small double layer charging before and after the redox wave indicates either an interaction of the thiol with the Pt electrode, or convective mass transport at the small scan rates. The $E^{o'}$ of the free thiol is 0.61 V.

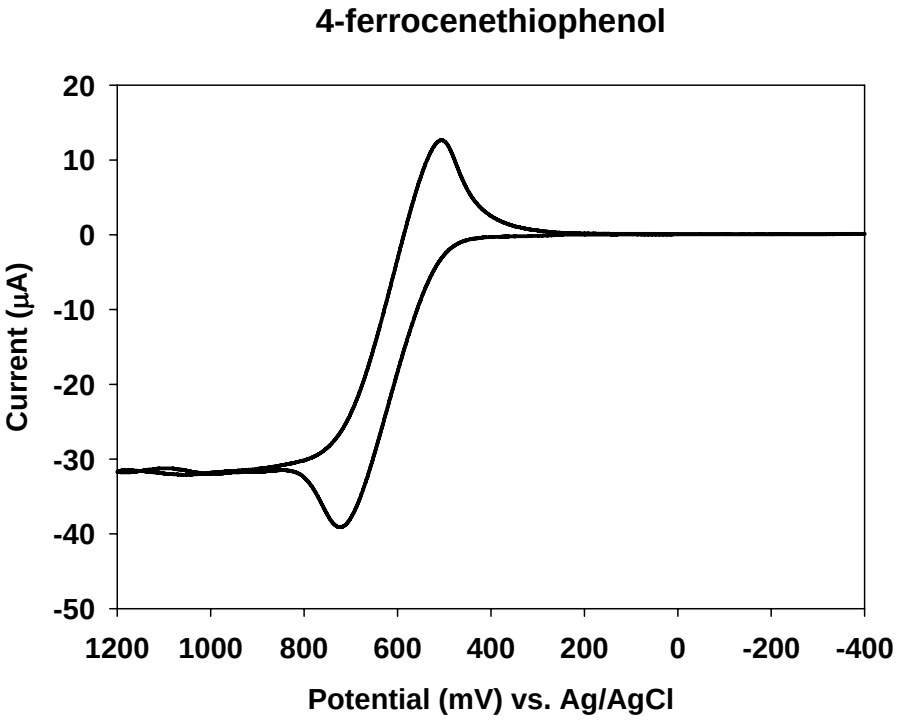
4-ferrocenethiophenol
20
10
0
-10
-20
-30
-40
-50
Current (μA)
1200
1000
800
600
400
200
0
-200
-400
Potential (mV) vs. Ag/AgCl

Table A5.1. Molecular formula assignment possibilities for the peaks in Figure 5.3. Because the difference in molecular weight in $-S(CH_2)_2Ph$ and –SPhBr is about 51 m/z and the difference between $-S(CH_2)_2Ph$ and –SPhFc is 156 m/z (156 is nearly divisible by 51), there are overlapping possibilities for each peak. However, for reasons given in the main text, the most likely distribution of products is those with 5 –SPhBr ligands and from zero to two –SPhFc ligands.

Peak	**Actual m/z**	**Possibilities $Au_{25}(SC2Ph)_x(SPhBr)_y(SPhFc)_z$ (x,y,z)**	**Theoretical m/z for the possibilities**
1	7494.5	**(16,2,0)**	7496.64
2	7546.1	**(15,3,0)**	7547.48
		(17,0,1)	7550.92
3	7601.2	**(14,4,0)**	7598.32
		(16,1,1)	7601.76
4	7652.6	**(13,5,0)**	7649.16
		(15,2,1)	7652.60
5	7700.6	**(12,6,0)**	7700.00
		(14,3,1)	7703.44
6	7754.6	**(11,7,0)**	7750.84
		(13,4,1)	7754.28
		(15,1,2)	7757.72
7	7806.4	**(10,8,0)**	7801.68
		(12,5,1)	7805.12
		(14,2,2)	7808.56
8	7854.9	(9,9,0)	7852.52
		(11,6,1)	7855.96
		(13,3,2)	7859.40
9	7911.2	**(12,4,2)**	7910.24
		(14,1,3)	7913.68
10	7965.4	**(11,5,2)**	7961.08

		(13,2,3)	7964.52
11	8015.0	**(10,6,2)**	8011.92
		(12,3,3)	8015.36
12	8068.3	**(9,7,2)**	9062.76
		(11,4,3)	8066.20
13	8119.4	**(8,8,2)**	8113.60
		(10,5,3)	8117.04

Figure A5.3. A closer look at the MALDI-TOF data for the ligand exchange using both $-SPhNO_2$ and –SPhFc. (A) shows the ligand exchange product in the range of 7400-8000 m/z. The broad peak centered at 7564 m/z is labeled $Au_{25}(S(CH_2)_2Ph)_8(SPhNO_2)_{10}$. Because the difference in molecular weight between $-S(CH_2)_2Ph$ and $-SPhNO_2$ is only 17 m/z, the defined binomial distribution is not clearly resolved (as in Figure 5.3A of the main text). (B) shows the simulated binomial distribution centered around 10 exchanged with a peak separation of 17 m/z, which would be observed barring no instrumental limitations.

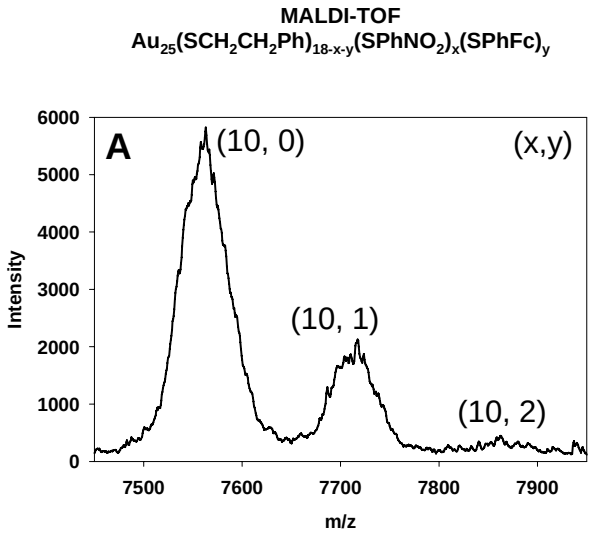
MALDI-TOF
$Au_{25}(SCH_2CH_2Ph)_{18-x-y}(SPhNO_2)_x(SPhFc)_y$
A
(10, 0)
(x,y)
(10, 1)
(10, 2)
Intensity
6000
5000
4000
3000
2000
1000
0
7500
7600
7700
7800
7900
m/z

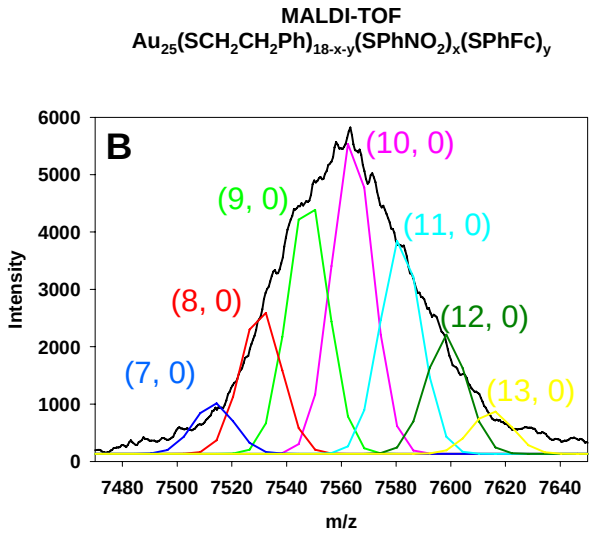
MALDI-TOF
$Au_{25}(SCH_2CH_2Ph)_{18-x-y}(SPhNO_2)_x(SPhFc)_y$
B
(10, 0)
(9, 0)
(11, 0)
(8, 0)
(12, 0)
(7, 0)
(13, 0)
Intensity
6000
5000
4000
3000
2000
1000
0
7480
7500
7520
7540
7560
7580
7600
7620
7640
m/z

Chapter 6

Survey of Ligand Exchange Reactions on Small Gold Nanoparticles

6.1 Introduction

Small gold nanoparticles with thiolate ligands are heavily studied materials with very interesting size-dependent properties[1] and an emerging potential for use in various applications, including biological[2] and catalytic reactions.[3] The extent of the knowledge obtained over the past decade of nanoparticle research has heavily relied on the identity of the organothiolate ligand bound to the nanoparticle. For synthetic reasons, the initial ligand of choice is chosen for ease of purification.[4] The two most heavily synthesized nanoparticles are $Au_{25}(S(CH_2)_2Ph)_{18}$ and $Au_{144}(S(CH_2)_5CH_3)_{59}$. These nanoparticles are stable at room temperature, fully soluble in many organic solvents, amenable to theoretical approaches, and in the case of Au_{25}, a crystal structure has been solved for the anionic form.[5,6] For some experiments and applications, however, it is desirable to replace the default ligands with those with differing properties, including various functional groups, chain lengths, biological relevance, etc. The past several years have seen enormous success in the use of ligand exchange reactions to further understand the structure and function of gold nanoparticles, as well as to introduce chemical functionality for more application-based materials.

The kinetics and statistical nature of these ligand exchange reactions have been heavily studied. For example, when *para*-substituted thiophenols (*p*-X-PhSH) are exchanged onto Au_{25} and Au_{144}, the reaction follows a second-order associative mechanism, from which rate constants (*k*) can be extracted.[7,8] Varying the X-group functionality (X = NO_2, Br, CH_3, OCH_3, and OH) allows comparison to Hammett σ_p-constants, showing a strong dependence of ligand exchange rate on the electron-withdrawing nature of the X-group. The size difference of Au_{25} and Au_{144} (1.0 nm vs. 1.6 nm) does not have an effect on the magnitude of the rate, which gives interesting insight into the relative structure of the two sizes.

The aforementioned ligand exchange reactions were monitored using ^{1}H NMR. The relative integration of the peaks on the cluster can be used to solve for the number of ligands exchanged up to a given time. This is the most versatile and facile way to observe the *average* extent of ligand exchange. In order to gain a clearer description of the ligand exchange process, electrospray-ionization mass spectrometry[9,10] (ESI-MS) and matrix-assisted laser desorption ionization[11,12] (MALDI-MS) can be used to demonstrate the binomial distribution of reaction products with different numbers of exchanged ligands that result from exchange reactions. With the assumption that all 18 ligand sites on $Au_{25}(SR)_{18}$ are identical, a simulated kinetic model of ligand exchange shows binomial distributions which conform well to experimental data obtained from MALDI-MS. In some cases, however, the distribution of products is narrower than predicted (as in –SPh), suggesting nonrandom exchanges at Au_{25}'s various ligand sites, possibly due to sterics, or differing sulfur environments throughout $Au_{25}(SR)_{18}$.[12]

Ligand exchange reactions performed in the past have contributed to the understanding of fundamental properties of gold nanoparticles, as well as introduced functionality for various applications. Tracy, *et al.*,[9] introduced a monodisperse polyethylene glycol thiolate (–S-PEG) into the ligand shell of $Au_{25}(SR)_{18}$ and observed the ESI-MS in the presence of binding cations. This marked the first time high resolution mass spectrometry was used to characterize, with certainty, the molecular formula of Au_{25}. Guo, *et al.*,[7] along with previous information presented in this dissertation,[13] demonstrated the reaction of electron-withdrawing ligands and their effect on the polarization of the nearest-neighbor atoms and the electrochemistry of the gold core. Dass, *et al.*,[14] presented on the introduction of a perfluorinated thiolate ligand (1*H*,1*H*,2*H*,2*H*-perfluorodecanethiolate) in an effort to affect the solubility properties for potential applications in separations, purification, and synthetic chemistry. Ligand exchange reactions have also been used for potential biological purposes, including the introduction of fluorescent dansyl ligands[15] and biotinylated ligands[10] as proof of concepts for using nanoparticles for biomarker applications. As outlined in this dissertation and in previous work,[16,17] redox labeled ligands have been introduced for various electrochemical studies.

This chapter will detail several relevant ligand exchange reactions which have contributed to the study of small gold nanoparticles, and will focus primarily on the introduction of charged ligands, full ligand shell conversion, and electron-withdrawing ligands for solid-state electrochemistry. A brief discussion of using mixed-monolayers presented *ab initio* in the Brust synthesis will also be addressed.

6.2 Experimental

6.2.1 Synthesis of $Au_{25}(S(CH_2)_2Ph)_{18}$. Au_{25} was synthesized by two routes. In the first method,[18,19] $HAuCl_4 \cdot 3H_2O$ (3.10 g, 7.87 mmol) was transferred into toluene from water using the phase-transfer reagent *tetra*-n-octylammonium bromide (Oct_4NBr). A 3.2 molar excess of phenylethanethiol was added to the solution at room temperature, forming the intermediate colorless gold-thiolate polymer, followed by immediate reduction by ice-cold sodium borohydride in excess, stirring for 20 hours. The black product solution contains a mixture of nanoparticle core sizes and oxidation states; the reduced (which we also call the "native form") $[Oct_4N^+][Au_{25}(S(CH_2)_2Ph)_{18}^-]$ is fortuitously the only species with appreciable solubility in acetonitrile and thus was extracted from the dried reaction mixture and copiously washed with methanol to remove excess free thiol and Oct_4N^+ salts.

In the next method,[20] a single-phase reaction was utilized. In this synthesis, $HAuCl_4 \cdot 3H_2O$ (1.00 g, 2.54 mmol) and Oct_4NBr (1.56 g, 2.85 mmol) were co-dissolved in tetrahydrofuran (THF, 70 mL) and stirred for 15 minutes. Phenylethanethiol (1.80 mL, 12.6 mmol) was added at room temperature and stirred for at least 12 hours until the solution was completely colorless. Meanwhile, sodium borohydride ($NaBH_4$, 0.967 g, 25.6 mmol) was dissolved in 24 mL Nanopure water and stirred at 0^oC for 1 hour prior to rapid addition to the THF solution. The reaction mixture was allowed to quietly stir for no less than 48 hours. Over the course of the reaction, the product color slowly evolves from blackish to a murky brown color which is indicative of a high proportion of $Au_{25}(S(CH_2)_2Ph)_{18}^-$. The product solution was then gravity filtered to remove any insoluble materials, rotovapped to dryness, and then dissolved in toluene (30 mL). The

toluene solution was extracted five times using 150 mL Nanopure water. The toluene layer was subsequently rotovapped to dryness and the resulting product washed thoroughly with methanol to remove any traces of excess thiol and Oct_4NBr, leaving pure $[Oct_4N^+][Au_{25}(S(CH_2)_2Ph)_{18}^-]$ (243 mg, 30% yield by Au).

6.2.2 Ligand Exchange with 4-Mercaptobenzoic Acid. For 18 hours, $Au_{25}(S(CH_2)_2Ph)_{18}$ (3.0 mg, 0.4 μmol) was stirred with HSPhCOOH (9.9 mg, 64 μmol) in 2 mL acetone. The acetone was removed by rotary evaporation. The exchanged product was dissolved in 500 μL methanol and transferred to a centrifuge tube, where toluene was added to a total volume of 10 mL, which caused the nanoparticles to flocculate. Following centrifugation at 4,000 rpm for 5 minutes, the supernatant containing excess incoming and outgoing thiol was discarded. The solid product was redispersed in 500 μL methanol, and the flocculation and centrifugation steps were repeated three more times to ensure complete removal of excess thiols. ESI-MS data was obtained on a Bruker BioTOF II mass spectrometer (Billerica, MA) equipped with the Apollo electrospray ionization source. Samples were infused at a flow rate of 65 μL/hour in negative mode in 100% methanol (0.50 mg/mL). The ion transfer time was set to 120 μs, and 50,000 scans were averaged in the data presented. The raw data were smoothed using the Savitzky-Golay (17-point quadratic) method.

6.2.3 Ligand Exchange with *N*,*N*,*N*-trimethyl(11-mercaptoundecyl)-ammonium chloride. This thiol was synthesized as previously described.[21,22] Briefly, trimethylamine in methanol solution was added to 11-bromo-1-undecene in methanol at a

3:1 molar ratio and stirred for 2 days at room temperature, resulting in 1-undecene terminated with a quaternary ammonium bromide. The solution was dried with a rotary evaporator, resulting in a viscous yellow liquid, which was precipitated several times with large volumes of hexanes and then dissolved in dichloromethane. Thioacetic acid was added to the solution in a 3:1 molar ratio and stirred at room temperature while irradiated with an SP-200 mercury light source, resulting in the thioester terminated alkylammonium salt. The reaction mixture was dried, and the product washed several times with diethyl ether.

To convert the thioester into the thiol, the alkylammonium salt was dissolved in 10% HCl and refluxed at 90-100°C for 1 hour. The water was removed *in vacuo*, resulting in a solid white product $[HSC_{11}H_{22}N^{+}(CH_3)_3][Cl^{-}]$, or [HS-TMA^{+}][Cl^{-}]), as confirmed with ^{1}H NMR in D_2O as previously described.[21]

For the ligand exchange reaction of –S-TMA^{+} onto $Au_{144}(S(CH_2)_5CH_3)_{59}$ (Au_{144}), 0.02 μmol of *N*,*N*,*N*-trimethyl(11-mercaptoundecyl)ammonium chloride ([HS-TMA^{+}][Cl^{-}]) was added to 0.14 μmol of Au_{144} in 300 μL of dichloromethane for 48 h. The sample was dried and washed of excess ligands with acetonitrile. Positive-mode ESI-MS spectra were acquired on a Bruker BioTOF II instrument (Billerica, MA), a reflectron time-of-flight mass spectrometer equipped with an Apollo electrospray ionization source. The ligand exchange nanoparticles were run with a concentration of 25 μM in 70:30 chloroform/methanol. The ESI source was operated with flow rates of 60-90 μL/hour, the ion transfer time was set at 120 μs, and 50,000 scans were averaged.

6.2.4 Ligand Exchange with benzyl mercaptan. In order to achieve full coverage of a newly introduced ligand, a series of ligand exchanges were performed back-to-back. In these reactions, $[Oct_4N^+][Au_{25}(S(CH_2)_2Ph)_{18}^-]$ was dissolved in dichloromethane to give a final concentration of 0.63 mM along with excess benzyl mercaptan ($HSCH_2Ph$) at a concentration of 57 mM (which is 5× the concentration of already bound thiol). This exchange was allowed to proceed over the course of 24 hours. At the end of the 24 hours, the solution was dried on a rotary evaporator followed by thorough washing with methanol to remove excess $HSCH_2Ph$ and liberated $HS(CH_2)_2Ph$. This entire process was then repeated two or three times with varying lengths of reaction on the same nanoparticle solution in order to achieve complete monolayer exchange. Nuclear magnetic resonance (^1H NMR) and MALDI-TOF Mass Spectrometry was then used to confirm the complete ligand exchange.

6.2.5 Ligand Exchange with *para*-substituted thiophenolates. In these large scale (often greater than 100 mg) ligand exchange reactions, $[Oct_4N^+][Au_{25}(S(CH_2)_2Ph)_{18}^-]$ was dissolved in dichloromethane at concentrations of 0.63 mM and incoming *para*-substituted thiophenol (HSPhX, X = Br, OCH_3) at concentrations of 23 mM to 57 mM. After reactions times ranging from 12-24 hours, the nanoparticle product solution was dried using a rotary evaporator and washed thoroughly with methanol to achieve pure ligand exchanged materials. MALDI-TOF Mass Spectrometry was then used to quantify the extent of ligand exchange and solid-state electrochemistry was used to measure the conductivity and subsequently the electron-exchange rate information as described previously.[23]

6.3 Results and Discussion

6.3.1 Ligand Exchange with 4-Mercaptobenzoic Acid. The negative mode ESI-MS results of the ligand exchange reaction of $Au_{25}(S(CH_2)_2Ph)_{18}$ with HSPhCOOH are given in Figure 6.1. No other reagents (such as metal cations) were needed in order to analyze the mixed monolayer $Au_{25}(S(CH_2)_2Ph)_{18-x}(SPhCOOH)_x$. Adducts of the deprotonated $–SPhCOO^–$ with the ever-present cation (Oct_4N^+) were also observed, suggesting the primary mechanism of ionization in negative mode ESI of these exchange products was deprotonation. At the time of publication, this material produced the largest signal intensity in ESI seen to date for $Au_{25}(SR)_{18}$ nanoparticles.[10] The 3- ions (Figure 6.1, red curves) gave the highest ion flux and were used for high-resolution analysis. Ions with z = 2- (black curves) were also observed. The [25,18,0] sample ([Au,ligand,Oct_4N^+]) of $Au_{25}(S(CH_2)_2Ph)_{18-x}(SPhCOO)_xH_{x-n}^{z–}$ series of peaks resembles those for -SPh and -SC6 exchanged reported concurrently,[10] with the peak separation arising from the difference in molecular weights between the bound ligands. Assignments and high-resolution analyses for this series of peaks are given in Figure 6.1b and 1c, and in general the matches are very good. Additional sets of peaks were also observed at higher masses ([25,18,1] and [25,18,2]) for gas-phase adducts formed through binding of *tetra*-n-octylammonium (Oct_4N^+) to deprotonated $–SPhCOO^–$ sites in the ligand shell of [25,18,0]. Oct_4N^+ was present in the original nanoparticle synthesis and serves as a necessary counterion for the native 1- charge in $Au_{25}(S(CH_2)_2Ph)_{18}^–$.

A lower-intensity set of peaks in Figure 6.1 matches [24,16,0] = $Au_{24}(S(CH_2)_2Ph)_{16-x}(SPhCOO)_xH_{x-n}^{z–}$, which we believe is a fragment of [25,18,0] by

Figure 6.1. Mass spectra for HSPhCOOH ligand exchange products in 100% CH_3OH: (a) 3- and 2- charge states for a series of peaks that show $Au_{25}(SC2Ph)_{18-x}(SPhCOO)_xH_{x-n}^{z-}$, Oct_4N^+ binding, and the loss of $Au(ligand)_2$. The z = 3- ions have core charge 1-; the 2- ions have average core charge between 0 and 1+. (b) Expansion of the set of peaks for $Au_{25}(SC2Ph)_{18-x}(SPhCOO)_xH_{x-n}^{z-}$. The data for the 2- ions are scaled up by 4×. High-resolution analysis shows an excellent match between the data (thin lines) and simulations (thick lines) for (c) $Au_{25}(SC2Ph)_5(SPhCOO)_{13}H_{11}^{3-}$ and (d) $Au_{25}(SC2Ph)_4(SPhCOO)_{14}H_{11}(Oct_4N)^{3-}$.

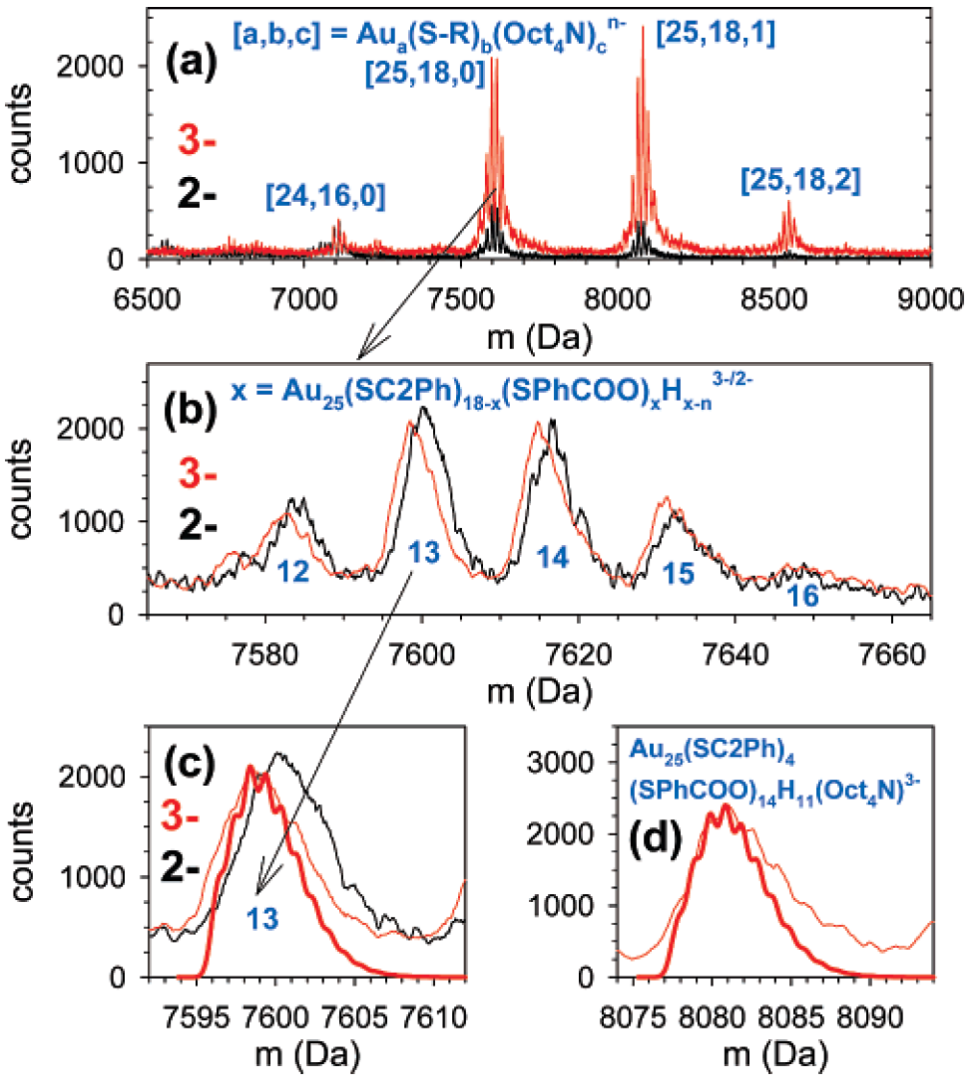
(a)
[a,b,c] = Au$_a$(S-R)$_b$(Oct$_4$N)$_c$$^{n-}$
[25,18,0]
[25,18,1]
[25,18,2]
[24,16,0]
3-
2-
counts
m (Da)
(b)
x = Au$_{25}$(SC2Ph)$_{18-x}$(SPhCOO)$_x$H$_{x-n}$$^{3-/2-}$
12
13
14
15
16
(c)
(d)
Au$_{25}$(SC2Ph)$_4$
(SPhCOO)$_{14}$H$_{11}$(Oct$_4$N)$^{3-}$

loss of a gold atom and two ligands. This was the first fragmentation of this kind observed, and had not been previously observed in positive-mode ESI-MS experiments. High-resolution spectra matches for peaks selected from [25,18,2], [24,16,0], and a comparison to show that [25,18,0] does not match with a hypothetical peak for Oct_4N^+ bound to [24,16,0] are presented in Figure A6.1. For z = 3- ions, the predominant core charge for the [25,18,0], [25,18,1], and [25,18,2] sets of ions is 1-, as evidenced by the high-resolution matches for $Au_{25}(S(CH_2)_2Ph)_5(SPhCOO)_{13}H_{11}^{3-}$, $Au_{25}(S(CH_2)_2Ph)_4(SPhCOO)_{14}H_{11}(Oct_4N)^{3-}$, and $Au_{25}(S(CH_2)_2Ph)_4(SPhCOO)_{14}H_{10}(Oct_4N)_2^{3-}$. This core charge is consistent with the observation of $Au_{25}(S(CH_2)_2Ph)_{18}^-$ and was further evidence that the native Au_{25} nanoparticles contained a 1- core charge. The 2- ions are expected to be shifted to 1 m/z higher mass than the 3- ions due to the presence of an additional proton. The shift is observed, but in some cases, it appears to be a 1 to 2 m/z shift, which suggests a mixture of 1- and 0 oxidation core charges.

6.3.2 Ligand Exchange with *N,N,N*-trimethyl(11-mercaptoundecyl)-ammonium chloride.

The ESI-TOF mass spectrum of the reaction replacing $-S(CH_2)_5CH_3$ with $-S\text{-}TMA^+$ ligands on what we previously referred to as "Au_{140}" nanoparticles is presented in Figure 6.2. The interesting low mass fragments, identified as $[Au_4L_4]^{4+}$ are particularly useful for analyzing the structure of this larger nanoparticle, and how it may be similar to $Au_{25}(SR)_{18}$. No other familiar and recognizable fragments were identified in this mass spectrum. Recent theoretical and experimental results confirm that "Au_{140}" is actually $Au_{144}(SR)_{60}$ or $Au_{144}(SR)_{59}$ or a mixture of the two.[24,25]

Figure 6.2. ESI-TOF-MS data of a "Au_{144}" sample with a hexanethiolate monolayer that has undergone ligand exchange with $[HSC_{11}N^{+}(CH_3)_3][Cl^{-}]$ or HS-TMA. Among the many low mass peaks in the spectrum can be found Au_4L_4 fragments of the parent ion that are ionized via the presence of the ammonium ligands. The Au_4L_4 peaks are labeled with (number), e.g., the number of –S-TMA ligands (which directly determines z) that are bound to the presumably cyclic gold tetramer. The inset shows a close-up of one experimental (black) peak, $[Au_4(S\text{-}TMA)_4]^{4+}$, and a simulation (red). No other familiar fragments were identified.

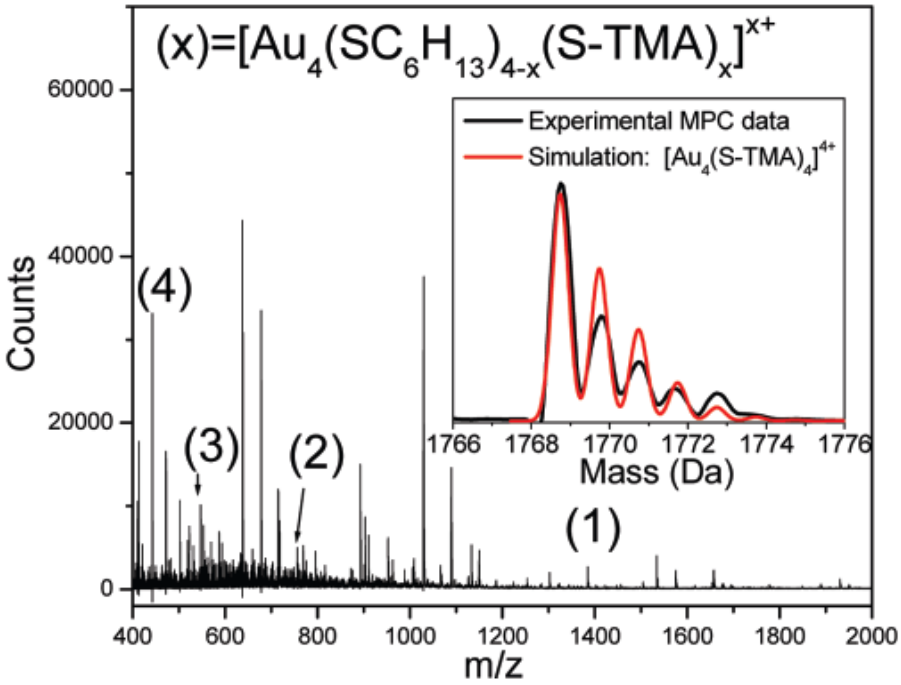
(x)=[Au4(SC6H13)4-x(S-TMA)x]x+
Experimental MPC data
Simulation: [Au4(S-TMA)4]4+
Counts
m/z
Mass (Da)
(1)
(2)
(3)
(4)

Furthermore, theory[24] suggests that $Au_{144}L_{60}$ is comprised of a Au_{114} core surrounded by 30 AuL_2 "semirings," which are shorter than the semirings observed in $Au_{25}(SR)_{18}$. These AuL_2 units are not detected in our experiment, which further suggests that $[Au_4L_4]^{4+}$ is the result of rearrangements of possible surface units.

That small gold nanoparticles fragment under CID and non-CID conditions has been established previously.[26] Specifically, Au_{25} was exchanged with –S-PEG ligands ($–S(CH_2CH_2O)_5CH_3$) and analyzed using low-energy collision induced dissociation tandem mass spectrometry (CID-MS/MS). Studying the resulting fragments in the 100-2000 m/z range allows for a direct correlation with the published crystal structure[5] and the small ions formed during CID. It was determined that $[Na_2Au_2L_3]^{1+}$ was formed, representing an entire loss of a semiring, as well as the further fragmented $[Na_2AuL_2]^{1+}$. In addition to these fragments, $[NaAu_3L_3]^{1+}$ and $[NaAu_4L_4]^{1+}$ were also observed, representing a more complicated dissociation/rearrangement from a mechanism that is currently unknown. Interestingly, $[NaAu_4L_4]^{1+}$ was the second most prominent of these fragment ions, and is the same fragment that is observed in the aforementioned experiment with Au_{144} and its fragmentation after ligand exchange with –S-TMA^+. That the two different sized nanoparticles produce identical fragment ions shed possible light on the surface structure of Au_{144}, which currently lacks experimental crystal structure evidence, yet theoretical approaches[24] predict the presence of semirings.

6.3.3 Ligand Exchange with benzyl mercaptan. It is often desirable to analyze Au_{25} with a complete ligand shell that differs from the original native shell composed of $–S(CH_2)_2Ph$ ligands. Guo, *et al.*,[7] performed a set of ligand exchange

reactions using the *para*-substituted thiophenols and reported the electrochemistry and optical properties of $Au_{25}(SPhX)_{18}$ nanoparticles (at the time mislabeled as $Au_{38}(SPhX)_{24}$). In the modified Brust reaction in toluene,[18,19] only a few ligands are compatible with the clean-up procedure described in 6.2.1. Thus, the synthesis of $Au_{25}(SCH_2Ph)_{18}$ nanoparticles fails, due to problems with purification steps. It became therefore desirable to attempt a ligand exchange reaction to fully convert the $–S(CH_2)_2Ph$ ligand shell to completely another ligand (in this example, $–SCH_2Ph$).

Depending on the initial nanoparticle and incoming thiol concentration, ligand exchange reactions reach either an equilibrium state, a near-complete exchange, or are at a kinetically determined mixed-monolayer state.[12] The generalized form of the ligand exchange reaction is given below.

$$MX_mY_{N-m} + Y \underset{k_{Xon}}{\overset{k_{Xoff}}{\rightleftharpoons}} MX_{m-1}Y_{N-m+1} + X \qquad \text{(Equation 6.1)}$$

where X is the original ligand of choice, in this case $–S(CH_2)_2Ph$, and Y is the incoming ligand, in this case $–SCH_2Ph$. When the ratio of Y/X is large, the kinetics follow a pseudo-first order rate.[7,8,12] The details of the kinetic model of the ligand exchange reaction were given in reference 12, successfully predicting binomial distributions for the equilibrium conditions of ligand exchange reactions. The equilibrium state not only depends on the concentration of the reactants, but also on the forward (k_{Xoff}) and reverse (k_{Xon}) rate constants. For example, in the case of a ligand exchange with –SPh at a very large excess concentration of 50× per bound ligand (900× per Au_{25}), the reaction still only reached an average of 16 ligands exchanged over the course of 72 hours. This method shows that even at large excesses of incoming thiol, replacing all 18 ligands becomes increasingly difficult as the reaction proceeds. To overcome this kinetic barrier,

we utilized a set of back-to-back ligand exchange reactions, with very long reaction times. Starting with an initial nanoparticle concentration of 0.63 mM in dichloromethane and a thiol excess of 5× per ligand (90× per Au_{25}), we allowed the reaction to proceed for 24 hours. Subsequently, the reaction mixture was dried and washed thoroughly with methanol to remove excess $–S(CH_2)_2Ph$ and $–SCH_2Ph$. The product was re-dissolved at a concentration of 0.63 mM with the same excess as before and allowed to react for 72 hours. The process was completed for a third (24 hours) and a fourth (48 hours) reaction, each time removing the liberated $–S(CH_2)_2Ph$.

The final product of the ligand exchange reaction, as observed by MALDI-MS, is shown in Figure 6.3, demonstrating the complete ligand exchange of $Au_{25}(S(CH_2)_2Ph)_{18}$ to the final product of $Au_{25}(SCH_2Ph)_{18}$. The main peak at 7142 m/z represents the fully exchanged $Au_{25}(SCH_2Ph)_{18}$. The smaller peak near 5862 m/z represents the most common fragment observed in these nanoparticles: $Au_{21}(SCH_2Ph)_{14}$, or a loss of $Au_4(SCH_2Ph)_4$. The other peaks are most likely further fragmentations and coordination with Na^+ (See Figure A6.2 for a detailed analysis of the remaining peaks).

6.3.4 Ligand Exchange with *para*-substituted thiophenolates (–SPhX). This section briefly outlines the electron self-exchange dynamics in solid state gold nanoparticle films. It has been shown previously,[23,27] that the self-exchange rate depends on the size of the nanoparticle core. $Au_{25}(SR)_{18}$ has a second-order rate constant(k_{EX}) that is ~10^3× smaller than that for $Au_{144}(SR)_{59}$, and an activation energy barrier that is ~3× as large. For this experiment, we aimed to study if the nature of the monolayer plays a role in electron self-exchange dynamics of solid-state films. There has been a lot of

Figure 6.3: MALDI-TOF MS of the fully exchanged product $Au_{25}(SCH_2Ph)_{18}$. The mass at 7142 m/z represents the fully exchanged material and the peak near 5862 m/z is the fragmented $Au_{21}(SCH_2Ph)_{14}$, which is commonly observed in $Au_{25}(SR)_{18}$ MALDI data. Other peaks are further fragments arising from losses of Au and $–SCH_2Ph$ and coordination with Na^+ cations.

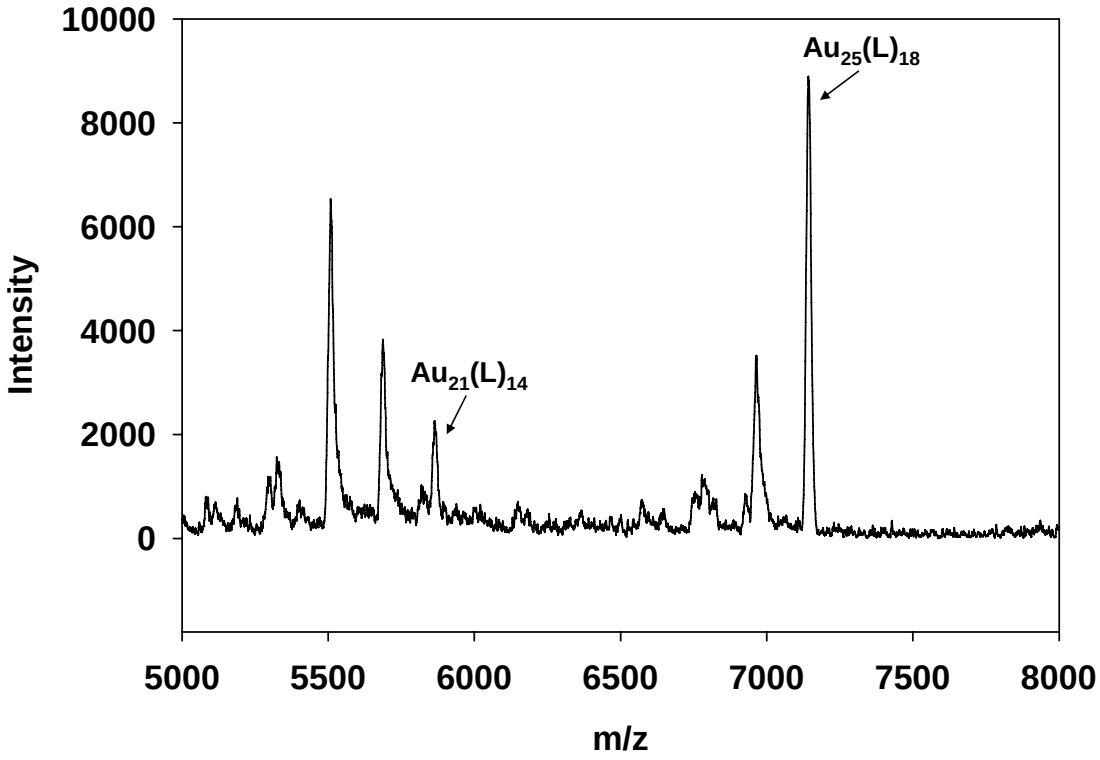
10000
8000
6000
4000
2000
0
Intensity
Au25(L)18
Au21(L)14
5000
5500
6000
6500
7000
7500
8000
m/z

research observing the drastic effects that electronically coupled ligands have on the core of Au_{25} nanoparticles. Specific focus has been on the rate of ligand exchange reactions,[7,8] their electrochemical and optical behavior,[7] and in experimental and theoretical studies on how they polarize the bonds on the semirings.[13] In these experiments, we performed ligand exchange reactions to introduce an electron-withdrawing and electron-donating ligand (–SPhBr and $–SPhOCH_3$, respectively). Figure 6.4 shows the resultant MALDI-TOF mass spectrum of the ligand exchange products. The binomial distributions for the –SPhBr and $–SPhOCH_3$ products are centered at 11 and 6 ligands exchanged respectively. Figure 6.5 presents the dependence of the electronic conductivities (σ_{EL}) on the percent of the studied nanoparticle in the oxidized state, which were prepared as described previously.[23] These conductivities are related to the electron self-exchange rate constant (k_{EX}) in the film by the relationship given below:

$$k_{EX} = \frac{6RT\sigma_{EL}}{10^{-3}F^2\delta^2[Au_{25}^{1-}][Au_{25}^{0}]} \qquad \text{(Equation 6.2)}$$

where F is Faraday's constant, δ is the center-to-center electron hopping distance, and $[Au_{25}^{z}]$ is the concentration of the nanoparticle in the respective oxidation state (z). From the curves in Figure 6.5, the electron self-exchange rate constant can be extrapolated. That for $Au_{25}(S(CH_2)_2Ph)_{18}^{1-/0}$ was extrapolated previously (1.6×10^6 $M^{-1}s^{-1}$).[23] The presence of electron-withdrawing ligands (-SPhBr) slightly increases the self-exchange rate to 2.5×10^6 $M^{-1}s^{-1}$, while electron-donating ligands ($-SPhOCH_3$) slightly decreases that rate to 0.7×10^6 $M^{-1}s^{-1}$. Detailed analysis and theoretical approaches examining these results is yet to be published and currently only speculative. The authors from reference 23 speculate that the differences in the conductivities and electron self-exchange of Au_{25} and Au_{144} are largely due to the inner-sphere reorganization component that is present

Figure 6.4: MALDI-TOF MS of the ligand exchange products (left) $Au_{25}(S(CH_2)_2Ph)_{18-x}(SPhBr)_x$ and (right) $Au_{25}(S(CH_2)_2Ph)_{18-x}(SPhOCH_3)_x$. In the –SPhBr exchange, the separation of the peaks represent the difference in molecular weight of the two ligands (50.8 m/z) centered around eleven ligands exchanged. In the $–SPhOCH_3$ exchange, that difference is only 2 m/z, so the peaks in the binomial distribution overlap due to instrument limitation and thus appears as only one broad peak centered around six ligands exchanged.

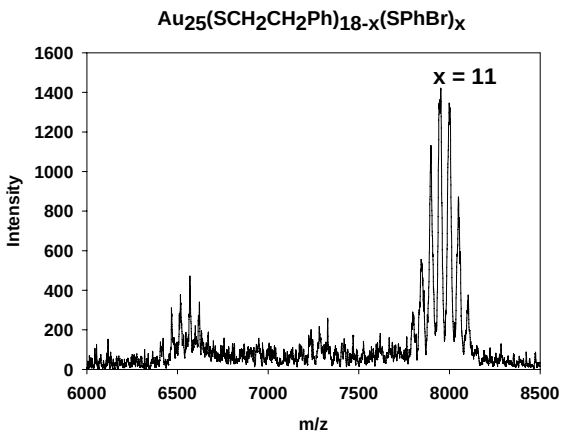
Au25(SCH2CH2Ph)18-x(SPhBr)x
x = 11
Intensity
m/z
1600
1400
1200
1000
800
600
400
200
0
6000
6500
7000
7500
8000
8500

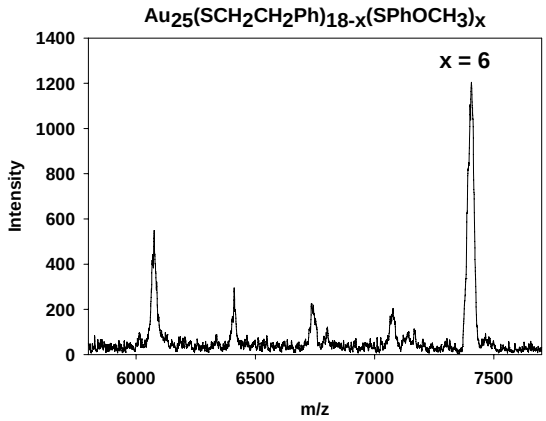
Au25(SCH2CH2Ph)18-x(SPhOCH3)x
x = 6
Intensity
m/z
1400
1200
1000
800
600
400
200
0
6000
6500
7000
7500

Figure 6.5: Effect of the percent in the oxidized form, $Au_{25}(S(CH_2)Ph)_{18-x}(SR)_x^0$, on electron hopping conductivity σ_{EL} in solid state films for (black) SR = $S(CH_2)_2Ph$ (red) SR = SPhBr and (green) SR = $SPhOCH_3$. The red curves are σ_{EL} values simulated for a bimolecular reaction with rate constants (black) 1.5×10^6 $M^{-1}s^{-1}$ (red) 2.5×10^6 $M^{-1}s^{-1}$ and (green) 0.7×10^6 $M^{-1}s^{-1}$. These are all compared to that of (yellow) $Au_{144}(S(CH_2)_5CH_3)_{59}$ which is fitted with a bimolecular rate constant of 4.3×10^9 $M^{-1}s^{-1}$.

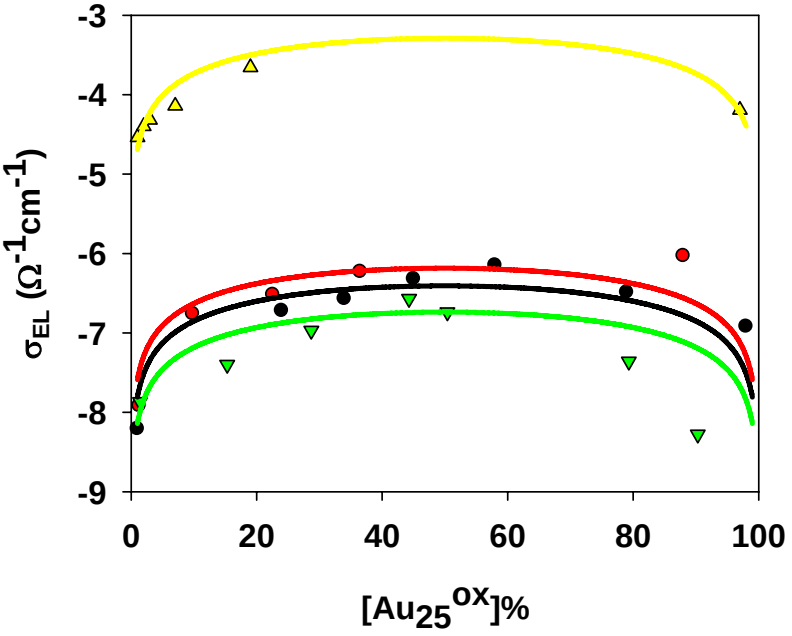
-3
-4
-5
-6
-7
-8
-9
0
20
40
60
80
100
σEL (Ω-1cm-1)
[Au25OX]%

solely in $Au_{25}(SR)_{18}$ nanoparticles. They compared the experimental activation parameters with the calculated outer-sphere reorganization component giving by the equation below:

$$\Delta G_{os} = \frac{\lambda}{4} = \frac{e^2 N_A}{16\pi\varepsilon_o}\left(\frac{1}{2r_1}+\frac{1}{2r_2}-\frac{1}{r_{12}}\right)\left(\frac{1}{\varepsilon_{op}}-\frac{1}{\varepsilon_s}\right) \qquad \text{(Equation 6.3)}$$

where e is the charge on an electron, N_A is Avogadro's number, ε_o is the permittivity of free space, r_1 and r_2 are the reactant radii, and r_{12} is the center-to-center separation distance. ε_{op} and ε_s are the optical (square of the refractive index) and the static dielectric constants respectively. Analyzing this equation with respect to $Au_{25}(S(CH_2)_2Ph)_{18}$ and the newly introduced ligands (–SPhX) presented in this chapter, it is apparent that a number of outer-sphere variables presented in equation 6.3 (the radii of the reactants, the center-to-center distances, and the optical dielectric constants) differ in the presence of these new thiolates. Furthermore, it has been shown that strongly-electron withdrawing ligands induce a strong polarization effect on the atoms of the ligands, as well as the S and the Au on the semirings (though to a lesser degree).[13] Since there is a structural alteration between oxidation states of $Au_{25}(S(CH_2)_2Ph)_{18}$, as proven by ^{1}H NMR and crystallographic techniques,[27,5,28] it remains possible that the magnitude of the change experienced during oxidation differs with these electron-withdrawing ligands, leading to slight differences in the calculated reorganization energies, and thus varying rates. These are speculations from preliminary data, of which a more detailed description will be required to further explain these interesting changes.

6.3.5 *Ab Initio* Introduction of Mixed-Monolayers. Ligand exchange reactions are not the only method for introducing multiple ligands onto the core of Au_{25}.

In this experiment, two different ligands ($–S(CH_2)_5CH_3$ and $–S(CH_2)_2Ph$) were introduced at varying feed ratios in the initial two-phase Brust reaction. The distribution of the two ligands on the nanoparticle is equivalent to binomial distributions described above; however, the average amount does not coincide with the relative concentrations of the two starting materials. For example, a 50:50 feed ratio of $–S(CH_2)_5CH_3$ and $–S(CH_2)_2Ph$ does not produce a nanoparticle with an average number of nine ligands each. The results of these experiments are given in Figure 6.6. The orange line in Figure 6.6 displays the results of the Brust reaction with a feed ratio of 50:50, but is centered around seven $–S(CH_2)_5CH_3$ and eleven $–S(CH_2)_2Ph$. Agreeing ^1H NMR results are shown in Figure A6.4. The preference of Au_{25} to bind $–(S(CH_2)_2Ph$ may arise from multiple reasons: including relative rates of thiol reaction, solubility properties during work-up, and favored formation of $Au^I(S(CH_2)_2Ph)$ during formation of the gold-thiolate polymer.

6.4 Conclusions

The information on electronic and structural properties of small gold nanoparticles, such as $Au_{25}(SR)_{18}$ and $Au_{144}(SR)_{59}$, would be vastly limited if it were not for the incredible versatility of the ligand shell. For synthetic reasons, the default ligands are normally phenylethanethiol ($HS(CH_2)_2Ph$) and hexanethiol ($HS(CH_2)_5CH_3$) for Au_{25} and Au_{144} respectively. In many very important cases, it has been necessary to replace these default ligands using ligand exchange reactions to introduce molecules with specific functional groups. This chapter presents a survey of important ligand exchange reactions performed over the last five years, and how the resulting mixed-monolayer participated in

Figure 6.6. Monolayer ligand distribution of the mixed Brust reaction product $Au_{25}(S(CH_2)_2Ph)_{18-x}(S(CH_3)_5CH_3)x$ as observed by MALDI-MS spectrum using different starting ligand ratios 25:75, 50:50, and 75:25.

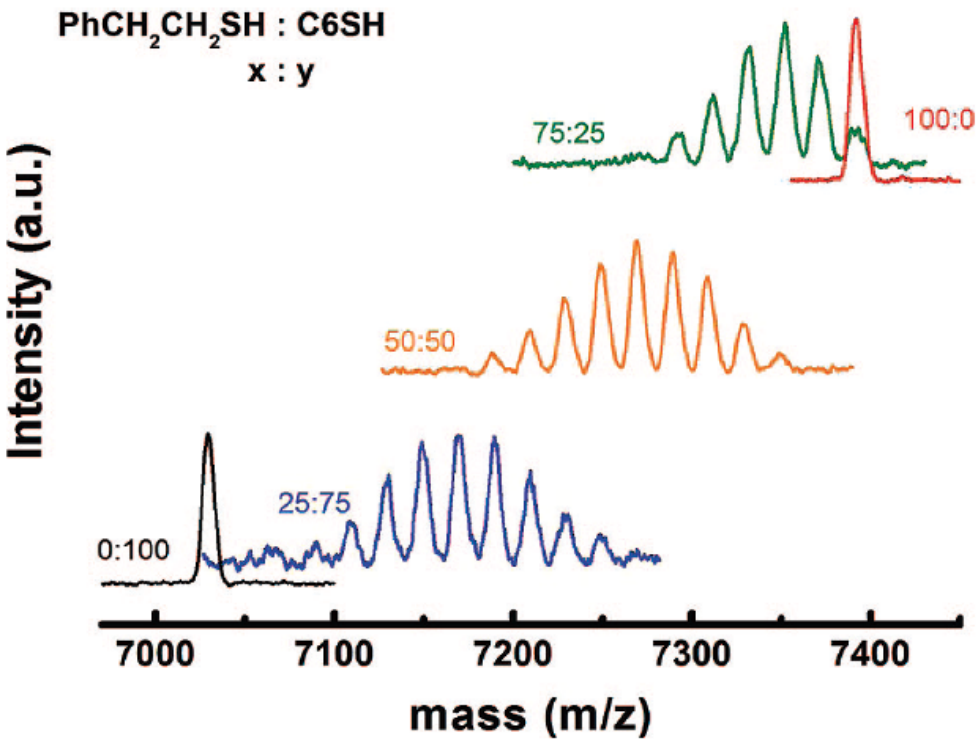
PhCH2CH2SH : C6SH
x : y
Intensity (a.u.)
75:25
100:0
50:50
25:75
0:100
7000
7100
7200
7300
7400
mass (m/z)

obtaining crucial information on molecular formula, oxidation state, kinetics, electron transfer dynamics, and more.

6.5 Acknowledgments

The materials presented in this chapter were my contributions towards larger body of works now published as references 10, 12, and 20, as well as research that is yet to be published. I would like to thank my co-authors of those publications for the opportunity to participate in such interesting research, as well as undergraduates that have worked with me over the years: Alexander deNey, Laura Huff, and Finlay McCallum. I urge the readers to read those papers for a more detailed and comprehensive analysis of the implications of those studies.

6.6 References

(1) Sardar, R.; Funston, A. M.; Mulvaney, P.; Murray, R. W. *Langmuir*. **2009**, *25*, 13840-13851.

(2) Rothrock, A. R.; Donkers, R. L.; Schoenfisch, M. H. *J. Am. Chem. Soc.* **2005**, *127*, 9362-9363.

(3) Zhu, Y.; Qian, H.; Drake, B. A.; Jin, R. *Angew. Chem. Int. Ed.* **2010**, *49*, 1295-1298.

(4) Donkers, R. L.; Lee, D.; Murray, R. W. *Langmuir* **2004**, *20*, 1945-1952.

(5) Heaven, M. W.; Dass, A.; White, P. S.; Holt, K. M.; Murray, R. W. *J. Am. Chem. Soc.* **2008**, *130*, 3754-3755.

(6) Akola, J.; Walter, M.; Whetten, R. L.; Häkkinen, H.; Grönbeck, H. *J. Am. Chem. Soc.* **2008**, *130*, 3756-3757.

(7) Guo, R.; Murray, R. W. *J. Am. Chem. Soc.* **2005**, *127*, 12140-12143.

(8) Guo, R.; Song, Y.; Wang, G.; Murray, R. W. *J. Am. Chem. Soc.* **2005**, *127*, 2752-2757.

(9) Tracy, J. B.; Kalyuzhny, G.; Crowe, M. C.; Balasubramanian, R.; Choi, J.-P.; Murray, R. W. *J. Am. Chem. Soc.* **2007**, *129*, 6706-6707.

(10) Tracy, J. B.; Crowe, M. C.; Parker, J. F.; Hampe, O.; Fields-Zinna, C. A.; Dass, A.; Murray, R. W. *J. Am. Chem. Soc.* **2007**, *129*, 16209-16215.

(11) Dass, A.; Stevenson, A.; Dubay, G. R.; Tracy, J. B.; Murray, R. W. *J. Am. Chem. Soc.* **2008**, *130*, 5940-5946.

(12) Dass, A.; Holt, K.; Parker, J. F.; Feldberg, S. W.; Murray, R. W. *J. Phys. Chem. C.* **2008**, 112, 20276-20283.

(13) a) Parker, J. F.; Kacprzak, K. A.; Lopez-Acevedo, O.; Hakkinen, H.; Murray, R. W. *J. Phys. Chem. C* **2010**, *114,* 8276-8281. b) Chapters 4 and 5 of this Dissertation.

(14) Dass, A.; Guo, R.; Tracy, J. B.; Balasubramanian, R.; Douglas, A. D.; Murray, R. W. *Langmuir*, **2008**, *24*, 310-315.

(15) Aguila, A.; Murray, R. W. *Langmuir*, **2000**, *16*, 5949-5954.

(16) Ingram, R. S.; Murray, R. W. *Langmuir*, **1998**, *14*, 4115-4121.

(17) Wolfe, R. L.; Balasubramanian, R.; Tracy, J. B.; Murray, R. W. *Langmuir*, **2007**, *23*, 2247-3354.

(18) Brust, M.; Walker, M.; Bethell, D.; Schiffrin, D. J.; Whyman, R. *J. Chem. Soc., Chem. Commun.* **1994**, 801-802.

(19) Donkers, R. L.; Lee, D.; Murray, R. W. *Langmuir* **2004**, *20*, 1945-1952.

(20) Parker, J. F.; Weaver, J. E. F.; McCallum, F.; Murray, R. W. **2010**, *Unpublished Results*

(21) Tien, J.; Terfort, A.; Whitesides, G. *Langmuir* **1997**, *13*, 5349-5355.

(22) Cliffel, D. E.; Zamborini, F. P.; Gross, S. M.; Murray, R. W. *Langmuir* **2000**, *16*, 9699-9702.

(23) Choi, J-P; Murray, R. W. *J. Am. Chem. Soc.* **2006**, *128*, 10496-10502.

(24) Lopez-Acevedo, O.; Akola, J.; Whetten, R. L.; Gronbeck, H.; Hakkinen, H. *J. Phys. Chem. C* **2009**, *113*, 5035–5038.

(25) Chaki, N. K.; Negishi, Y.; Tsunoyama, H.; Shichibu, Y.; Tsukuda, T. *J. Am. Chem. Soc.* **2008**, *130*, 8608–8610.

(26) Fields-Zinna, C. A.; Sampson, J. S.; Crowe, M. C.; Tracy, J. B.; Parker, J. F.; deNey, A. M.; Muddiman, D. C.; Murray, R. W. *J. Am. Chem. Soc.* **2009**, *131*, 13844-13851.

(27) Parker, J. F.; Choi, J-P.; Wang, W.; Murray, R. W. *J. Phys. Chem. C* **2008**, *112*, 13976-13981.

(28) Zhu, M.; Eckenhoff, W. T.; Pintauer, T.; Jin, R. *J. Phys. Chem. C* **2008**, *112*, 14221-14224.

Appendix 6

Survey of Ligand Exchange Reactions on Small Gold Nanoparticles

Some of the materials in this Appendix are selected supplementary data published as Supporting Information from references 10 and 12. Others are unpublished figures; all are used to support the data in Chapter 6.

Figure A6.1. Mass spectra for the HSPhCOOH exchange product from Figure 6.1, acquired in 100% CH_3OH. The data for the 2- ions are scaled by 4×. Left column: sets of peaks for (a) $Au_{25}(S(CH_2)_2Ph)_{18-x}(SPhCOO)_xH_{x-n}(Oct_4N)^{z-}$, (b) $Au_{25}(S(CH_2)_2Ph)_{18-x}(SPhCOO)_xH_{x-n}(Oct_4N)_2^{z-}$, and (d) $Au_{24}(S(CH_2)_2Ph)_{16-x}(SPhCOO)_xH_{x-n}^{z-}$. Right column: high-resolution comparison between data (thin lines) and simulations (thick lines) shows an excellent match for (c) $Au_{25}(S(CH_2)_2Ph)_4(SPhCOO)_{14}H_{10}(Oct_4N)_2^{3-}$ and (e) $Au_{24}(S(CH_2)_2Ph)_4(SPhCOO)_{12}H_9^{3-}$ and a mismatch for (f) the simulation, $Au_{24}(S(CH_2)_2Ph)_2(SPhCOO)_{14}H_{10}(Oct_4N)^{3-}$. Ref. 10.

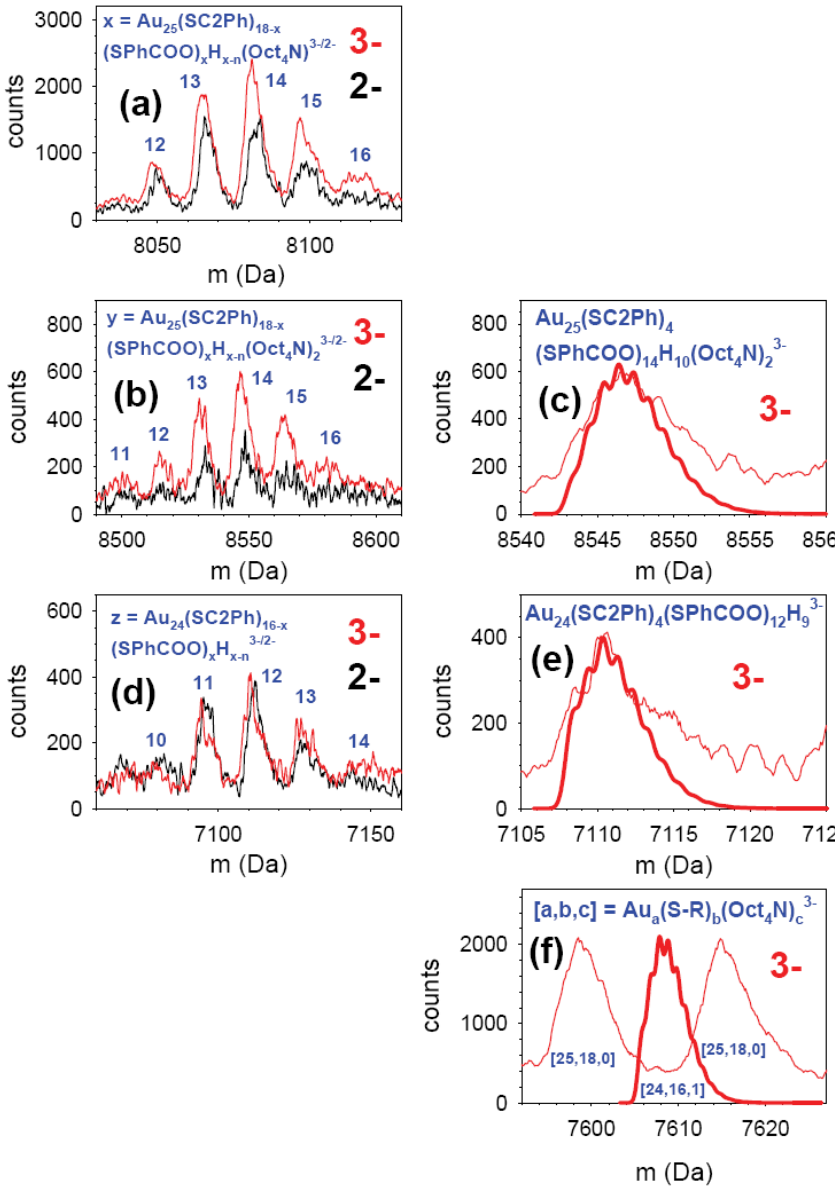
x = Au25(SC2Ph)18-x
(SPhCOO)xHx-n(Oct4N)3-/2-
3-
2-
(a)
12
13
14
15
16
counts
m (Da)
y = Au25(SC2Ph)18-x
(SPhCOO)xHx-n(Oct4N)2 3-/2-
(b)
11
Au25(SC2Ph)4
(SPhCOO)14H10(Oct4N)2 3-
(c)
z = Au24(SC2Ph)16-x
(SPhCOO)xHx-n 3-/2-
(d)
10
Au24(SC2Ph)4(SPhCOO)12H9 3-
(e)
[a,b,c] = Aua(S-R)b(Oct4N)c 3-
(f)
[25,18,0]
[24,16,1]

Figure A6.2. MALDI-TOF MS of the fully ligand exchanged product $Au_{25}(SCH_2Ph)_{18}$. This is the first mass spectrum observed for a fully exchanged nanoparticle product. The left panel shows the identification of the peaks, starting with $Au_{25}L_{18}$ at 7142 m/z and the resulting fragmentations. Interestingly, a fragmentation pattern involving a loss of Au and coordination with Na^+ is observed several times in the spectrum. Such fragmentation is not observed with $Au_{25}(S(CH_2)_2Ph)_{18}$ and the mechanism of their formation is currently unknown. However, the right panel shows an overlay (red) of the theoretical m/z for these assignments, indicating a very nice match. The green curves demonstrate where $Au_{25}(S(CH_2)_2Ph)_{18}$ would lie in this mass spectrum and its common fragmentation to $Au_{21}L_{14}$.

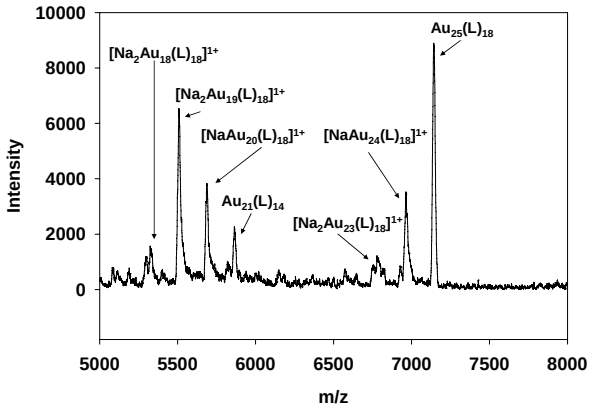
10000
8000
6000
4000
2000
0
Intensity
5000
5500
6000
6500
7000
7500
8000
m/z
[Na2Au18(L)18]1+
[Na2Au19(L)18]1+
[NaAu20(L)18]1+
[NaAu24(L)18]1+
Au25(L)18
Au21(L)14
[Na2Au23(L)18]1+

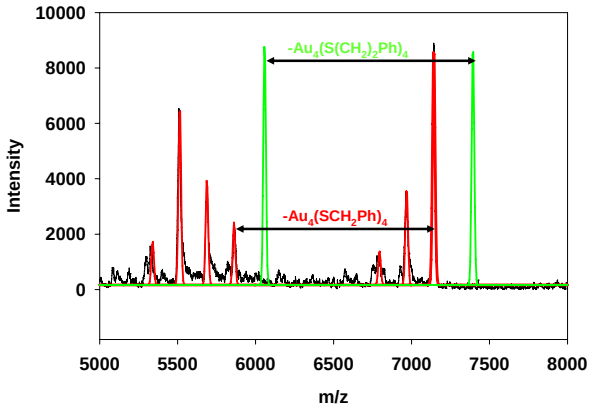
10000
8000
6000
4000
2000
0
Intensity
5000
5500
6000
6500
7000
7500
8000
m/z
-Au4(S(CH2)2Ph)4
-Au4(SCH2Ph)4

Figure A6.3. (left panel) Comparison of (red) the fully ligand exchanged product $Au_{25}(SCH_2Ph)_{18}$ and that of the one synthesized using the method described in (black) Chapter 2 of this dissertation. The profiles are similar, with the exchanged product appearing slightly oxidized based on the relative position of the 680 nm peak. The extremely large absorbance less than 450 nm is still yet to be explained, but may be due to excess thiolates present, even though none were observed in the ^1H NMR. (right panel) Cyclic Voltammetry of $Au_{25}(SCH_2Ph)_{18}$ in 0.1 M But_4NClO_4 in CH_2Cl_2, with a Pt-disc working, Pt-coil counter, and Ag/AgCl reference electrodes. Scan rate was 100 mV/s with a sampling rate at 1 mV/s. The peaks have a separation roughly equal to that of the $–S(CH_2)_2Ph$ counterpart, yet the peaks are shifted about 100 mV pore positive.

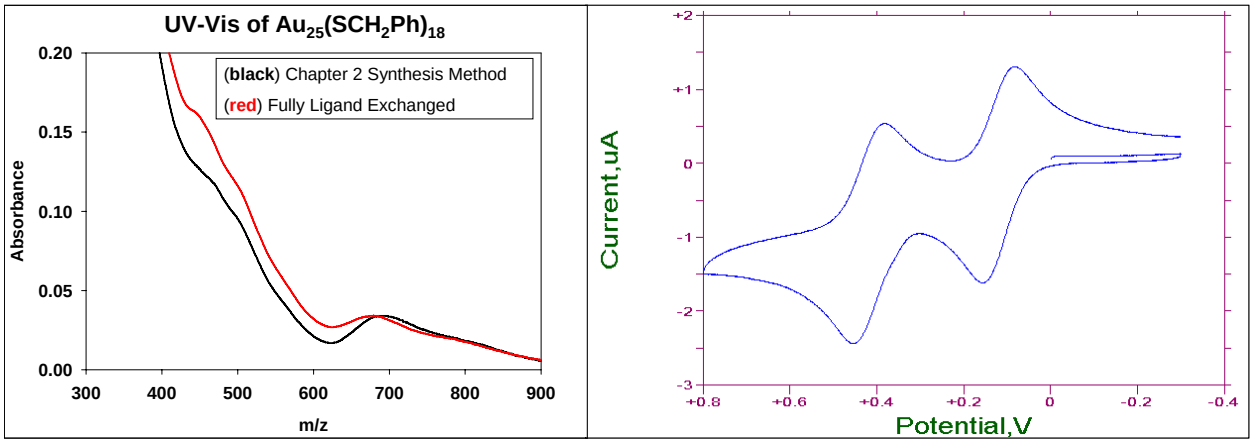
UV-Vis of $Au_{25}(SCH_2Ph)_{18}$
(black) Chapter 2 Synthesis Method
(red) Fully Ligand Exchanged
Absorbance
0.20
0.15
0.10
0.05
0.00
300
400
500
600
700
800
900
m/z
Current,uA
+2
+1
0
-1
-2
-3
+0.8
+0.6
+0.4
+0.2
0
-0.2
-0.4
Potential,V

Figure A6.4: ^{1}H NMR spectrum of $Au_{25}(S(CH_2)_2Ph)_x(S(CH_2)_5CH_3)_y$ as prepared using a 50:50 mixture of phenylethanethiol and hexanethiol in the Brust reaction. The spectrum was obtained in methylene chloride-d_2 using a Bruker 400 MHz widebore spectrometer at 300 K. The integration of the phenyl protons of the phenylethanethiolate were compared with those of the terminal methyl protons of the hexanethiolate. The terminal methyl proton resonances of hexanethiolate slightly overlap those of the tetraoctylammonium counterion, so only the right half of the peak was integrated. The area of the half-peak was multiplied by two to estimate the total integration and a phenyl:methyl ratio of 1.00:0.42, which is indicative of an *average* ligand composition of 10.6 phenylethanethiolates and 7.4 hexanethiolates per NP. Ref. 12.

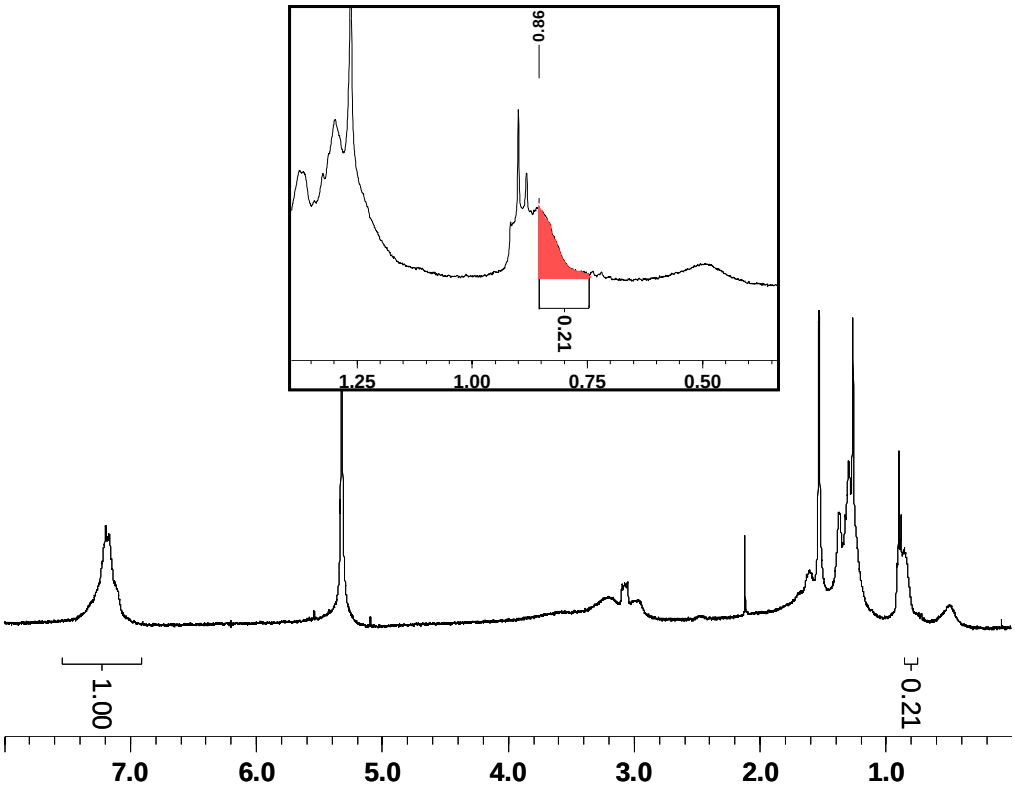
98.0
0.21
1.25
1.00
0.75
0.50
1.00
0.21
7.0
6.0
5.0
4.0
3.0
2.0
1.0